frontiers | Research Topics

Advancing our understanding of the cardiac conduction system to prevent arrhythmias

Edited by
Edward Joseph Vigmond and Jason D. Bayer

Published in
Frontiers in Physiology

ISSN 1664-8714
ISBN 978-2-8325-7321-1
DOI 10.3389/978-2-8325-7321-1

Generative AI statement
Any alternative text (Alt text) provided alongside figures in the articles in this ebook has been generated by Frontiers with the support of artificial intelligence and reasonable efforts have been made to ensure accuracy, including review by the authors wherever possible. If you identify any issues, please contact us.

About Frontiers

Frontiers is more than just an open access publisher of scholarly articles: it is a pioneering approach to the world of academia, radically improving the way scholarly research is managed. The grand vision of Frontiers is a world where all people have an equal opportunity to seek, share and generate knowledge. Frontiers provides immediate and permanent online open access to all its publications, but this alone is not enough to realize our grand goals.

Frontiers journal series

The Frontiers journal series is a multi-tier and interdisciplinary set of open-access, online journals, promising a paradigm shift from the current review, selection and dissemination processes in academic publishing. All Frontiers journals are driven by researchers for researchers; therefore, they constitute a service to the scholarly community. At the same time, the *Frontiers journal series* operates on a revolutionary invention, the tiered publishing system, initially addressing specific communities of scholars, and gradually climbing up to broader public understanding, thus serving the interests of the lay society, too.

Dedication to quality

Each Frontiers article is a landmark of the highest quality, thanks to genuinely collaborative interactions between authors and review editors, who include some of the world's best academicians. Research must be certified by peers before entering a stream of knowledge that may eventually reach the public - and shape society; therefore, Frontiers only applies the most rigorous and unbiased reviews. Frontiers revolutionizes research publishing by freely delivering the most outstanding research, evaluated with no bias from both the academic and social point of view. By applying the most advanced information technologies, Frontiers is catapulting scholarly publishing into a new generation.

What are Frontiers Research Topics?

Frontiers Research Topics are very popular trademarks of the *Frontiers journals series*: they are collections of at least ten articles, all centered on a particular subject. With their unique mix of varied contributions from Original Research to Review Articles, Frontiers Research Topics unify the most influential researchers, the latest key findings and historical advances in a hot research area.

Find out more on how to host your own Frontiers Research Topic or contribute to one as an author by contacting the Frontiers editorial office: frontiersin.org/about/contact

Advancing our understanding of the cardiac conduction system to prevent arrhythmias

Topic editors
Edward Joseph Vigmond — Université de Bordeaux, France
Jason D. Bayer — Université de Bordeaux, France

Citation
Vigmond, E. J., Bayer, J. D., eds. (2026). *Advancing our understanding of the cardiac conduction system to prevent arrhythmias*. Lausanne: Frontiers Media SA.
doi: 10.3389/978-2-8325-7321-1

Topic Editor Dr. Edward Joseph Vigmond is a co-founder of Numericor GmbH, a private company which performs cardiac simulations and licenses simulation software. Both Dr. Vigmond and Dr. Jason D Bayer declare no conflict of interest with regard to the Research Topic subject.

Table of contents

frontiers | Frontiers in Physiology

TYPE Editorial
PUBLISHED 11 December 2025
DOI 10.3389/fphys.2025.1754225

OPEN ACCESS

EDITED AND REVIEWED BY
Ademuyiwa S. Aromolaran,
The University of Utah, United States

*CORRESPONDENCE
Edward Joseph Vigmond,
edward.vigmond@u-bordeaux.fr

RECEIVED 25 November 2025
ACCEPTED 27 November 2025
PUBLISHED 11 December 2025

CITATION
Vigmond EJ and Bayer J (2025) Editorial: Advancing our understanding of the cardiac conduction system to prevent arrhythmias. *Front. Physiol.* 16:1754225.
doi: 10.3389/fphys.2025.1754225

Editorial: Advancing our understanding of the cardiac conduction system to prevent arrhythmias

Edward Joseph Vigmond* and Jason Bayer

Univ. Bordeaux, CNRS, Bordeaux INP, IMB, UMR 5251, IHU Liryc, Talence, France

KEYWORDS

purkinje system, left bundle branch area pacing, cardiac conduction system, arrhythmia, ECG

Editorial on the Research Topic
Advancing our understanding of the cardiac conduction system to prevent arrhythmias

Introduction

The cardiac conduction system is responsible for the heart's rapid activation and is vital for its optimal functioning. Its ventricular components were only discovered and satisfactorily explained at the beginning of the 20th century when Tawara meticulously traced the cardiac conduction system (CCS) from its origin at the atrioventricular node to the Purkinje fibres, which had been described some 70 years earlier but with an unknown function. Its fine and integrated structure prevents it from being seen in its entirety by the naked eye, as well as limits the magnitudes of the electrical signals produced by it. However, despite its small mass, the CCS greatly affects propagation through myocardial tissue. Even during non-sinus activation, the CCS is activated retrogradely, and exerts its influence on activation (Pollard et al., 1997).

Dysfunction of the CCS has serious consequences. Pathologies involving it can lead to arrhythmias through several mechanisms (Haissaguerre et al., 2016); the CCS can be a source of ectopic beats which interact with the sinus beat to produce reentry (Deo et al., 2010); it can help sustain arrhythmias by providing escape conduction pathways to allow wave propagation to continue (Bayer et al., 2022); finally, unidirectional block within the CCS can lead to CCS reentries (Wald et al., 1980).

It is the goal of this Research Topic to elucidate how the CCS may contribute to arrhythmias, how to identify CCS involvement when presented with an arrhythmia, as well as how to repair/manipulate the CCS to restore heart function. In this Research Topic, several research teams explored these questions from the basic science level, to the clinic using state-of-the-art biological experiments, clinical measurements, as well as computer modelling.

Basic science

In his review of Purkinje systems and their calcium handling, Stuyvers (*Calcium arrhythmogenicity of Purkinje fibers: importance of the animal model*) argues that large animal models are appropriate for human translation, showing the same mechanisms for arrhythmogenic behaviour in the ischemic and post myocardial infarction heart (ref the paper). For small animals, like mice, changes in gene expression may mimic those occurring in humans under these conditions.

Trying to gain insight for human disease, Vahdat et al. (*Conduction defects and arrhythmias in mdx mice are not associated with a degeneration of the cardiac Purkinje network*) examined conduction disturbances in mice with Duchenne muscular dystrophy. They performed experiments to conclude that the Purkinje system was not affected and conduction disruption was due to fibrosis and reduced sodium current. As Stuyvers argues, these results are translatable to humans.

The exact structure of the CCS is difficult to image in its entirety, given the lack of CCS specific contrast agents and its small mass with fine structures. Furthermore, the electrical signals produced by it are small in magnitude. In light of this, Boukens et al. (*Functional conduction system mapping in sheep reveals Purkinje spikes in the free wall of the right ventricular outflow tract*) further clarified whether Purkinje fibres were present in the right ventricular outflow tract, a region thought to be highly arrhythmogenic (Aras et al., 2022). They recorded signals corresponding to Purkinje activations and staining for connexon 40, a CCS gap junction protein, was positive, demonstrating the presence of the CCS. This has important implications for future treatment of arrhythmias arising from this region.

Clinical

ECG analysis cannot be performed without considering the role of the CCS, whether in a healthy or pathological state. The distribution of pulses by the CCS is reflected in the QRS for anterograde activation, and during arrhythmias, it also carries out retrograde atrial activation. Thus, for accurate diagnosis, the role of the CCS is vital, whether it be a source of ectopy, have regions of localized block, or be healthy. This is illustrated in two examples.

Wang et al. (*Case Report: Adenosine-induced atrioventricular dissociation: unmasking monomorphic tachycardia as a diagnostic challenge in a neonate*) removed the influence of the atrioventricular node to improve diagnosis in a neonate. By inhibiting the initial component of the CCS, the atrioventricular node, they blocked propagation of atrial signals into the ventricles and convincingly demonstrated that the arrhythmia continued in the ventricles and was a ventricular tachycardia.

Li et al. (*The λ pattern on time-RR interval scatter plot of neonatal ambulatory ECG: a marker of transient bradycardia*) defined a new rhythm based on time-RR interval scatter plots in neonates. They identified junctional escape rhythms (which often originate in the atrioventricular node or other parts of the CCS) and the gradual return to normal sinus rhythm. Again, the CCS is integral to understanding what is happening, so that the proper treatment may be employed.

Modelling

Due to the fine and integrated structure of the CCS, along with its small mass yielding weak electrical signals, investigating the electrophysiology of both the healthy and pathological states of the CCS in three-dimensions is challenging using the basic science and clinical approaches discussed above. Therefore, computer modelling is used to investigate the CCS in its entirety with both high spatial and temporal resolutions. This allows investigators to test a wider range of hypotheses for the structure/function of the CCS, as illustrated in the following three examples.

Jabbour et al. (*Acute ischaemia and gap junction modulation modify propagation patterns across Purkinje-myocardial junctions*) investigated an unexpected observation that rabbit ischemic right ventricular preparations activated in less time than healthy hearts. By combinging experiments with computer modelling, they suggest that more Purkinje-myocyte junctions become functional during ischemia.

The CCS architecture influences the activation of the ventricles, but whether it also influences reentry is unclear. Bayer et al. (*To reconnect or not reconnect distal Purkinje fibers, that is the question when modelling the Purkinje fiber network*) show in a biophysically-detailed three-dimensional human ventricles model that representing the Purkinje network with a simple tree-like branching structure as opposed to a mesh, results in similar sinus activation, but different retrograde activation and reentry behaviours. This highlights the need for accurate modelling of the CCS, particularly for ectopic foci and pacing studies when activation originates from the ventricular myocardium.

From a more clinical perspective, Strocchi et al. (*Comparing the effects of left bundle branch pacing and leadless right ventricular pacing on intraventricular and interventricular dyssynchrony using in silico modelling*) used a similar modelling methodolgy to investigate the efficacy of resynchronizaton therapies, specifically leadless right ventricular pacing versus left bundle branch pacing. They showed that under most circumstances, directly stimulating the proximal left bundle branch leads improved ventricular synchrony.

Conclusion

The CCS profoundly affects the propagation of electrical signals into and within the ventricles. It is directly responsible for the PQ interval and the shape of the QRS on the ECG which is the major diagnostic tool of cardiology. Treatment of pathologies involving the CCS include ablation of ectopic sources (Nogami et al., 2023), denetworking (Sciacca et al., 2022), and resynchronization therapy (Joza et al., 2025). Indeed, His and left bundle branch area pacing have recently revolutionized cardiac resynchronization therapy (Yeshwant and Upadhyay, 2025).

This Research Topic has contributed to the development of the above by demonstrating that mice and sheep are good animal models for understanding CCS abnormalities, elucidating functional aspects of CCS activation through modellingand experiments, helping to distinguish CCS diseases seen in the

ECG, and determining the most optimal pacing protocols for restoring heart function. As we understand more about the CCS, we will be in a better position to further exploit it for preventing life threatening arrhythmias and restoring normal heart function.

Author contributions

EV: Writing – review and editing, Writing – original draft. JB: Writing – review and editing, Conceptualization.

Funding

The authors declare that no financial support was received for the research and/or publication of this article.

Conflict of interest

The authors declare that the research was conducted in the absence of any commercial or financial relationships that could be construed as a potential conflict of interest.

The authors declared that they were an editorial board member of Frontiers, at the time of submission. This had no impact on the peer review process and the final decision.

Generative AI statement

The authors declare that no Generative AI was used in the creation of this manuscript.

Any alternative text (alt text) provided alongside figures in this article has been generated by Frontiers with the support of artificial intelligence and reasonable efforts have been made to ensure accuracy, including review by the authors wherever possible. If you identify any issues, please contact us.

Publisher's note

References

Aras, K., Gams, A., Faye, N. R., Brennan, J., Goldrick, K., Li, J., et al. (2022). Electrophysiology and arrhythmogenesis in the human right ventricular outflow tract. *Circ. Arrhythmia Electrophysiol.* 15, e010630. doi:10.1161/CIRCEP.121.010630

Bayer, J. D., Sobota, V., Moreno, A., Jaïs, P., and Vigmond, E. J. (2022). The Purkinje network plays a major role in low-energy ventricular defibrillation. *Comput. Biol. Med.* 141, 105133.

Deo, M., Boyle, P. M., Kim, A. M., and Vigmond, E. J. (2010). Arrhythmogenesis by single ectopic beats originating in the Purkinje system. *Am. J. Physiol. Heart Circ. Physiol.* 299, H1002–H1011.

Haissaguerre, M., Vigmond, E., Stuyvers, B., Hocini, M., and Bernus, O. (2016). Ventricular arrhythmias and the his-purkinje system. *Nat. Rev. Cardiol.* 13, 155–166. doi:10.1038/nrcardio.2015.193

Joza, J., Luermans, J., Mardigyan, V., Burri, H., Jastrzębski, M., Vijayaraman, P., et al. (2025). Left bundle branch pacing in patients with structural heart disease: personalizing cardiac resynchronization therapy. *Eur. Eur. Pacing, Arrhythm. Cardiac Electrophysiol. j. Work. Groups Cardiac Pacing, Arrhythm. Cardiac Cell. Electrophysiol. Eur. Soc. Cardiol.* 27, euaf154. doi:10.1093/europace/euaf154

Nogami, A., Komatsu, Y., Talib, A. K., Phanthawimol, W., Naeemah, Q. J., Haruna, T., et al. (2023). Purkinje-related ventricular tachycardia and ventricular fibrillation: solved and unsolved questions. *JACC Clin. Electrophysiol.* 9, 2172–2196. doi:10.1016/j.jacep.2023.05.040

Pollard, A. E., Spitzer, K. W., and Burgess, M. J. (1997). Contributions of the specialized conduction system to the activation sequence in the canine pulmonary conus. *Am. J. Physiol.* 273, H446–H463. doi:10.1152/ajpheart.1997.273.1.H446

Sciacca, V., Fink, T., Guckel, D., El Hamriti, M., Khalaph, M., Braun, M., et al. (2022). Catheter ablation in patients with ventricular fibrillation by purkinje de-networking. *Front. Cardiovasc. Med.* 9, 956627. doi:10.3389/fcvm.2022.956627

Wald, R. W., Waxman, M. B., and Downar, E. (1980). The effect of antiarrhythmic drugs on depressed conduction and unidirectional block in sheep Purkinje fibers. *Circ. Res.* 46, 612–619.

Yeshwant, S., and Upadhyay, G. A. (2025). The evolution of conduction system pacing and gaps in understanding. *Prog. Cardiovasc. Dis.* 91, 113–120.

frontiers | Frontiers in Physiology

TYPE Original Research
PUBLISHED 02 December 2024
DOI 10.3389/fphys.2024.1500159

OPEN ACCESS

EDITED BY
Juan Pablo Martínez,
University of Zaragoza, Spain

REVIEWED BY
Raimondo Calvanese,
Centro Sanitario Locale Napoli 1 Centro, Italy
Rafał Gardas,
Medical University of Silesia, Poland

*CORRESPONDENCE
Ying-Xue Dong,
dong_yingxue@126.com

†These authors have contributed equally to this work

RECEIVED 22 September 2024
ACCEPTED 19 November 2024
PUBLISHED 02 December 2024

CITATION
Chen Y, Ma Z-L, Liu F, Wang N, Ma Y-Y, Guan Z-A, Zhe Z-C, Xia Y-L and Dong Y-X (2024) Is conduction system pacing more effective than right ventricular pacing in reducing atrial high-rate episodes in patients with heart failure and preserved ejection fraction?
Front. Physiol. 15:1500159.
doi: 10.3389/fphys.2024.1500159

Is conduction system pacing more effective than right ventricular pacing in reducing atrial high-rate episodes in patients with heart failure and preserved ejection fraction?

Ying Chen†, Zhu-Lin Ma†, Fei Liu, Nan Wang, Yue-Yang Ma, Zi-An Guan, Zhuang-Chuan Zhe, Yun-Long Xia and Ying-Xue Dong*

Department of Cardiology, First Affiliated Hospital of Dalian Medical University, Dalian, China

Background: The relationship between conduction system pacing (CSP) and the incidence of atrial fibrillation (AF) in patients with heart failure and preserved ejection fraction (HFpEF) remains uncertain. This study aims to investigate the occurrence of atrial high-rate episodes (AHREs) following CSP in patients with HFpEF, in comparison to right ventricular pacing (RVP).

Methods: Patients with HFpEF who received dual-chamber pacemakers for atrioventricular block were retrospectively enrolled from January 2018 to January 2023. Both new-onset and progressive AHREs were recorded, along with other clinical data, including cardiac performance and lead outcomes.

Results: A total of 498 patients were enrolled, comprising 387 patients with RVP and 111 patients with CSP, with a follow-up duration of 44.42 ± 10.41 months. In patients without a prior history of AF, CSP was associated with a significantly lower incidence of new-onset AHREs when the percentage of ventricular pacing was ≥20% (9.52% vs. 29.70%, $P = 0.001$). After adjusting for confounding factors, CSP exhibited a lower hazard ratio for new-onset AHREs compared to RVP (HR 0.336; [95% CI: 0.142–0.795]; $P = 0.013$), alongside left atrial diameter (LAD) (HR 1.109; [95% CI: 1.048–1.173]; $P < 0.001$). In patients with a history of AF, the progression of AHREs in CSP and RVP did not differ significantly (32.35% vs. 34.75%, $P = 0.791$). Cardiac performance metrics, including left ventricular end-diastolic diameter (LVEDD) (49.09 ± 4.28 mm vs. 48.08 ± 4.72 mm; $P = 0.015$), LAD (40.68 ± 5.49 mm vs. 39.47 ± 5.24 mm; $P = 0.001$), and NYHA class (2.31 ± 0.46 vs. 1.59 ± 0.73; $P < 0.001$), improved obviously following CSP, while LVEDD (48.37 ± 4.57 mm vs. 49.30 ± 5.32 mm; $P < 0.001$), LAD (39.77 ± 4.58 mm vs. 40.83 ± 4.80 mm; $P < 0.001$), NYHA class (2.24 ± 0.43 vs. 2.35 ± 0.83; $P = 0.018$), and left ventricular ejection fraction (LVEF) (57.41 ± 2.42 vs. 54.24 ± 6.65; $P < 0.001$) deteriorated after RVP.

Conclusion: Our findings suggest that CSP may be associated with improvements in cardiac performance and a reduction in new-onset AHREs compared to RVP in patients with HFpEF. However, prospective randomized trials are anticipated to confirm these potential benefits.

KEYWORDS

conduction system pacing, right ventricular pacing, atrial high-rate episodes, atrial fibrillation, heart failure with preserved ejection fraction

Introduction

Atrial fibrillation (AF) is prevalent among patients with heart failure with preserved ejection fraction (HFpEF), with prevalence rate ranging from 15% to 41%, this condition is associated with an increased risk of hospitalization and elevated mortality rates (Gierula et al., 2022; Sartipy et al., 2019). Unfortunately, right ventricular pacing (RVP) has been shown to exacerbate the heart failure and increase occurrence of AF in patients with a high percentage of ventricular pacing, as demonstrated in previous randomized controlled trials (Sweeney et al., 2003; Sweeney et al., 2007).

Conduction system pacing (CSP) has emerged as a more physiological pacing modality that facilitates cardiac electrical resynchronization compared to RVP. Recent data indicated that both his bundle pacing (HBP) and left bundle branch pacing (LBBP) were associated with a lower incidence of new-onset AF compared to RVP (Ravi et al., 2020; Zhu et al., 2023). Atrial high-rate episodes (AHREs) can be continuously monitored by implanted cardiac devices, are strongly linked to the development of clinical AF and stroke (Toennis et al., 2023; Gonzalez et al., 2014). However, it remains unclear whether CSP would reduce the occurrence of AHREs in patients with HFpEF. This study aims to illustrate the incidence of new-onset AHREs and progressive AF following different pacing modalities in patients with HFpEF, while also exploring improvements in cardiac performance.

Methods

Patient enrollment

Patients with HFpEF who had indications for a dual-chamber pacemaker due to atrioventricular conduction block (AVB) were retrospectively and consecutively enrolled at our center from January 2018 to January 2023. Exclusion criteria included atrial lead rupture or unreliable atrial signal detection, loss to follow-up, severe valvular disease (mitral or aortic regurgitation/stenosis of severe grade), heart surgery within the 6 months prior to implantation, a known history of persistent or permanent AF, a history of an atrioventricular node ablation and device upgrades or generator replacements.

Pacemaker implantation procedure

CSP was performed using lead 3,830 (Medtronic, Minneapolis, MN). His bundle electrogram and left bundle branch electrogram were recorded in a unipolar configuration (Prucka Cardiolab, GE Healthcare, Waukesha, WI, United States). HBP was not considered if 1:1 His–ventricular conduction was not detected while pacing at a rate of 120 beats per minute or patients with infranodal AVB. The unipolar configuration and pacing impedance were monitored alongside the left ventricular activation time (LVAT) (Zhang et al., 2023). Stim-left ventricular active time (LVAT) less than 75 ms, an abrupt decrease in LVAT of longer than 10 ms and the morphologies of Qr, qR, or rSR' in lead V_1 were the simple criteria for left bundle branch capture.

Data collection and patients follow-up

All patients were followed up at 1, 3, 6, and then every 6 months after the procedure. The 12-lead ECG, atrial high-rate episode burden (AHREs), echocardiographic parameters, comorbidities, and medications were documented. The pacing percentage and AHREs were noted at the initial 1-month visit and at each subsequent device interrogation, including remote interrogations. Anticoagulation therapy was recommended according to the guidelines established. The sizes of the left ventricle (LV) and left atrium (LA), as well as cardiac function, were monitored annually via cardiac ultrasound (video, GE Healthcare). The left ventricular ejection fraction (LVEF) was calculated using the modified Simpson method. The incidence of progressive AF and new-onset AHREs was noted and compared between the CSP and RVP pacing modalities.

Definitions and criteria

AHREs were defined as episodes characterized by an atrial rate of 200 beats per minute or greater, lasting for a minimum of 5 min. The burden of AHREs was quantified as the average percentage of total AHREs occurring throughout the entire follow-up period (Healey et al., 2012). New-onset AHREs were identified as those detected in patients without a prior history of AF before the procedure (Kohno et al., 2011; Minamiguchi et al., 2012). Atrial fibrillation progression was defined as an absolute increase of 10% or more in the average AHREs burden compared to the initial assessment conducted 1 month after device implantation (Ravi et al., 2020). HFpEF was characterized by objective evidence of cardiac structural and/or functional abnormalities indicative of left ventricular (LV) diastolic dysfunction or elevated LV filling pressures, including elevated levels of natriuretic peptides (McDonagh et al., 2021).

Statistical analysis

Continuous variables exhibiting a normal distribution were reported as mean ± standard deviation and analyzed using a

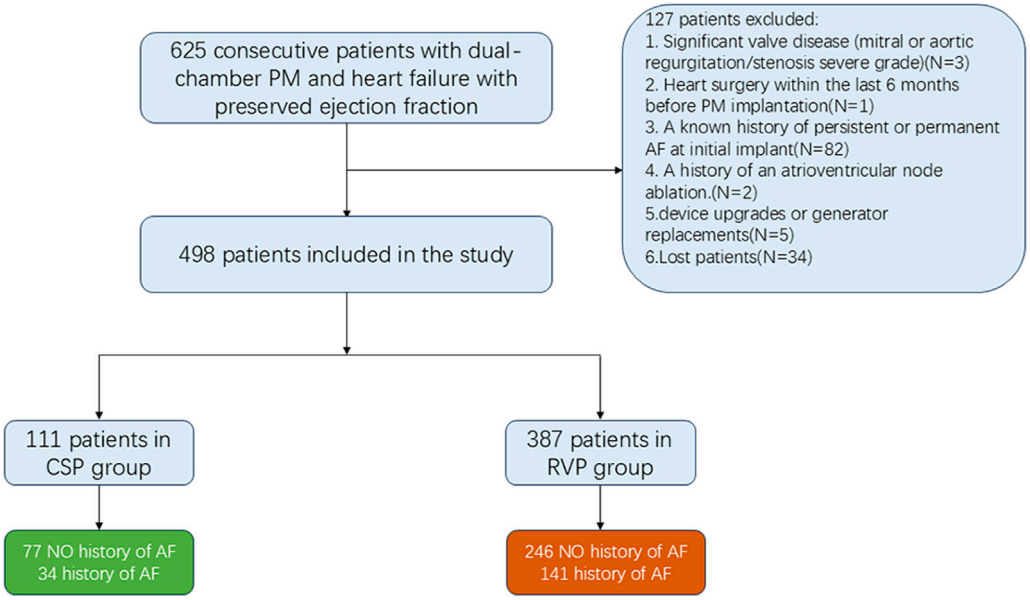

FIGURE 1
Flowchart showing the patients included in and excluded from the study. CSP: conduction system pacing; RVP: right ventricular pacing; AF: atrial fibrillation; PM: pacemaker.

t-test. For non-normally distributed variables, data were expressed as medians with interquartile ranges, and the Mann-Whitney U test was employed. Categorical variables were compared using either the Chi-square test or Fisher's exact test, with results reported as percentages. Survival curves were estimated using the Kaplan–Meier method. Univariate and multivariable Cox proportional hazard models were utilized to identify predictors of AHREs, where univariate predictors with a P value of less than 0.05 were incorporated into the multivariate Cox proportional hazard model. All statistical analyses were performed using SPSS Version 26.0, with a significance threshold set at $P < 0.05$.

Results

Patient population characteristics

A total of 625 patients (mean age 73.21 ± 10.00 years; 45.4% male) diagnosed with HFpEF and implanted with dual-chamber pacemakers for AVB were continuously screened from January 2018 to January 2023. Out of these, 498 patients (387 with RVP and 111 with CSP) were enrolled, as illustrated in Figure 1. Among the CSP group, 21 patients (18.92%) received HBP and 90 patients (81.08%) received LBBP. The average follow-up duration was 44.42 ± 10.41 months.

The baseline clinical characteristics of the study population are detailed in Table 1. No statistically significant differences were observed in age, gender, comorbidities, medication usage, left ventricular end-diastolic diameter (LVEDD), left atrial diameter (LAD), left ventricular ejection fraction (LVEF), or New York Heart Association (NYHA) class between the patients receiving CSP and those receiving RVP (all $P > 0.05$).

Procedure outcomes in different pacing modalities

The paced QRS duration was significantly shorter in CSP compared to RVP (116.86 ± 23.75 ms vs. 144.53 ± 32.00 ms, $P < 0.001$). The capture threshold was higher in the CSP than in RVP (1.05 ± 0.31 V vs. 0.83 ± 0.18 V, $P < 0.001$). An increase in capture threshold of ≥2 V at 0.4 ms was observed in 4 patients with CSP and 2 patients with RVP (3.60% vs. 0.52%, $P = 0.033$). The incidence of procedural complications was similar between the CSP and RVP groups (0.90% vs. 0.26%, $P = 0.926$). Details of the procedures were shown in Table 2.

Clinical outcomes in different pacing modalities

Clinical outcomes in different pacing modalities demonstrated significant differences. Patients with RVP experienced deterioration in NYHA class (2.24 ± 0.43 vs. 2.35 ± 0.83, $P = 0.018$), LVEDD (48.37 ± 4.57 mm vs. 49.30 ± 5.32 mm, $P < 0.001$), LAD (39.77 ± 4.58 mm vs. 40.83 ± 4.80 mm, $P< 0.001$), and LVEF (57.41% ± 2.42% vs. 54.24% ± 6.65%, $P < 0.001$) after follow-up. In contrast, patients with CSP showed improvement in NYHA class (2.31 ± 0.46 vs. 1.59 ± 0.73, $P < 0.001$), LVEDD (49.09 ± 4.28 mm vs. 48.08 ± 4.72 mm, $P = 0.015$), and LAD (40.68 ± 5.49 mm vs. 39.47 ± 5.24 mm, $P = 0.001$), as illustrated in Table 3.

New-onset AHREs in different pacing modalities

Regarding new-onset AHREs in different pacing modalities, 77 patients with CSP and 246 patients with RVP had no prior

TABLE 1 Baseline characteristics of all patients.

	Patients without history of AF			Patients with history of AF		
	CSP(N = 77)	RVP(N = 246)	*P*-Value	CSP(N = 34)	RVP(N = 141)	*P*-Value
Age, years	71.19 ± 9.96	73.81 ± 10.34	0.051	71.21 ± 7.19	74.06 ± 9.08	0.089
Male, n (%)	38 (49.35)	113 (45.93)	0.600	19 (55.88)	54 (38.30)	0.062
BMI, kg/m^2	30.72 ± 0.73	30.59 ± 1.71	0.350	27.73 ± 3.52	28.71 ± 3.84	0.184
NYHA class			0.079			0.638
NYHA II, n (%)	49 (63.64)	182 (73.98)		28 (82.35)	111 (78.72)	
NYHA III, n (%)	28 (36.36)	64 (26.02)		6 (17.65)	30 (21.28)	
SND	25 (32.47)	57 (23.17)	0.102	23 (67.65)	105 (74.47)	0.421
Hypertension, n (%)	69 (89.60)	218 (88.60)	0.809	29 (85.29)	115 (81.56)	0.609
CAD, n (%)	7 (9.09)	39 (15.85)	0.138	10 (29.41)	33 (23.40)	0.465
DM, n (%)	18 (23.38)	80 (32.52)	0.128	13 (38.24)	33 (23.40)	0.078
CKD, n (%)	4 (5.19)	22 (8.94)	0.291	5 (14.71)	6 (4.26)	0.063
LVEDD, mm	49.60 ± 4.62	48.88 ± 4.35	0.218	47.94 ± 3.10	47.46 ± 4.83	0.588
LAD, mm	40.15 ± 4.79	39.34 ± 4.14	0.158	41.91 ± 6.74	40.53 ± 5.20	0.198
LVEF, %	57.57 ± 2.01	57.50 ± 2.48	0.806	56.73 ± 2.48	57.27 ± 2.29	0.231
E/e'	17.73 ± 2.54	17.37 ± 2.17	0.221	18.21 ± 4.54	17.37 ± 2.75	0.171
ACEI/ARB/ARNI, n (%)	23 (29.87)	79 (32.11)	0.712	10 (29.41)	48 (34.04)	0.607
AAD, n (%)	6 (7.79)	20 (8.13)	0.924	6 (17.65)	22 (15.27)	0.770
AF ablation	—	—	—	3 (8.82)	20 (14.18)	0.584
BNP, pg/mL	188.00 (152.50,392.86)	227.00 (154.92,393.44)	0.533	201.23 (152.50,374.35)	233.35 (158.23,446.73)	0.612

BMI: body mass index; SND: sinus node disease; CAD: coronary artery disease; DM: diabetes mellitus; CKD: chronic kidney disease; LVEDD: left ventricular end-diastolic diameter; LAD: left atrial diameter; LVEF: left ventricular ejection fraction; ARNI: angiotensin receptor-neprilysin inhibitors; ACEI: angiotensin-converting enzyme inhibitors; ARB: angiotensin receptor blockers; AAD: antiarrhythmic drug; CSP: conduction system pacing; RVP: right ventricular pacing; AF: atrial fibrillation.

TABLE 2 Procedures and clinical outcomes.

	CSP (N = 111)	RVP (N = 387)	*P*-Value
Baseline QRS duration, ms	108.20 ± 27.57	107.84 ± 31.90	0.914
Paced QRS duration, ms	116.86 ± 23.75	144.53 ± 32.00	<0.001
Threshold, V	1.05 ± 0.31	0.83 ± 0.18	<0.001
Threshold increase≥2 V, n (%)	4 (3.60)	2 (0.52)	0.033
Procedural complications	1 (0.90)	1 (0.26)	0.926
Pericardial effusion	0	0	
Pneumothorax	1	0	
Lead dislodgement	0	1	
Infection	0	0	
VP%≥20%, n (%)	80 (72.07)	256 (66.15)	0.240

VP%: percentage of ventricular pacing; CSP: conduction system pacing; RVP: right ventricular pacing.

history of AF before the procedure. New-onset AHREs were identified in 7 patients (7/77, 9.09%) with CSP and 68 patients (68/246, 27.64%) with RVP (P = 0.001), as shown in Figure 2. CSP was associated with a significantly lower incidence of new-onset AHREs compared to RVP, particularly in patients with a ventricular pacing percentage of ≥20% (9.52% vs. 29.70%, P = 0.001), while no significant difference was observed in those with a ventricular pacing percentage of less than 20%, as depicted in Figure 2. Univariate and

TABLE 3 Clinical outcomes comparation in different pacing modalities.

	Baseline	After follow-up	*P*-Value
NYHA class in CSP	2.31 ± 0.46	1.59 ± 0.73	<0.001
NYHA class in RVP	2.24 ± 0.43	2.35 ± 0.83	0.018
LAD in CSP, mm	40.68 ± 5.49	39.47 ± 5.24	0.001
LAD in RVP, mm	39.77 ± 4.58	40.83 ± 4.80	<0.001
LVEDD in CSP, mm	49.09 ± 4.28	48.08 ± 4.72	0.015
LVEDD in RVP, mm	48.37 ± 4.57	49.30 ± 5.32	<0.001
LVEF in CSP, %	57.32 ± 2.18	56.57 ± 4.96	0.121
LVEF in RVP, %	57.41 ± 2.42	54.24 ± 6.65	<0.001

LAD: left atrial diameter; LVEDD: left ventricular end-diastolic diameter; LVEF: left ventricular ejection fraction; CSP: conduction system pacing; RVP: right ventricular pacing.

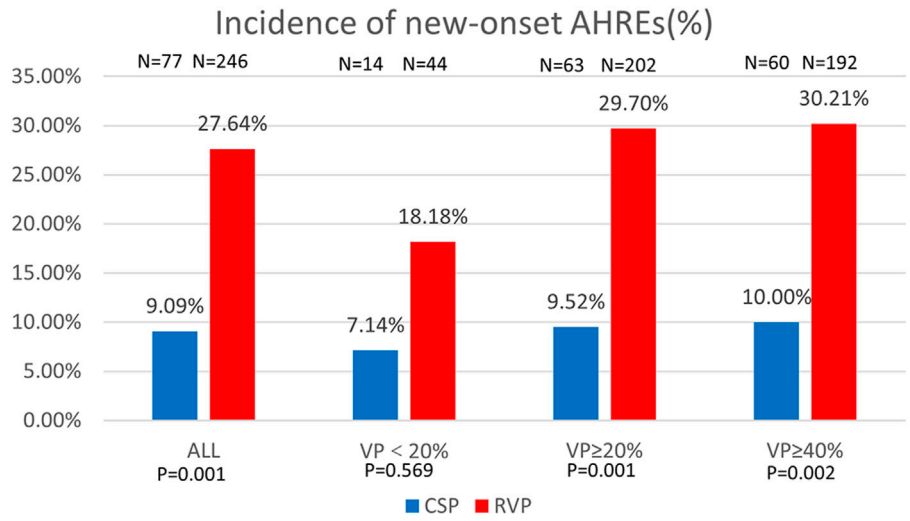

FIGURE 2
Comparison of new-onset AHREs by percentage between CSP and RVP in all patients and the subgroups based on ventricular pacing (%). AHREs: atrial high-rate episodes; VP: ventricular pacing.

multivariate Cox regression models were employed to identify predictors of new-onset AHREs, as presented in Table 4. CSP exhibited a lower hazard ratio for new-onset AHREs compared to RVP (HR 0.336; [95% CI: 0.142–0.795]; $P = 0.013$), as well as LAD (HR 1.109; [95% CI: 1.048–1.173]; $P < 0.001$). The cumulative risks of new-onset AHREs across different pacing modalities are illustrated in Figure 3.

Progression of AHREs in different pacing modalities

In terms of the progression of AF in different pacing modalities, 34 patients with CSP and 141 patients with RVP had paroxysmal AF prior to pacemaker implantation. Progression of AF occurred in 11 patients (11/34, 32.35%) with CSP and 49 patients (49/141, 34.75%) with RVP ($P = 0.791$). The progression of AF was comparable between CSP and RVP, regardless of the ventricular pacing percentage, as shown in Figure 4.

Discussion

Main findings

This study first demonstrates that CSP might be effective than RVP in improving cardiac performance and reducing AHREs in patients with HFpEF. Furthermore, it suggests CSP and LAD are independent predictors of new-onset AHREs.

Pacing modalities on cardiac performances in patients with HFpEF

Current randomized trials have demonstrated the superiority of biventricular pacing (BiVP) over RVP in enhancing quality of life, NYHA class, and echocardiographic outcomes in patients with moderate to severe systolic dysfunction (Filho et al., 2010; Curtis et al., 2013; Kindermann et al., 2006). However, the high

TABLE 4 Cox regression analysis for risk factors of new-onset AHREs in patients without history of AF.

	Patients with VP ≥ 20%					
	Univariate analysis			Multivariate analysis		
	HR	95% CI	*P*-Value	HR	95% CI	*P*-Value
CSP	0.396	0.169–0.923	0.032	0.336	0.142–0.795	0.013
Age	1.018	0.993–1.044	0.156			
Male	1.245	0.768–2.018	0.374			
BMI	1.106	0.893–1.369	0.357			
SND	1.195	0.727–1.965	0.483			
Hypertension	0.794	0.415–1.520	0.487			
DM	0.867	0.505–1.491	0.607			
CAD	1.008	0.499–2.036	0.983			
AAD	2.494	0.998–6.233	0.050			
ACEI/ARB/ARNI	1.186	0.710–1.980	0.515			
LAD	1.091	1.036–1.150	0.001	1.109	1.048–1.173	<0.001
LVEDD	1.009	0.953–1.068	0.759			
LVEF	1.016	0.924–1.117	0.745			
AP%	1.005	0.993–1.018	0.409			

BMI: body mass index; SND: sinus node disease; DM: diabetes mellitus; CAD: coronary artery disease; AAD: antiarrhythmic drug; ACEI: angiotensin-converting enzyme inhibitors; ARB: angiotensin receptor blockers; ARNI: angiotensin receptor-neprilysin inhibitors; LAD: left atrial diameter; LVEDD: left ventricular end-diastolic diameter; LVEF: left ventricular ejection fraction; CSP: conduction system pacing; RVP: right ventricular pacing; AP%: percentage of atrial pacing; AHREs: atrial high-rate episodes.

cost and limited response of BiVP rendered it inaccessible for some patients. Zhang et al. demonstrated that CSP significantly improve NYHA class, LVEF, and LVEDD in patients with HFmrEF and a high percentage of ventricular pacing (Zhang et al., 2023). HFpEF is characterized by increasing rates of hospitalization and mortality, highlighting the need for new therapeutic options (Infeld et al., 2023).

CSP has been recommended as an alternative to RVP in patients with AVB (Chung et al., 2023). Reports indicated that LBBP resulted in greater improvement in BNP levels compared to RVP (O et al., 2022). Moreover, HBP has been shown to improve NYHA class and reduce diuretic use in HFpEF patients after 1 year (Huang et al., 2017). However, data regarding the long-term impact of CSP on cardiac remodeling in HFpEF remained scarce. Consistent with previous studies, this research also demonstrated favorable cardiac function, including improvements in LVEF and NYHA class following CSP. Additionally, it explored the benefits of CSP on cardiac reverse remodeling, revealing significant improvements in LVEDD (P = 0.015) and LAD (P = 0.001) after long-term follow-up. In contrast, RVP was associated with deterioration in LVEDD (P < 0.001), LAD (P< 0.001), NYHA class (P = 0.018), and LVEF (P< 0.001). These positive outcomes might result from a combination of factors, and the individual atrioventricular interval optimization could play a role except for the physiological electrical conduction facilitated by CSP (Cobb and Gold, 2017).

Predictors of new-onset AHREs in patients with HFpEF

AF was prevalent among patients with a significant proportion of ventricular pacing (Sweeney et al., 2003). Recent studies have demonstrated that the incidence of AHREs in patients with RVP was approximately 2.3 times greater than those with LBBP (Takahashi et al., 2023; Zhang et al., 2024). In line with these observations, our analysis revealed that CSP was associated with a reduced incidence of AHREs (HR 0.336, 95% CI: 0.142–0.795) after adjusting for confounding variables using multifactorial regression analysis. Notably, the prevalence of AHREs was found to be as high as 29.70% in patients with RVP of VP%≥20%, compared to only 9.52% in those receiving CSP (P = 0.001).

Structural alterations in chronic heart failure patients, compounded by neurohormonal activation, significantly increased the prevalence of AF (Kotecha and Piccini, 2015). HFpEF was primarily characterized by left ventricular concentric remodeling, hypertrophy, and diastolic dysfunction (CS et al., 2007). Additionally, left atrial enlargement, along with cardiac volume and pressure overload, has been shown to correlate with the occurrence of AF (Hoit, 2014). Study has confirmed that left atrial enlargement is a significant risk factor for AHREs (Kim et al., 2021). However, this cohort study is the first to demonstrate that left atrial enlargement is associated with the development of AHREs in patients with HFpEF. In patients with HFpEF, left atrial enlargement served as a well-established proarrhythmic substrate associated with atrial

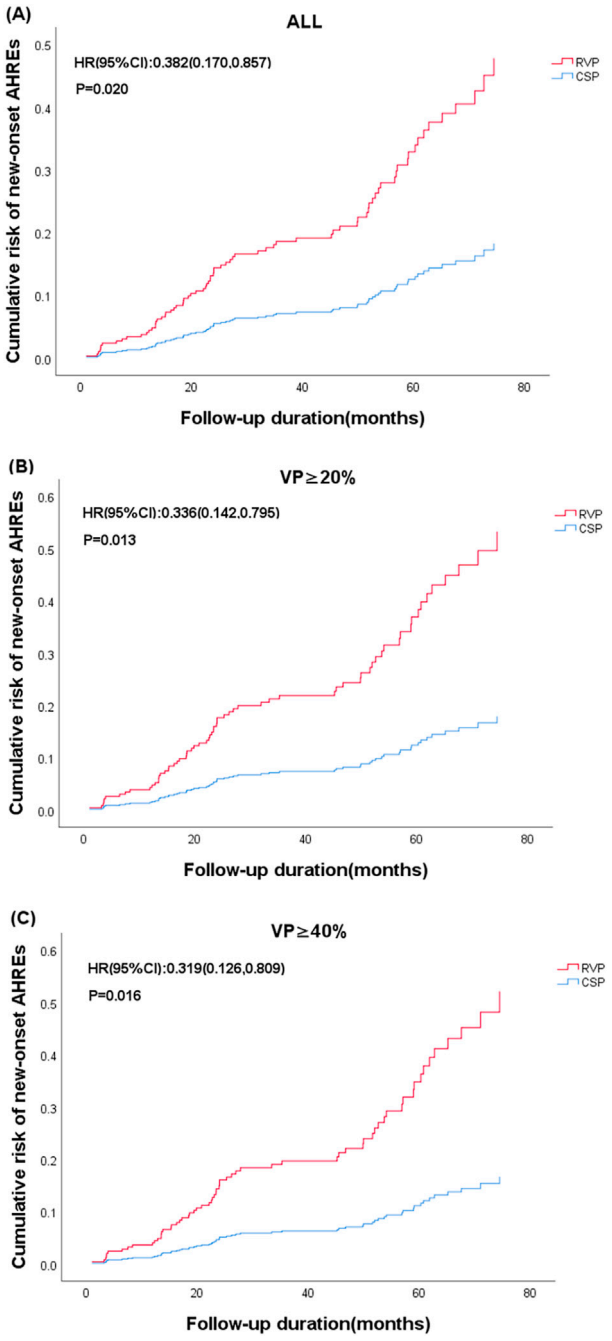

FIGURE 3
Cumulative risk of new-onset AHREs based on the type of device (CSP vs. RVP) and subgroups stratified by ventricular pacing (%). **(A)** All enrolled patients; **(B)** Ventricular pacing (VP)≥20%; **(C)** Ventricular pacing (VP)≥40%. The representations derived from stratified multifactorial Cox model risk function. The P values from Cox proportional risk model. CSP: Conduction system pacing; RVP: right ventricular pacing; HR: hazard ratio.

fibrosis (Knackstedt et al., 2008). Importantly, our findings explored that CSP contributed to left atrial remodeling (40.68 ± 5.49 vs. 39.47 ± 5.24, $P = 0.001$) when compared to RVP (39.77 ± 4.58 vs. 40.83 ± 4.80, $P < 0.001$), which might play a role in the prevention of AF.

Previous studies had demonstrated that the risks of ventricular desynchrony, adverse remodeling, and atrial arrhythmia increased when the percentage of ventricular pacing exceeded 20%–40% (Sweeney et al., 2003; Ravi et al., 2020; Kiehl et al., 2016; Khurshid et al., 2014).Additionally, several studies had established a correlation between elevated atrial pacing percentages and an increased risk of atrial arrhythmias (Bukari et al., 2018; Fontenla et al., 2016; Biffi et al., 2019; Ziacchi et al., 2018). However, the population enrolled in this study primarily consisted of patients with atrioventricular block, and the atrial pacing percentages within this cohort limited its ability to predict the incidence of AHREs.

Different pacing modalities on AHREs in patients with HFpEF

Current data suggested that HBP was associated with a reduced risk of AHREs compared to RVP in patients without AF history (Takahashi et al., 2023). However, the extent to which the physiological advantages of CSP in preventing AHREs could be counterbalanced by the effects of heart failure in patients with HFpEF remains unclear. Our study first confirmed the benefits of CSP in reducing new-onset AHREs even among patients with HFpEF. However, in the patients with a prior history of AF, no statistically significant differences were observed in the progression of AHREs between CSP and RVP. Additionally, Pastore et al. found no difference in the progression of AF between HBP and RVP (Pastore et al., 2020). These findings underscore the necessity of early AF management and the importance of primary prevention. It was noteworthy that a higher proportion of patients with a history of AF in the RVP group had previously undergone AF ablation compared to those in the CSP group (14% vs. 8%). This disparity might diminish the potential benefits of CSP in reducing AF burden among patients who had already undergone ablation.

RVP-related diastolic dysfunction, asynchronous mitral regurgitation and enlarged left atrial expansion increased the risk of AF occurrence (Naqvi and Chao, 2023). CSP would be beneficial in reducing the incidence of AF by enhancing the cardiac electrical and mechanical synchronization, as well as delaying left atrial reverse remodeling (Cai et al., 2020; Hou et al., 2019). HFpEF was associated with progressive left atrial myopathy which served as the substrate of AF occurrence (Kotecha et al., 2016). Consequently AF recurrence was more prevalent in patients with HFpEF regardless of the type of AF (Younis et al., 2024). These findings suggested that managing AF in patients with concomitant heart failure presented significant challenges, particularly for those with a prior history of AF. Merely altering the pacing modality without addressing multiple risk factors is unlikely to effectively prevent AF recurrence. Therefore, the management of various risk factors associated with AF, such as diabetes mellitus, obesity, alcohol consumption, and sleep apnea syndrome, should be considered essential for the prevention of AF.

Although the age difference between the CSP and RVP did not reach statistical significance ($P = 0.051$), we agreed that younger patients generally present a lower risk of atrial arrhythmias. Notably, all enrolled patients in this study were elderly, which somewhat diminished the influence of age on the final results. And it was further demonstrated that age was not identified as a statistically significant factor associated with the incidence of AHREs in the univariate regression analyses ($P = 0.156$).

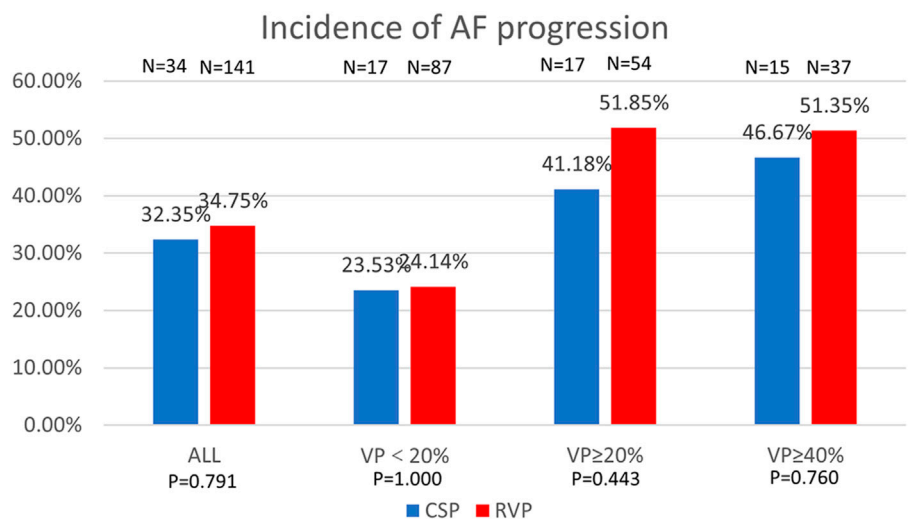

FIGURE 4
Comparison of AF progression by percentage between CSP and RVP in all patients and the subgroups based on ventricular pacing (%). AF: atrial fibrillation; VP: ventricular pacing.

Limitations

This study was a single-center, retrospective observational analysis. Given the potential for selection bias associated with its non-randomized design, caution should be exercised when interpreting the results. A randomized multi-center trial with a larger sample size may be necessary to validate these findings.

Conclusion

Our findings suggest that CSP may be associated with improvements in cardiac performance and a reduction in new-onset AHREs compared to RVP in patients with HFpEF. However, prospective randomized trials are anticipated to confirm these potential benefits.

Data availability statement

The raw data supporting the conclusions of this article will be made available by the authors, without undue reservation.

Ethics statement

The studies involving humans were approved by Ethics Committee of the First Affiliated Hospital of Dalian Medical University. The studies were conducted in accordance with the local legislation and institutional requirements. Written informed consent for participation was not required from the participants or the participants' legal guardians/next of kin in accordance with the national legislation and institutional requirements.

Author contributions

YC: Conceptualization, Data curation, Formal Analysis, Investigation, Methodology, Software, Visualization, Writing–original draft. Z-LM: Data curation, Formal Analysis, Software, Writing–original draft. FL: Methodology, Writing–original draft. NW: Software, Writing–original draft. Y-YM: Data curation, Writing–original draft. Z-AG: Data curation, Writing–original draft. Z-CZ: Data curation, Writing–original draft. Y-LX: Resources, Writing–original draft. Y-XD: Data curation, Funding acquisition, Project administration, Resources, Supervision, Validation, Writing–review and editing.

Funding

The author(s) declare that financial support was received for the research, authorship, and/or publication of this article. supported by the Scientific and Technological Innovation Foundation of Dalian City (2024JJ12PT016).

Conflict of interest

The authors declare that the research was conducted in the absence of any commercial or financial relationships that could be construed as a potential conflict of interest.

Publisher's note

All claims expressed in this article are solely those of the authors and do not necessarily represent those of their affiliated organizations, or those of the publisher, the editors and the reviewers. Any product that may be evaluated in this article, or claim that may be made by its manufacturer, is not guaranteed or endorsed by the publisher.

References

Biffi, M., D'Onofrio, A., Pignalberi, C., Pisanò, E. C., Iacopino, S., Curnis, A., et al. (2019). Rate-responsive pacing and atrial high rate episodes in cardiac resynchronization therapy patients: is low heart rate the key? *Clin. Cardiol.* 42 (9), 820–828. doi:10.1002/clc.23227

Bukari, A., Wali, E., Deshmukh, A., Aziz, Z., Broman, M., Beaser, A., et al. (2018). Prevalence and predictors of atrial arrhythmias in patients with sinus node dysfunction and atrial pacing. *J. Interventional Cardiac Electrophysiol.* 53 (3), 365–371. doi:10.1007/s10840-018-0463-7

Cai, B., Huang, X., Li, L., Guo, J., Chen, S., Meng, F., et al. (2020). Evaluation of cardiac synchrony in left bundle branch pacing: insights from echocardiographic research. *J. Cardiovasc. Electrophysiol.* 31 (2), 560–569. doi:10.1111/jce.14342

Chung, M. K., Patton, K. K., Lau, C.-P., Dal Forno, A. R. J., Al-Khatib, S. M., Arora, V., et al. (2023). 2023 HRS/APHRS/LAHRS guideline on cardiac physiologic pacing for the avoidance and mitigation of heart failure. *Heart Rhythm.* 20 (9), e17–e91. doi:10.1016/j.hrthm.2023.03.1538

Cobb, D. B., and Gold, M. R. (2017). The role of atrioventricular and interventricular optimization for cardiac resynchronization therapy. *Heart Fail. Clin.* 13 (1), 209–223. doi:10.1016/j.hfc.2016.07.017

Cs, P., Lam, M., Rodeheffer, R. J., Bursi, F., Borlaug, B. A., Ommen, S. R., et al. (2007). Cardiac structure and ventricular-vascular function in persons with heart failure and preserved ejection fraction from Olmsted County, Minnesota. *Circulation* 115 (15), 1982–1990. doi:10.1161/CIRCULATIONAHA.106.659763

Curtis, A. B., Worley, S. J., Adamson, P. B., Chung, E. S., Niazi, I., Sherfesee, L., et al. (2013). Biventricular pacing for atrioventricular block and systolic dysfunction. *N. Engl. J. Med.* 368 (17), 1585–1593. doi:10.1056/NEJMoa1210356

Filho, M. M., de Siqueira, S. F., Costa, R., Greco, O. T., Moreira, L. F., D'avila, A., et al. (2010). Conventional versus biventricular pacing in heart failure and bradyarrhythmia: the COMBAT study. *J. Cardiac Fail.* 16 (4), 293–300. doi:10.1016/j.cardfail.2009.12.008

Fontenla, A., Salguero, R., Martinez-Ferrer, J. B., Rodriguez, A., Alzueta, J., Garcia, E., et al. (2016). Atrial rate-responsive pacing and incidence of sustained atrial arrhythmias in patients with implantable cardioverter defibrillators. *Pacing Clin. Electrophysiol.* 39 (6), 548–556. doi:10.1111/pace.12856

Gierula, J., Cole, C. A., Drozd, M., Lowry, J. E., Straw, S., Slater, T. A., et al. (2022). Atrial fibrillation and risk of progressive heart failure in patients with preserved ejection fraction heart failure. *Esc. Heart Fail.* 9 (5), 3254–3263. doi:10.1002/ehf2.14004

Gonzalez, M., Keating, R. J., Markowitz, S. M., Liu, C. F., Thomas, G., Ip, J. E., et al. (2014). Newly detected atrial high rate episodes predict long-term mortality outcomes in patients with permanent pacemakers. *Heart Rhythm.* 11 (12), 2214–2221. doi:10.1016/j.hrthm.2014.08.019

Healey, J. S., Connolly, S. J., Gold, M. R., Israel, C. W., Van Gelder, I. C., Capucci, A., et al. (2012). Subclinical atrial fibrillation and the risk of stroke. *N. Engl. J. Med.* 366 (2), 120–129. doi:10.1056/NEJMoa1105575

Hoit, B. D. (2014). Left atrial size and function: role in prognosis. *J. Am. Coll. Cardiol.* 63 (6), 493–505. doi:10.1016/j.jacc.2013.10.055

Hou, X., Qian, Z., Wang, Y., Qiu, Y., Chen, X., Jiang, H., et al. (2019). Feasibility and cardiac synchrony of permanent left bundle branch pacing through the interventricular septum. *EP Eur.* 21 (11), 1694–1702. doi:10.1093/europace/euz188

Huang, W., Su, L., Wu, S., Xu, L., Xiao, F., Zhou, X., et al. (2017). Benefits of permanent his bundle pacing combined with atrioventricular node ablation in atrial fibrillation patients with heart failure with both preserved and reduced left ventricular ejection fraction. *J. Am. Heart Assoc.* 6 (4), e005309. doi:10.1161/jaha.116.005309

Infeld, M., Wahlberg, K., Cicero, J., Plante, T. B., Meagher, S., Novelli, A., et al. (2023). Effect of personalized accelerated pacing on quality of life, physical activity, and atrial fibrillation in patients with preclinical and overt heart failure with preserved ejection fraction: the myPACE randomized clinical trial. *JAMA Cardiol.* 8 (3), 213–221. doi:10.1001/jamacardio.2022.5320

Khurshid, S., Epstein, A. E., Verdino, R. J., Lin, D., Goldberg, L. R., Marchlinski, F. E., et al. (2014). Incidence and predictors of right ventricular pacing-induced cardiomyopathy. *Heart Rhythm.* 11 (9), 1619–1625. doi:10.1016/j.hrthm.2014.05.040

Kiehl, E. L., Makki, T., Kumar, R., Gumber, D., Kwon, D. H., Rickard, J. W., et al. (2016). Incidence and predictors of right ventricular pacing-induced cardiomyopathy in patients with complete atrioventricular block and preserved left ventricular systolic function. *Heart Rhythm.* 13 (12), 2272–2278. doi:10.1016/j.hrthm.2016.09.027

Kim, M., Kim, T.-H., Yu, H. T., Choi, E. K., Park, H. S., Park, J., et al. (2021). Prevalence and predictors of clinically relevant atrial high-rate episodes in patients with cardiac implantable electronic devices. *Korean Circulation J.* 51 (3), 235–247. doi:10.4070/kcj.2020.0393

Kindermann, M., Hennen, B., Jung, J., Geisel, J., Böhm, M., and Fröhlig, G. (2006). Biventricular versus conventional right ventricular stimulation for patients with standard pacing indication and left ventricular dysfunction: the Homburg Biventricular Pacing Evaluation (HOBIPACE). *J. Am. Coll. Cardiol.* 47 (10), 1927–1937. doi:10.1016/j.jacc.2005.12.056

Knackstedt, C., Gramley, F., Schimpf, T., Mischke, K., Zarse, M., Plisiene, J., et al. (2008). Association of echocardiographic atrial size and atrial fibrosis in a sequential model of congestive heart failure and atrial fibrillation. *Cardiovasc. Pathol.* 17 (5), 318–324. doi:10.1016/j.carpath.2007.12.003

Kohno, R., Abe, H., Oginosawa, Y., Tamura, M., Takeuchi, M., Nagatomo, T., et al. (2011). Reliability and characteristics of atrial tachyarrhythmias detection in dual chamber pacemakers. *Circulation J.* 75 (5), 1090–1097. doi:10.1253/circj.CJ-10-0896

Kotecha, D., Lam, C. S. P., Van Veldhuisen, D. J., Van Gelder, I. C., Voors, A. A., and Rienstra, M. (2016). Heart failure with preserved Ejection Fraction and Atrial fibrillation: vicious twins. *J. Am. Coll. Cardiol.* 68 (20), 2217–2228. doi:10.1016/j.jacc.2016.08.048

Kotecha, D., and Piccini, J. P. (2015). Atrial fibrillation in heart failure: what should we do? *Eur. Heart J.* 36, 3250–3257. doi:10.1093/eurheartj/ehv513

McDonagh, T. A., Metra, M., Adamo, M., Gardner, R. S., Baumbach, A., Böhm, M., et al. (2021). 2021 ESC Guidelines for the diagnosis and treatment of acute and chronic heart failure. *Eur. Heart J.* 42 (36), 3599–3726. doi:10.1093/eurheartj/ehab368

Minamiguchi, H., Abe, H., Kohno, R., Oginosawa, Y., Tamura, M., Takeuchi, M., et al. (2012). Incidence and characteristics of far-field R-wave sensing in low right atrial septum pacing. *Circulation J.* 76 (3), 598–606. doi:10.1253/circj.CJ-11-0745

Naqvi, T. Z., and Chao, C.-J. (2023). Adverse effects of right ventricular pacing on cardiac function: prevalence, prevention and treatment with physiologic pacing. *Trends Cardiovasc. Med.* 33 (2), 109–122. doi:10.1016/j.tcm.2021.10.013

Okubo, Y., Miyamoto, S., Uotani, Y., Ikeuchi, Y., Miyauchi, S., Okamura, S., et al. (2022). Clinical impact of left bundle branch area pacing in heart failure with preserved ejection fraction and mid-range ejection fraction. *Pacing Clin. Electrophysiol.* 45 (4), 499–508. doi:10.1111/pace.14470_ORG

Pastore, G., Marcantoni, L., Lanza, D., Maines, M., Noventa, F., Corbucci, G., et al. (2020). Occurrence of persistent atrial fibrillation during pacing for sinus node disease: the influence of His bundle pacing versus managed ventricular pacing. *J. Cardiovasc. Electrophysiol.* 32 (1), 110–116. doi:10.1111/jce.14810

Ravi, V., Beer, D., Pietrasik, G. M., Hanifin, J. L., Ooms, S., Ayub, M. T., et al. (2020). Development of new-onset or progressive atrial fibrillation in patients with permanent HIS bundle pacing versus right ventricular pacing: results from the RUSH HBP registry. *J. Am. Heart Assoc.* 9 (22), e018478. doi:10.1161/jaha.120.018478

Sartipy, U., Savarese, G., Dahlström, U., Fu, M., and Lund, L. H. (2019). Association of heart rate with mortality in sinus rhythm and atrial fibrillation in heart failure with preserved ejection fraction. *Eur. J. Heart Fail.* 21 (4), 471–479. doi:10.1002/ejhf.1389

Sweeney, M. O., Bank, A. J., Nsah, E., Koullick, M., Zeng, Q. C., Hettrick, D., et al. (2007). Minimizing ventricular pacing to reduce atrial fibrillation in sinus-node disease. *N. Engl. J. Med.* 357 (10), 1000–1008. doi:10.1056/NEJMoa071880

Sweeney, M. O., Hellkamp, A. S., Ellenbogen, K. A., Greenspon, A. J., Freedman, R. A., Lee, K. L., et al. (2003). Adverse effect of ventricular pacing on heart failure and atrial fibrillation among patients with normal baseline QRS duration in a clinical trial of pacemaker therapy for sinus node dysfunction. *Circulation* 107 (23), 2932–2937. doi:10.1161/01.Cir.0000072769.17295.B1

Takahashi, M., Kujiraoka, H., Arai, T., Kimura, T., Hojo, R., and Fukamizu, S. (2023). New-onset atrial high-rate episodes between his bundle pacing and conventional right ventricular septum pacing in patients with atrioventricular conduction disturbance. *J. Interventional Cardiac. Electrophysiol.* 67 (3), 471–477. doi:10.1007/s10840-023-01605-w

Toennis, T., Bertaglia, E., Brandes, A., Dichtl, W., Fluschnik, N., de Groot, J. R., et al. (2023). The influence of atrial high-rate episodes on stroke and cardiovascular death: an update. *Europace* 25 (7), euad166. doi:10.1093/europace/euad166

Younis, A., Tabaja, C., Santangeli, P., Nakagawa, H., Sipko, J., Madden, R., et al. (2024). Outcomes of atrial fibrillation ablation in heart failure subtypes. *Circulation Arrhythmia Electrophysiol.* 17, e012926. doi:10.1161/circep.124.012926

Zhang, D.-d., Zhao, F.-l., Yang, Y.-h., Ma, C. M., Ma, P. P., Zhao, Y. N., et al. (2023). Conduction system pacing improves the outcomes on patients with high percentage of ventricular pacing and heart failure with mildly reduced ejection fraction. *Front. Cardiovasc. Med.* 10, 1132520. doi:10.3389/fcvm.2023.1132520

Zhang, S., Yang, W., Wang, S., Cheng, Y., Jiang, Z., Zhou, X., et al. (2024). New-onset atrial high-rate episodes in left bundle branch area pacing versus right ventricular pacing for patients with atrioventricular block. *Pol. Heart J.* 82 (6), 632–639. doi:10.33963/v.phj.100403

Zhu, H., Li, X., Wang, Z., Liu, Q., Chu, B., Yao, Y., et al. (2023). New-onset atrial fibrillation following left bundle branch area pacing vs. right ventricular pacing: a two-centre prospective cohort study. *EP Eur.* 25 (1), 121–129. doi:10.1093/europace/euac132

Ziacchi, M., Palmisano, P., Biffi, M., Ricci, R. P., Landolina, M., Zoni-Berisso, M., et al. (2018). Clinically oriented device programming in bradycardia patients: part 1 (sinus node disease). Proposals from AIAC (Italian Association of Arrhythmology and Cardiac Pacing). *J. Cardiovasc. Med.* 19 (4), 161–169. doi:10.2459/jcm.0000000000000630

frontiers | Frontiers in Physiology

TYPE Original Research
PUBLISHED 06 May 2025
DOI 10.3389/fphys.2025.1540400

OPEN ACCESS

EDITED BY
Jichao Zhao,
The University of Auckland, New Zealand

REVIEWED BY
Huiliang Qiu,
Mayo Clinic Arizona, United States
Callum Michael Zgierski-Johnston,
University Heart Center Freiburg, Germany

*CORRESPONDENCE
Edward J. Vigmond,
edward.vigmond@u-bordeaux.fr

†These authors share first authorship

‡These authors share last authorship

RECEIVED 05 December 2024
ACCEPTED 10 April 2025
PUBLISHED 06 May 2025

CITATION
Jabbour RJ, Behradfar E, Debney M, Nygren A, Hartley A, Efimov I, Hocini M, Peters NS, Ng FS and Vigmond EJ (2025) Acute ischaemia and gap junction modulation modify propagation patterns across Purkinje-myocardial junctions. *Front. Physiol.* 16:1540400. doi: 10.3389/fphys.2025.1540400

Acute ischaemia and gap junction modulation modify propagation patterns across Purkinje-myocardial junctions

Richard J. Jabbour[1†], Elham Behradfar[2,3†], Michael Debney[1], Anders Nygren[2,3], Adam Hartley[1], Igor Efimov[4], Mélèze Hocini[5,6], Nicholas S. Peters[1], Fu Siong Ng[1‡] and Edward J. Vigmond[2,6,7*‡]

[1]National Heart and Lung Institute, Imperial College London, London, United Kingdom, [2]Department of Biomedical Engineering, University of Calgary, Calgary, AB, Canada, [3]Department of Electrical and Software Engineering, University of Calgary, Calgary, AB, Canada, [4]McCormick School of Engineering, Northwestern University, Chicago, IL, United States, [5]Bordeaux University Hospital (CHU), Electrophysiology and Ablation Unit, Pessac, France, [6]IHU Liryc, Heart Rhythm Disease Institute, Fondation Bordeaux Université, Bordeaux, France, [7]University Bordeaux, Lab IMB, UMR 5251, Talence, France

Background: The Purkinje network is essential for normal electrical impulse propagation in the heart but has also been implicated in ventricular arrhythmias. Previous experimental work has suggested that not all Purkinje-myocardial junctions (PMJs) are active at rest due to source-sink mismatch at the PMJs.

Objective: We hypothesized that pathological conditions that cause gap junction uncoupling (e.g., acute ischaemia), would increase the number of active PMJs, leading to more complex activation patterns.

Methods: We investigated this using a whole-heart intact Purkinje system preparation that allowed direct high-resolution endocardial mapping to interrogate PMJ function. Twelve (7 control, five rotigaptide) Langendorff-perfused hearts from New Zealand white rabbits were subjected to an ischaemia-reperfusion protocol and optically mapped. Computational modelling was performed to determine the effects of gap junction coupling on PMJ function, and on the complexity of endocardial activation.

Results: During ischaemia, the percentage of right ventricle area activated within the first 5 ms decreased from baseline 62% ± 7% to 52% ± 8% during early ischaemia ($p = 0.04$), consistent with slowing of conduction. This was followed by a paradoxical increase in late-ischaemia (60% ± 8%) due to extra regions of early activation. Gap junction enhancement with rotigaptide during ischaemia abolished the aforementioned pattern. Parallel computational experiments replicated experimental findings only when the number of functional PMJs was increased during ischaemia. With more active PMJs, there were more breakthrough sites with increased complexity of activation, as also measured in biological preparations.

Conclusion: Normally-quiescent PMJs can become active in the context of gap junction uncoupling during acute ischaemia. Pharmacological gap

junction modulation may alter propagation patterns across PMJs and may be used as a therapeutic strategy for Purkinje system associated arrhythmias.

KEYWORDS

purkinje system, Purkinje-myocardial junction, ischaemia, computer modelling, cardiac electrophysiology

1 Introduction

The Purkinje network consists of specialized conduction tissue that plays a key role in the rapid transmission of electrical impulses across the ventricles to allow for more synchronous contraction (Mendez et al., 1970; Robinson et al., 1987). However, the Purkinje system has also been implicated in the pathogenesis of several ventricular arrhythmias. For example, fascicular ventricular tachycardia (VT) and bundle-branch reentry both utilize the Purkinje network as part of their reentrant circuits (Haissaguerre et al., 2016). Furthermore, ventricular arrhythmias can also be triggered by Purkinje cells, for example, in idiopathic ventricular fibrillation (VF), and targeted ablation of Purkinje fibers is a feasible treatment for idiopathic VF (Nakagawa et al., 1993; Haïssaguerre et al., 2002; Haissaguerre et al., 2016).

The Purkinje network is connected to ventricular myocardium via Purkinje-myocardial junctions (PMJs) (Boyden, 2018). It has been postulated that many PMJs are normally in a non-functional state as there is significant source-sink mismatch at many PMJs, with the current from small Purkinje fibers being insufficient to anterogradely activate the larger bulk of ventricular myocardium (Joyner, 1982; Overholt et al., 1984). The susceptibility of PMJ transmission to changes in local environment has also been demonstrated experimentally (Tan et al., 1989). Other preclinical work has suggested the existence of a transitional cell type, coupled to both Purkinje and ventricular muscle cells via short thin strands and with distinct action potentials. These cells act as a high resistance barrier that could modulate anterograde impulse propagation (Tranum-Jensen et al., 1991).

Intracardiac recordings during catheter ablation in humans have confirmed that not all Purkinje potentials conduct into ventricular myocardium, supporting the source-sink mismatch hypothesis (Figure 1; central illustration). Partial gap junction uncoupling at the PMJs and of ventricular myocardium may improve the source-sink match at the PMJs to allow for propagation across previously-quiescent PMJs, as suggested indirectly in epicardial mapping studies in Cx43 knockout mice (Rohr et al., 1997; Morley et al., 2005).

We, therefore, hypothesized that pathological conditions that cause gap junction uncoupling, for example, acute ischaemia, may modify the source-sink relationship at PMJs sufficiently to allow for propagation of electrical impulses across previously-quiescent PMJs, leading to more complex activation patterns. We investigated this using a whole-heart intact Purkinje system preparation that allowed for direct high-resolution endocardial mapping to interrogate PMJ function. In parallel, we performed whole organ computational modelling to determine the effects of gap junction coupling on PMJ function, and on the complexity of endocardial activation.

2 Methods

2.1 Optical mapping

Experimental protocols were approved by the Washington University Institutional Animal Care and Use Committee, and by the Imperial College London Ethical Review Board (carried out under Project License PPL 70/7419), and were performed in accordance with standards set out in the United Kingdom Animals (Scientific Procedures) Act 1986.

Twelve Langendorff-perfused hearts from New Zealand white rabbits (~4 months old, 2.0–2.5 kg) were studied in total. Briefly, after administration of anesthesia (sodium pentobarbital 30 mg/kg IV) and heparin, hearts were rapidly explanted and perfused on a Langendorff apparatus with oxygenated (95% O2-5% CO2) Tyrode's solution (128.2 NaCl, 4.7 KCl, 1.19 NaH2PO4, 1.05 MgCl2, 1.3 CaCl2, 20.0 NaHCO3, and 11.1 glucose [all mmol/L], calibrated to pH = 7.35; 37°C; mean arterial pressure = 60 mmHg).

The aortic-perfused right ventricular endocardial mapping preparation was set up as shown in Figure 2A. Our endocardial mapping model was based on the work by Cates et al. (2001), to allow for mapping of the endocardial surface of the RV (Figure 2B). Unlike Cates et al., we did not remove the atria. Cuts were made along the right coronary artery and posterior descending artery, preserving them and maintaining perfusion of the RV, but also allowing the RV to be opened as a flap to allow for endocardial mapping (Figure 2C).

After a period of stabilization, hearts were perfused with a potentiometric dye (di-4-ANEPPS 20–40 µL of 1.25 mg/mL solution; Invitrogen, Carlsbad, CA) and an excitation-contraction uncoupler (10 µM Blebbistatin). Hearts were paced via the high right atrium using a bipolar silver electrode, to allow for physiological activation of the ventricles through the Purkinje system.

Optical mapping of transmembrane voltage was performed as previously described (Ng et al., 2013; Ng et al., 2014; Ng et al., 2016).

Excitation was provided by a 530 nm LED light and emitted light passed through a 650 nm emission filter. A 100 × 100 pixel MiCAM Ultima-L CMOS camera (SciMedia, United States Ltd., CA) was used to detect the optical signals (1,000 frames/sec). Optical signals were recorded during sinus rhythm and right atrial pacing at a range of pacing cycle lengths at baseline (400 ms).

Two groups of hearts were studied experimentally. Seven hearts were subjected to 40 min global ischaemia (no flow ischaemia model) and subsequent reperfusion for 30 min, with recordings at regular intervals during atrial pacing. At fixed intervals, ventricular conduction properties were studied during right ventricular pacing (Figure 2B). Atrial pacing was performed every 10 min, to look at RV activation. For RV pacing to assess CV, this was done at baseline (0 min), peak ischaemia (40 min) and

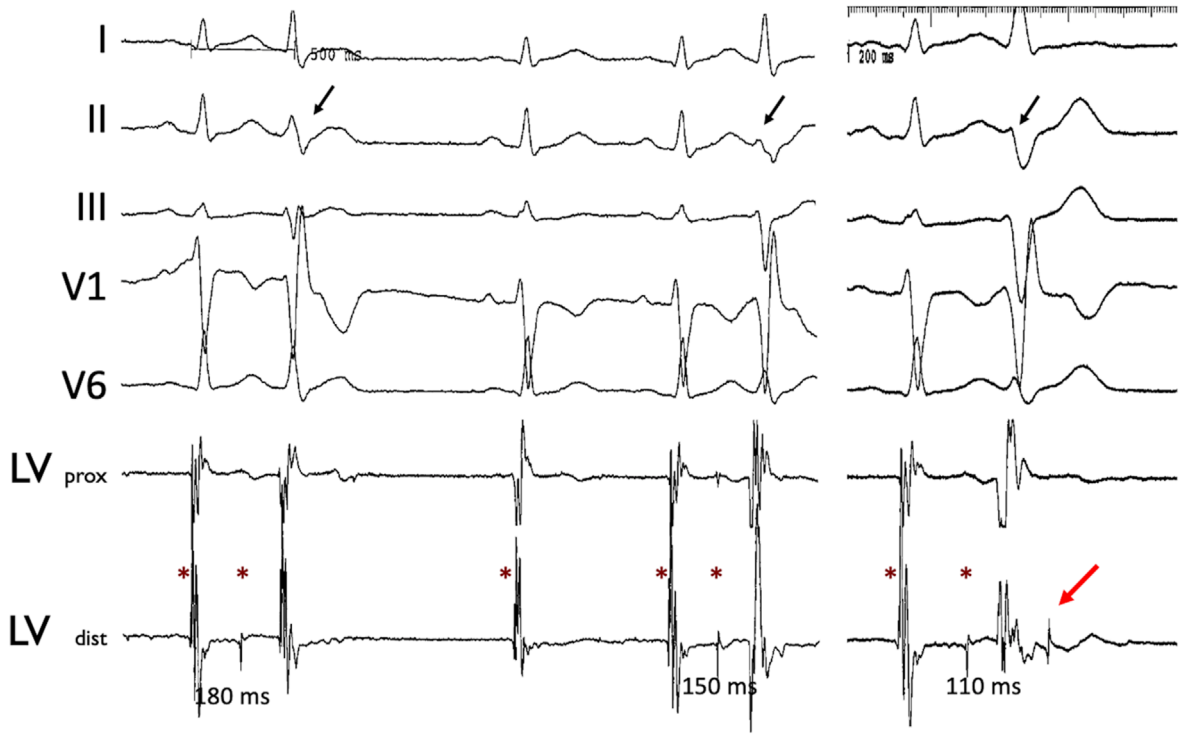

FIGURE 1
Concealed Purkinje discharge. Examples of ectopic beats arising from the LV Purkinje system, recorded during an invasive electrophysiological procedure in a patient. Left ventricle Purkinje beats with varying conduction times. Stars indicate the Purkinje potential. Note the varying Purkinje to ventricular muscle conduction times associated with the different QRS morphologies (black arrow) as well as non-conducted Purkinje beat (red arrow). Abbreviations: LV: left ventricle; prox: proximal; dist: distal.

after 30 min reperfusion. A further five hearts were subjected to pretreatment with 50 nM rotigaptide before being subjected to the acute ischaemia-reperfusion protocol. Rotigaptide is a peptide analogue that has been shown to increase gap junction conductance in cardiac muscle cells, acting primarily via connexin 43 (Ng et al., 2016). Since ischaemia shortens action potential duration (APD) in a time dependent manner, APD measurements were taken to confirm that progressive ischaemia had occurred during the experiments (Ng et al., 2014).

2.2 Data analysis

Optical mapping data were processed and analyzed as previously described (Laughner et al., 2012). Results were analysed in GraphPad Prism six software (GraphPad Software) and represented as mean ± SEM with $p < 0.05$ indicating significance. Paired Student's t-tests were used for relative changes between two groups.$^{*}= p < 0.05,^{**}= p < 0.01,^{***}= p < 0.001$.

2.3 Computational cable experiments

To isolate effects of ischaemia on conduction velocity, we performed *in silico* experiments in a cable. Since ischaemia is well known to increase extracellular K+, we performed a series of cable experiments with a range of K+ concentrations and determined the resting membrane potential and conduction velocities.

2.4 Computational ventricular and purkinje system modelling

Computer simulations were performed on our well established 3D finite element rabbit ventricular mesh incorporating a detailed representation of the Purkinje system, using rabbit ionic models for the ventricles (Mahajan et al., 2008) and Purkinje cells (Aslanidi et al., 2010). The ventricular mesh comprised about 550k tetrahedral nodes with an average edge spacing of 280 μm. Monodomain simulations were performed with a time step of 25 microseconds. The His-Purkinje mesh was a separate mesh of cubic Hermite one-dimensional elements of 300 μm mean length. PMJs were located at the free ends of the cables, where all nodes in a small volume of myocardium (500 μm radius) were connected to the terminal node of the Purkinje branch through a fixed electrical resistance (R_{PMJ}) (Boyle et al., 2010; Behradfar et al., 2014).

Propagation across the PMJ was set by setting R_{PMJ}. Values were chosen so that propagation was asymmetric across the PMJ with retrograde transmission easier with less of a delay (~1–3 ms) than anterograde transmission (5–8 ms delay)(Tan et al., 1989) There

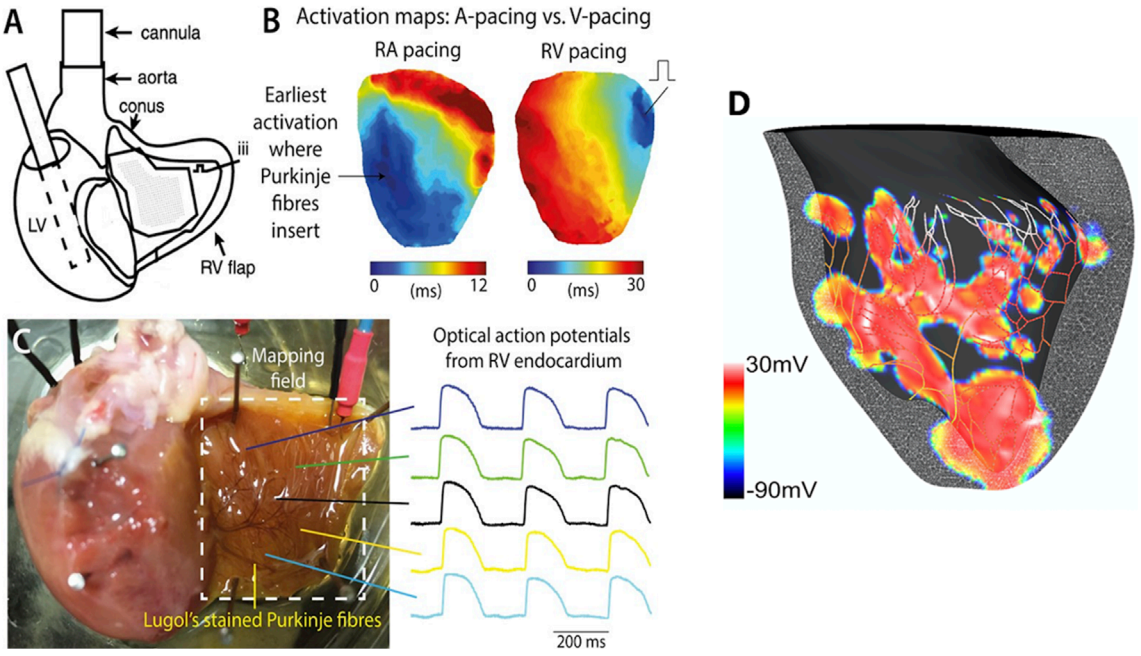

FIGURE 2
Experimental setup for the global ischaemia-reperfusion optical mapping. **(A)** Schematic diagram of aortic-perfused RV endocardial mapping preparation (modified from Cates et al., AJP Heart 2001). **(B)** Representative RV endocardial activation maps for RA and RV pacing. **(C)** Representative optical APs recorded at multiple sites on RV flap. potential map shows areas of early activation (surrogate of active PMJs) in red (+30 mV). **(D)** Computational model of RV endocardium and Purkinje fibers after His stimulation. This transmembrane voltage map shows areas of early activation (surrogate of active PMJs) in red (+30 mV).

were about 1,000 PMJs, but the number of functional PMJs (NPMJ) was varied by changing the global value of R_{PMJ} to arrive at eight different percentages of functional PMJs: 5, 10, 15, 20, 25, 50, 80% and 100%. Functional PMJs were distributed almost evenly on the Purkinje branches. Computations were performed using carpentry (Numericor GmbH), which required 1 minute to simulate 30 ms using 12 cores on a 2.2 GHz AMD Ryzen nine desktop computer.

Sinus activation in the ventricles was performed by current stimulation of the proximal His-bundle. CV in the His/Purkinje system was 1.8 m/s while myocardial tissue conductivities were adjusted to reproduce measured healthy CVs, approximately 60–70 *cm*/sec longitudinally and 25–34 *cm*/sec transversely (Kelly et al., 2013), while reproducing measured activation times. For His pacing, epicardial activation took about 21 ms, which is in the range measured experimentally (16 ms by electrodes array *versus* 25 ms by optical mapping) (Azarov et al., 2007; Bordas et al., 2011).

Myocardial uncoupling during ischaemia was effected by 25% and 50% reductions in all tissue conductivities. Since neither the time course nor the exact extent of uncoupling are known, we sought to cover a plausible range. Ischaemic cellular electrophysiological changes were as suggested by Tice et al. (2007): maximum conductances of Na and L-type Ca channels reduced by 25%, $[K^+]_e$ increased to 11 mM, and the fraction of ATP-sensitive K^+ channels increased to 0.045%. The His/Purkinje system was assumed unaffected by ischaemia (Argentieri et al., 1990).

2.5 Measuring velocity

2.5.1 Experimental activation

Activation patterns of the endocardial surface of the RV free wall were analyzed as represented in Figure 2D. Activation time (AT) was defined as the instant the maximum rate of rise of the upstroke for experimental data. ATs were spatially smoothed and the divergence of the propagation velocity was used to quantify alterations in activation pattern complexity (Fitzgerald et al., 2005).

The approximate area of endocardial surface mapped was 2 × 2 cm. To assess the contribution of changes in propagation across PMJs and the RV activation pattern during ischaemia and reperfusion, the proportion of pixels activated within the first 5 ms was quantified during RA pacing.

For each AT map, the average AT value was subtracted and outliers (more than 2-standard deviations from the mean) were excluded. ATs were averaged over several cycles and finally, spatially filtered by a 2D Gaussian smoothing kernel with a standard deviation of five pixels. For calculating the gradient of AT, a 3 × 3 pixel moving window was applied to the optical image. The gradient was found by fitting a plane to activation time values over that window, using principal component analysis. The gradient was calculated only for windows with less than half of the pixels being outliers.

2.5.2 Computational activation

For computer simulation data, AT for each node on the RV endocardial surface was defined as the time of positive crossing of the −20 mV threshold. For His pacing, the portion of pixels in the first 8 ms was counted, not first 5 ms as with experiment, since <4% of the tissue was ever activated within the first 3 ms, and the higher resolution of the model also influenced this. In our finite element model, the endocardial surface was defined by an unstructured triangular mesh, and the gradient was found by using the gradient of the shape functions.

2.6 Velocity and complexity

Velocity at point n was obtained from:

$$v(n) = \frac{\nabla AT}{|\nabla AT|^2}$$

The divergence of the propagation velocity was used to quantify alterations in activation pattern complexity. The divergence of velocity, $\nabla \cdot v(n) = \frac{\partial v_x}{\partial x} + \frac{\partial v_y}{\partial y}$ was calculated by finding the gradients of each of the components of the velocity field and adding them. The integral of the absolute value of the divergence (IVD) over the endocardial surface was used to quantify overall complexity:

$$IVD = \int_{RV_{endo}} |\nabla \cdot v| d\Omega$$

3 Results

3.1 Effect of acute ischaemia–reperfusion on endocardial activation

Activation maps during baseline, acute ischaemia and reperfusion are shown in Figure 3A. At baseline, a single anterior region of RV endocardium was activated first. With acute ischaemia, the percentage of RV area activated early (i.e., within the first 5 ms) decreased from 64% ± 3% at baseline to 52% ± 8% during early ischaemia ($p = 0.04$), consistent with slowing of conduction. However, during late ischaemia, extra regions of early activation (e.g., in the posterior RV), consistent with areas of functioning PMJs previously-quiescent under baseline, pre-ischaemic conditions were seen (Figure 3A). The percentage of RV area activated early (0–5 ms) in late-ischaemia (>15 min) was similar to that at baseline, with a maximum of 80% ± 5% RV early activation after 40 min (p = NS vs. baseline; (Figure 3B). The values returned towards baseline following reperfusion, decreasing back to 63% ± 11% of RV early activation after 30 min of reperfusion. Representative activation maps with the divergence maps at baseline and after 40 min are shown in Figure 3C. More early breakthrough sites (indictaed by radiating arrows), consistent with newly activated PMJs, were seen at 40 min of ischemmia than at baseline.

3.2 Effects of acute ischaemia-reperfusion in rotigaptide treated hearts

We next assessed the effect of gap junction enhancement, with rotigaptide, on RV activation times and patterns during acute ischaemia and reperfusion. During acute global ischaemia, shortening of APD and slowing of conduction were observed, with normalization following reperfusion (Figure 4A-C) with and without rotigaptide. Control APD90 decreased from 199 ± 6 ms to 137 ± 6 ms after 40 min of ischaemia ($p < 0.05$). This then normalized after 10 min of reperfusion (200 ± 25 ms). Similar trends were also noted in the rotigaptide group. APD90 decreased from 187 ± 5 ms to 104 ± 5 ms after 40 min of ischaemia ($p < 0.05$) and normalized after 20 min of reperfusion (172 ± 7 ms).

The control CV (Figure 4D) decreased from 53.1 ± 6.5 cm/s to 29.9 ± 6.5 cm/s after 40 min of ischaemia ($p < 0.05$), which then normalized to 68.1 ± 16.2 cm/s after 30 min of reperfusion. Local CV slowed in the rotigaptide group following 40 min of global ischaemia (baseline 51.3 ± 5.0 vs. ischaemia 18.6 ± 3.3 cm/s, $p < 0.05$). Figure 4E shows examples of RV activation under RV pacing from which CV measurements were made. With rotigaptide after 40 min of ischaemia, the rotigaptide-treated heart counter-intuitively took longer to activate.

With RA pacing (Figure 4F), the activation of the RV was much faster compared to RV pacing, less than one half of the time. At baseline, rotigaptide treated hearts behaved similarly to control hearts, with the anterior region of the RV endocardium activating first, and the percentage of RV area activated within the first 5 ms decreased during ischaemia. However, unlike the control hearts, no extra regions of early activation were observed, and the paradoxical increase in the percentage of RV area activated within 5 ms in late ischaemia seen in the control hearts was not observed in rotigaptide-treated hearts, with a progressive reduction in percentage of early-activated regions in the RV (baseline: 49% ± 10%; 10 min ischaemia: 46% ± 13%, 20 min ischaemia: 41% ± 14%). The relative decrease in early RV activation appeared to be due to a reduction in the number of functional PMJs, for the same stage of acute ischaemia, when compared to control hearts (Figure 4F). The percentage of early-activated regions in the RV in the rotigaptide group was significantly reduced compared with baseline at 30 and 40 min of ischaemia (both $p < 0.05$, Figure 4G).

3.3 Modelling experiments

3.3.1 Cable propagation

With nominal $[K^+]$ of 5.4 mM, CV was 51.3 cm/s, the resting membrane potential was −87.15 mV, and the threshold for excitation was 27.1 uA/cm^2. Increasing $[K^+]$ to 8 mM yielded a CV of 56.3 cm/s, a resting membrane potential of −76.9 mV, and a threshold of excitation of 19 uA/cm^2. A further increase of $[K^+]$ to 12 mM resulted in a slower CV of 41.7 cm/s, a resting level of −66.5 mV, and a excitation threshold of 14.30 uA/cm^2. With $[K^+]$ of 8 mM, implementing 25% reductions in Na and L-type Ca conductances reduced CV to 50.8 cm/s, and reducing myocardial coupling by 25% further reduced CV to 44.1 cm/s. Under normoxic conditions, tranverse CV was 24 cm/s, and implementing ischaemic ionic and coupling changes resulted in a CV of 20.5 cm/s.

3.3.2 RV simulation

Anterograde conduction occurred after only a 6% reduction in conductivity.

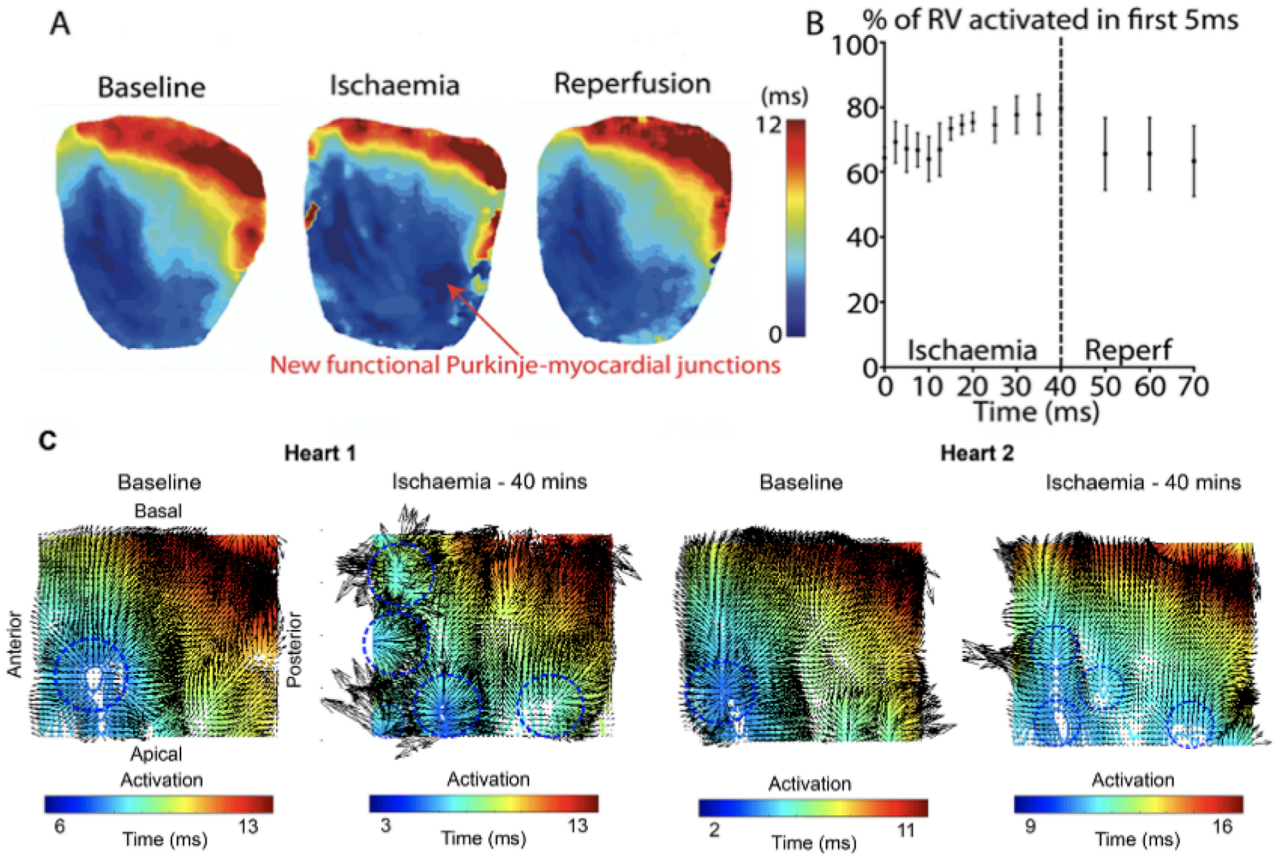

FIGURE 3
Representative activation maps during ischaemia and reperfusion **(A)** Activation maps following RA pacing during baseline, ischaemia and reperfusion. **(B)** Percentage of RV activated in first 5 ms during ischaemia and reperfusion. Data are presented from four control hearts where there were more frequent recordings during early ischaemia (every 2.5 min during the first 20 min), to provide more detail on the time course of these changes. **(C)** Representative activation maps with local conduction vectors at baseline and after 40 mins ischaemia. At baseline, the earliest activation is at the anterior-apical region of the RV, but multiple areas of early activation can be seen at peak ischaemia. Blue circles indicate breakthorough sites.

Figure 5A depicts the isochronal activation maps on the RV endocardium for low (5%) and high numbers (80%) of active PMJs. More active PMJs account for more breakthrough sites in the model, a reduced endocardial activation time and increased complexity of activation. We simulated ischaemia in the ventricular model and measured local CV following RV endocardial stimulation to emulate experiment. Using an ischaemic ventricular ionic model, the myocardial conductivity and number of active PMJs were varied to evaluate their effects on local apparent RV endocardial CV, that is, the CV obtained from naively differencing local activation times without regard for multiple activation sites. Results of a model without the Purkinje system (zero PMJ) were added to compare the CV derived only from myocardial propagation. Significant increases in apparent local CV because of a greater number of active PMJs implies a contribution of the Purkinje system through retrograde and anterograde conduction, which can be greater than effects of increased conductivity on local CV.

RV endocardial activation duration altered in the range of 13–21 ms for different numbers of active PMJs, while epicardial activation was hardly affected. Figure 5B illustrates the value of divergence on the RV endocardial surface for the model with 5% active PMJs. Figure 5C depicts a sample of the activation map and its associated velocity divergence. In both optical and modelling maps, values of divergence were very small (close to zero) in most regions of the surface where the wave-front propagated normally without collisions. Positive divergence is indicative of breakthroughs and negative divergence identifies wave front collisions.

3.3.3 Activation complexity

Results shown in Figure 6 suggest important effects of PMJ density on activation acceleration which was more significant than slowing as result of reduced conductivity. The endocardial area that activated within the first 8 ms mainly increased with greater PMJ density and reduced with decreasing myocardial conductivity. The integral of divergence over the RV endocardial surface was then calculated to quantify differences in propagation patterns. The absolute value of the sum of the divergence over the surface, which represents the complexity of activation pattern, was calculated for optical maps as represented in Figure 6C. Graphs show mean values of IVD, which were normalized to the value at baseline for each heart. Ischaemia increased the IVD, indicative of more breakthrough during ischaemia relative to baseline and reperfusion (Figure 6, n = 4 rabbit hearts). IVD values for different PMJ densities and conductivities are represented in Figure 6C. As the number of active

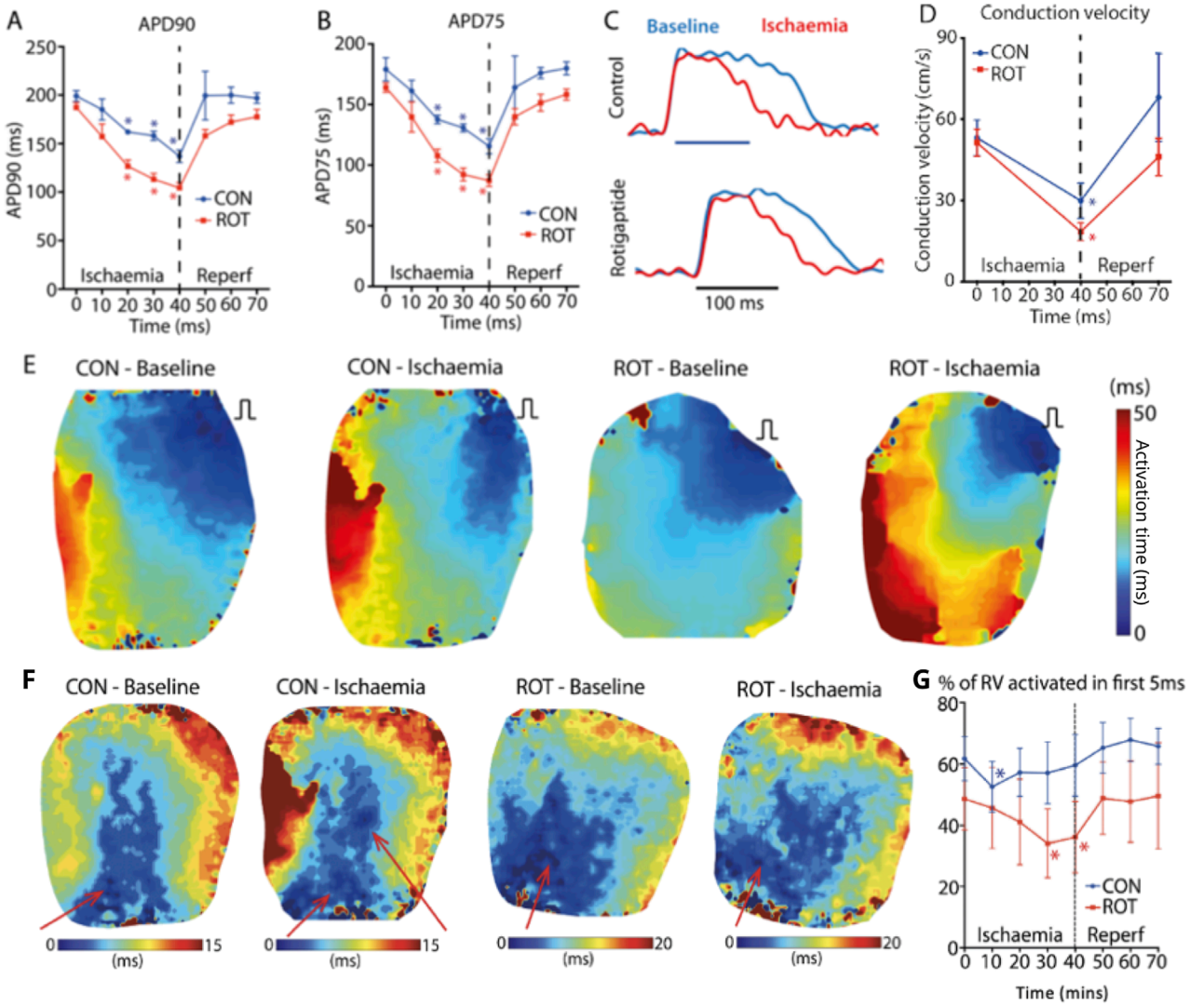

FIGURE 4
Effect of Gap Junction Enhancer Rotigaptide. Compared to control, rotigaptide shortened **(A)** APD90 and **(B)** APD75 over the course of the ischaemia. **(C)** Representative action potentials at baseline (blue) and 40 min ischaemia (red) for control and rotigaptide treated heart. **(D)** Conduction velocity for control and rotigaptide treated hearts. **(E)** RV pacing activation maps at baseline and 40 min of ischaemia for control and rotigaptide treated hearts. **(F)** RA pacing activation maps at baseline and 40 min of ischaemia for control and rotigaptide treated hearts. There are new areas of early activation (functional PMJs indictaed by red arrow) in a control heart during RA pacing, which was not seen in the rotigaptide treated heart. **(G)** Effect of ischaemia and reperfusion on control and rotigaptide treated hearts on percentage of right ventricle activated within the first 5 ms. Likely because of more functional PMJs during ischaemia, the percentage of RV area activated early (within 5 ms) was maintained around 60% in control group, but not in the rotigaptide group. CON–control; ROT–rotigaptide. Data are for control (n = 7) and rotigaptide (n = 5) groups in their entirety. Asteriskes indicate statistical significance.

PMJs increased, more breakthroughs and wave collisions occurred and as a result, IVD increased (6.6 at 5% functional vs 11.0 at 80% functional). Reducing ventricular conductivity (50% decrease) did not impact IVD considerably at low PMJ density (7.1 vs 6.4) but it inversely altered IVD with more active PMJs (12.7 vs 11.0). The recruitment of PMJs by changing R_{PMJ} was not spatially uniform, accounting for the non-monotonic curves in Figures 6A–C.

4 Discussion

The main findings of this study are: 1) many PMJs are quiescent or non-functioning at rest; 2) acute ischaemia leads to an increase in the number of active PMJs, which consequently resulted in faster total ventricular endocardial activation; and 3) this finding was mitigated by enhancing gap junction coupling using rotigaptide.

10.3389/fphys.2025.1540400

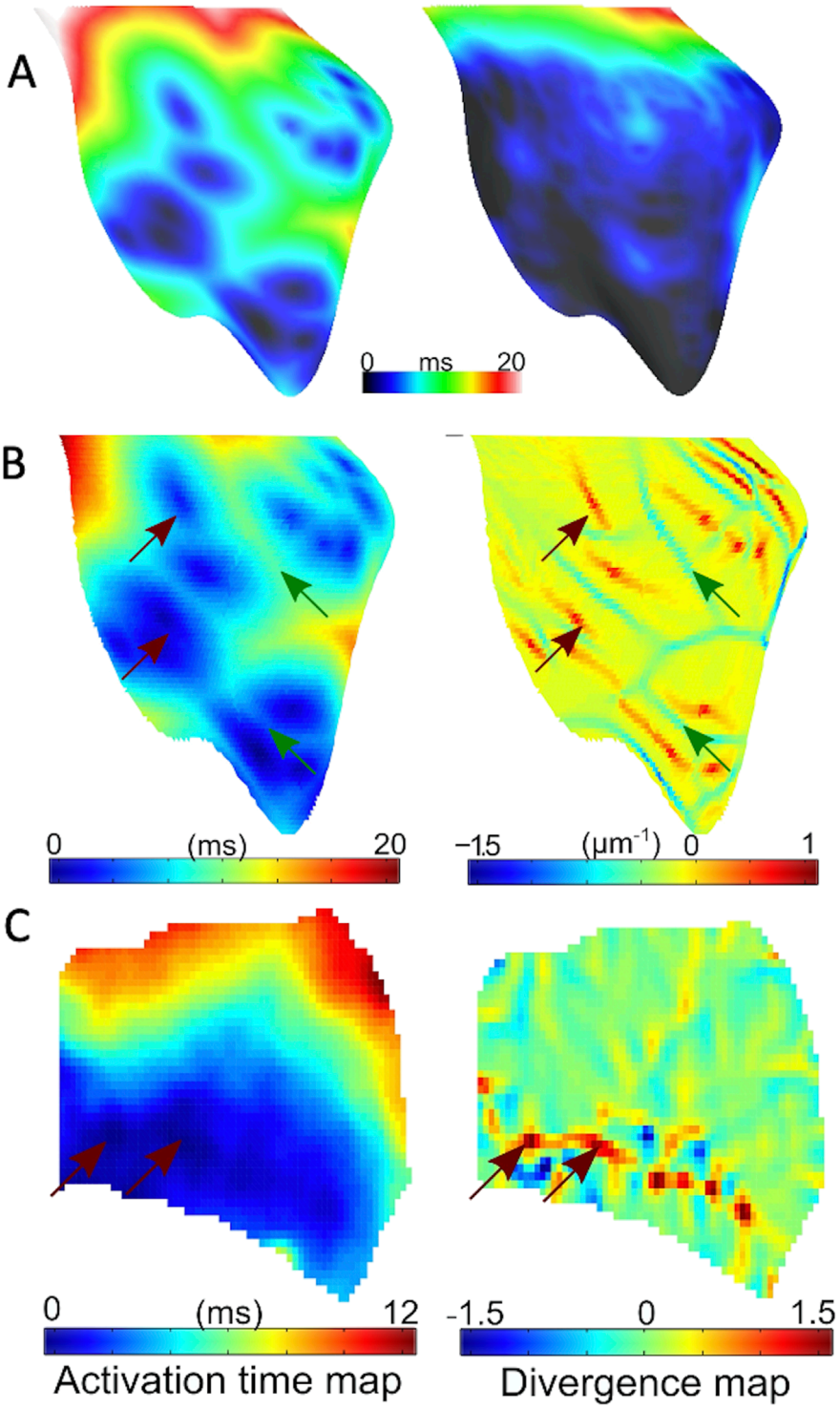

FIGURE 5
Endocardial activation and divergence maps **(A)** Simulated RV endocardial area isochoronal activation maps during His bundle pacing for 5% (left panel) and 80% (right panel) active junctions. **(B)** Representative simulated activation (left panel) with 10% active junctions, and corresponding endocardial divergence map (right panel). Sites of breakthrough are indicated in red arrows on the activation map. Corresponding points on divergence map have large positive divergence, while green arrows represent wave collisions with matching points indicating a large negative divergence. **(C)** Representative experimental activation (left panel) and corresponding endocardial divergence map (right panel). Arrows point to breakthrough sites on activation maps that match the location of large positive divergence on the divergence map.

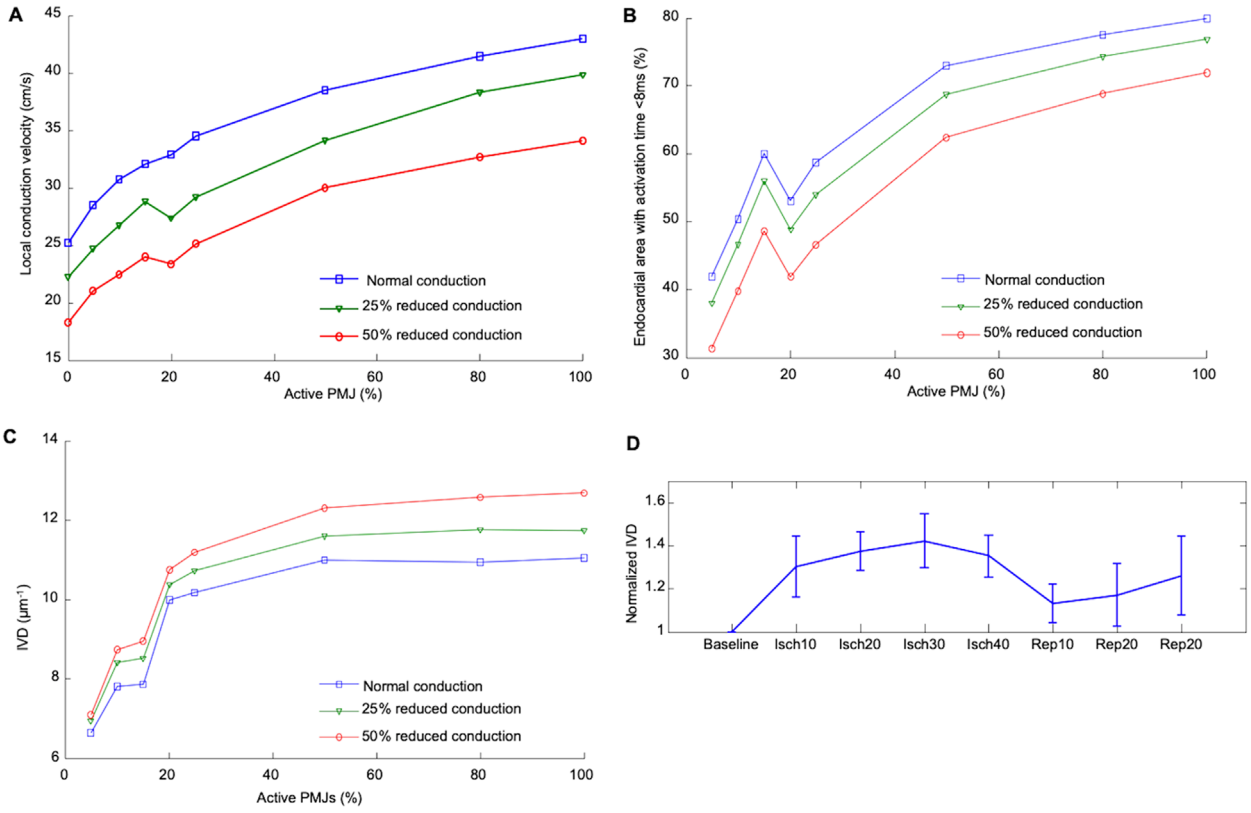

FIGURE 6
Effect of percentage active PMJs on activation time and conduction velocities **(A)** Alteration in median local CV in ischaemic computer model by conductivity and number of active PMJs following RV pacing. **(B)** Variations in the activated area with changes of percentage of active PMJs and myocardial conductance in computer model of sinus activation. The endocardial area that activated within the first 8 ms mainly was increased by increasing PMJ density and reduced by decreasing myocardial conductivity. **(C)** Calculated IVD relative to number of active PMJs and myocardial conductance in computer model during sinus activation. **(D)** Experimental effect of ischaemia and reperfusion on calculated IVD during atrial pacing.

4.1 Acute ischaemia increases the number of active PMJs

Preclinical data have indicated that many PMJs are non-functioning at baseline and this is thought to be due to source-sink mismatch at these junctions (Mendez et al., 1970; Joyner, 1982; Overholt et al., 1984). This hypothesis is supported by a study in connexin43 knockout mice, where multiple extra epicardial wavefronts were observed when compared to control hearts. It was thought that alterations in source-sink relationships due to Cx43 knockout led to paradoxical conduction across normally quiescent PMJs and resulted in the aberrant activation profiles and wavefront collisions (Morley et al., 2005). Our results suggest that most anterograde PMJ transmission failures occur because of too much coupling, instead of too little. This might be expected since most modulating factors tend to reduce gap junction conductance (increased $[Ca_i^{2+}]$ or decreased pH), and reducing weak coupling would little affect the quiescence of the gap junctions.

Consistent with the above, we showed that acute ischaemia, which causes gap junction uncoupling and a decrease in CV (Janse et al., 1986), was associated with an increase in activation complexity, resulting from activation breakthroughs, which led to a similar paradoxical acceleration in RV activation. We postulate that ischaemia-induced gap junction closure facilitated more successful anterograde PMJ propagation by reducing electrical load at normally quiescent PMJs all along the conduction system, including towards the base. Therefore, despite reduced local CV, the activation time of the total endocardium was shortened. In contrast to the previously mentioned Cx43 knockout study, we analyzed PMJs located at the endocardial surface rather than the epicardial surface, which notably does not contain PMJs and therefore indirectly assesses PMJ function (Morley et al., 2005).

Tranum-Jensen et al. reported an intermediate cell type between Purkinje and myocardial cells consisting of distinct morphological features and postulated protection of anterograde propagation (Tranum-Jensen et al., 1991). However, in that paper, there was insufficient functional support for what they describe since the tissue environment was not manipulated nor were any electrical propagation delays across the PMJ reported. In contrast, Tan et al. did explore this and they reported that transmission was modulated and could fail depending on changes in potassium concentration and hypoxia (Joyner, 1982). Therefore, electronic interaction is important at the PMJ, whether it be from Purkinje to transitional cell or transitional cell to muscle.

Unfortunately, due to the limitations of even state-of-the-art optical mapping techniques, we were unable to individually

visualize PMJs and it must be stated that areas of early activation may be because of several mechanisms including: 1) Increased PMJ activations; 2) Ectopic foci; 3) A wavefront travelling on an epicardium decoupled from the endocardium except at distinct regions. Our modelling data showed that the activation times were confluent with sinus activation, ordered and consistent, which argues against ectopic foci (point 2). Point 3 cannot explain our results. If ischaemic uncoupling essentially divided the wall into epicardial and endocardial regions with a few discrete connection points resulting in more breakthroughs, the CV would still by reduced and result in longer activation. Arguing that propagation in the thin layer is faster than the complete wall is unfounded, as plane waves will eventually result in both cases. Therefore, we believe that increased PMJ activation remains the most plausible option.

4.2 Gap junction enhancement prevents PMJ activation during ischaemia

Simulations in the cable indicated that ischaemia could lead to increased early activation sites via K^+ concentration if it was the dominant change, by reducing current thresholds for excitation. However, other ischaemic effects will cause an overall decrease in CV. Increased tissue excitability could also explain the findings of increased early activation sites: it may be possible that the reduced current thresholds for excitation, as shown in the cable simulations, and the improved source-sink match at the PMJs due to change in gap junction coupling are both important in explaining the observed changes in RV activation pattern during ischaemia. In the organ simulations, however, reduced current thresholds were not necessary. The Purkinje system is less affected by schema than myocardial tissue (Fenoglio et al., 1976), with CV remaining unaffected even 1 day after ligation in a dog model (Argentieri et al., 1990).

We further explored our hypothesis by assessing the effect of pharmacological modification of gap junction coupling using rotigaptide, which enhanced gap junction coupling during ischaemia. In hearts treated with rotigaptide, we postulate that PMJs which were usually quiescent, but became functional during ischaemia, were again rendered quiescent since the number of breakthroughs decreased. These findings support our hypothesis changes in gap junction coupling can alter PMJ anterograde impulse propagation. Under normal conditions, there is a high level of safety (redundancy) in the number of open gap junctions; thus, rotigaptide did not affect tissue conduction velocity. Treatment with rotigaptide during ischaemia reduced the number of new functional PMJs, mitigating ischaemia-induced gap junction uncoupling, and maintained the level of source-sink mismatch present during baseline conditions.

The divergence maps could also have been used to build estimates of the Purkinje network as has been performed previously (Barber et al., 2021). Breakthrough sites are clearly identified, as in Figure 5, and show activations in the lower region which anatomically correspond to the region around the moderator band, where PMJs are know to be located. The greater IVF during ischaemia results from more breakthroughs, and allows a more complete depiction of the Purkinje network.

4.3 Local increases in CV by gap junction enhancement were not seen endocardially

Rotigaptide has previously been shown to improve local CV during acute ischaemia and in the context of metabolic stress by maintaining gap junction coupling (Eloff et al., 2003; Ng et al., 2016). However, this effect was not observed in our study. It should be noted that we used a novel endocardial mapping preparation, whilst the other studies on the effects of rotigaptide were based on epicardial mapping. Local apparent endocardial CV was calculated based on a 2D projection of 3D conduction and, therefore, indicative of overall endocardial activation velocity. In rabbit hearts, Purkinje fibers only penetrate a shallow subendocardial layer, and therefore this measure partially depends on activation through the Purkinje system. This may explain why rotigaptide did not result in an improvement in CV that has been reported by other groups who analyzed the epicardial surface, which does not contain PMJs, and where the calculated epicardial CV is predominantly based on myocardial wavefront propagation (Dhein et al., 2010).

4.4 Modelling insight

To ascertain whether our observed findings were due to enhanced PMJ function, we performed a series of modelling experiments mimicking the experimental set up. Myocardial conductivity and the number of active PMJs were varied in the model to evaluate effects on local apparent RV endocardial CV. A model without the Purkinje system (zero PMJs) allowed comparison of the CV derived solely from endocardial activation times. Significant increases in local apparent CV because of more active PMJs implied a contribution of the Purkinje system through both retrograde and anterograde conduction, which could be greater than effects of conductivity on local CV. Moreover, the changes in apparent endocardial CV that occurred with different PMJ densities, implied that measured CV is not solely dependent on myocardial cell-to-cell conduction but also via the Purkinje system as well. Comparison of modeling and experiment results in Figures 5, 6 suggests a potential mechanism for accelerated activation during acute ischaemia. Increasing the number of active PMJs in the model accelerates endocardial activation and compensates for the slowing of propagation. Thus, the area activated in a model with reduced conductivity and a high percentage of active PMJs (ischaemia) can be equal to or larger than the area activated under normal conditions. Note that in Figure 6, the curve is not monotonic due to the nonuniform distribution of active PMJs and a random sampling of them. At an active PMJ level of 15%, the active PMJs were very well separated, resulting in a large area activated through local CV conduction.

Normally, severe uncoupling conditions cause discontinuity and meandering of activation wavefronts, where islands of uncoupled cells enforce twisting of the activation wavefront. However, we do not believe that this is the reason underlying the observed increased activation complexity during ischaemia since the CV reduced to 20–30 cm/s due to both reduced excitability and reduced coupling, which is a modest reduction compared to the CV measured during critical gap junction uncoupling. In addition, CV completely recovered following reperfusion in our biological

experiments. Therefore, we conclude that the observed increase in activation complexity under ischaemia can be attributed to function of normally inactive PMJs. In addition, ischaemic hearts treated with rotigaptide could be analogous to the model of increased conductivity and few active PMJs, which could lead to lower local endocardial CVs.

4.5 Clinical implications

The Purkinje system is pivotal in the pathogenesis of several pathological ventricular arrhythmias including Purkinje-triggered VF, bundle branch reentry and fascicular VT (Haissaguerre et al., 2016). Since we were able reduce the number of active PMJs during acute ischaemia pharmacologically by enhancing gap junction function, this could be a viable therapeutic strategy to reduce the propagation of Purkinje system arrhythmias into the ventricular myocardium, either as a temporizing measure prior to definitive management (catheter ablation) or even periprocedurally as an adjunctive therapy.

4.6 Study limitations

Our interpretation of data is based on relative changes in activation, which was used as a surrogate to indicate active PMJ density. Nevertheless, with current state-of-the-art optical mapping techniques, it is impossible measure individual PMJs and, as such, indirect evidence of activation is taken from clusters or groups of PMJs becoming active and manifesting as a breakthrough. However, this method does have significant advantages, in that it allows for simultaneous mapping of the entire RV endocardial surface to look at changes RV activation patterns and infer propagation across multiple PMJs simultaneously. Secondly, our model of the PMJ replicates transmission behavior at junctions, but we were not able to study complete effects of ischaemia using this simple representation. For example, the models used for this research did not account for myocardial heterogeneity, which contributes to disparate response of different layers of ventricular wall to ischaemia. Thirdly, we did not include any ischaemic effects on the Purkinje system since it is known to be more resistant to ischaemia.

In this study, our objective was to investigate the changes in acute ischaemia only and the reversibility of these changes following reperfusion, and we were therefore not able to study the changes associated with longer durations of ischaemia. In this experiental model, we did not bubble the physiological solution with nitrogen. There was likely a reduced depth of ischaemia than if we had bubbled with nitrogen, though the slowing of conduction and changes in APD confirm that there was significant myocardial effects.

5 Conclusion

In this study, using an endocardial mapping preparation that allowed for the interrogation of propagation patterns across PMJs, we found behaviour consistent with a significant majority of PMJs at baseline being quiescent. Activation of these normally-quiescent PMJs by gap junction uncoupling during acute ischaemia could explain a paradoxical acceleration in RV endocardial activation, and an increased activation complexity. Pharmacological gap junction modulation significantly altered propagation patterns during ischaemia, presumably through changing source-sink mismatch, and could be a therapeutic strategy for arrhythmia control.

Data availability statement

The raw data supporting the conclusions of this article will be made available by the authors, without undue reservation.

Ethics statement

The animal study was approved by the Imperial College London Ethical Review Board (carried out under Project License PPL 70/7419). The study was conducted in accordance with the local legislation and institutional requirements.

Author contributions

RJ: Formal Analysis, Investigation, Methodology, Writing - original draft, Writing - review and editing. EB: Formal Analysis, Investigation, Methodology, Writing - original draft, Writing - review and editing. MD: Investigation, Writing - original draft, Writing - review and editing. AN: Supervision, Writing - original draft, Writing - review and editing. AH: Investigation, Writing - original draft, Writing - review and editing. IE: Resources, Writing - original draft, Writing - review and editing. MH: Investigation, Resources, Validation, Writing - original draft, Writing - review and editing. NP: Resources, Supervision, Writing - original draft, Writing - review and editing. FN: Conceptualization, Funding acquisition, Investigation, Project administration, Resources, Supervision, Writing - original draft, Writing - review and editing. EV: Conceptualization, Funding acquisition, Methodology, Software, Supervision, Writing - original draft, Writing - review and editing.

Funding

The author(s) declare that financial support was received for the research and/or publication of this article. FN was funded by the British Heart Foundation (FS/11/69/29017, RG/16/3/32175 and RG/F/22/110078), The UK National Institute for Health Research (NIHR Clinical Lectureship CL-2011-21-011 and Imperial Biomedical Research Centre) and an Academy of Medical Sciences Starter Grant (AMS-SGCL8-Ng). EV was funded by National Research Agency (ANR), Grant reference ANR-10-IAHU-04 and

the National Institutes of Health, grant number R01HL101196. EV and IE were supported by the LeDucq Foundation 23CVD04. ANR - EV salary BHF - experiment costs/fellows NIH - experiments LeDucq - collaborative travel.

Conflict of interest

Author EV was employed by IMB, UMR5251.

The remaining authors declare that the research was conducted in the absence of any commercial or financial relationships that could be construed as a potential conflict of interest.

The author(s) declared that they were an editorial board member of Frontiers, at the time of submission. This had no impact on the peer review process and the final decision.

Generative AI statement

The author(s) declare that no Generative AI was used in the creation of this manuscript.

Publisher's note

References

Argentieri, T., Frame, L., and Colatsky, T. (1990). Electrical properties of canine subendocardial Purkinje fibers surviving in 1-day-old experimental myocardial infarction. *Circulation Res.* 66, 123–134. doi:10.1161/01.res.66.1.123

Aslanidi, O., Sleiman, R., Boyett, M., Hancox, J., and Zhang, H. (2010). Ionic mechanisms for electrical heterogeneity between rabbit Purkinje fiber and ventricular cells. *Biophysical J.* 98, 2420–2431. doi:10.1016/j.bpj.2010.02.033

Azarov, J., Shmakov, D., Vityazev, V., Roshchevskaya, I., and Roshchevsky, M. (2007). Activation and repolarization patterns in the ventricular epicardium under sinus rhythm in frog and rabbit hearts. *Mol. and Integr. physiology* 146, 310–316. doi:10.1016/j.cbpa.2006.10.036

Barber, F., Langfield, P., Lozano, M., Garcia-Fernandez, I., Duchateau, J., Hocini, M., et al. (2021). Estimation of personalized minimal Purkinje systems from human electro-anatomical maps. *IEEE Trans. Med. imaging* 40, 2182–2194. doi:10.1109/TMI.2021.3073499

Behradfar, E., Nygren, A., and Vigmond, E. (2014). The role of Purkinje-myocardial coupling during ventricular arrhythmia: a modeling study. *PloS one* 9, e88000. doi:10.1371/journal.pone.0088000

Bordas, R., Gillow, K., Lou, Q., Efimov, I., Gavaghan, D., Kohl, P., et al. (2011). Rabbit-specific ventricular model of cardiac electrophysiological function including specialized conduction system. *Prog. biophysics Mol. Biol.* 107, 90–100. doi:10.1016/j.pbiomolbio.2011.05.002

Boyden, P. (2018). Purkinje physiology and pathophysiology. *J. interventional cardiac Electrophysiol. Int. J. Arrhythm. pacing* 52, 255–262. doi:10.1007/s10840-018-0414-3

Boyle, P., Deo, M., Plank, G., and Vigmond, E. (2010). Purkinje-mediated effects in the response of quiescent ventricles to defibrillation shocks. *Ann. Biomed. Eng.* 38, 456–468. doi:10.1007/s10439-009-9829-4

Cates, A., Smith, W., Ideker, R., and Pollard, A. (2001). Purkinje and ventricular contributions to endocardial activation sequence in perfused rabbit right ventricle. *Am. J. physiology. Heart circulatory physiology* 281, H490–H505. doi:10.1152/ajpheart.2001.281.2.H490

Dhein, S., Hagen, A., Jozwiak, J., Dietze, A., Garbade, J., Barten, M., et al. (2010). Improving cardiac gap junction communication as a new antiarrhythmic mechanism: the action of antiarrhythmic peptides. *Naunyn-Schmiedeberg's archives Pharmacol.* 381, 221–234. doi:10.1007/s00210-009-0473-1

Eloff, B., Gilat, E., Wan, X., and Rosenbaum, D. (2003). Pharmacological modulation of cardiac gap junctions to enhance cardiac conduction: evidence supporting a novel target for antiarrhythmic therapy. *Circulation* 108, 3157–3163. doi:10.1161/01.CIR.0000101926.43759.10

Fenoglio, J., Albala, A., Silva, F., Friedman, P., and Wit, A. (1976). Structural basis of ventricular arrhythmias in human myocardial infarction: a hypothesis. *Hum. Pathol.* 7, 547–563. doi:10.1016/s0046-8177(76)80102-5

Fitzgerald, T., Brooks, D., and Triedman, J. (2005). Identification of cardiac rhythm features by mathematical analysis of vector fields. *IEEE Trans. bio-medical Eng.* 52, 19–29. doi:10.1109/TBME.2004.839636

Haïssaguerre, M., Shoda, M., Jaïs, P., Nogami, A., Shah, D., Kautzner, J., et al. (2002). Mapping and ablation of idiopathic ventricular fibrillation. *Circulation* 106, 962–967. doi:10.1161/01.cir.0000027564.55739.b1

Haissaguerre, M., Vigmond, E., Stuyvers, B., Hocini, M., and Bernus, O. (2016). Ventricular arrhythmias and the His-Purkinje system. *Nat. Rev. Cardiol.* 13, 155–166. doi:10.1038/nrcardio.2015.193

Janse, M., Kleber, A., Capucci, A., Coronel, R., and Wilms-Schopman, F. (1986). Electrophysiological basis for arrhythmias caused by acute ischemia. Role of the subendocardium. *J. Mol. Cell. Cardiol.* 18, 339–355. doi:10.1016/s0022-2828(86)80898-7

Joyner, R. (1982). Effects of the discrete pattern of electrical coupling on propagation through an electrical syncytium. *Circulation Res.* 50, 192–200. doi:10.1161/01.res.50.2.192

Kelly, A., Ghouri, I., Kemi, O., Bishop, M., Bernus, O., Fenton, F., et al. (2013). Subepicardial action potential characteristics are a function of depth and activation sequence in isolated rabbit hearts. *Arrhythmia Electrophysiol.* 6, 809–817. doi:10.1161/CIRCEP.113.000334

Laughner, J., Ng, F., Sulkin, M., Arthur, R., and Efimov, I. (2012). Processing and analysis of cardiac optical mapping data obtained with potentiometric dyes. *Am. J. physiology. Heart circulatory physiology* 303, H753–H765. doi:10.1152/ajpheart.00404.2012

Mahajan, A., Shiferaw, Y., Sato, D., Baher, A., Olcese, R., Xie, L., et al. (2008). A rabbit ventricular action potential model replicating cardiac dynamics at rapid heart rates. *Biophysical J.* 94, 392–410. doi:10.1529/biophysj.106.98160

Mendez, C., Mueller, W., and Urguiaga, X. (1970). Propagation of impulses across the Prukinje fiber-muscle junctions in the dog heart. *Circulation Res.* 26, 135–150. doi:10.1161/01.res.26.2.135

Morley, G., Danik, S., Bernstein, S., Sun, Y., Rosner, G., Gutstein, D., et al. (2005). Reduced intercellular coupling leads to paradoxical propagation across the Purkinje-ventricular junction and aberrant myocardial activation. *PNAS* 102, 4126–4129. doi:10.1073/pnas.0500881102

Nakagawa, H., Beckman, K., McClelland, J., Wang, X., Arruda, M., Santoro, I., et al. (1993). Radiofrequency catheter ablation of idiopathic left ventricular tachycardia guided by a Purkinje potential. *Circulation* 88, 2607–2617. doi:10.1161/01.cir.88.6.2607

Ng, F., Holzem, K., Koppel, A., Janks, D., Gordon, F., Wit, A., et al. (2014). Adverse remodeling of the electrophysiological response to ischemia-reperfusion in human heart failure is associated with remodeling of metabolic gene expression. *Circulation. Arrhythmia Electrophysiol.* 7, 875–882. doi:10.1161/CIRCEP.113.001477

Ng, F., Kalindjian, J., Cooper, S., Chowdhury, R., Patel, P., Dupont, E., et al. (2016). Enhancement of gap junction function during acute myocardial infarction modifies healing and reduces late ventricular arrhythmia susceptibility. *JACC. Clin. Electrophysiol.* 2, 574–582. doi:10.1016/j.jacep.2016.03.007

Ng, F., Shadi, I., Peters, N., and Lyon, A. (2013). Selective heart rate reduction with ivabradine slows ischaemia-induced electrophysiological changes and reduces ischaemia-reperfusion-induced ventricular arrhythmias. *J. Mol. Cell. Cardiol.* 59, 67–75. doi:10.1016/j.yjmcc.2013.02.001

Overholt, E., Joyner, R., Veenstra, R., Rawling, D., and Wiedmann, R. (1984). Unidirectional block between Purkinje and ventricular layers of papillary muscles. *Am. J. physiology* 247, H584–H595. doi:10.1152/ajpheart.1984.247.4.H584

Robinson, R., Boyden, P., Hoffman, B., and Hewett, K. (1987). Electrical restitution process in dispersed canine cardiac Purkinje and ventricular cells. *Am. J. physiology* 253, H1018–H1025. doi:10.1152/ajpheart.1987.253.5.H1018

Rohr, S., Kucera, J., Fast, V., and Kléber, A. (1997). Paradoxical improvement of impulse conduction in cardiac tissue by partial cellular uncoupling. *Sci. (New York, N.Y.)* 275, 841–844. doi:10.1126/science.275.5301.841

Tan, R., Ramza, B., and Joyner, R. (1989). Modulation of the Purkinje-ventricular muscle junctional conduction by elevated potassium and hypoxia. *Circulation* 79, 1100–1105. doi:10.1161/01.cir.79.5.1100

Tice, B., Rodríguez, B., Eason, J., and Trayanova, N. (2007). Mechanistic investigation into the arrhythmogenic role of transmural heterogeneities in regional ischaemia phase 1A. *Europace* 9 (Suppl. 6), vi46–vi58. doi:10.1093/europace/eum204

Tranum-Jensen, J., Wilde, A., Vermeulen, J., and Janse, M. (1991). Morphology of electrophysiologically identified junctions between Purkinje fibers and ventricular muscle in rabbit and pig hearts. *Circulation Res.* 69, 429–437. doi:10.1161/01.res.69.2.429

frontiers | Frontiers in Physiology

TYPE Original Research
PUBLISHED 26 June 2025
DOI 10.3389/fphys.2025.1607916

OPEN ACCESS

EDITED BY
Edward Joseph Vigmond,
Université de Bordeaux, France

REVIEWED BY
Guglielmo Sorci,
University of Perugia, Italy
Sridharan Rajamani,
Janssen Pharmaceutical Companies of Johnson and Johnson, United States
Adekunle Adeoye,
Georgia State University, United States

*CORRESPONDENCE
Lucile Miquerol,
lucile.miquerol@univ-amu.fr

RECEIVED 08 April 2025
ACCEPTED 09 June 2025
PUBLISHED 26 June 2025

CITATION
Vahdat J, Sauer J, Marksteiner J, Hilber K and Miquerol L (2025) Conduction defects and arrhythmias in *mdx* mice are not associated with a degeneration of the cardiac Purkinje network.
Front. Physiol. 16:1607916.
doi: 10.3389/fphys.2025.1607916

Conduction defects and arrhythmias in *mdx* mice are not associated with a degeneration of the cardiac Purkinje network

Juliette Vahdat[1], Jakob Sauer[2], Jessica Marksteiner[2], Karlheinz Hilber[2] and Lucile Miquerol[1]*

[1]Aix-Marseille Université, CNRS UMR 7288, Developmental Biology Institute of Marseille, Marseille, France, [2]Department of Neurophysiology and Neuropharmacology, Center for Physiology and Pharmacology, Medical University of Vienna, Vienna, Austria

Duchenne muscular dystrophy (DMD) is a severe X-chromosomal disease characterised by progressive muscle weakness and degeneration. Cardiac involvement is inevitable in DMD patients and ventricular arrhythmias are a high-risk factor for mortality in these patients. Ventricular arrhythmias are often triggered by a dysfunctional ventricular conduction system, which serves as an electrical circuit in the heart to ensure the synchronization of the heartbeat. This system includes Purkinje fibers which are susceptible to degeneration in DMD patients, leading to cardiac conduction disorders. To unravel whether a defective ventricular conduction system may account for arrhythmogenesis in a DMD mouse model, we performed a longitudinal study of the cardiac electrical activity in *mdx* mice. ECG recordings showed a progressive increase in PR interval over time and a prolonged QRS in *mdx* compared to wild-type (WT) mice. At baseline, only *mdx* mice presented premature ventricular complexes (PVC), and a greater prevalence of PVC was observed after β-adrenergic stimulation in these mice. These conduction defects and arrhythmias occurred while no defects in the morphology and maturation of the Purkinje fiber network were observed. However, *mdx* mice had a larger heart and showed signs of fibrosis and hypertrophy. Furthermore, conduction defects in *mdx* mice were associated with ventricular dyssynchrony and sodium current (I_{Na}) reduction in ventricular myocytes and Purkinje fibers. Altogether, these data demonstrated that *mdx* mice develop a progressive arrhythmogenic cardiomyopathy in association with I_{Na} loss, ventricular fibrosis but without degeneration of the ventricular conduction system.

KEYWORDS

conduction system anatomy, DMD, Purkinje fibers, ECG, sodium current

Introduction

Duchenne muscular dystrophy (DMD) is primarily characterized by skeletal muscle degeneration resulting from mutations in the X-linked gene encoding the structural cytoskeletal Dystrophin. Besides this skeletal muscle degeneration, cardiomyopathy is highly prevalent in DMD patients, being observed in 50% of

patients by the age of 10 and almost 100% by adulthood (Nigro et al., 1990). DMD-associated cardiomyopathies are prone to ventricular arrhythmias and lead to chronic congestive heart failure, which is now the leading cause of death in DMD patients (Kamdar and Garry, 2016; Shirokova and Niggli, 2013; Spurney, 2011; Tsuda and Fitzgerald, 2017). As the specific mechanisms behind these arrhythmias are poorly understood, current treatment strategies do not prevent life-threatening ventricular tachycardias.

Various cardiac arrhythmias, recorded by ECG in DMD patients, implicate dysfunction of the ventricular conduction system (VCS) (Chenard et al., 1993; Perloff, 1984). The VCS is composed of the His bundle, bundle branches (BB) and ends in a complex network of Purkinje fibers (PF) and is responsible for synchronizing the heartbeat. Left bundle branch block (LBBB) is relatively frequent in DMD patients and is a major predictive factor for cardiac events and mortality (Fayssoil et al., 2018). Moreover, dystrophin-deficient Purkinje fibers have been reported to exhibit vacuole degeneration in patients with DMD (Nomura and Hizawa, 1982) and in dystrophic dogs (Urasawa et al., 2008; Echigoya et al., 2017). In addition, dystrophin protein rescue in cardiac Purkinje fibers contributed to the improvement or prevention of conduction abnormalities in the dystrophic dog heart (Echigoya et al., 2017). Thus, dystrophin may play a primary role in the function and integrity of cardiac Purkinje fibers. Besides, dystrophin is more abundantly expressed in human Purkinje fibers in comparison with contractile cardiomyocytes (Bies et al., 1992). Among the multiple causes of conduction defects, we have previously shown that morphological defects of the Purkinje network induce a slow conduction and ventricular dyssynchrony in mice, leading to ventricular dysfunction (Choquet et al., 2018; Choquet et al., 2023; Meysen et al., 2007). However, the structure of the ventricular PF network in *mdx* mice, the most commonly used animal model for DMD (Bulfield et al., 1984), is unknown.

Dystrophin-deficient (*mdx*) mice share important clinical features with the cardiomyopathy of DMD patients (Chu et al., 2002). Electrical disturbances such as reduced PR, PQ and elongated QRS have been observed in *mdx* males and females while dilated cardiomyopathy with cardiac dysfunction arises with age (Branco et al., 2007; Koenig et al., 2014). In *mdx* mice, conduction defects have been assigned to multiple causes such as abnormal calcium homeostasis, elevated reactive oxygen species or impaired sodium current (I_{Na}) in cardiomyocytes (Gavillet et al., 2006; Koenig et al., 2011; Wang et al., 2018). Our previous studies have indeed shown that both mdx ventricular cardiomyocytes from the working myocardium and mdx Purkinje fibers have abnormally diminished I_{Na} densities (Ebner et al., 2022; Ebner et al., 2020; Koenig et al., 2011; Sauer et al., 2024). However, this does not explain all conduction defects observed in DMD patients. A core issue for the cardiac pathogenesis in DMD is to determine whether defective morphogenesis of the conduction system may explain the life-threatening arrhythmogenesis and associated heart failure of these patients. To answer this question, we studied cardiac function and the morphology of the PF network in *mdx* mice in parallel by crossing them with Cx40-GFP mouse line in which GFP is specifically expressed in the entire ventricular conduction system (Miquerol et al., 2004).

Materials and methods

Ethics statement

All studies and procedures involving animals were in strict accordance with the recommendations of the European Community Directive Article (2010/63/UE) for the protection of vertebrate animals used for experimental and other scientific purposes. The project was specifically approved by the regional ethics committee and by the French Ministry of Research (APAFIS N° 36487-2022040816108385 v.7). All experimental protocols for the patch clamp studies were approved by the Austrian Science Ministry (BMWFW-66.009/0175-WF/V/3b/2015).

Mouse models

Dystrophin-deficient *mdx* mice on the BL10 background (C57BL/10ScSn-Dmdmdx/J) (Ebner et al., 2020) were cross-bred with a transgenic mouse line (Cx40eGFP/+; BL10 background) expressing eGFP under the control of the connexin 40 (Cx40) gene (Miquerol et al., 2004). Only males aged between 1 and 12 months were used for the experiments. Genotyping of the mice was performed using standard PCR assays.

Macroscopic and histological analyses

Mice were euthanized by cervical dislocation and hearts from 12-month-old animals were excised and immediately received a perfusion of PBS-KCl (50 mM) by the aorta.

For histological studies, adult hearts were fixed overnight in 4% paraformaldehyde (vol/vol) in PBS, washed in sucrose gradient, then embedded in OCT and cryosectioned. For immunofluorescence, sections were permeabilized in PBS 1X/0.2% Triton X100 for 20 min and incubated for 1 h in saturation buffer (PBS 1X/3% BSA/0.1% Triton X100). Primary antibodies were incubated in saturation buffer overnight at 4°C. Secondary antibodies coupled to fluorescent molecules were incubated in saturation buffer and after washes, hearts were observed under a Zeiss Apotome microscope.

For whole-mount immunofluorescence, the left ventricular wall of adult hearts was opened by scissors and pinned on a petri dish to expose the septal surface and fixed in 4% paraformaldehyde for 2 h at 4°C, washed in PBS, permeabilized in PBS 1X/0.5% Triton X100 for 1 h and incubated for 3 h in saturation buffer (PBS 1X/3% BSA/0.1% Triton X100). The primary antibodies were incubated in saturation buffer for 24 h at 4°C. Secondary antibodies coupled to fluorescent molecules were incubated in saturation buffer and after washes, hearts were observed under a Zeiss LSM780 confocal microscope.

Antibodies used in this study were specific to Contactin-2 (AF1714, R&D system), GFP (AbD Serotec), dystrophin (12715-1-AP, ProteinTech), WGA-Cy3 (29076-1, Clinisciences) and WGA-Cy5 (29024-1, Clinisciences). The antibody against Cx43 is homemade and previously described (Gros and Jongsma, 1996).

Fibrosis measurements

Wheat Germ Agglutinin (WGA) staining was quantified using Fiji (Fiji Is Just ImageJ). Images were converted to 8-bit grayscale, and a manual threshold was applied to isolate the WGA-positive signal. Threshold values were adjusted consistently across all samples, based on intensity histograms and visual observation, to ensure that the stained regions were accurately defined. A region of interest (ROI) was manually delineated to include only cardiac tissue, excluding background and non-specific areas. Within the ROI, the number of WGA-positive pixels was expressed as a percentage of the total number of tissue pixels: (number of WGA-positive pixels/total number of tissue pixels) × 100.

Surface electrocardiography

Surface ECGs were performed on anesthetized mice. An induction with 5% isoflurane was followed by maintenance at 1%–2% in a constant flow of oxygen at 700 mL/min. ECGs were recorded with a bipolar system in which the electrodes were placed subcutaneously at the right (negative) and left forelimb (reference) and the left hindlimb (positive) for lead II, at the right (reference) and left forelimb (negative) for lead III. Electrodes were connected to a Bioamp amplifier (AD Instruments) and were digitalized through a PowerLab 26T (AD Instruments). Digital recordings were analyzed with LabChart software version 8.1.13 (AD Instruments). Events were registered to 100 K/s and were filtered to 50 Hz. ECG recordings were obtained for 3 min after stabilization of the signal. Post-analysis was performed for heart rate, PR, QRS, QT intervals, T, R and S durations and T, R, S and QRS amplitudes. Body temperature was monitored using a temperature probe and maintained above 36°C and a warm pad (A-2101-00298, Intellibio). The two first electrocardiograms were recorded at 1 month and 3 months of age, then every 3 months until 12 months of age.

An Isoproterenol (ISO) stress test was performed at 12 months of age. After recording an ECG as described above, mice received a single intraperitoneal injection of ISO at a dose of 2 µg/g body weight. ISO was prepared as follows: DL-Isoproterenol hydrochloride (I5627, Sigma) was dissolved in ddH2O and vortexed to provide a 10 µg/µL ISO stock solution.

Vector cardiograms were obtained based on lead I (X-axis) and aVF (Y-axis) (lower) and represent the orientation of the main electrical axis of the heart.

Cardiomyocyte isolation

Cardiac Purkinje fibers were isolated from wild-type (WT)- and *mdx-Cx40*$^{eGFP/+}$ mice as previously described (Ebner et al., 2020). The mice were anesthetized with isoflurane (2%, inhalation) and killed by cervical dislocation. After excision of the heart, a cannula was inserted into the aorta. The heart was then retrogradely perfused with calcium-free solution comprising 0.17 mg/mL Liberase TH (Roche) at 37°C for 18 min using a Langendorff setup. To further liberate Purkinje fibers, a second digestion step was applied, for which the ventricles were cut open along the aorta and placed in a culture dish containing 0.17 mg/mL Liberase TH (in calcium-free solution) for 8 min at room temperature. The tissue was then pulled into small pieces and incubated on a shaker at 37°C. Over 30 min, the Ca concentration was increased to 150 µM in four steps. The cells were then resuspended in Minimum Essential Medium (MEM)-α containing ITS media supplement (diluted 1:100), 2 mM L-glutamine, 100 U/mL penicillin, 0.1 mg/mL streptomycin and 17 µM blebbistatin (Sigma-Aldrich). Cells were then seeded on Matrigel (Corning)-coated 3.5 cm culture dishes for electrophysiological recordings. For experiments with ventricular cardiomyocytes of the working myocardium, hearts from mdx mice lacking Cx40-controlled eGFP expression were used for cell isolation. The procedure was as for Purkinje fiber isolation, except for the use of only a single digestion step, for which the hearts were perfused with 0.17 mg/mL Liberase TH (in calcium-free solution) at 37 °C for 10 min using a Langendorff setup (Hugo Sachs Elektronik).

Sodium current recordings

I_{Na} in isolated cardiac Purkinje fibers and ventricular cardiomyocytes of the working myocardium was recorded up to 6 h after cell isolation utilizing the whole cell patch clamp technique. The measurements were performed at room temperature (22°C ± 1.5 °C) using an Axopatch 200B patch clamp amplifier, a Digidata1440 digitizer and Clampex 10.7 software (Axon Instruments, Union City, CA, United States). Patch pipettes were formed with a P-97 horizontal puller (Sutter Instruments, Novato, CA, United States) from aluminosilicate glass capillaries (A120-77-10; Science Products, Hofheim, Germany). They were filled with a solution consisting of (in mM) 5 NaCl, 110 CsF, 10 EGTA and 10 HEPES, adjusted to pH 7.3 with CsOH. Tip resistances lay between 1 and 1.5 MΩ. The bath solution contained (in mM) 5 NaCl, 135 N-methyl-D-glucamine, 2.5 KCl, 1 $CaCl_2$, 1 $MgCl_2$, 10 HEPES and 0.017 blebbistatin, adjusted to pH 7.4 with HCl. Fresh bath solution was continuously administered to the patched cells using a DAD-8-VC superfusion system (ALA Scientific Instruments, Westbury, NY, United States). Purkinje fibers were identified by their eGFP signal and morphological characteristics, as previously described (Ebner et al., 2020). I_{Na} was activated by 25 ms depolarizations ranging from −87 to −7 mV. Voltages were corrected for the liquid junction potential. Recordings were low-pass filtered with 10 kHz and digitized at 35 kHz. Analysis of the data was carried out with Clampfit 10.7 (Axon Instruments) and GraphPad Prism 8 (San Diego, CA, United States). I_{Na} peaks were measured and divided by the membrane capacitance to calculate current densities. To obtain current density-voltage relationships, these values were then plotted against the test pulse voltages. For curve fitting, the following function was used: $I = G_{max} \cdot (V - V_{rev}) / (1 + \exp((V_{50} - V)/K))$, where I is the current, G_{max} is the maximal conductance, V is the membrane potential, V_{rev} is the reversal potential, V_{50} is the voltage at which the half-maximal activation occurred, and K is the slope factor.

Statistical analysis

Data are expressed as means ± standard deviation (SD). The I_{Na} data are expressed as means ± standard error (SE). Significant differences for electrocardiogram parameters were determined using two-way analysis of variance (ANOVA) followed by Sidak *post hoc* testing. Significant differences for heart size were determined using an unpaired t-test. All tests were made with Graphpad Prism software (Graphpad Prism 9.5.1, La Jolla, CA, United States). A nested analysis respecting the hierarchical data structure (Sikkel et al., 2017) was used for statistical comparisons of the patch clamp data. A p-value <0.05 was considered statistically significant.

Results

Conduction defects and arrhythmias in mdx mice increase with age

In order to evaluate conduction defects in mdx mice we crossed mice carrying the mdx mutation with a Cx40-GFP allele to generate double transgenic mice mdx::Cx40-GFP (C57BL/10ScSn-Dmdmdx/J). Cx40-GFP mice express the GFP reporter gene under the control of the gap junction alpha 5 (Gja5) promoter (Miquerol et al., 2004). Gja5 encodes for Connexin 40 specifically expressed in atrial cardiomyocytes and in the ventricular conduction system (VCS). Firstly we evaluated the survival rate of these mice to study the age-related progression of DMD associated cardiac defects. We observed that 27% of *mdx::Cx40-GFP* mice died after 1 year while 100% of control animals survived (Figure 1a). A follow-up of the cardiac activity was made through six-lead surface electrocardiogram (ECG) recordings on mice anesthetized with isoflurane. The two first electrocardiograms were recorded at 1 month and 3 months of age, then every 3 months until 12 months of age (Figure 1b). The *mdx::Cx40-GFP* mice presented a statistically significant increased PR interval compared to controls at 12-month-old, indicative of first degree atrioventricular block (36.6 ± 1.4 ms for WT vs. 41.5 ± 4.6 ms for mdx). QRS-II duration in *mdx::Cx40-GFP* mice was significantly increased compared to the controls at 3-month (16.1 ± 1.2 ms for WT vs. 17.1 ± 0.9 ms for *mdx*) and at 12-month (16.3 ± 0.8 ms for WT vs. 17.9 ± 1.8 ms for *mdx*), indicating a slower ventricular activation in the *mdx::Cx40-GFP* mice. The other ECG parameters did not present any differences between *mdx* and WT mice (Table 1). As expected, *mdx::Cx40-GFP* mice presented a dystrophic myocardial phenotype. Normalization of the heart size by the body weight of each mouse revealed a greater heart length (0.17 ± 0.01 for WT vs. 0.20 ± 0.02 for mdx) and a greater heart width (0.15 ± 0.01 for WT vs. 0.18 ± 0.02 for mdx) in *mdx::Cx40-GFP* mice (Figure 1c).

During ECG follow-up, we scored spontaneous ventricular arrhythmic events and found that *mdx::Cx40-GFP* but not WT mice presented premature ventricular complexes (PVC) under basal conditions (Figures 2a,b). To mimic physiological stress, the mice were subjected to β-adrenergic stimulation by injection of Isoproterenol (2 μg/g) at the age of 12 months. The increase in heart rate after Isoproterenol injection was not significantly different between WT and *mdx::Cx40-GFP* mice (28.8% ± 9.0% of increase for WT vs. 26.66% ± 10.3% of increase for *mdx*). β-adrenergic stimulation increased the number of mice with PVC in both groups, with a greater prevalence in *mdx::Cx40-GFP* mice (33% for WT vs. 65% for mdx) (Figure 2b). One *mdx::Cx40-GFP* mouse displayed ventricular tachycardia (VT) (Figure 2a). In summary, the progressive onset of cardiomyopathy in *mdx::Cx40-GFP* mice is associated with a larger heart, ventricular conduction defects and arrhythmias at 12 months of age.

Preserved Purkinje fiber network in mdx::Cx40-GFP mice

Since Purkinje fiber degeneration has been observed in human and canine DMD (Urasawa et al., 2008; Echigoya et al., 2017; Nomura and Hizawa, 1982), we used the *Cx40-GFP* mouse line to study the morphology and histology of Purkinje fibers in *mdx::Cx40-GFP* mice. In these mice GFP is expressed in the entire VCS including the His bundle, bundle branches and the Purkinje fiber network as seen in a luminal view of the endocardial surface of an opened WT left ventricle (Figure 3a). The PF network in *mdx::Cx40-GFP* mice is similar to WT mice in terms of number, distribution and structure of ellipsoids. Thus, there was no difference in the morphology of the Purkinje fiber network between control and *mdx::Cx40-GFP* mice (Figure 3a). As recent data have suggested that Cx43 lateralization contributes to DMD arrhythmogenesis in *mdx* mice (Gonzalez et al., 2015), we performed whole-mount immunostaining with a Cx43 antibody to examine the distribution of Cx43 gap junctions in working cardiomyocytes and in Purkinje fibers. Under high magnification, Cx43 gap junctions are present mainly at the intercalated discs (ID) of working cardiomyocytes, whereas they are distributed all along the plasma membrane of Purkinje fibers in WT (Figure 3a). We found a similar distribution of Cx43 gap junction localisation in *mdx::Cx40-GFP* hearts in both PF or working myocardium (Figure 3a). These data show that the Purkinje fiber network structure and the overall distribution of Cx43 are not affected in *mdx::Cx40-GFP* mice at 12 months of age when the arrhythmia-associated cardiomyopathy is in place.

To further investigate this, we performed histological analysis of Purkinje fibers on cryosections of WT and *mdx* hearts. Purkinje fibers were identified using a contactin-2 (Cntn2) antibody and cardiomyocytes were identified using DMD and WGA (Wheat germ agglutinin) staining. In WT hearts, DMD is present on the membrane of all cardiomyocytes with higher levels found in Purkinje fibers (Figure 3b). As expected, no staining with DMD antibody was detected in *mdx* hearts (Figure 3b). WGA staining showed that the membrane and the size of cardiomyocytes are overall larger in *mdx* hearts compared to WT. Cntn2 is a well-known marker of mature Purkinje fibers and play an important role in the electrical propagation in the heart (Pallante et al., 2010). Cntn2 staining was similar in WT and *mdx* hearts (Figure 3b), demonstrating the preservation of mature Purkinje fibers in the murine DMD model.

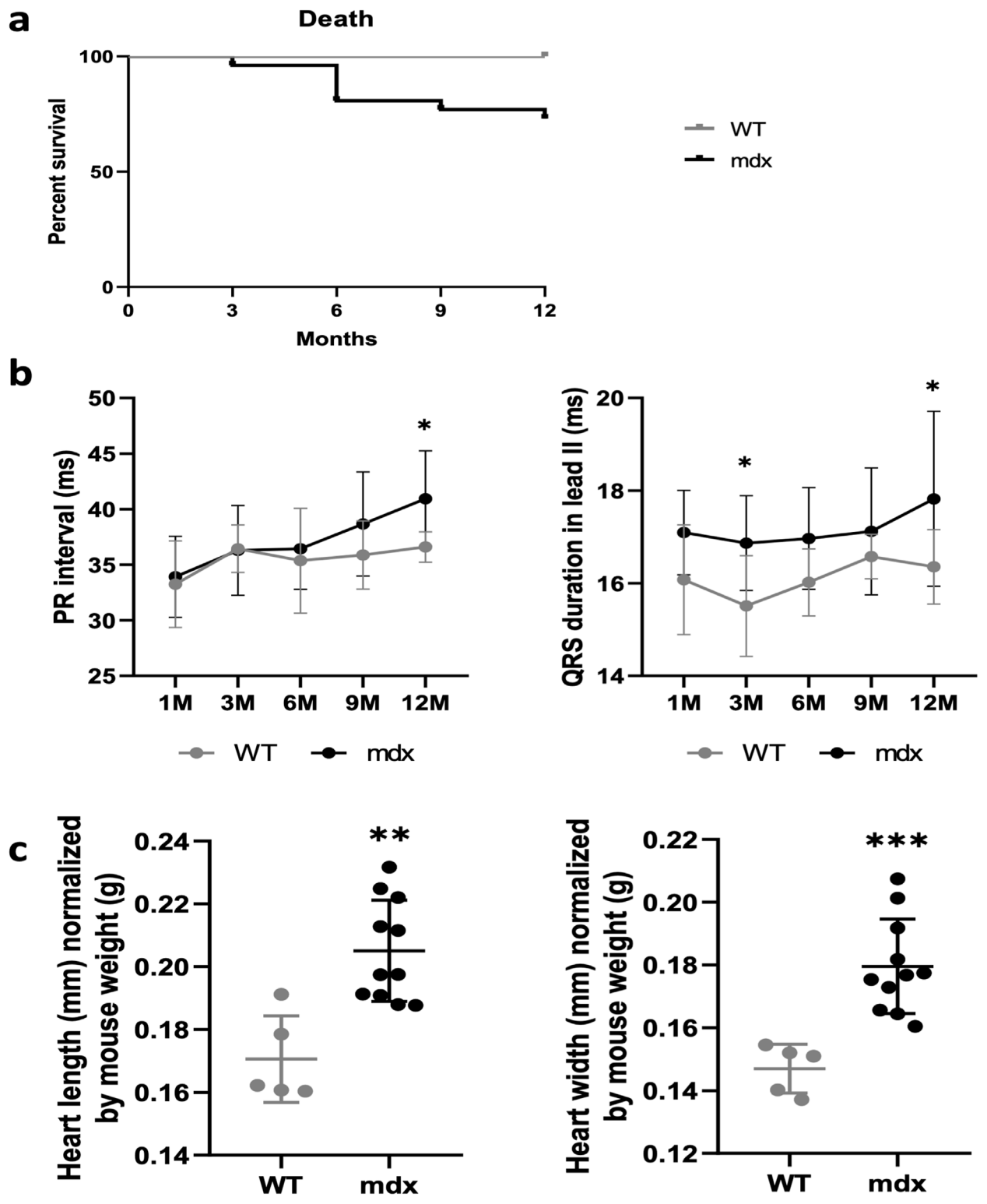

FIGURE 1
Progressive cardiac conduction defects in *mdx* mice. **(a)** Kaplan-Meier survival plot. The survival curves showed that 27% of the *mdx* mice (n = 26) died at 12-month-old, whereas all WT survived (n = 9). **(b)** Measurements of cardiac parameters in WT and *mdx* mice by electrocardiography. Graphs representing the evolution of the PR-II and QRS-II intervals measured in the same mice over a year show a progressive increase in these parameters in *mdx* (n = 26) compared to WT (n = 9) mice. **(c)** Graphs representing heart size measurements in WT (n = 5) and *mdx* mice (n = 11). *Mdx* mice present a significantly greater heart length and width compared to WT.*p < 0.1;**p < 0.01;***p < 0.001.

TABLE 1 Surface ECG parameters in Lead II.

Age	1-month-old		3-month-old		6-month-old		9-month-old		12-month-old	
Genotype	WT	mdx	WT	mdx	WT	mdx	WT	mdx	WT	mdx
N	9	26	9	26	9	25	9	21	9	20
RR (ms)	146 ± 16.9	141.3 ± 15.6	153.3 ± 15.4	138.8 ± 27.2	146 ± 13.7	141.4 ± 19.5	137.5 ± 16.6	128.7 ± 18.3	141.6 ± 13.9	133.4 ± 19.0
PR (ms)	33.2 ± 3.9	33.9 ± 3.6	36.5 ± 2.1	36.3 ± 4.0	35.4 ± 4.7	36.4 ± 3.6	35.9 ± 3.1	38.7 ± 4.7	36.6 ± 1.4	**41.6 ± 4.6***
P (ms)	15.9 ± 1.1	16.7 ± 1.4	17.1 ± 1.3	18.2 ± 2.5	15.8 ± 1.4	17.3 ± 1.6	15.4 ± 2.6	17.1 ± 1.9	16.4 ± 1.4	17.8 ± 1.8
QRS-I (ms)	15.2 ± 0.9	16.3 ± 1.4	15.1 ± 0.7	15.7 ± 1.2	16 ± 1.9	16.3 ± 0.8	15.7 ± 0.9	17.1 ± 1.6	15.8 ± 1.1	**17.7 ± 1.9****
QRS-II (ms)	16.1 ± 1.2	17.1 ± 0.9	15.5 ± 1.1	**16.9 ± 1.0***	16 ± 0.7	17 ± 1.1	16.6 ± 0.5	17.1 ± 1.4	16.3 ± 0.8	**17.9 ± 1.8***
QRS-III (ms)	18.2 ± 2.1	17.5 ± 2.3	16 ± 1.9	17.5 ± 1.5	15.7 ± 1.6	17.3 ± 1.1	16 ± 1.5	17.4 ± 1.3	16.4 ± 2.0	18.0 ± 1.4
QT (ms)	39.7 ± 3.0	39.3 ± 2.7	40.8 ± 5.2	41.5 ± 4.5	40.6 ± 4.2	42.7 ± 3.9	41 ± 3.5	40.3 ± 3.8	45.6 ± 3.3	43.4 ± 4.1
P (μV)	65.4 ± 22.2	63.3 ± 19.2	53.8 ± 14.5	49.7 ± 13.8	44.7 ± 11.6	41.8 ± 11.3	44.6 ± 30.7	39.3 ± 11.4	41.9 ± 11.8	38.8 ± 14.6
R (μV)	692.9 ± 129.9	641.2 ± 117.4	585.4 ± 134.0	521.7 ± 102.3	505.9 ± 106.0	447.7 ± 90.3	509.7 ± 131.0	403.3 ± 99.6	494.4 ± 92.7	392.6 ± 111.5
S (μV)	−133.5 ± 43.5	−188.3 ± 76.0	−105.3 ± 54.2	−119.8 ± 89.3	−98.9 ± 49.8	−75.8 ± 71.4	−75.5 ± 38.6	−64.2 ± 62.9	−83.8 ± 62.0	−55.4 ± 65.3

*$p < 0.05$;**$p < 0.01$.

10.3389/fphys.2025.1607916

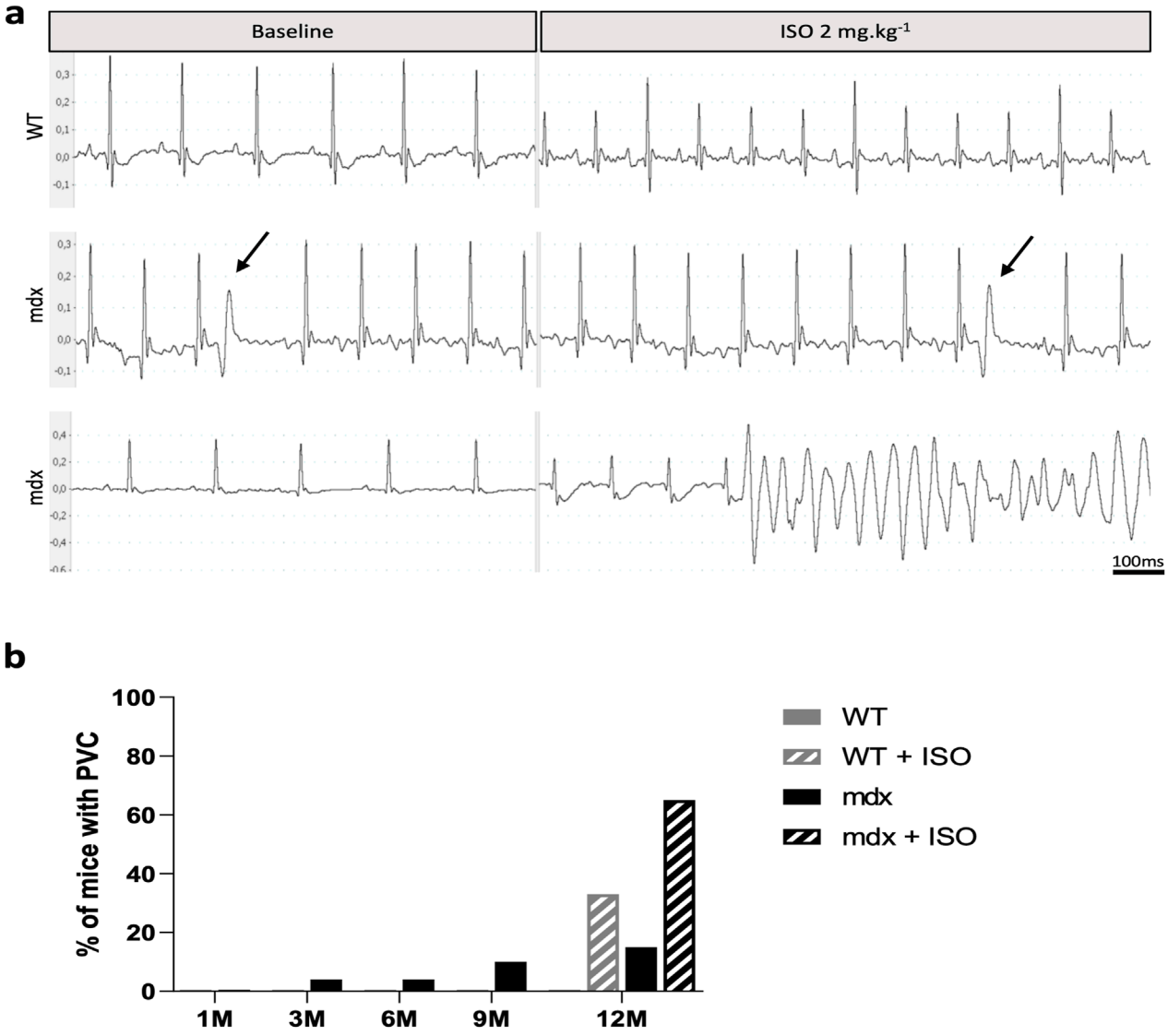

FIGURE 2
Spontaneous ventricular arrhythmic events in *mdx* mice. **(a)** Representative tracings from surface ECG measured in lead II in anaesthetized mice before and after ISO (2 mg/kg) IP injection. At baseline, only *mdx* mice present premature ventricular complexes (PVC, black arrow). After ISO challenge, the cardiac rhythm is accelerated in all mice and PVCs and ventricular tachycardia are mainly observed in *mdx* mice (VT). **(b)** Histograms showing that PVCs are more frequent in *mdx* mice with age. ISO stimulation revealed a greater prevalence of PVC in *mdx* mice compared to WT at 12 months of age. WT (n = 9) and *mdx* mice (n = 26).

Ventricular conduction defects in mdx mice are associated with I_{Na} reduction in ventricular cardiomyocytes and Purkinje fibers over a wide animal age range

Slowed ventricular conduction, as represented by QRS interval prolongation in the ECGs of *mdx* mice, may result from reduced I_{Na} in *mdx* compared to WT in ventricular cardiomyocytes and Purkinje fibers. Here, we addressed whether the age of mice (range: neonatal – 1-year-old) has an impact on the severity of I_{Na} loss in the dystrophic *mdx* mouse heart. In Koenig et al. (2011), we reported that ventricular cardiomyocytes isolated from neonatal *mdx* mice show less severe I_{Na} loss than ventricular myocytes from adult (4-6-month-old) *mdx* mice. This suggested that, although already present at neonatal age, I_{Na} loss in dystrophic ventricular cardiomyocytes becomes more pronounced at adulthood. This result was in line with a normal QRS interval in neonatal, but prolonged QRS interval in adult *mdx* compared to WT mice (Koenig et al., 2011).

Here, in Figures 4a–d, the I_{Na} properties of Purkinje fibers derived from 11–13-week-old and 19–21-week-old WT and *mdx* mice were compared. We observed that the current densities of Purkinje fibers in WT mice were independent of the age of the animal. At 11–13 weeks, current densities in *mdx* Purkinje fibers were only slightly reduced compared to those in WT Purkinje fibers (Figure 4c). In contrast, at 19–21 weeks, *mdx* Purkinje fibers showed a significantly reduced current density (Figure 4d). This suggests an increase in I_{Na} loss in Purkinje fibers with age in dystrophic *mdx* mice.

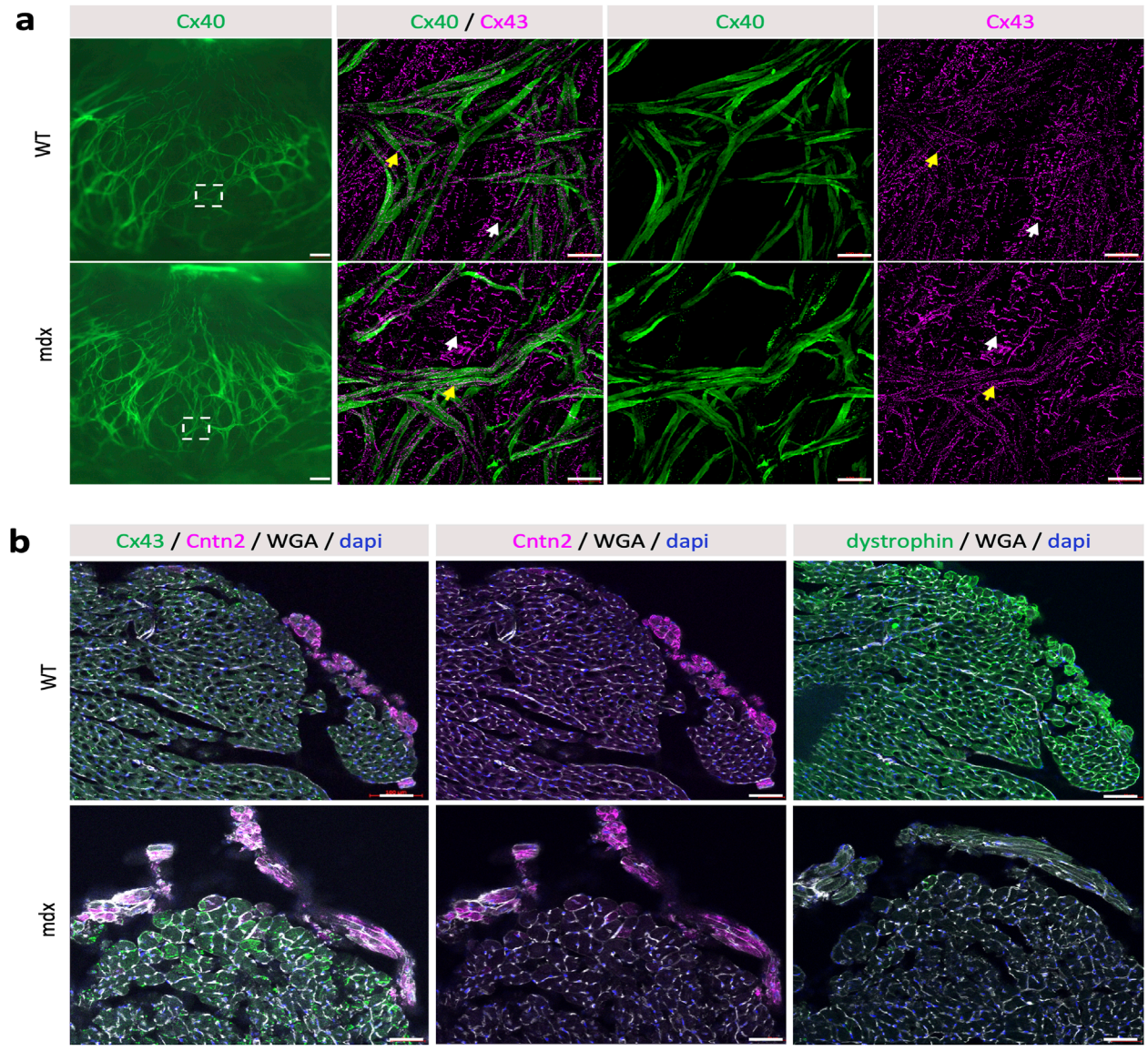

FIGURE 3
No morphological and maturation defects of the Purkinje Fiber network enriched in dystrophin. **(a)** Whole-mount immunofluorescence with Cx43 antibodies and Cx40-GFP on opened LV from WT and *mdx* adult mice. On the left image, the GFP fluorescence indicates a similar pattern of the Purkinje Fiber network between *mdx* and WT mice. Scale bar = 500 µm. Higher magnifications indicated by squares show the normal expression of the gap junction Cx43 at the intercalated discs (IDs) in contractile cardiomyocytes (white arrows) or along the membrane in PF (Yellow arrows) in both *mdx* and WT mice. Scale bar = 100 µm (WT n = 3; mdx n = 9). **(b)** Immunofluorescence with Contactin-2, Cx43, DMD and WGA-cy3 antibodies on transversal sections at the mid-ventricular level from WT and *mdx* mice. While Cntn2 expression, the marker of VCS maturation is similar in WT and *mdx* mice, DMD is absent in mdx hearts and enriched in their Purkinje fibers compared to other cardiomyocytes in WT. WGA and Cx43 staining at the membrane highlight the cardiac hypertrophy seen in *mdx* hearts. Scale bar = 50 µm (n = 11).

Finally, we tested whether the loss of I_{Na} was even more severe in old *mdx* mice, an age known to be associated with the onset of arrhythmogenic cardiomyopathy (Quinlan et al., 2004). In Figure 4e the I_{Na} densities of ventricular cardiomyocytes derived from 16–17 and 50–51-week-old *mdx* mice were similar.

Taken together, our I_{Na} recordings suggest that current loss in dystrophic ventricular cardiomyocytes and Purkinje fibers is already present in *mdx* mice at a very young age, worsens from juvenile to full adulthood, and finally persists with similar severity until 1 year of age, when arrhythmogenic cardiomyopathy is present.

Conduction defects are associated with ventricular dyssynchrony and fibrosis in mdx::Cx40-GFP mice

To detect any other cardiac activation defects, we calculated the angle of the main electrical axis of the heart from ECG recordings for each mouse. At 1 month of age, all WT and *mdx* mice presented a normal axis comprised between 0° and 120° (Figure 5a). At 6 months of age, three out of the 26 *mdx* mice presented a left deviation of the electrical axis whereas none of the WT mice had a deviated axis (Figure 5a). At 12-month-old, 4 out of the 26 *mdx*

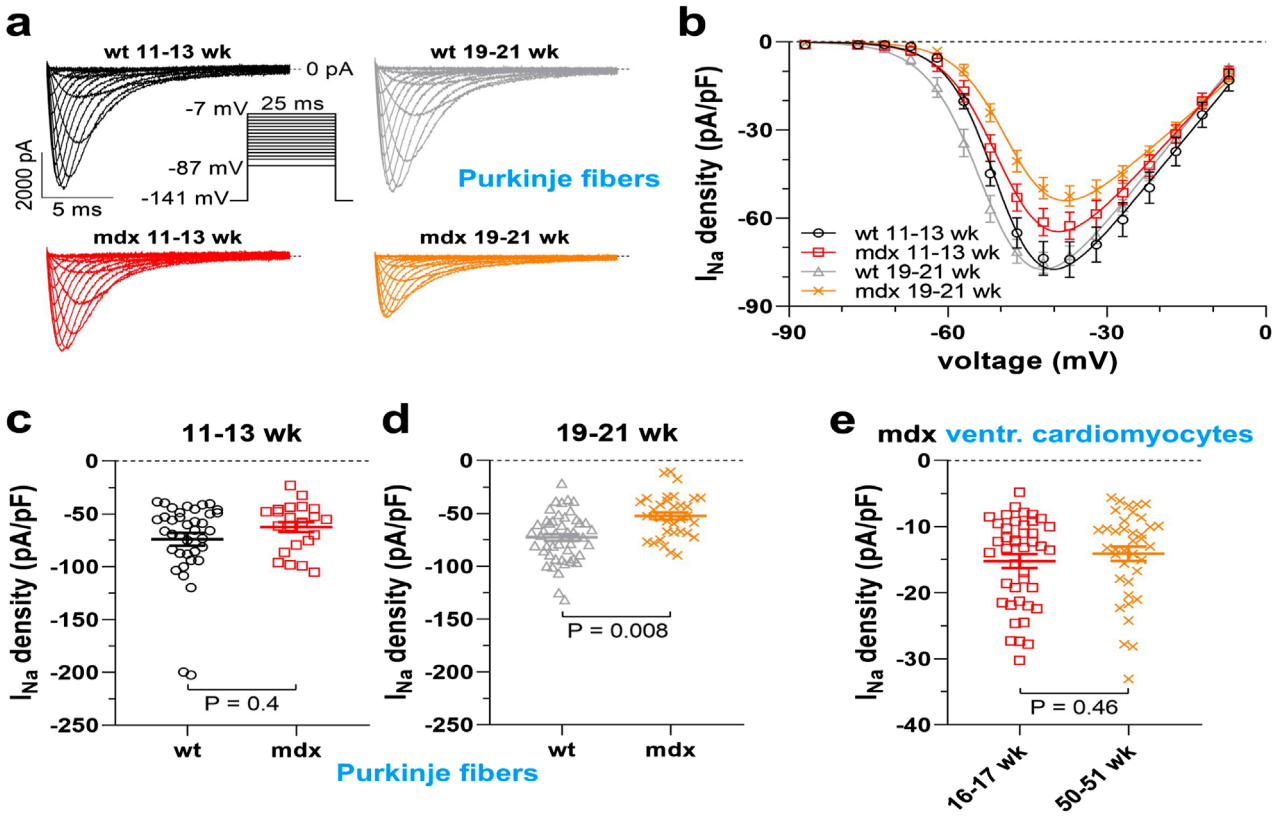

FIGURE 4
Sodium current (I_{Na}) densities in cardiac Purkinje fibers and ventricular cardiomyocytes from dystrophin-deficient mdx and wild-type (WT) mice at different animal ages. **(a)** Representative original whole cell I_{Na} traces recorded from Purkinje fibers from 11–13- or 19–21-week-old WT and *mdx* mice. The pulse protocol to elicit the currents is shown in the inset. **(b)** Current density-voltage relationships derived from a series of experiments as displayed in a (38 cells, six animals, WT 11–13 weeks; 23 cells, five animals, mdx 11–13 weeks; 48 cells, six animals, WT 19–21 weeks; 34 cells, five animals, mdx 19–21 weeks). The solid lines represent fits with a function given in the methods section. **(c)** Statistical comparison of current density values at −37 mV between WT and mdx Purkinje fibers from 11–13-week-old mice. In this age range, current densities in mdx Purkinje fibers (−62.6 ± 4.7 pA/pF) were only reduced by trend when compared to WT Purkinje fibers (−74.1 ± 6 pA/pF). **(d)** Comparison of current density values at −37 mV between WT and mdx Purkinje fibers from 19–21-week-old mice. Here, a significant difference between WT (−72.7 ± 3.3 pA/pF) and mdx (−52.5 ± 3.5 pA/pF) Purkinje fibers existed. **(e)** I_{Na} densities at −37 mV of ventricular cardiomyocytes of the working myocardium isolated from 16–17-week-old (42 cells from three animals) or 50–51-week-old (38 cells from three animals) mdx mice. There was no significant difference (−15.2 ± 1 pA/pF vs. −14.1 ± 1.1 pA/pF, 16–17 weeks vs. 50–51 weeks). Values represent means ± SE. A nested analysis respecting the hierarchical data structure was used for statistical comparisons (Sikkel et al., 2017).

mice presented a left deviation of their electrical axis (Figure 5a). Moreover, the angle of the main activation axis was highly variable (Figure 5a) though remaining in a normal range (0°–120°), showing that the stereotypical depolarization pattern is slightly affected in *mdx* hearts. To better understand the origin of the axis deviation, we analyzed the presence of fibrosis in these hearts using WGA staining which can serve as a readout of fibrosis (Emde et al., 2014). At 12 months of age, 5/7 of the *mdx* hearts showed ventricular fibrosis (Figures 5b,c). However, there was no significant correlation between fibrosis density and cardiac axis deviation (Figure 5d; r = 0.58; p = 0.06). Thus, the deviation of the main electrical axis may not result only from the presence of fibrosis in *mdx* hearts.

Discussion

All DMD patients develop a cardiomyopathy with age associated with ventricular arrhythmias, which are the leading cause of death in these patients. In this study, we showed conduction defects worsening with age in *mdx* mice which could explain the premature death in one-quarter of *mdx* mice. ECG revealed a prolonged QRS in *mdx* mice which is associated with the progressive apparition of ventricular dyssynchrony and spontaneous premature ventricular complexes that are exacerbated by ß-adrenergic stimulation. The ventricular conduction defects and arrhythmias in *mdx* mice occur in absence of morphological anomalies in the Purkinje fibers network or connexin dysregulation but in association with I_{Na} loss and fibrosis.

In the literature, there is a strong heterogeneity in the ECG parameters recorded from *mdx* mice or in DMD patients (Perloff, 1984; Spurney, 2011; Fauconnier et al., 2010; Gavillet et al., 2006; Koenig et al., 2011). In contrast to previous studies, we found a progressive increase in PR intervals, indicative of first degree atrioventricular block. These differences may arise from the age, the sex of the animals and the conditions of ECG recordings. We performed ECG on anesthetized mice while earlier studies

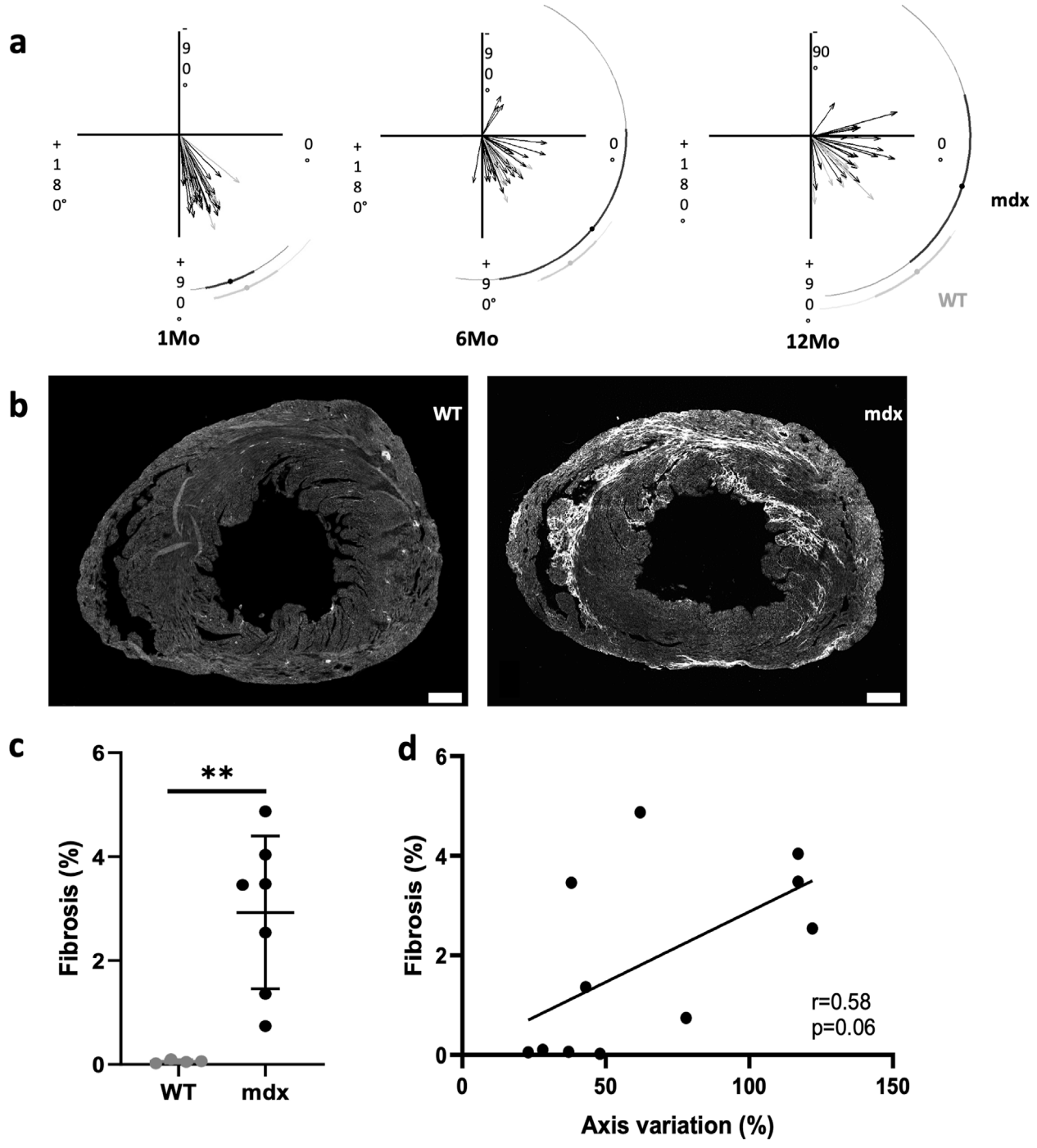

FIGURE 5
Arrhythmogenic cardiomyopathy associated with ventricular dyssynchrony and fibrosis. **(a)** The cardiac electrical axis calculated from surface electrocardiograms is normally comprised between 0° and 120° in WT while a progressive deviation towards the left is observed with age in *mdx* mice (WT n = 9; *mdx* n = 26). **(b)** WGA staining by immunofluorescence shows the presence of cardiac fibrosis only in *mdx* mice. Scale bar = 500 µm. **(c)** Fibrosis was quantified by measuring the percentage of WGA positive area in the LV and is significantly increased in *mdx* (n = 7) mice in comparison to WT (n = 4)-II (unpaired t-test,**p = 0.0042). **(d)** Cardiac fibrosis correlates with cardiac axis deviation in *mdx* mice (n = 11) (r = 0.58; p = 0.06).

were performed using telemetry, and finally, measurements of ECG parameters are not as standardized in mice as in humans. Here, the follow-up of the ECG recordings revealed the progressive onset of arrhythmogenic cardiomyopathy in *mdx* mice as described in DMD patients. However, cardiac conduction defects remain mild compared to humans. We also found a constant durable QRS elongation which indicates a slow ventricular conduction. As previously shown (Megeney et al., 1999), *mdx* mice present morphological signs of cardiac hypertrophy with a larger heart and bigger cardiomyocytes which can lead to an increase of the

QRS interval. Cardiac hypertrophy has been prevented in *mdx* mice using peptide-conjugated phosphorodiamidate morpholino oligomer (PPMO), however cardiac conduction has not been studied in these mice to determine whether this treatment can reduce QRS prolongation (Jearawiriyapaisarn et al., 2010).

An important feature of *mdx* mice is their susceptibility to develop spontaneous PVC which is increased by ß-adrenergic stimulation. In the vast majority of previous publications, ventricular arrhythmias arise only after isoprenaline stimulation (Gonzalez et al., 2015; Himelman et al., 2020; Lillo et al., 2019), and only one paper found PVC by telemetry in 6-month-old *mdx* mice (Fauconnier et al., 2010). The susceptibility to develop spontaneous PVC in our model may be explained by the age of the mice studied or by the conditions of ECG recording and ISO stimulation. In addition, most of our mice also carried the *Cx40-GFP* allele which could interfere with ventricular conduction. However, spontaneous and induced PVCs were also detected in *mdx* mice that do not carry the Cx40-GFP allele, suggesting that this genetic interaction may play a minor role in this arrhythmogenesis. Moreover, I_{Na} reduction induced by dystrophic-deficiency was similar from both Cx40-GFP+ and Cx40-GFP- ventricular cardiomyocytes (data not shown), suggesting that I_{Na} impairment is independent of the presence of the Cx40-GFP allele.

Our data showed an increase in the prevalence of ventricular arrhythmia with age which suggested a progressive degradation of the electrical conduction over time. To explain this phenomenon, we tested whether the Purkinje fiber network is altered as reported in human and canine DMD (Bies et al., 1992). Cx40-GFP mice were used to easily visualize the entire VCS: His bundle, bundle branches and PF network (Miquerol et al., 2004). No anomalies were observed in *mdx::Cx40-GFP* mice either in the structure or the density of the Purkinje fiber network. Thus, the VCS does not degenerate in *mdx* mice as it has been reported for human patients. Furthermore, we did not find any maturation defects in the mdx PF, which are just as numerous as in WT and express the Cntn2 marker. Although dystrophin is overexpressed in murine PFs as in humans and dogs, our data show that its absence has no effect on the formation and maintenance of the PF network in the mouse. It is well-known that PF present anatomical and histological discrepancies between mammals (Ono et al., 2009). Human and dog PFs belong to group II while those of mice belong to group III (Ono et al., 2009). Indeed, PF are thin and elongated in mice while they are larger than contractile cardiomyocytes and have a paler cytoplasm in dogs and humans. The histological difference between these species may explain the less severe damage of the PF network in dystrophic mice. Thus, our data showed that conduction defects and arrhythmias arise in *mdx* mice in absence of PF network structural defects and, in contrast to the dog, this mouse model is not suitable for translational research into cardiac conduction defects in DMD. Indeed, restored dystrophin in the heart including in PF reduced conduction defects in DMD dogs treated with micro-dystrophin (Echigoya et al., 2017).

Previous studies have suggested that conduction defects in *mdx* mice arise from a pathological mislocalisation of the gap junction Cx43 to the lateral sides of cardiomyocyte (Colussi et al., 2011; Gonzalez et al., 2015; Himelman et al., 2020; Lillo et al., 2019). Inhibiting this lateralization or blocking the activity of Cx43 hemichannels or expressing a mimicked-phosphorylated Cx43 all prevent ISO-stimulated ventricular arrhythmia and death in *mdx* mice (Gonzalez et al., 2015; Himelman et al., 2020; Lillo et al., 2019). Although, abolishing Cx43 remodeling was shown to reduce ventricular arrhythmias, conduction defects were not observed in these models (Himelman et al., 2020). These data suggest that targeting Cx43 represents a potential therapeutic strategy in the prevention of ventricular arrhythmias in human patients. Using whole-mount immunostaining, we showed that Cx43 is mainly present at the level of the IDs in contractile cardiomyocytes in both WT and *mdx* mice. In our hands, Cx43 did not show lateralization of Cx43 in contractile cardiomyocytes at the subendocardial surface in *mdx* mice. These differences may be due to the technique used or the cardiac region from which the cardiomyocytes originate. Cx43 is mainly expressed in contractile cardiomyocytes but it is also present in PF to define Purkinje-myocardium junctions (Olejnickova et al., 2021). However, in contrast to contractile cardiomyocytes, our data showed that Cx43 expression is milder and distributed all along the PF. The normally lateralized of Cx43 in PF could explain why no Cx43 mislocalisation has been observed in *mdx* mice in these cells. The impact of Cx43 on conduction defects requires further exploration to validate its significance and implications for therapy.

We observed that QRS elongation is constantly increased in *mdx* mice, however, it significatively increased in old mice. Interestingly, we found that I_{Na} loss worsens between the juvenile and the adult stage, while I_{Na} is constant in the old adults. Thus, our results suggest that I_{Na} loss in ventricular cardiomyocytes and Purkinje fibers, but not impaired ventricular conduction system development or degeneration or Cx43 dysregulation explains slowed ventricular conduction in *mdx* mice. I_{Na} reduction increases with age between juvenile to adult, however, our results show that it did not worsen at old age. However, progressive PR increase and ventricular arrhythmias that appear in *mdx* mice with age may not occur exclusively from I_{Na} decreases. Conduction defects are known to arise from the presence of fibrosis which is considered to be a non-conductive tissue (Oebel et al., 2017; Souidi et al., 2024). Progressive fibrosis has been previously described in DMD patients, dogs and mice (Marchal et al., 2021; Amedro et al., 2019; Ghaleh et al., 2023). Here, we found fibrosis in the majority of *mdx* mice and all fibrotic mice are associated with a main axis deviation. A deviation in the main cardiac axis indicates that the depolarising pattern of the ventricles is disturbed. This deviation may also indicate dyssynchrony and it is important to notice that strain defects detected by cardiac magnetic resonance are more sensitive criteria to detect cardiac dysfunction in DMD patients compared to ejection fraction (EF) (Amedro et al., 2019; Ghaleh et al., 2023). However, one limitation of this study is the limited number of mice and further experiments are necessary to determine the exact correlation between fibrosis and dyssynchrony.

Collectively, our data strongly suggest that the conduction defects in *mdx* mice are caused by the development of an arrhythmogenic cardiomyopathy associated with reduced I_{Na} and fibrosis and not by a structural remodeling of the PF network.

Data availability statement

The original contributions presented in the study are included in the article/supplementary material, further inquiries can be directed to the corresponding author.

Ethics statement

The animal study was approved by French Ministry of Research (APAFIS N° 36487-2022040816108385 v.7) and Austrian Science Ministry (BMWFW-66.009/0175-WF/V/3b/2015). The study was conducted in accordance with the local legislation and institutional requirements.

Author contributions

JV: Conceptualization, Data curation, Formal Analysis, Investigation, Methodology, Validation, Visualization, Writing – review and editing. JS: Data curation, Formal Analysis, Investigation, Writing – review and editing. JM: Data curation, Formal Analysis, Investigation, Visualization, Writing – review and editing. KH: Conceptualization, Formal Analysis, Funding acquisition, Methodology, Project administration, Validation, Visualization, Writing – review and editing. LM: Conceptualization, Funding acquisition, Project administration, Supervision, Visualization, Writing – original draft, Writing – review and editing.

Funding

The author(s) declare that financial support was received for the research and/or publication of this article. This work was supported by the French foundation AFM-Telethon, the Agence nationale de la recherche (ANR) "PurkinjeNet" (to LM) and the Austrian Science Fund (FWF), Grants P35542-B and P35878-B (to KH). JV is an AFM-Telethon and Marmara PhD fellow.

Acknowledgments

We are very grateful to Robert Kelly for his careful reading of the manuscript.

Conflict of interest

The authors declare that the research was conducted in the absence of any commercial or financial relationships that could be construed as a potential conflict of interest.

Generative AI statement

The author(s) declare that no Generative AI was used in the creation of this manuscript.

Publisher's note

References

Amedro, P., Vincenti, M., De La Villeon, G., Lavastre, K., Barrea, C., Guillaumont, S., et al. (2019). Speckle-tracking echocardiography in children with duchenne muscular dystrophy: a prospective multicenter controlled cross-sectional study. *J. Am. Soc. Echocardiogr.* 32 (3), 412–422. doi:10.1016/j.echo.2018.10.017

Bies, R. D., Friedman, D., Roberts, R., Perryman, M. B., and Caskey, C. T. (1992). Expression and localization of dystrophin in human cardiac Purkinje fibers. *Circulation* 86 (1), 147–153. doi:10.1161/01.cir.86.1.147

Branco, D. M., Wolf, C. M., Sherwood, M., Hammer, P. E., Kang, P. B., and Berul, C. I. (2007). Cardiac electrophysiological characteristics of the mdx (5cv) mouse model of Duchenne muscular dystrophy. *J. Interv. Card. Electrophysiol.* 20 (1-2), 1–7. doi:10.1007/s10840-007-9168-z

Bulfield, G., Siller, W. G., Wight, P. A., and Moore, K. J. (1984). X chromosome-linked muscular dystrophy (mdx) in the mouse. *Proc. Natl. Acad. Sci. U. S. A.* 81 (4), 1189–1192. doi:10.1073/pnas.81.4.1189

Chenard, A. A., Becane, H. M., Tertrain, F., de Kermadec, J. M., and Weiss, Y. A. (1993). Ventricular arrhythmia in Duchenne muscular dystrophy: prevalence, significance and prognosis. *Neuromuscul. Disord.* 3 (3), 201–206. doi:10.1016/0960-8966(93)90060-w

Choquet, C., Nguyen, T. H. M., Sicard, P., Buttigieg, E., Tran, T. T., Kober, F., et al. (2018). Deletion of Nkx2-5 in trabecular myocardium reveals the developmental origins of pathological heterogeneity associated with ventricular non-compaction cardiomyopathy. *PLoS Genet.* 14 (7), e1007502. doi:10.1371/journal.pgen.1007502

Choquet, C., Sicard, P., Vahdat, J., Nguyen, T. H. M., Kober, F., Varlet, I., et al. (2023). Nkx2-5 loss of function in the his-purkinje system hampers its maturation and leads to mechanical dysfunction. *J. Cardiovasc Dev. Dis.* 10 (5), 194. doi:10.3390/jcdd10050194

Chu, V., Otero, J. M., Lopez, O., Sullivan, M. F., Morgan, J. P., Amende, I., et al. (2002). Electrocardiographic findings in mdx mice: a cardiac phenotype of Duchenne muscular dystrophy. *Muscle Nerve* 26 (4), 513–519. doi:10.1002/mus.10223

Colussi, C., Rosati, J., Straino, S., Spallotta, F., Berni, R., Stilli, D., et al. (2011). Nε-lysine acetylation determines dissociation from GAP junctions and lateralization of connexin 43 in normal and dystrophic heart. *Proc. Natl. Acad. Sci. U. S. A.* 108 (7), 2795–2800. doi:10.1073/pnas.1013124108

Ebner, J., Pan, X., Yue, Y., Sideromenos, S., Marksteiner, J., Koenig, X., et al. (2022). Microdystrophin therapy rescues impaired Na currents in cardiac Purkinje fibers from dystrophin-deficient mdx mice. *Circ. Arrhythm. Electrophysiol.* 15 (8), e011161. doi:10.1161/CIRCEP.122.011161

Ebner, J., Uhrin, P., Szabo, P. L., Kiss, A., Podesser, B. K., Todt, H., et al. (2020). Reduced Na(+) current in Purkinje fibers explains cardiac conduction defects and arrhythmias in Duchenne muscular dystrophy. *Am. J. Physiol. Heart Circ. Physiol.* 318 (6), H1436–H1440. doi:10.1152/ajpheart.00224.2020

Echigoya, Y., Nakamura, A., Nagata, T., Urasawa, N., Lim, K. R. Q., Trieu, N., et al. (2017). Effects of systemic multiexon skipping with peptide-conjugated morpholinos in the heart of a dog model of Duchenne muscular dystrophy. *Proc. Natl. Acad. Sci. U. S. A.* 114 (16), 4213–4218. doi:10.1073/pnas.1613203114

Emde, B., Heinen, A., Godecke, A., and Bottermann, K. (2014). Wheat germ agglutinin staining as a suitable method for detection and quantification of fibrosis in cardiac tissue after myocardial infarction. *Eur. J. Histochem* 58 (4), 2448. doi:10.4081/ejh.2014.2448

Fauconnier, J., Thireau, J., Reiken, S., Cassan, C., Richard, S., Matecki, S., et al. (2010). Leaky RyR2 trigger ventricular arrhythmias in Duchenne muscular dystrophy. *Proc. Natl. Acad. Sci. U. S. A.* 107 (4), 1559–1564. doi:10.1073/pnas.0908540107

Fayssoil, A., Ben Yaou, R., Ogna, A., Chaffaut, C., Leturcq, F., Nardi, O., et al. (2018). Left bundle branch block in Duchenne muscular dystrophy: Prevalence, genetic relationship and prognosis. *PLoS One* 13 (1), e0190518. doi:10.1371/journal.pone.0190518

Gavillet, B., Rougier, J. S., Domenighetti, A. A., Behar, R., Boixel, C., Ruchat, P., et al. (2006). Cardiac sodium channel Nav1.5 is regulated by a multiprotein complex composed of syntrophins and dystrophin. *Circ. Res.* 99 (4), 407–414. doi:10.1161/01.RES.0000237466.13252.5e

Ghaleh, B., Barthelemy, I., Sambin, L., Bize, A., Corboz, D., Hittinger, L., et al. (2023). Spatial and temporal non-uniform changes in left ventricular myocardial strain in dogs with duchenne muscular dystrophy. *J. Cardiovasc Dev. Dis.* 10 (5), 217. doi:10.3390/jcdd10050217

Gonzalez, J. P., Ramachandran, J., Xie, L. H., Contreras, J. E., and Fraidenraich, D. (2015). Selective Connexin43 inhibition prevents isoproterenol-induced arrhythmias and lethality in muscular dystrophy mice. *Sci. Rep.* 5, 13490. doi:10.1038/srep13490

Gros, D. B., and Jongsma, H. J. (1996). Connexins in mammalian heart function. *Bioessays* 18 (9), 719–730. doi:10.1002/bies.950180907

Himelman, E., Lillo, M. A., Nouet, J., Gonzalez, J. P., Zhao, Q., Xie, L. H., et al. (2020). Prevention of connexin-43 remodeling protects against Duchenne muscular dystrophy cardiomyopathy. *J. Clin. Invest.* 130 (4), 1713–1727. doi:10.1172/JCI128190

Jearawiriyapaisarn, N., Moulton, H. M., Sazani, P., Kole, R., and Willis, M. S. (2010). Long-term improvement in mdx cardiomyopathy after therapy with peptide-conjugated morpholino oligomers. *Cardiovasc Res.* 85 (3), 444–453. doi:10.1093/cvr/cvp335

Kamdar, F., and Garry, D. J. (2016). Dystrophin-deficient cardiomyopathy. *J. Am. Coll. Cardiol.* 67 (21), 2533–2546. doi:10.1016/j.jacc.2016.02.081

Koenig, X., Dysek, S., Kimbacher, S., Mike, A. K., Cervenka, R., Lukacs, P., et al. (2011). Voltage-gated ion channel dysfunction precedes cardiomyopathy development in the dystrophic heart. *PLoS One* 6 (5), e20300. doi:10.1371/journal.pone.0020300

Koenig, X., Rubi, L., Obermair, G. J., Cervenka, R., Dang, X. B., Lukacs, P., et al. (2014). Enhanced currents through L-type calcium channels in cardiomyocytes disturb the electrophysiology of the dystrophic heart. *Am. J. Physiol. Heart Circ. Physiol.* 306 (4), H564–H573. doi:10.1152/ajpheart.00441.2013

Lillo, M. A., Himelman, E., Shirokova, N., Xie, L. H., Fraidenraich, D., and Contreras, J. E. (2019). S-nitrosylation of connexin43 hemichannels elicits cardiac stress-induced arrhythmias in Duchenne muscular dystrophy mice. *JCI Insight* 4 (24), e130091. doi:10.1172/jci.insight.130091

Marchal, G. A., van Putten, M., Verkerk, A. O., Casini, S., Putker, K., van Amersfoorth, S. C. M., et al. (2021). Low human dystrophin levels prevent cardiac electrophysiological and structural remodelling in a Duchenne mouse model. *Sci. Rep.* 11 (1), 9779. doi:10.1038/s41598-021-89208-1

Megeney, L. A., Kablar, B., Perry, R. L., Ying, C., May, L., and Rudnicki, M. A. (1999). Severe cardiomyopathy in mice lacking dystrophin and MyoD. *Proc. Natl. Acad. Sci. U. S. A.* 96 (1), 220–225. doi:10.1073/pnas.96.1.220

Meysen, S., Marger, L., Hewett, K. W., Jarry-Guichard, T., Agarkova, I., Chauvin, J. P., et al. (2007). Nkx2.5 cell-autonomous gene function is required for the postnatal formation of the peripheral ventricular conduction system. *Dev. Biol.* 303 (2), 740–753. doi:10.1016/j.ydbio.2006.12.044

Miquerol, L., Meysen, S., Mangoni, M., Bois, P., van Rijen, H. V., Abran, P., et al. (2004). Architectural and functional asymmetry of the His-Purkinje system of the murine heart. *Cardiovasc Res.* 63 (1), 77–86. doi:10.1016/j.cardiores.2004.03.007

Nigro, G., Comi, L. I., Politano, L., and Bain, R. J. (1990). The incidence and evolution of cardiomyopathy in Duchenne muscular dystrophy. *Int. J. Cardiol.* 26 (3), 271–277. doi:10.1016/0167-5273(90)90082-g

Nomura, H., and Hizawa, K. (1982). Histopathological study of the conduction system of the heart in Duchenne progressive muscular dystrophy. *Acta Pathol. Jpn.* 32 (6), 1027–1033. doi:10.1111/j.1440-1827.1982.tb02082.x

Oebel, S., Dinov, B., Arya, A., Hilbert, S., Sommer, P., Bollmann, A., et al. (2017). ECG morphology of premature ventricular contractions predicts the presence of myocardial fibrotic substrate on cardiac magnetic resonance imaging in patients undergoing ablation. *J. Cardiovasc Electrophysiol.* 28 (11), 1316–1323. doi:10.1111/jce.13309

Olejnickova, V., Kocka, M., Kvasilova, A., Kolesova, H., Dziacky, A., Gidor, T., et al. (2021). Gap junctional communication via Connexin43 between Purkinje fibers and working myocytes explains the epicardial activation pattern in the postnatal mouse left ventricle. *Int. J. Mol. Sci.* 22 (5), 2475. doi:10.3390/ijms22052475

Ono, N., Yamaguchi, T., Ishikawa, H., Arakawa, M., Takahashi, N., Saikawa, T., et al. (2009). Morphological varieties of the Purkinje fiber network in mammalian hearts, as revealed by light and electron microscopy. *Arch. Histol. Cytol.* 72 (3), 139–149. doi:10.1679/aohc.72.139

Pallante, B. A., Giovannone, S., Fang-Yu, L., Zhang, J., Liu, N., Kang, G., et al. (2010). Contactin-2 expression in the cardiac Purkinje fiber network. *Circ. Arrhythm. Electrophysiol.* 3 (2), 186–194. doi:10.1161/CIRCEP.109.928820

Perloff, J. K. (1984). Cardiac rhythm and conduction in Duchenne's muscular dystrophy: a prospective study of 20 patients. *J. Am. Coll. Cardiol.* 3 (5), 1263–1268. doi:10.1016/s0735-1097(84)80186-2

Quinlan, J. G., Hahn, H. S., Wong, B. L., Lorenz, J. N., Wenisch, A. S., and Levin, L. S. (2004). Evolution of the mdx mouse cardiomyopathy: physiological and morphological findings. *Neuromuscul. Disord.* 14 (8-9), 491–496. doi:10.1016/j.nmd.2004.04.007

Sauer, J., Marksteiner, J., Lilliu, E., Hackl, B., Todt, H., Kubista, H., et al. (2024). Empagliflozin treatment rescues abnormally reduced Na(+) currents in ventricular cardiomyocytes from dystrophin-deficient mdx mice. *Am. J. Physiol. Heart Circ. Physiol.* 326 (2), H418–H425. doi:10.1152/ajpheart.00729.2023

Shirokova, N., and Niggli, E. (2013). Cardiac phenotype of Duchenne Muscular Dystrophy: insights from cellular studies. *J. Mol. Cell Cardiol.* 58, 217–224. doi:10.1016/j.yjmcc.2012.12.009

Sikkel, M. B., Francis, D. P., Howard, J., Gordon, F., Rowlands, C., Peters, N. S., et al. (2017). Hierarchical statistical techniques are necessary to draw reliable conclusions from analysis of isolated cardiomyocyte studies. *Cardiovasc Res.* 113 (14), 1743–1752. doi:10.1093/cvr/cvx151

Souidi, M., Resta, J., Dridi, H., Sleiman, Y., Reiken, S., Formoso, K., et al. (2024). Ryanodine receptor dysfunction causes senescence and fibrosis in Duchenne dilated cardiomyopathy. *J. Cachexia Sarcopenia Muscle* 15 (2), 536–551. doi:10.1002/jcsm.13411

Spurney, C. F. (2011). Cardiomyopathy of Duchenne muscular dystrophy: current understanding and future directions. *Muscle Nerve* 44 (1), 8–19. doi:10.1002/mus.22097

Tsuda, T., and Fitzgerald, K. K. (2017). Dystrophic cardiomyopathy: complex pathobiological processes to generate clinical phenotype. *J. Cardiovasc Dev. Dis.* 4 (3), 14. doi:10.3390/jcdd4030014

Urasawa, N., Wada, M. R., Machida, N., Yuasa, K., Shimatsu, Y., Wakao, Y., et al. (2008). Selective vacuolar degeneration in dystrophin-deficient canine Purkinje fibers despite preservation of dystrophin-associated proteins with overexpression of Dp71. *Circulation* 117 (19), 2437–2448. doi:10.1161/CIRCULATIONAHA.107.739326

Wang, Q., Quick, A. P., Cao, S., Reynolds, J., Chiang, D. Y., Beavers, D., et al. (2018). Oxidized CaMKII (Ca(2+)/calmodulin-dependent protein kinase II) is essential for ventricular arrhythmia in a mouse model of duchenne muscular dystrophy. *Circ. Arrhythm. Electrophysiol.* 11 (4), e005682. doi:10.1161/CIRCEP.117.005682

frontiers | Frontiers in Physiology

TYPE Brief Research Report
PUBLISHED 01 July 2025
DOI 10.3389/fphys.2025.1631426

OPEN ACCESS

EDITED BY
Jason D. Bayer,
Université de Bordeaux, France

REVIEWED BY
Leonor Parreira,
Hospital Center of Setúbal, Portugal
Wen-Han Cheng,
Taipei Veterans General Hospital, Taiwan
Kang Li,
Peking University First Hospital, China

*CORRESPONDENCE
Bastiaan J. Boukens,
b.boukens@maastrichtuniversity.nl

RECEIVED 19 May 2025
ACCEPTED 16 June 2025
PUBLISHED 01 July 2025

CITATION
Blok M, den Ouden BL, Kuiper M, Ophelders DRMG, Jongbloed MRM, Zeemering S, Jensen B, van Hunnik A and Boukens BJ (2025) Functional conduction system mapping in sheep reveals Purkinje spikes in the free wall of the right ventricular outflow tract.
Front. Physiol. 16:1631426.
doi: 10.3389/fphys.2025.1631426

Functional conduction system mapping in sheep reveals Purkinje spikes in the free wall of the right ventricular outflow tract

Michiel Blok[1,2], Bram L. den Ouden[3,4], Marion Kuiper[5], Daan R. M. G. Ophelders[6,7], Monique R. M. Jongbloed[1,8], Stef Zeemering[5], Bjarke Jensen[2], Arne van Hunnik[5] and Bastiaan J. Boukens[3,5]*

[1]Department of Anatomy and Embryology, Leiden University Medical Center, Leiden, Netherlands, [2]Department of Medical Biology, Amsterdam Cardiovascular Sciences, Amsterdam University Medical Center, location Academic Medical Center, Amsterdam, Netherlands, [3]Laboratory of Experimental Cardiology, Department of Cardiology, Leiden University Medical Center, Leiden, Netherlands, [4]Department of Microelectronics, Delft University of Technology, Delft, Netherlands, [5]Department of Physiology, Cardiovascular Research Institute Maastricht, Maastricht University, Maastricht, Netherlands, [6]Department of Pediatrics, Maastricht University Medical Center, MosaKids Children's Hospital, Maastricht, Netherlands, [7]GROW Research Institute for Oncology and Reproduction, Maastricht University, Maastricht, Netherlands, [8]Department of Cardiology, Centre for Congenital Heart Disease Amsterdam-Leiden (CAHAL), Leiden University Medical Center, Leiden, Netherlands

Ablation of sites displaying Purkinje activity is highly effective against idiopathic ventricular fibrillation which often originates in the right ventricular outflow tract. However, during endocardial mapping Purkinje potentials are rarely, if never, detected in the right ventricular outflow tract. In the present study, we aimed to determine whether the Purkinje system extends into the right ventricular outflow tract. Hearts of five female sheep were blood-perfused in a Langendorff setup in which we performed epicardial and endocardial voltage mapping. During atrial pacing, the right ventricular outflow tract epicardium activated later than the epicardium of the left and right ventricular free walls. Endocardial mapping revealed Purkinje spikes at several sites in the free wall of the right ventricular outflow tract. In one heart, Purkinje spikes preceded ventricular premature beats during mapping, but were not visible during sinus rhythm. Subsequent immuno-histological examination showed a network of Connexin 40-positive Purkinje fibers across and within the wall of the right ventricular outflow tract. Quantitative analysis revealed that the transmural Purkinje fiber network was more abundant near the endocardium than epicardium. In conclusion, the Purkinje system extends into the right ventricular outflow tract of the sheep heart. These findings demonstrate that the sheep could be a valuable model for studying Purkinje-related arrhythmias in the right ventricular outflow tract.

KEYWORDS

right ventricular outflow tract, cardiac Purkinje system, cardiac arrhythmia, cardiac electrophysiology, cardiac conduction system

Introduction

The cardiac Purkinje system is made up of fast-conducting fibers, which are responsible for an orderly propagation of electrical impulses through the ventricles and ensure synchronous contractions of the left and right ventricles (Boyden et al., 2010; Tawara, 1906). While much of the Purkinje system has been well-characterized in various species, including the sheep heart, whether it extended into the right ventricular outflow tract (RVOT) was often not determined (Tawara, 1906; Lhamon, 1912; King, 1916; Hondeghem and Stroobandt, 1974; Canale et al., 1983; Ansari et al., 1999; Ryu et al., 2009). Given that the RVOT activates later during the cardiac cycle than the left and right ventricles, it is conceivable that it would be devoid of a fast-conducting Purkinje system.

The Purkinje system is frequently the substrate for life-threatening ventricular arrhythmias, including monomorphic and polymorphic ventricular tachycardias, as well as ventricular fibrillation (Haissaguerre et al., 2016). In patients with idiopathic ventricular fibrillation, sites showing Purkinje spikes serve as a target for electrogram-based catheter ablation (Haïssaguerre et al., 2002a; Haïssaguerre et al., 2002b; Coronel et al., 2021). In some cases, the Purkinje system itself can also be the origin of arrhythmia, for example, in patients suffering from ventricular premature beats (VPBs). Similar to the Purkinje system, the RVOT is often the origin of ventricular arrhythmia, including idiopathic ventricular fibrillation and VPBs (Enriquez et al., 2024). Therefore, determining whether the Purkinje system extends into the RVOT would provide valuable insight into the origin of VPBs and potentially the arrhythmia mechanisms underlying idiopathic ventricular fibrillation originating from the RVOT.

Evidence for the presence of a Purkinje system in the human RVOT comes from a single study in which conventional histological stains were used on material from two hearts, revealing a few subendocardial bundles of myocardium somewhat insulated by fibrous tissue (De Almeida et al., 2020). A subsequent study investigated two bovine hearts and found that the Purkinje system extends beyond the subendocardium and deeper into the myocardium of the RVOT (De Almeida et al., 2017; De Almeida et al., 2021). Building upon Jan Purkinje's initial findings in the sheep heart (Tawara, 2000), our study aimed to establish whether the Purkinje system extends into the RVOT. This was achieved through epicardial and endocardial voltage mapping of the RVOT free wall in Langendorff-perfused sheep hearts, as well as immunohistochemical detection of Connexin 40. Overall, our findings support the presence of a functional Purkinje system in the sheep RVOT, making it a suitable model for studying RVOT-related arrhythmias.

Methods

Animal approval

Hearts were explanted from sheep that had just undergone caesarean section to deliver near-term fetuses as part of a separate investigation. This was conducted in accordance with national and institutional guidelines, in compliance with the European Commission Directive, and was approved by the local Animal Experiments Committee (approval number: AVD10700202216526).

Langendorff experiments

Five female sheep (approximately 40 kg) were premedicated with zolazepam and atropine, and received propofol for induction and a combination of propofol and fentanyl for maintenance of anesthesia. The animal was euthanatized with pentobarbital. Before explanting the heart, 25,000 IU heparin was intravenously administered and approximately 600 mL of blood was collected from the femoral artery. Ventricular fibrillation was induced by touching the right ventricular myocardium with the poles of a 9V battery. During explantation, the heart was rapidly excised and submerged in ice-cold Tyrode's solution. The aorta was then cannulated and mounted on a Langendorff perfusion setup. The heart was then perfused with around 1.4 L of recirculating blood-Tyrode's mixture (1:1) that was gassed with 95% O_2/5% CO_2 and kept at room temperature by running the perfusate through a coil shaped glass heat exchanger. After an equilibration period, the heart was defibrillated using a single direct current shock of 20 J. A reference electrode was connected to the aortic root. Both the reference electrode and recording multi-electrode were connected to an ActiveTwo acquisition setup (BioSemi, Amsterdam, Netherlands). Recordings were performed at a sampling rate of two or 16 KHz. For simultaneous unipolar electrogram recordings of the RVOT epicardium and endocardium, we used an 8.5 × 6.5 mm large 13 × 16 electrode grid (0.5 mm interelectrode distance) and a 4 × 3.7 mm large 3 × 3 + 1 electrode grid (0.6–0.7 mm interelectrode distance), respectively. Data was analyzed using custom-made software based on Matlab R2021a (Mathworks Inc., Natick, MA). Local activation time was determined using the maximal -dV/dt from the unipolar electrogram. Activation was measured in relation to the onset of the earliest ventricular (Purkinje or working myocardium) deflection within the entire electrode grid.

Histology and immunohistochemistry

After Langendorff experiments, the RVOT free wall was dissected and fixed 24 h in 4% paraformaldehyde and embedded in paraffin. Tissues were longitudinally sectioned 7 µm-thick and mounted on glass slides. Prior to staining, sections were deparaffinised by incubating twice in xylene followed by rehydration through a series of graded ethanol (EtOH) steps (100% EtOH - 100% EtOH - 90% EtOH - 80% EtOH - 70% EtOH) into demineralized H_2O.

For immunofluorescence staining, sections were subjected to heat-induced antigen retrieval in citric acid buffer (10 mM citric acid, 0.05% Tween 20, pH 6.0) for 12 min at 97°C using the Shandon TissueWave 2 (Thermo Fisher Scientific). Next, sections were rinsed twice with PBS and once with PBS containing 0.02% Tween 20 (PBS-T) and incubated overnight at room temperature with IgG primary antibody against human Connexin 40 (1 µg/mL; Santa Cruz Biotechnology Inc.; sc-20466) in blocking solution containing PBS-T and 1% bovine serum albumin. After rinsing twice with PBS and once with PBS-T, sections were incubated for 1 h at room

temperature with Alexa Fluor 647 donkey anti-goat IgG secondary antibody (10 µg/mL; Invitrogen; A-21447). Afterwards, sections were rinsed twice with PBS and once with PBS-T and incubated for 10 min at room temperature with DAPI (5 µg/mL; Invitrogen; D3571). Finally, sections were rinsed twice with PBS and mounted in ProLong Gold Antifade Mountant (Invitrogen; P36930). Super-resolution imaging was done with the ZEISS LSM 900 with Airyscan.

Picrosirius Red staining, cross-stained with Weigert's Haematoxylin, was used to visualize collagenous tissue in red, cytoplasm in yellow, and nuclei in black. For quantitative analysis, stainings were performed on 19 sections taken throughout the entire thickness of the RVOT free wall (N = 2). Briefly, rehydrated sections were incubated with Weigert's Haematoxylin for 10 min followed by 10 min of washing in running tap water. Next, sections were incubated with Picrosirius Red for 1 h. Subsequently, sections were rinsed twice with acidified water and rapidly dehydrated trice by dipping 5 times in EtOH 100%. Finally, sections were cleared by three incubation steps of 2 min each with xylene and mounted in Entellan. Brightfield images were captured with the 3DHistech Pannoramic 250 slidescanner (3DHISTECH, Hungary).

Purkinje fiber quantification

Individual Purkinje fibers were counted within 0–5 mm, 5–10 mm, and 10–15 mm below the hinge-line of the pulmonary valvular leaflets. The shortest Purkinje fiber distance relative to the endocardial and epicardial wall was analyzed using QuPath v0.6.0-rc3 [https://github.com/qupath/qupath/releases/tag/v0.6.0-rc3].

Statistics

Variables are presented as mean ± standard error of the mean (SEM). Epicardial activation times within the RVOT, left ventricular free wall, and right ventricular free wall and the number of Purkinje fibers within areas below the pulmonary valve leaflets were compared using a One-Way analysis of variance (ANOVA). Post-Hoc analysis was done with the Bonferroni test. For each statistical test, $p \leq 0.05$ was considered significant. All statistical analysis were done in SPSS (SPSS Statistics v29.0.0.0 (241); IBM).

Results

Delayed activation of the RVOT in the sheep heart

Figure 1A shows an epicardial activation map recorded from the anterior side of a Langendorff-perfused sheep heart, highlighting delayed activation in the RVOT (trace c) compared to the left ventricular free wall (trace a) and right ventricular free wall (trace b). Quantitative analysis of recordings from five sheep hearts revealed that the RVOT was activated, on average, 25.6 ± 1 ms after the onset of ventricular activation. This was significantly later than neighboring parts of the left ventricle and right ventricle which activated at 12.3 ± 2.6 ms and 16.3 ± 2.0 ms, respectively (Figure 1B). To further investigate activation patterns across the RVOT wall, we performed simultaneous epicardial and endocardial mapping of the RVOT just below the pulmonary trunk. Doing so, we found that epicardial activation occurred towards the pulmonary trunk, while the endocardium activated from left to right (Figure 1C). During these measurements we did not detect any Purkinje activity. Next, we continued endocardial mapping by moving the multi-electrode more to inferior into the RVOT. Left and right panels of Figure 1D show two individual activation maps with corresponding electrogram traces. In these electrograms, sharp deflections consistently preceded the larger main deflection, indicative of Purkinje activity. Overall, these findings show functional evidence for Purkinje activity in the sheep RVOT.

To gain further insight into Purkinje activity from the RVOT endocardium, we opened the right ventricular cavity allowing us to reach luminal side and perform mapping with high-resolution using the 8.5 × 6.5 mm electrode grid previously used for epicardial mapping (see Figure 1). As indicated by an isoelectric ST segment, the opening of the RVOT did not result in ischemia, enabling physiological mapping of the RVOT myocardium (Figure 2A). We identified Purkinje spikes in all five hearts. In one heart, mapping of the exposed RVOT endocardium did not reveal Purkinje activity during sinus rhythm. To confirm that we had only measured the electrical activity of the working myocardium, we calculated coaxial electrograms (Hoogendijk et al.), which revealed a single moment of activation. In this heart, slight movement of the multielectrode catheter along the endocardial surface while applying light pressure initiated VPBs that showed Purkinje activity preceding activation of the working myocardium (Figure 2B). Local activation maps corresponding to the maximal -dV/dt for Purkinje activation (top row) and myocardial activation (bottom row) for each consecutive VPB are shown in Figure 2C. These functional findings show that Purkinje fiber activation from the RVOT endocardium does not necessarily precede activation of the working myocardium. The working myocardium is most likely activated earlier by transmural or subepicardial Purkinje fibers.

The sheep RVOT contains a Purkinje network that extends into the myocardial wall

After the Langendorff experiments, the RVOT free wall was dissected from the heart for the purpose of histological and immunohistochemical examination. On macroscopic level, we observed a dense network composed of grey, flat, gelatinous fibers on the luminal side of the myocardial wall which resembled typical features of the Purkinje system (Figure 3A). The left of Figure 3B displays a dissected RVOT free wall in which histological examination revealed bundles of presumably Purkinje fibers within the subendocardium and deeper within the myocardial wall (Figure 3B'–3B"). Within the bundles, individual myocardial cells were larger and had a paler cytoplasm, which is indicative of a lower myofibril density (Tawara, 1906; De Almeida et al., 2020). Typically, Purkinje fibers were surrounded by a dense fibrous sheath and showed various configurations including cylinders, ovals, and stellate-shaped structures (Figure 3B). To confirm Purkinje cell identity, we next performed immunohistochemical staining for the

10.3389/fphys.2025.1631426

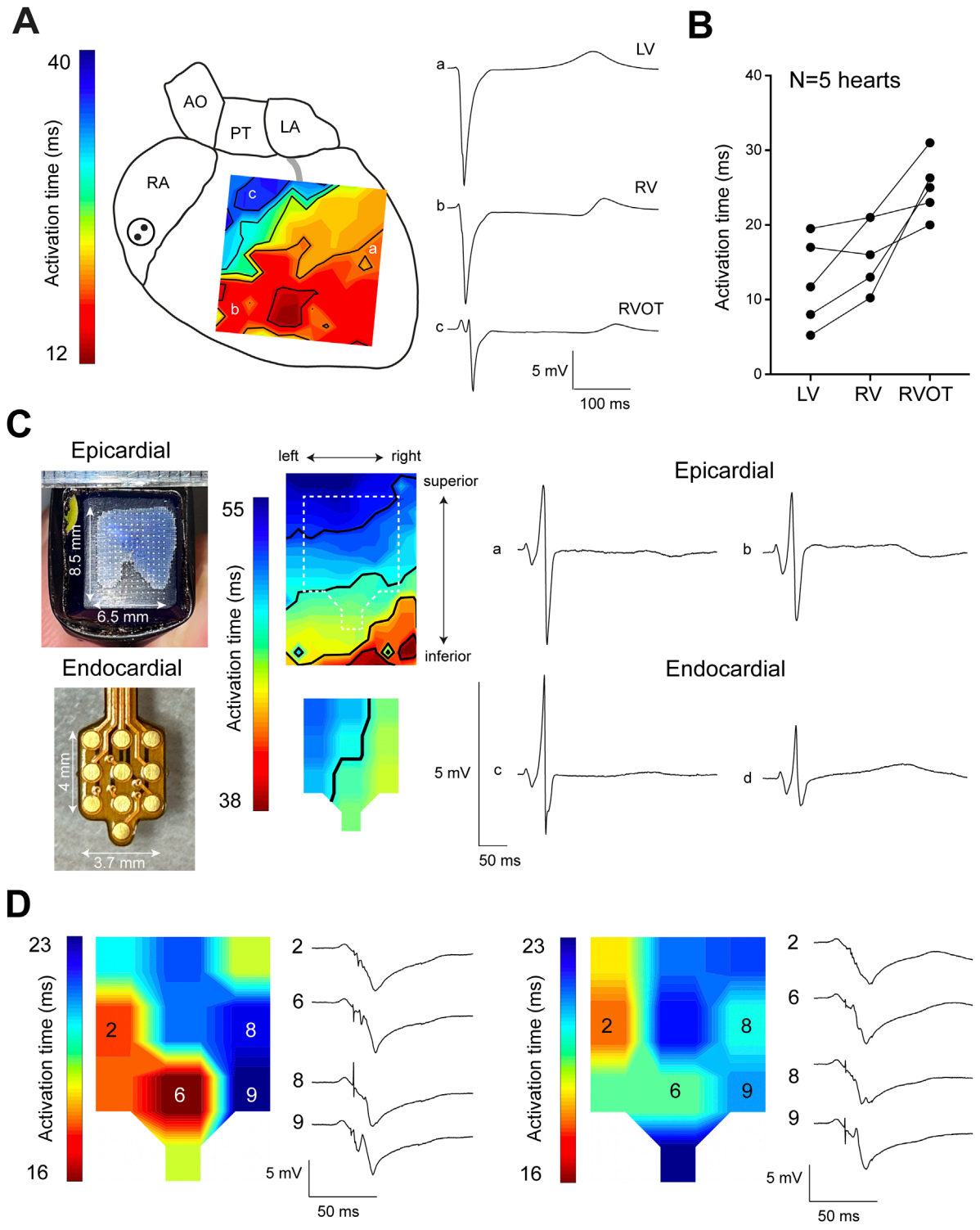

FIGURE 1
Delayed activation of the sheep RVOT. **(A)** Epicardial activation map of one sheep heart showing late activation of the RVOT. **(B)** Quantitative analysis of the average activation time in the RVOT, right ventricular free wall, and left ventricular free wall. **(C)** Epicardial and endocardial activation maps of the RVOT were simultaneously measured using separate electrode grids. **(D)** Endocardial activation maps of the distal RVOT showing the occurrence of Purkinje spikes preceding myocardial activation. RA, right atrium; AO, aorta; PT, pulmonary trunk; LA, left atrium; RV, right ventricle; LV, left ventricle.

10.3389/fphys.2025.1631426

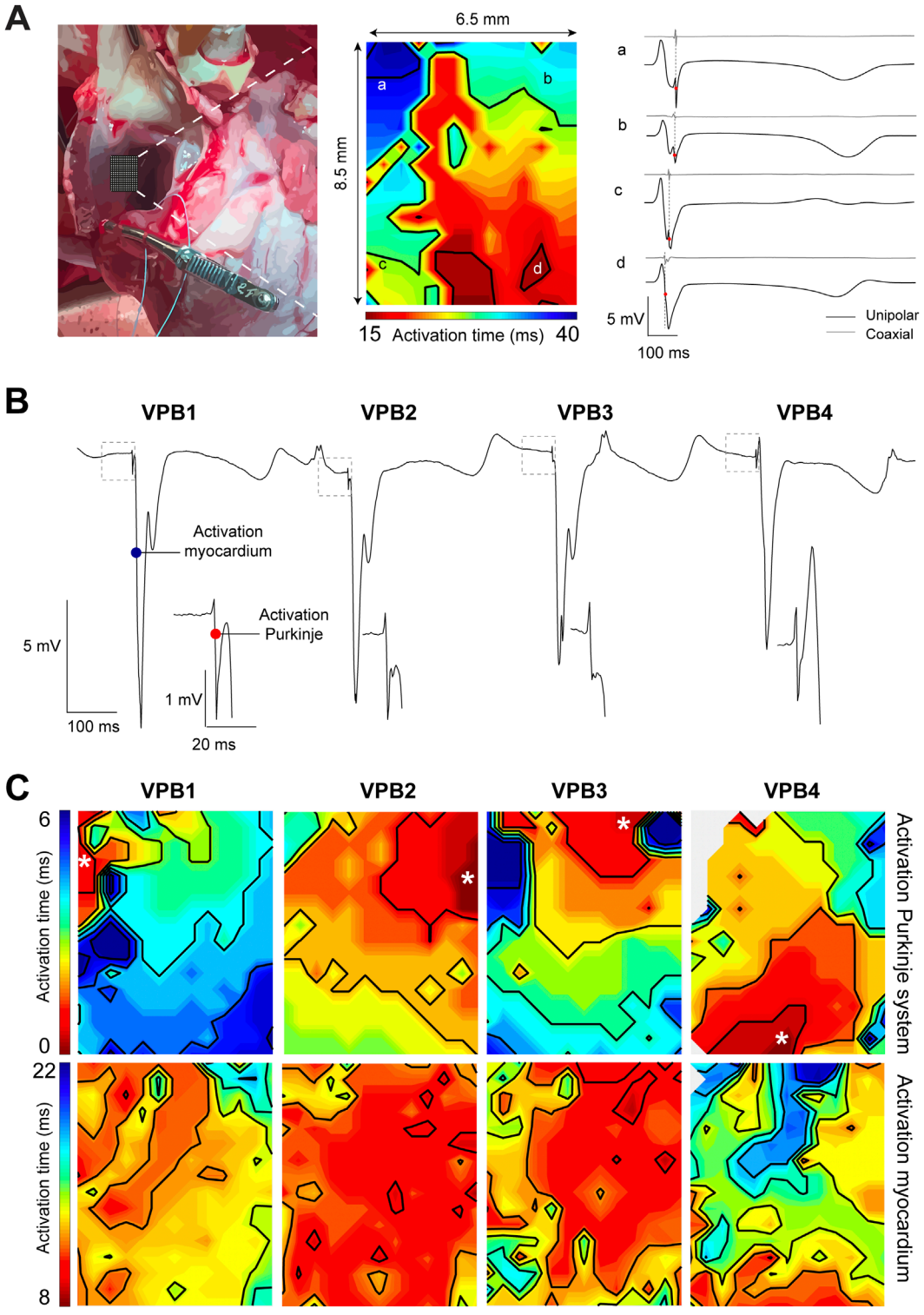

FIGURE 2
High-resolution endocardial activation mapping of the RVOT reveals Purkinje activity preceding ventricular premature beats (VPBs). **(A)** Left: photograph of the opened right ventricular cavity exposing the endocardial surface of the RVOT free wall. Middle: endocardial activation map of the RVOT recorded during sinus rhythm. Right: corresponding unipolar and coaxial (Hoogendijk et al.) electrogram traces from sites a-d in the activation map. Note the absence of Purkinje spikes in the unipolar electrogram and the single moment of activation in the coaxial electrogram. **(B)** Unipolar electrograms recorded from the RVOT endocardium while moving the catheter multi-electrode. Each VPB was preceded by a Purkinje spike (see insets). **(C)** Local activation maps corresponding to the maximal -dV/dT for Purkinje activation (top row) and myocardial activation (bottom row).

Purkinje marker Connexin 40 (Miquerol et al., 2004). Purkinje fibers in the RVOT showed marked Connexin 40 expression, which was not present in the working myocardium (Figure 3C). These Purkinje fibers were located within the subendocardium as well as deeper within the myocardial wall.

Although we did measure Purkinje activity on the endocardial side of the RVOT, we did not find it directly below the pulmonary valves. To determine the distribution of Purkinje fibers in the RVOT, we counted the number of individual, insulated Purkinje fibers in longitudinal sections (N = 2 hearts, n = 38 RVOT sections) across two sheep hearts within 0–5 mm, 5–10 mm, and 10–15 mm distance below the valves (Figure 4A). Nineteen sections were chosen from the right to the left side of the RVOT, with an intersection distance of ± 150 µm. We did not observe any major differences in Purkinje fiber count between the left and right side of the RVOT free wall (Figure 4B). However, the number of Purkinje fibers was significantly lower directly below the valves (0–5 mm) than further towards the right ventricular free wall (Figure 4C). Next, we analyzed the shortest distance for each Purkinje fiber relative to endocardium and epicardium for each area (Figure 4D). Figure 4E shows heatmaps for both RVOT free walls in which color intensity corresponds to the average number of Purkinje fibers in each transmural segment (equals to 10% wall thickness) across all 19 sections. Purkinje fiber distribution between endocardium and epicardium was highly similar between both walls. Purkinje fibers were located deeper within the myocardial wall within all areas below the pulmonary valves, but most predominantly when moving closer to more inferior. Altogether, these results confirm the presence of a Purkinje network in the RVOT near the endocardium and extending into the myocardial wall.

Discussion

We present evidence for the presence of a functional Purkinje system in the RVOT of the sheep heart. Using unipolar mapping, we identified brief sharp spike-shaped deflections preceding the myocardial activation complex. The presence of Purkinje cells was further supported by the a network composed of grey, gelatinous fibers across the RVOT endocardial surface that expressed Purkinje cell marker Connexin 40. This network extended from the right ventricular free wall into the RVOT free wall in close vicinity to the pulmonary valves. The clear presence of a Purkinje network elevates the sheep heart to a model system for studying Purkinje-related RVOT arrhythmia mechanisms.

Our findings are the first to simultaneously provide functional and structural evidence for the presence of a Purkinje network in the RVOT. An earlier study performed by De Almeida et al. demonstrated the presence of a Purkinje system in the RVOT of the cow heart (De Almeida et al., 2020; De Almeida et al., 2017; De Almeida et al., 2021). To do so, the investigators injected Barium-based contrast medium into the Purkinje network and visualized the potential Purkinje system by Computed Tomography. Similarly, we found that the free wall of the RVOT contains a Purkinje fiber network that extends further into the wall. Sheep and cow belong to the ungulates, or hooved mammals, which possess a Purkinje system that extends into the myocardial wall and is more extensive than in human, rodents, and carnivores such as dog (Ansari et al., 1999; Ryu et al., 2009; Ohkawa, 2008; Duan et al., 2017; Elbrønd et al., 2023). A recent study, however, suggests the human ventricular wall may also contain a transmural Purkinje network (Hillestad et al., 2025). The mechanism giving rise to such a transmural Purkinje network is unknown. Research on mice have found that the embryonic ventricular trabecular layer contains precursor cells of the Purkinje network (Christoffels and Moorman, 2009; Jensen et al., 2012). During heart development, some of the cells in the trabecular layer specialize towards a Purkinje phenotype, while others acquire a compact working myocardial phenotype and become part of the compact ventricular wall. In pigs, which are also members of the ungulates, late embryonic hearts have relatively deep intertrabecular recesses and an extensive trabecular layer (Jensen et al., 2024a). This setting appears different from that of human and should the basal parts of this extensive layer undergo compaction further in development, Purkinje precursors could become trapped within the compact wall. Whether such process takes place in pigs and ungulates in general requires further investigation.

The Purkinje fibers we found in the sheep RVOT showed characteristics that aligned with early descriptions (Tawara, 1906; Lhamon, 1912; King, 1916; Hondeghem and Stroobandt, 1974; Canale et al., 1983; Ansari et al., 1999; Ryu et al., 2009). Whether the extension of the Purkinje network into the RVOT is unique to ungulates requires further investigation. Recently, we showed that myocardial trabeculations can exist in the human RVOT. In this study, we found that RVOT trabeculations considerably varied between individuals (Jensen et al., 2024b). Given that Purkinje fibers and trabecular myocardium have a similar origin, this could mean that in some individuals the Purkinje network is present in the RVOT, while in other individuals it is absent.

De Almeida et al. demonstrated the presence of Purkinje fibers in two human RVOT samples using conventional histology along with historic anatomical definitions (De Almeida et al., 2020). To confirm the identity of the Purkinje fibers, we performed an immunohistochemical stain for Connexin 40, a widely accepted marker of the ventricular conduction system in mice that also marks conduction system tissue in the human ventricle (Miquerol et al., 2004; Hillestad et al., 2025). *NPPA* and *MYL4* are expressed during cardiac development and are also specific to the human Purkinje network (Hillestad et al., 2025). The specificity of conventional Purkinje system markers including Contactin 2 (CNTN2) or hyperpolarization-activated channel 4 (HCN4) for the human ventricular conduction system requires further investigation (Pallante et al., 2010).

As reported by De Almeida et al., subendocardial Purkinje fibers in the human RVOT were usually no larger than 50–100 µm in diameter (De Almeida et al., 2020). During endocardial mapping procedures, filter settings in combination with low sampling frequency may hamper detection of electrical activity from these small fibers in patients. An advantage of our experimental Langendorff-perfusion heart model is the possibility to measure electrical activity in the heart without the need to apply filtering settings that are standard in clinical practice. Fundamental improvements in signal processing and filtering technology maybe crucial to identify Purkinje activity for effective catheter ablation of ventricular fibrillation in the RVOT in patients.

In all five sheep we measured, the Purkinje spikes were clearly visible. However, in one heart, Purkinje spikes were only observed

10.3389/fphys.2025.1631426

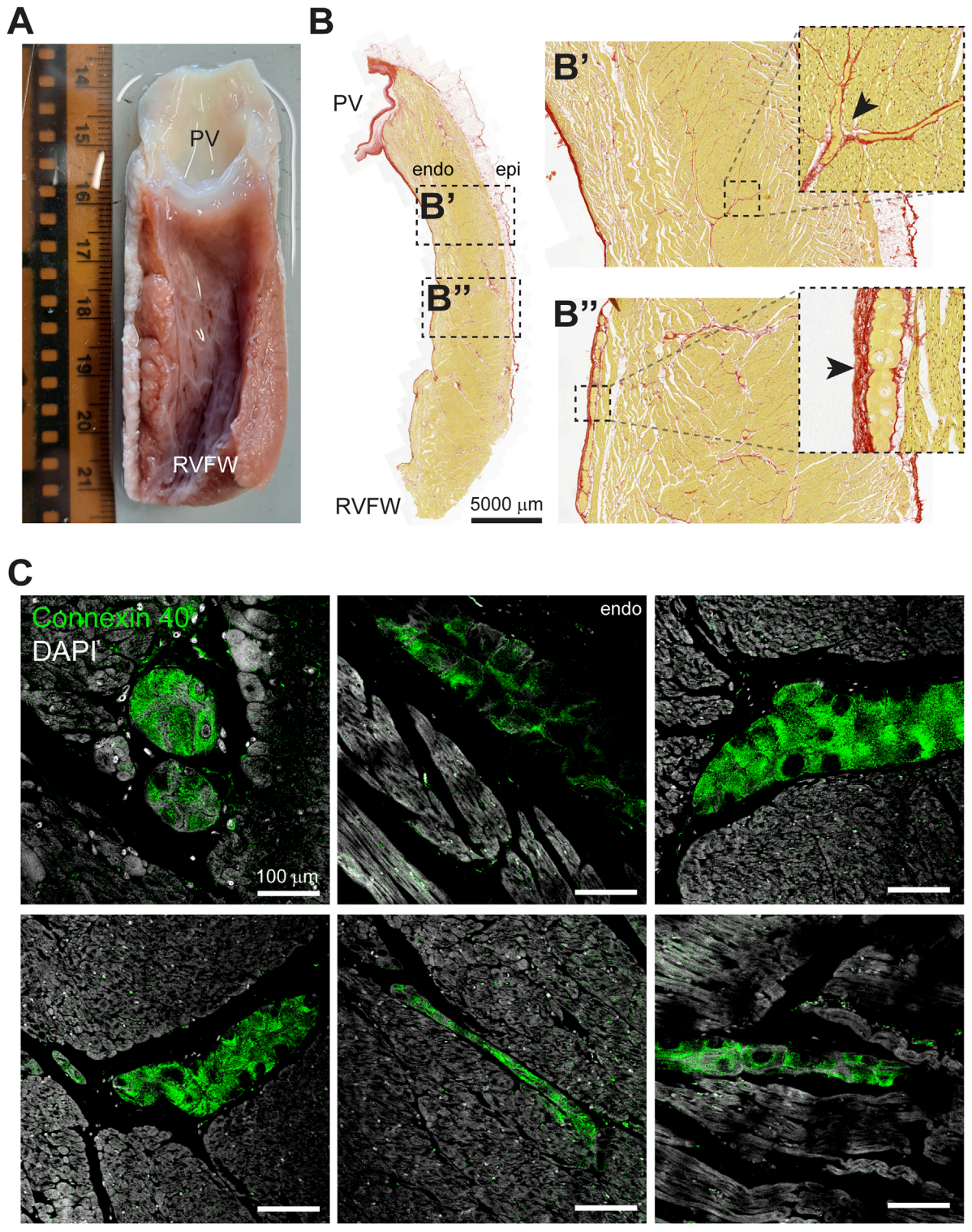

FIGURE 3
The sheep RVOT contains a Purkinje network that extends into the myocardial wall. **(A)** Photograph of the luminal side of the RVOT free wall after dissection. From this view, the presence of a Purkinje network is clearly visible. Scale in cm. **(B)** Example of a RVOT section stained with Picrosirius Red. Purkinje fibers were identified immediately below the pulmonary valve leaflets **(B')** and toward the right ventricular free wall **(B")**. **(C)** Super-resolution microscopy images of Connexin 40-positive Purkinje fibers in the RVOT endocardium and within the myocardial wall.

10.3389/fphys.2025.1631426

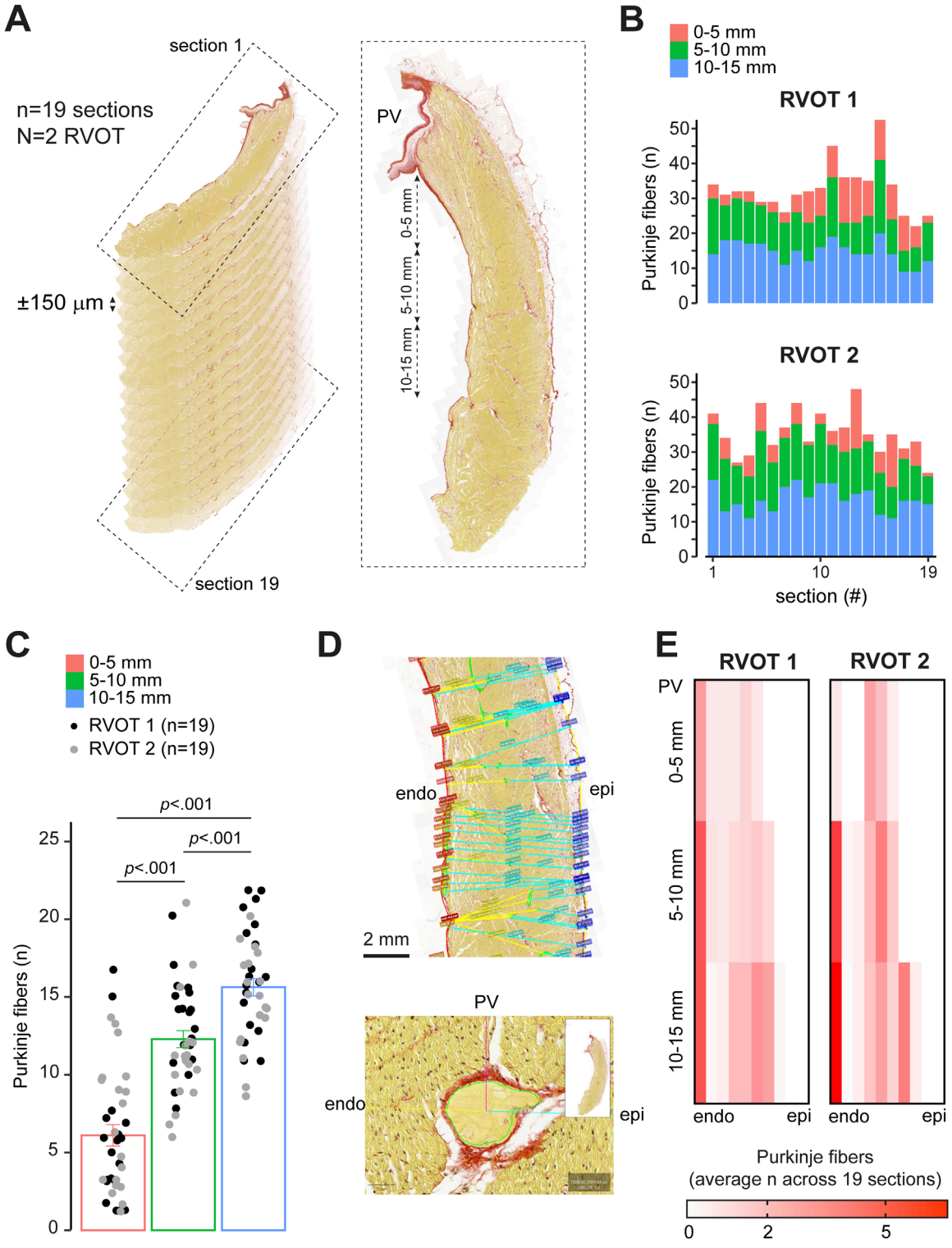

FIGURE 4
Quantitative analysis of Purkinje fiber distribution in the sheep RVOT. **(A)** Schematic explaining the selection of longitudinal sections from the RVOT free wall. **(B)** Purkinje fiber distribution per section from left-right of the RVOT wall (N = 2) within 0–5 mm, 5–10 mm, and 10–15 mm below the valve. **(C)** Quantitative analysis of Purkinje fiber number within 0–5 mm, 5–10 mm, and 10–15 mm below the valve (n = 38 sections). **(D)** Analysis of the shortest distance from Purkinje fiber to the endocardial (endo) and epicardial (epi) wall. **(E)** Heatmaps of quantitative analysis of the average number of Purkinje fibers for each RVOT between the endocardium and epicardium. Segment width equals 10% RVOT wall thickness.

following application of light pressure while navigating the electrode catheter against the RVOT endocardial surface. This suggests that the Purkinje system could interfere with baseline RVOT conduction, for example, when the RVOT wall is subjected to increased hemodynamic stresses (Gülan et al., 2019; Hurley et al., 2023a; Hurley et al., 2023b). One such possibility can be examined during studies of the beating heart, in which physiological parameters, including pump function and cardiac pressures, can be measured while blood is pumped through the *ex vivo* heart as would naturally occur (Kappler et al., 2019). Some stretch-activated ion channels, including TRPM4, have been shown to be expressed at higher levels in Purkinje fibers than in ventricular myocardium (Hurley et al., 2023a; Somberg et al., 1981). Activation of these channels produces an inward current that causes diastolic depolarization which enhancing Purkinje automaticity. Mechanical manipulation of Purkinje activity can be avoided by using flexible, stretchable membrane devices for high-resolution electrogram mapping, which are applied directly to the endocardial surface (Gutbrod et al., 2014).

Despite the presence of a Purkinje network, the RVOT does activate later compared to the left and right ventricles. We speculate that this is the result of a longer pathway, originating from the His bundle, that is required for electrical impulse propagation to reach the RVOT free wall compared to the other cardiac regions.

Similar to the RVOT, the Purkinje system is frequently the origin of VPBs (Enriquez et al., 2024). During cardiac repolarization, these VPBs can give rise to polymorphic ventricular tachycardia which may transition into ventricular fibrillation (Haïssaguerre et al., 2002b; Smirk, 1949; Knecht et al., 2009). Currently, it is unknown whether intramural extension of the Purkinje network correlates to a higher susceptibility to idiopathic ventricular fibrillation. However, it is conceivable that a more extensive Purkinje network could give rise to an increased anatomical substrate for reentry (Coronel et al., 2021; Schmitt and Erlanger, 1928).

Conclusion

The RVOT of the sheep heart contains a functional Purkinje system which can initiate VPBs. This places the sheep heart as an attractive model for experimental research to investigate the role of the Purkinje system in initiation of arrhythmias, including ventricular fibrillation, in the RVOT. Furthermore, the sheep heart could be used as a model for testing novel approaches for Purkinje network ablation.

Data availability statement

The raw data supporting the conclusions of this article will be made available by the authors, without undue reservation.

Ethics statement

The animal study was approved by the Animal Experiments Committee of Maastricht University. The study was conducted in accordance with the local legislation and institutional requirements.

Author contributions

MB: Conceptualization, Data curation, Formal Analysis, Investigation, Methodology, Project administration, Software, Validation, Visualization, Writing – original draft, Writing – review and editing. BdO: Methodology, Writing – review and editing. MK: Resources, Writing – review and editing. DO: Resources, Writing – review and editing. MJ: Funding acquisition, Resources, Software, Writing – review and editing. SZ: Software, Writing – review and editing. BJ: Conceptualization, Resources, Writing – review and editing. AvH: Investigation, Writing – review and editing. BB: Conceptualization, Data curation, Formal Analysis, Funding acquisition, Investigation, Methodology, Project administration, Resources, Software, Supervision, Validation, Visualization, Writing – review and editing.

Funding

The author(s) declare that financial support was received for the research and/or publication of this article. This work was supported by the Rembrandt Research Grant 2021 (RESHAPE-study to BB and MJ) and the Leducq International Network of Excellence Award (23CVD04) on Bioelectronics for Neurocardiology.

Acknowledgments

We kindly thank M.W. Paul for providing the code that was used in QuPath v0.6.0-rc3 for semi-automatic analysis of Purkinje fiber distance from the epicardium, the endocardium, and the pulmonary valve.

Conflict of interest

The authors declare that the research was conducted in the absence of any commercial or financial relationships that could be construed as a potential conflict of interest.

Generative AI statement

The author(s) declare that no Generative AI was used in the creation of this manuscript.

Publisher's note

References

Ansari, A., Ho, S. Y., and Anderson, R. H. (1999). Distribution of the purkinje fibres in the sheep heart. *Anat. Rec.* 254 (1), 92–97. doi:10.1002/(SICI)1097-0185(19990101)254:1<92:AID-AR12>3.0.CO;2-3

Boyden, P. A., Hirose, M., and Dun, W. (2010). Cardiac purkinje cells. *Heart rhythm.* 7 (1), 127–135. doi:10.1016/j.hrthm.2009.09.017

Canale, E., Campbell, G. R., Uehara, Y., Fujiwara, T., and Smolich, J. J. (1983). Sheep cardiac purkinje fibers: configurational changes during the cardiac cycle. *Cell Tissue Res.* 232 (1), 97–110. doi:10.1007/BF00222376

Christoffels, V. M., and Moorman, A. F. (2009). Development of the cardiac conduction system: why are some regions of the heart more arrhythmogenic than others? *Circ. Arrhythm. Electrophysiol.* 2 (2), 195–207. doi:10.1161/CIRCEP.108.829341

Coronel, R., Potse, M., Haïssaguerre, M., Derval, N., Rivaud, M. R., Meijborg, V. M. F., et al. (2021). Why ablation of sites with purkinje activation is antiarrhythmic: the interplay between fast activation and arrhythmogenesis. *Front. Physiol.* 12, 648396. doi:10.3389/fphys.2021.648396

De Almeida, M. C., Araujo, M., Duque, M., and Vilhena, V. (2017). Crista supraventricularis purkinje network and its relation to intraseptal purkinje network. *Anat. Rec. Hob.* 300 (10), 1793–1801. doi:10.1002/ar.23620

De Almeida, M. C., Mori, S., and Anderson, R. H. (2021). Three-dimensional visualization of the Bovine cardiac conduction system and surrounding structures compared to the arrangements in the human heart. *J. Anat.* 238 (6), 1359–1370. doi:10.1111/joa.13397

De Almeida, M. C., Stephenson, R. S., Anderson, R. H., Benvenuti, L. A., Loukas, M., and Aiello, V. D. (2020). Human subpulmonary infundibulum has an endocardial network of specialized conducting cardiomyocytes. *Heart Rhythm.* 17 (1), 123–130. doi:10.1016/j.hrthm.2019.07.033

Duan, D., Yu, S., Cui, Y., and Li, C. (2017). Morphological study of the atrioventricular conduction system and purkinje fibers in yak. *J. Morphol.* 278 (7), 975–986. doi:10.1002/jmor.20691

Elbrønd, V. S., Thomsen, M. B., Isaksen, J. L., Lunde, E. D., Vincenti, S., Wang, T., et al. (2023). Intramural purkinje fibers facilitate rapid ventricular activation in the equine heart. *Acta Physiol. (Oxf)* 237 (3), e13925. doi:10.1111/apha.13925

Enriquez, A., Muser, D., Markman, T. M., and Garcia, F. (2024). Mapping and ablation of premature ventricular complexes: state of the art. *JACC Clin. Electrophysiol.* 10 (6), 1206–1222. doi:10.1016/j.jacep.2024.02.008

Gülan, U., Saguner, A. M., Akdis, D., Gotschy, A., Tanner, F. C., Kozerke, S., et al. (2019). Hemodynamic changes in the right ventricle induced by variations of cardiac output: a possible mechanism for arrhythmia occurrence in the outflow tract. *Sci. Rep.* 9 (1), 100. doi:10.1038/s41598-018-36614-7

Gutbrod, S. R., Sulkin, M. S., Rogers, J. A., and Efimov, I. R. (2014). Patient-specific flexible and stretchable devices for cardiac diagnostics and therapy. *Prog. Biophys. Mol. Biol.* 115 (2-3), 244–251. doi:10.1016/j.pbiomolbio.2014.07.011

Haïssaguerre, M., Shah, D. C., Jaïs, P., Shoda, M., Kautzner, J., Arentz, T., et al. (2002a). Role of purkinje conducting system in triggering of idiopathic ventricular fibrillation. *Lancet* 359 (9307), 677–678. doi:10.1016/S0140-6736(02)07807-8

Haïssaguerre, M., Shoda, M., Jaïs, P., Nogami, A., Shah, D. C., Kautzner, J., et al. (2002b). Mapping and ablation of idiopathic ventricular fibrillation. *Circulation* 106 (8), 962–967. doi:10.1161/01.cir.0000027564.55739.b1

Haissaguerre, M., Vigmond, E., Stuyvers, B., Hocini, M., and Bernus, O. (2016). Ventricular arrhythmias and the his-purkinje system. *Nat. Rev. Cardiol.* 13 (3), 155–166. doi:10.1038/nrcardio.2015.193

Hillestad, M. L., Amontree, M., Mahlberg, R. C., Bagwell, M. S., Rizzo, S. A., Arrell, D. K., et al. (2025). MYL4 identifies intramural anatomy of purkinje fibers in human hearts. *JACC Clin. Electrophysiol.* doi:10.1016/j.jacep.2025.03.039

Hondeghem, L. M., and Stroobandt, R. (1974). Purkinje fibers of sheep papillary muscle: occurrence of discontinuous fibers. *Am. J. Anat.* 141 (2), 251–261. doi:10.1002/aja.1001410207

Hoogendijk, M. G., Coronel, R., Arora, R., Kuiper, M., de Groot, N., de Boer, R. A., et al. (2025). Hexagonal multielectrode design for recording local electrograms with superior characteristics. *JACC Clin. Electrophysiol.* doi:10.1016/j.jacep.2025.03.011

Hurley, M., Kaur, S., Walton, R., Power, A., Haïssaguerre, M., Bernus, O., et al. (2023a). Endocardial role in arrhythmias induced by acute ventricular stretch and the involvement of purkinje fibres, in isolated rat hearts. *Curr. Res. Physiol.* 6, 100098. doi:10.1016/j.crphys.2023.100098

Hurley, M., Walton, R., Vigmond, E. J., Haïssaguerre, M., Bernus, O., and White, E. (2023b). Attenuation of stretch-induced arrhythmias following chemical ablation of purkinje fibres, in isolated rabbit hearts. *Front. Physiol.* 14, 1154157. doi:10.3389/fphys.2023.1154157

Jensen, B., Blok, M., Efimov, I. R., and Boukens, B. J. (2024b). The smooth-walled human right ventricular outflow tract could contain trabeculations that cause conduction delay. *Eur. Heart J. Cardiovasc Imaging* 25 (7), e176–e178. doi:10.1093/ehjci/jeae107

Jensen, B., Boukens, B. J., Postma, A. V., Gunst, Q. D., van den Hoff, M. J., Moorman, A. F., et al. (2012). Identifying the evolutionary building blocks of the cardiac conduction system. *PLoS One* 7 (9), e44231. doi:10.1371/journal.pone.0044231

Jensen, B., Salvatori, D., Schouten, J., Meijborg, V. M. F., Lauridsen, H., and Agger, P. (2024a). Trabeculations of the porcine and human cardiac ventricles are different in number but similar in total volume. *Clin. Anat.* 37 (4), 440–454. doi:10.1002/ca.24135

Kappler, B., Ledezma, C. A., van Tuijl, S., Meijborg, V., Boukens, B. J., Ergin, B., et al. (2019). Investigating the physiology of normothermic *ex vivo* heart perfusion in an isolated slaughterhouse porcine model used for device testing and training. *BMC Cardiovasc Disord.* 19 (1), 254. doi:10.1186/s12872-019-1242-9

King, M. R. (1916). The sino-ventricular system as demonstrated by the injection method. *Am. J. Anat.* 19 (2), 149–177. doi:10.1002/aja.1000190202

Knecht, S., Sacher, F., Wright, M., Hocini, M., Nogami, A., Arentz, T., et al. (2009). Long-term follow-up of idiopathic ventricular fibrillation ablation: a multicenter study. *J. Am. Coll. Cardiol.* 54 (6), 522–528. doi:10.1016/j.jacc.2009.03.065

Lhamon, R. M. (1912). The sheath of the sino-ventricular bundle. *Am. J. Anat.* 13 (1), 55–70. doi:10.1002/aja.1000130104

Miquerol, L., Meysen, S., Mangoni, M., Bois, P., van Rijen, H. V., Abran, P., et al. (2004). Architectural and functional asymmetry of the his-purkinje system of the murine heart. *Cardiovasc Res.* 63 (1), 77–86. doi:10.1016/j.cardiores.2004.03.007

Ohkawa, S.-i. (2008). Distribution of purkinje cells in hearts of human and various animals. *J. Arrhythmia* 24 (4), 177–179. doi:10.4020/jhrs.24.177

Pallante, B. A., Giovannone, S., Fang-Yu, L., Zhang, J., Liu, N., Kang, G., et al. (2010). Contactin-2 expression in the cardiac purkinje fiber network. *Circ. Arrhythm. Electrophysiol.* 3 (2), 186–194. doi:10.1161/CIRCEP.109.928820

Ryu, S., Yamamoto, S., Andersen, C. R., Nakazawa, K., Miyake, F., and James, T. N. (2009). Intramural purkinje cell network of sheep ventricles as the terminal pathway of conduction system. *Anat. Rec. Hob.* 292 (1), 12–22. doi:10.1002/ar.20827

Schmitt, F. O., and Erlanger, J. (1928). Directional differences in the conduction of the impulse through heart muscle and their possible relation to extrasystolic and fibrillary. *Am. J. Physiol.* 87 (2), 326–347. doi:10.1152/ajplegacy.1928.87.2.326

Smirk, F. H. (1949). R waves interrupting T waves. *Br. Heart J.* 11 (1), 23–36. doi:10.1136/hrt.11.1.23

Somberg, J. C., Barry, W. H., and Smith, T. W. (1981). Differing sensitivities of purkinje fibers and myocardium to inhibition of monovalent cation transport by digitalis. *J. Clin. Invest* 67 (1), 116–123. doi:10.1172/JCI110003

Tawara, S. (1906) Das Reizleitungssystem des Säugetierherzens: eine anatomisch-histologische Studie über das Atrioventrikularbündel und die Purkinjeschen Fäden: fischer.

Tawara, S. (2000). "Conduction system of the mammalian heart," in *The: an anatomico-histological study of the atrioventricular bundle and the purkinje fibers*. World Scientific.

frontiers | Frontiers in Physiology

TYPE Original Research
PUBLISHED 01 September 2025
DOI 10.3389/fphys.2025.1657611

OPEN ACCESS

EDITED BY
Bum-Rak Choi,
Brown University, United States

REVIEWED BY
Roel Meiburg,
University of Eindhoven, Netherlands
Benito Baldauf,
Hochschule Bremerhaven, Germany

*CORRESPONDENCE
Jason D. Bayer,
jason.bayer@ihu-liryc.fr

RECEIVED 01 July 2025
ACCEPTED 30 July 2025
PUBLISHED 01 September 2025

CITATION
Bayer JD, Gillette K, Coronel R, Plank G and Vigmond EJ (2025) To reconnect or not reconnect distal Purkinje fibers, that is the question when modeling the Purkinje fiber network.
Front. Physiol. 16:1657611.
doi: 10.3389/fphys.2025.1657611

To reconnect or not reconnect distal Purkinje fibers, that is the question when modeling the Purkinje fiber network

Jason D. Bayer[1,2]*, Karli Gillette[3,4,5], Ruben Coronel[6], Gernot Plank[5] and Edward J. Vigmond[1,2]

[1]Electrophysiology and Heart Modeling Institute, IHU Liryc, Fondation Bordeaux Université, Pessac-Bordeaux, France, [2]Institut de Mathématiques de Bordeaux, UMR5251, University of Bordeaux, Bordeaux, France, [3]Scientific Computing and Imaging Institute, University of Utah, Salt Lake City, UT, United States, [4]Department of Biomedical Engineering, University of Utah, Salt Lake City, UT, United States, [5]Department of Biophysics, Medical University of Graz, Graz, Austria, [6]Department of Experimental Cardiology, Amsterdam University Medical Centers, Location AMC, Amsterdam, Netherlands

Background and aims: Multiple rule-based approaches exist to model the structure of the His-Purkinje system (HPS). While some approaches reconnect Purkinje fibers in the Purkinje fiber network, others do not. The aim of this study was to determine the impact of distal Purkinje fiber reconnections on anterograde activation, retrograde activation, and reentrant arrhythmias.

Methods: In a human biventricular model with or without distal Purkinje fiber reconnections, normal sinus rhythm was simulated by His bundle pacing (anterograde activation), followed by an S1S2 protocol applied to the right ventricular apex (retrograde activation). Activation times in the myocardium and HPS were compared for both anterograde and retrograde HPS activation. Arrhythmia vulnerability windows and duration were determined by identifying the S1S2 coupling intervals that induced a reentry of at least two full rotations. Arrhythmia maintenance was further studied by inducing reentry with 4 Hz line pacing applied to the left ventricular epicardial surface. Reentry duration for each protocol was determined over a 20 s window. The S1S2 and line pacing protocols were repeated in the biventricular model without an HPS.

Results: Anterograde activation times and arrhythmia initiation vulnerability windows were mostly unaltered when removing distal Purkinje fiber reconnections. However, retrograde activation times were 18% longer in the HPS and 8% longer in the myocardium when removing distal Purkinje fiber reconnections. Reentrant arrhythmias from the S1S2 protocol and rapid line pacing lasted longer for the model with (11.2 and >20 s) versus without (3.2 and 8.2 s) distal Purkinje fiber reconnections. The S1S2 protocol did not induce reentrant arrhythmias in the human ventricles model without an HPS, and reentry induced with 4 Hz line pacing lasted only 3.6 s.

Conclusion: Retrograde activation times increased and the duration of reentrant arrhythmias shortened in the absence of Purkinje fiber reconnections in the Purkinje fiber network. This could be an important structural

HPS property to incorporate into computational heart models when investigating retrograde activation and/or reentrant arrhythmias. Modifying the structure of the Purkinje fiber network to remove Purkinje fiber reconnections in patients with life threatening ventricular arrhythmia might be antiarrhythmic.

KEYWORDS

Purkinje network, conduction system, modeling, simulation, retrograde activation, anterograde activation, arrhythmia

Introduction

The His-Purkinje system (HPS) is the ventricular component of the cardiac conduction system. It is composed of the His bundle with major fascicles that bifurcate into left and right bundle branches. At the distal regions of each bundle branch is the Purkinje fiber network, which is a complex structure of Purkinje fibers that electrically couples to the myocardium through Purkinje-Muscular Junctions (PMJs).

In the original description of the Purkinje fiber network by Tawara et al. (Tawara, 1906), it was shown to have Purkinje fibers that branch (bifurcate) and reconnect (converge) within the network. This was later confirmed by India ink injection, transparent specimens, and computed tomography (De Almeida et al., 2015). During the developmental stages of the heart, the expression of Nkx2-5 in the myocardium promotes this meshing of the Purkinje fibers into the Purkinje fiber network (Park and Fishman, 2017).

In computer simulations of the cardiac conduction system (Stephenson et al., 2017), it may be important to accurately model this mesh structure of the Purkinje fiber network within the HPS. In particular, it may play a critical role in the generation of activation patterns during normal sinus rhythm, ventricular pacing, and/or reentrant arrhythmias (Durrer et al., 1970). Unfortunately, it is difficult to model the complex structure of the HPS in its entirety in three dimensions from imaging alone (Peirlinck et al., 2021). Consequently, it is commonly reconstructed in human ventricular models using rule-based approaches (Liu and Cherry, 2015; Vigmond and Clements, 2007; Ijiri et al., 2008; Al-Nashash and Lvov, 1997; Atkinson et al., 2011).

Rule-based approaches for generating the HPS structure can differ noticeably in the Purkinje fiber network. Specifically, some rule-based approaches develop a mesh structure for the Purkinje fiber network by reconnecting distal Purkinje fibers (Gillette et al., 2021; Behradfar et al., 2014), while others have a tree structure without reconnecting distal Purkinje fibers (Costabal et al., 2016; Álvarez-Barrientos et al., 2025). In other words, the latter approach develops an HPS with unique pathways from the His bundle to the PMJs with only branching of Purkinje fibers. The impact of this difference on anterograde activation, retrograde activation, and reentrant arrhythmia initiation/maintenance is unknown. We hypothesize that modeling the Purkinje fiber network with reconnecting Purkinje fibers facilitates simulating activation times and reentrant behavior observed in patients.

The main objective of this study was to determine the impact of distal Purkinje fiber reconnections on anterograde activation, retrograde activation, and reentrant arrhythmia initiation/maintenance. To accomplish this, we utilized an established computer model of the human ventricles including an HPS (Bayer et al., 2022), and performed simulations in this model with the same major fascicles and PMJs either with or without reconnections of Purkinje fibers in the Purkinje fiber network. This computational study demonstrates that distal Purkinje connections may play an important role in retrograde activation and arrhythmia maintenance, but not anterograde activation.

Methods

Human biventricular model

The electrical activation of ventricular myocardium coupled to the HPS was investigated using an established computer model of the human ventricular conduction system (Bayer et al., 2022). The full details on the geometry and electrophysiology of the non-failing human ventricles can be found in (Bayer et al., 2016). The full details on the structure and electrophysiology of the HPS can be found in Behradfar et al. (2014), Bayer et al. (2022). In short, the parameters governing cellular and tissue electrophysiology in this anatomically accurate human model of the ventricular conduction system were fit to experimental and clinical data in order to reproduce physiologic depolarization and repolarization patterns that generate the human ECG (Durrer et al., 1970). Specifically, the human biventricular model includes transmural and apicobasal heterogeneity in cellular coupling, calcium handling, and ionic channel currents that generate the physiological depolarization and repolarization patterns intrinsic to human ventricular myocardium. These properties were essential to include since they can impact electrical conduction and arrhythmogenesis in the human heart (Han et al., 2021).

To introduce an arrhythmic substrate into this otherwise healthy heart model, the maximal conductance of the slow delayed rectifier potassium current (G_{Ks}) in the HPS was decreased from the value of 0.98 pS/pF as in Walton et al. (2014) to its default ventricular myocyte value of 0.392 pS/pF (Tusscher et al., 2004). The G_{Ks} parameter was chosen since it directly influences APD in the model and has been linked to ventricular arrhythmias (Varshneya et al., 2018). Importantly, the APD generated from this modification to G_{Ks} (maximum of 371 ms) was within the physiological data range reported for Purkinje fibers of non-diseased human hearts (Nagy et al., 2015). With this modification, at normal sinus rhythm rates action potential duration in the HPS is longer than in the myocardium on average by 56 ms across all PMJs in the model. This promotes unidirectional conduction block at short stimulus coupling intervals during the S1S2 programmed stimulation protocol described below. To prevent arrhythmia dynamics from

being dependent on variations in PMJ density (Behradfar et al., 2014), the PMJ density of the HPS in the myocardium was fixed to 15 PMJs per cm^3 with a junctional resistance of 100 kΩ.

HPS structure with or without distal Purkinje fiber reconnections

The structure of the HPS in the biventricular model was modified to exclude reconnections between Purkinje fibers within the Purkinje network of the left and right bundle branches (Figure 1). Specially, cross-bridging fibers between the major ascending fibers were disconnected to convert the meshed HPS structure to a tree structure. At each reunification point with two parent nodes, i.e., where two parent cables connected to one child, the second parent cable was removed up to the point where it originated at a bifurcation. Thus, no PMJs were left unconnected to a parent branch after these branch removals, while the major fascicles and bundle branches remained intact. As a result, there were two test cases to study anterograde and retrograde activation. The first test case was the human ventricles model with an HPS that had reconnected Purkinje fibers within the Purkinje fiber network (M_{rHPS}, Figure 1A), and the second was the human ventricles with the same HPS but with disconnected Purkinje fibers within the Purkinje fiber network (M_{dHPS}, Figure 1B). A third test case was used to investigate how the HPS contributes to reentrant arrhythmia initiation and/or maintenance. This case was the same human ventricles model as used for the other two cases, but with the HPS removed (M_{noHPS}, Figure 1C).

Anterograde activation

The His bundle was paced at a cycle length (CL) of 750 ms for 10 cycles. Activation times (ATs) were computed at each node of the myocardial and HPS meshes for the last cycle of pacing as the moment when the action potential upstroke exceeded the voltage threshold of −10 mV. Differences in the activation patterns between the two test cases in Figure 1 were quantified using the method of Han et al. (Han et al., 2012). Using this approach, the relative difference (RD), root mean square difference (RMSD) and correlation coefficient (CC) were computed for the comparisons M_{dHPS} versus M_{rHPS} and M_{noHPS} versus M_{rHPS}.

Retrograde activation

Following His pacing, the right ventricular endocardial apex was paced (S1) at a CL of 600 ms for 10 cycles from a spherical region with a diameter of 1.5 mm. This stimulus diameter was chosen to mimic a standard 5F catheter size used for clinical pacing studies. Activation times (ATs) were computed and compared in the same manner as previously described for anterograde conduction. Note, the CL of 600 ms was chosen since it is a commonly used CL for programmed electrical stimulation in cardiac electrophysiology laboratories. This CL is also within the range used to investigate retrograde activation (Sung et al., 1981). Since this CL mimics a heart rate slightly higher than normal resting heart rates (100 bpm vs. 60–90 bpm), it prevents sinus rhythm activation originating from the atria from interfering with S1 capture. Since APD restitution of the ventricular myocardium in the model does not steepen until S1 CL < 500 ms (120 bpm) (Bayer et al., 2016), retrograde activation patterns were not dependent on our choice of S1 CL > 500 ms.

Arrhythmia initiation

Following S1 pacing, premature S2 stimuli were applied at the same RV pacing site with a CI beginning at 400 ms, which mimics programmed electrical stimulation used to induce ventricular arrhythmias in cardiac electrophysiology laboratories. The S1S2 CI was then gradually reduced by decrements of 10 ms until a loss of stimulus capture. All pacing stimuli were administered with a 2 ms duration at a strength of twice the diastolic threshold. The diastolic stimulus threshold was determined for each new set of model parameters. Following each S2 stimulus, the transmembrane voltage maps of the ventricular myocardium and HPS were inspected for unidirectional conduction block and reentry that lasted for more than 2 full rotations. In other words, reentry was identified when a point in the HPS or ventricles was activated more than once following the S2. The vulnerable window of reentry was recorded by identifying the first and last S2 coupling intervals that generated reentry.

Arrhythmia maintenance

In addition to studying arrhythmia maintenance following reentries from the S1S2 protocol, reentry was induced with rapid line pacing using the protocol from our previous computational and animal studies (Moreno et al., 2022; Moreno et al., 2019; Bayer et al., 2024). This protocol consistently induces the same reentry in each of the three models to unbiasedly study how the arrhythmic substrate maintains the induced arrhythmia. In short, pacing was administered from an apicobasal line electrode 2 mm in diameter on the left ventricular epicardium by stimulating the entire line at 8x the diastolic stimulation threshold with a pacing CL of 400 ms for 10 cycles. The 8x capture threshold strength ensured homogeneous activation across the entire line. Subsequently, reentry was induced with rapid pacing from the same line electrode with a pacing CL of 250 ms for 10 cycles at 8x the diastolic stimulation threshold. Reentry was verified by visual inspection of the transmembrane voltage maps in the HPS and/or myocardium. The duration of this reentry, as well as the reentry induced for the longest S2 coupling interval from the S1S2 protocol, was recorded over a 20 s window until the reentry self-terminated or the end of the arrhythmia observation window was reached.

Simulation platform

Monodomain simulations were performed using the cardiac electrophysiology simulator CARP-EP (numericor.at) running in parallel on 512 cores. For this study, simulations for the preconditioning normal sinus rhythm protocol, S1S2 protocol, and rapid line pacing protocol were performed for the 2 cases

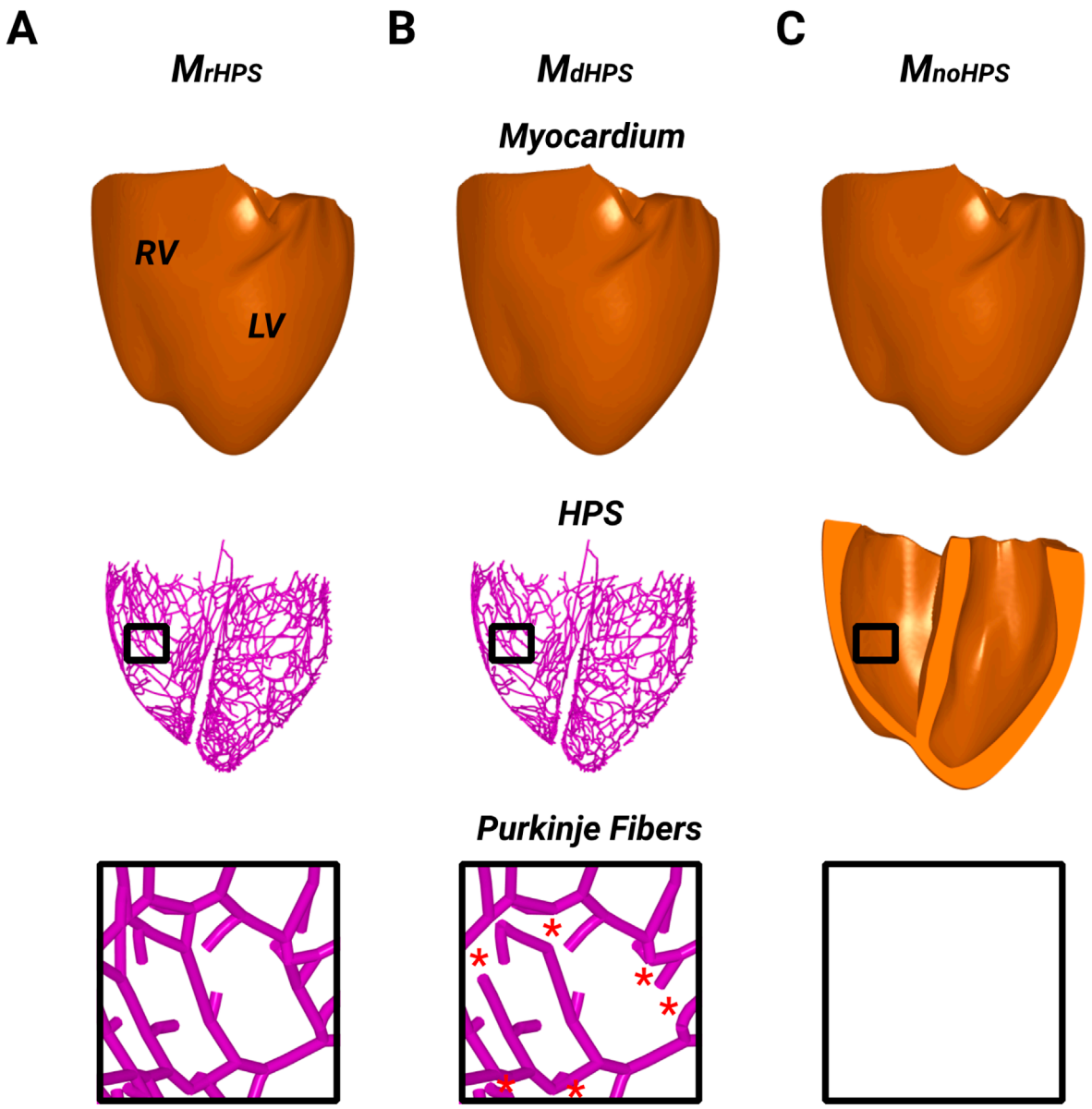

FIGURE 1
The three model cases showing the ventricular myocardium with reconnected distal Purkinje fibers **(A)**, disconnected distal Purkinje fibers **(B)**, and without the HPS **(C)**. Black boxes were placed in the RV of each model to zoom in on the Purkinje fiber structure to show the presence or absence of distal Purkinje fiber reconnections. Red stars in the inset of **(B)** indicates where distal Purkinje fiber reconnections were disconnected (removed) from the inset in **(A)**.

with different HPS structures and the case without an HPS. These simulations had a computational cost of 34,560 CPU hours on 512 cores of the high-performance analytics and computing platform IRENE (Joliot-Curie) at the TGCC supercomputing center. All simulations used a time step of 20 μs, and their results were visualized using the software Meshalyzer (https://git.opencarp.org/openCARP/meshalyzer). Stimuli for all protocols were administered by transmembrane current injection with diastolic stimulation thresholds obtained by increasing the stimulus strength in increments of 1 μA/cm (starting from zero) until action potential propagation was initiated in the myocardium from the stimulus site.

Results

Anterograde activation

For each test case in Figure 1, activation times were computed at the end of the normal sinus rhythm protocol to identify differences in anterograde conduction in the ventricular myocardium and HPS. Figure 2 shows the total activation times in the HPS and the myocardium for the models with distal Purkinje fiber reconnections (M_{rHPS}, Figure 2A) and without distal Purkinje fiber reconnections (M_{dHPS}, Figure 2B). Minor differences were observed in the isolines between the activation maps in the ventricular myocardium between

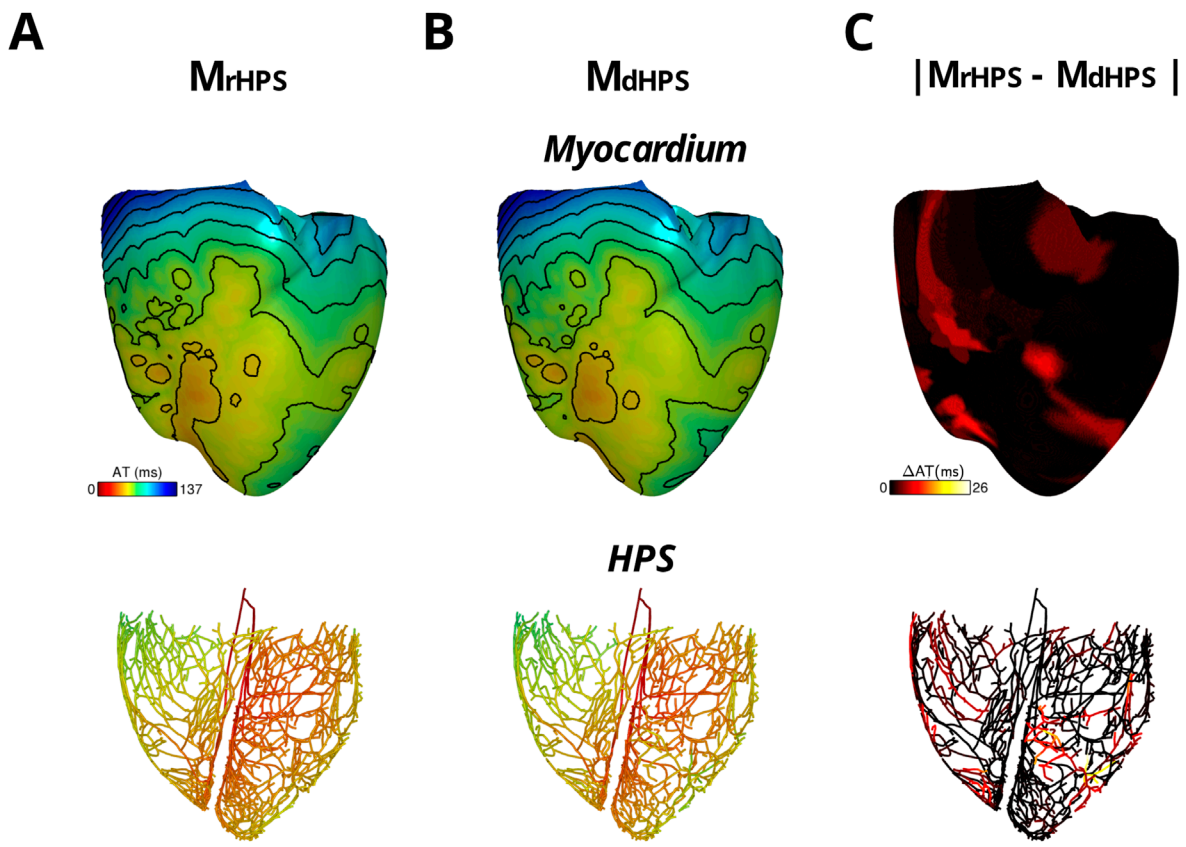

FIGURE 2
The two model cases with an HPN showing anterograde activation in transmembrane voltage maps of the HPS and myocardium either with reconnected distal Purkinje fibers **(A)** or disconnected distal Purkinje fibers **(B)** Isoline spacing is 10 ms. Activation times ranged from 21 to 136 ms in the myocardium and 0–67 ms in the HPS of **(A)** and 21–137 ms in the myocardium and 0–70 ms in the HPS of **(B)** The absolute difference in activation times between the two cases is shown in **(C)**.

TABLE 1 Comparison of anterograde and retrograde activation times between the models with reconnected distal Purkinje fibers and disconnected distal Purkinje fibers.

	%|Δ in total AT|	RD (%)	RMSD (ms)	CC
Anterograde M_{dHPS} vs. M_{rHPS}				
Myocardium	0.87	0.03	1.36 ± 1.43	0.99
HPS	4.41	0.08	3.21 ± 3.26	0.97
Retrograde M_{dHPS} vs. M_{rHPS}				
Myocardium	7.86	0.09	7.24 ± 5.08	0.98
HPS	18.18	0.20	8.95 ± 6.12	0.95

cases M_{rHPS} and M_{dHPS} (compare Figure 2A with Figure 2C). To quantify these differences, the RD, RMSD, and CC were computed for the comparison between the M_{dHPS} and M_{rHPS} models (Table 1).

For the comparison of the M_{dHPS} and M_{rHPS} models, in the myocardium for the HPS with disconnected distal Purkinje fibers, total activation time increased by only 1 ms, while the absolute change in total AT was less than 1% with the RMSD only slightly larger than a millisecond. In the HPS, these values were larger by only a few milliseconds. The CC values ≥ 0.97 showed a very strong linear relationship between the activation patterns for these two test cases. Figure 2C shows the distribution in the absolute difference in activation times between the two models.

The impact of using different G_{Ks} values between the default (0.98 pS/pF) and arrhythmogenic (0.392 pS/pF) values on anterograde activation was unnoticeable. For any value within this range differing by 0.1 pS/pF, we did not find changes >1 ms to anterograde activation times nor activation patterns. This was due to the CV restitution curves of the HPS and myocardium being flat at the His pacing CL of 750 ms.

Retrograde activation

For each test case in Figure 1, activation times were computed at the end of S1 pacing to identify differences in the retrograde activation of the ventricular myocardium and HPS. Figure 3 shows the total activation times in the HPS and the myocardium for the models M_{rHPS} Figure 3A and M_{dHPS} (Figure 3B). In contrast to

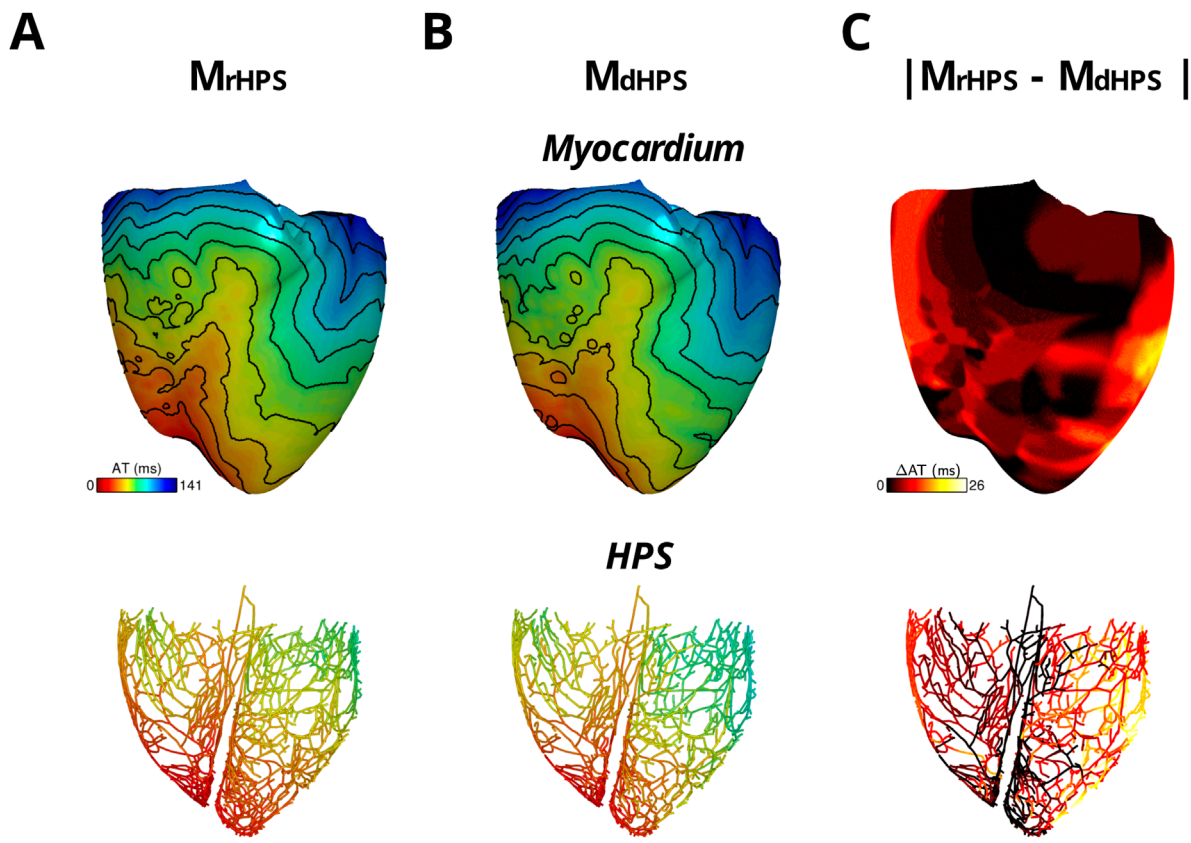

FIGURE 3
The two model cases with an HPN showing retrograde activation in transmembrane voltage maps of the HPS and myocardium either with reconnected distal Purkinje fibers **(A)** or disconnected distal Purkinje fibers **(B)**. Isoline spacing is 10 ms. Activation times ranged from 0 to 130 ms in the myocardium and 8–80 ms in the HPS of **(A)** and 0–141 ms in the myocardium and 8–96 ms in the HPS of **(B)**. The absolute difference in activation times between the two cases is shown in **(C)**.

anterograde conduction, differences in the activation maps between Figures 3A,B appeared larger in the ventricular myocardium and HPS. To quantify these differences, the RD, RMSD, and CC were computed in the same manner as for anterograde activation in order to compare between the M_{dHPS} and M_{rHPS} models (Table 1).

For the comparison of the M_{dHPS} and M_{rHPS} models, in the myocardium of M_{dHPS} total activation time increased by 11 ms, while the absolute change in total AT was 7.86% with an RMSD of 7.25 ms. In the HPS of M_{dHPS} compared to M_{rHPS}, the increase in total activation time was larger by 16 ms along with a larger absolute change in total AT of 18.18% and an RMSD of 8.95 ms. The CC values ≥ 0.95 still showed a strong linear relationship between the activation patterns for these two test cases. Figure 3C shows the distribution in the absolute difference in activation times between the two models.

The impact of using different G_{Ks} values between the default (0.98 pS/pF) and arrhythmogenic (0.392 pS/pF) values on retrograde activation was also unnoticeable. For any value within this range differing by 0.1 pS/pF, we did not find changes >1 ms to retrograde activation times nor activation patterns. This was due to the CV restitution curves of the HPS and myocardium being flat at the His pacing CL of 600 ms.

Arrhythmia initiation

Results for the arrhythmias induced with the S1S2 protocol applied to the RV endocardial apex of the three test models are shown in Table 2. Reentry was initiated in M_{rHPS} and M_{dHPS}, but not M_{noHPS}. The vulnerable windows for the test cases M_{rHPS} and M_{dHPS} were similar (S1S2 coupling intervals from 270 to 320 ms). Within the arrhythmia vulnerability windows for M_{rHPS} and M_{dHPS}, reentry was induced by unidirectional conduction block that lasted for at least 2 full rotations (Figure 4).

Arrhythmia maintenance

Arrhythmia maintenance was quantified as the duration of the reentry that was visible in the myocardium and/or HPS after the administration of rapid line pacing, as well as for reentry following the S1S2 coupling interval of 320 ms. The duration of these arrhythmias can be found in Table 2. Note, rapid line pacing initiated reentrant arrhythmias in all three models, with an example shown for M_{rHPS} in Figure 4. The reentries in all three models started out as a figure-of-eight reentry from conduction block along the electrode placed along the apicobasal axis of the ventricles. After a few seconds

TABLE 2 Arrhythmia initiation and maintenance of reentry following the S1S2 and rapid line pacing protocols.

	M_{rHPS}	M_{dHPS}	M_{noHPS}
Initiation			
Last S2 capture	260	260	260
First reentry after S2 (ms)	320	320	—
Last reentry after S2 (ms)	270	270	—
Maintenance			
Reentry duration following S2 = 320 ms (s)	11.2	3.2	—
Reentry duration following line pacing (s)	>20	8.2	3.6

the behavior of the reentry changed with respect to the structure or presence of the HPN. Specifically, these reentries lasted for the entire 20 s observation window in M_{rHPS} and less than 9 s in M_{dHPS}. Reentry was even shorter in M_{noHPS} lasting less than 4 s. Similar results were observed for the S1S2 coupling interval of 320 ms, where reentry duration was 3.2 s for M_{dHPS} and the entire 20 s observation period for M_{rHPS}.

Discussion

This study used a state-of-the-art computational model of the human ventricles and HPS to identify how Purkinje fiber reconnections in the Purkinje fiber network influence anterograde activation, retrograde activation, and reentrant arrhythmias. This *in silico* study demonstrates that retrograde activation patterns and arrhythmia maintenance can be impacted by distal Purkinje fiber reconnections, while antegrade activation patterns and arrhythmia initiation are not. In the model with disconnected distal Purkinje fibers, the total retrograde activation time increased by 8% in the myocardium and 18% in the HPS compared to the model with reconnected distal Purkinje fibers. Reentrant arrhythmias from the S1S2 protocol and rapid line pacing lasted longer in the model with reconnected (11.2 and >20 s) versus disconnected (3.2 and 8.2 s) distal Purkinje fibers.

The dependence of anterograde conduction on Purkinje fiber network structure was weak in the model

Numerous studies have implemented the rule-based approaches mentioned in the introduction (Liu and Cherry, 2015; Vigmond and Clements, 2007; Ijiri et al., 2008) into digital twinning pipelines (Gillette et al., 2021; Behradfar et al., 2014; Costabal et al., 2016). These pipelines aim to reproduce patient-specific activation patterns and ECGs during normal sinus rhythm. Regardless of the choice of the rule-based algorithm to generate HPS structure, they have shown success for reproducing physiological activation patterns underlying the ECG during normal sinus rhythm.

The universal success of these approaches indicates that reproducing the detailed structure of the Purkinje network may not be critical for generating patient activation patterns and QRS durations during normal sinus rhythm. In other words, changing the structure of the Purkinje network should not significantly impact activation patterns on the endocardium of the ventricles as long as the macrostructure of the HPS is modeled appropriately.

Figure 2 and Table 1 of our study show that when removing reconnections in the Purkinje fiber network, the difference in total anterograde activation time without Purkinje fiber network reconnections was only a few milliseconds. Therefore, we concluded that the generation of the initial endocardial activations observed in the human ventricles by Durrer et al. (1970) is more dependent on the major fascicles of the left and right bundle branches in the model than on the topology of the Purkinje fiber network. Thus, efforts should be focused more on the macrostructure of the left and right bundle branches in the HPS if the only goal is to simulate anterograde activation patterns in the ventricles. Furthermore, this independence on the algorithm used to generate HPS structures for normal sinus rhythm provides users with the flexibility to choose from a wider array of rule-base approaches that best fits their needs. For example, methods that simplify the HPS into a thin fast-conducting endocardial layer are computationally inexpensive and have shown promise for simulating sinus rhythm activation (Okada et al., 2018). Such approaches might be more practical to employ for studies that require a large number of sinus rhythm simulations to be performed in a large number of heart models.

The dependence of retrograde activation on Purkinje fiber network structure was stronger in the model

Few studies have investigated how Purkinje fiber network structure impacts retrograde activation patterns and reentrant arrhythmias in intact human ventricles (Bayer et al., 2022; Bayer et al., 2024). Our *in silico* study demonstrates that retrograde activation from ventricular pacing, ectopic foci, or reentrant arrhythmias can differ from anterograde activation depending on the structure of the Purkinje fiber network. This is due to electrical activation from the myocardium being able to re-enter the HPS at multiple locations at different times.

Our study suggests that reconnected Purkinje fibers in the Purkinje fiber network can be an essential feature to model when investigating retrograde activation in ventricles during ventricular pacing and reentrant arrhythmias. In models with disconnected distal Purkinje fibers, we expect that corroborating simulation results with animal and/or clinical data will be more challenging. Thus, drawing conclusions on activation patterns simulated during ventricular pacing and reentrant behaviors observed in models without distal Purkinje fiber reconnections should be done with extreme caution.

Imaging data supports the need for modeling a Purkinje fiber network with Purkinje fiber reconnections (Stephenson et al., 2017; Ono et al., 2009; Cha et al., 2020). From these studies, it is clear that

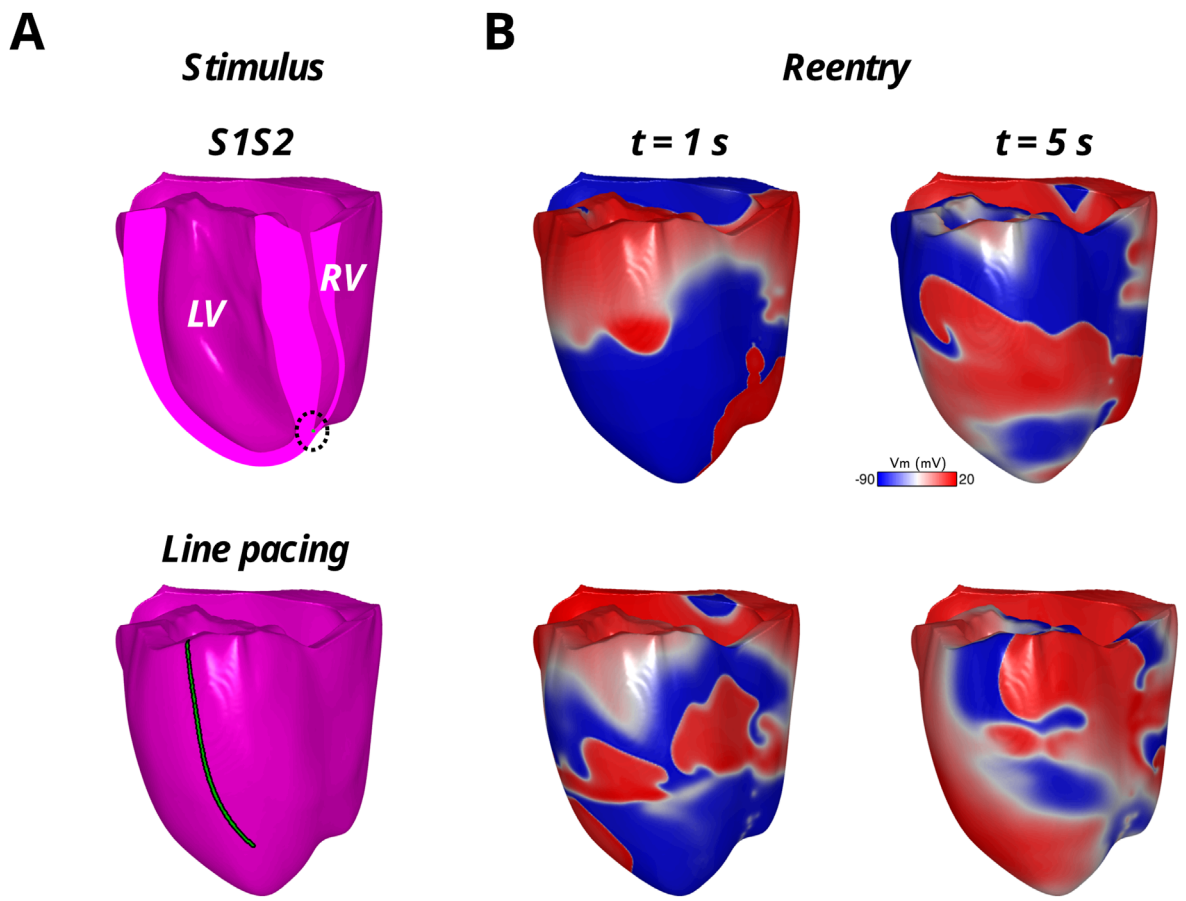

FIGURE 4
Reentrant arrhythmias in the model with reconnected distal Purkinje fibers with the S1S2 protocol applied to the endocardial RV apex (top row) and the rapid LV epicardial line pacing protocol (bottom row). The stimulus locations are shown in green in **(A)** and the reentrant arrhythmia in the transmembrane voltage maps (Vm) are shown in **(B)** at two time points during the first 5 s of reentry.

distal Purkinje fibers reconnect. Furthermore, the Purkinje network is generated from a contiguous endocardial layer of specialized myocardium during the early stages of development (Sedmera and Gourdie, 2014). Therefore, the branching and reconnection of distal Purkinje fibers is to be expected. Due to the impact of the Purkinje fiber network structure on retrograde activation maps and arrhythmia behavior, future studies should focus on modeling more accurately both the macrostructure and microstructure of the HPS, as well as making rule-based HPS algorithms more flexible to include new rules for HPS structure as imaging studies evolve.

Arrhythmia initiation and maintenance

Our *in silico* study suggests that arrhythmia initiation is less dependent on the structure of the Purkinje network than arrhythmia maintenance. This makes sense since the initiation of arrhythmias using the protocols from this study relies heavily on the presence of repolarization heterogeneity for induction. Specifically, the S1S2 protocol relies on the action potential duration heterogeneity across the PMJs to generate unidirectional conduction block and reentry (Behradfar et al., 2014; Martinez et al., 2018; Haissaguerre et al., 2016). For the rapid line pacing protocol, it relies on the apicobasal action potential duration heterogeneity in the ventricular myocardium to generate unidirectional conduction block and reentry (Bayer et al., 2016). Therefore, it is not surprising that distal Purkinje fiber reconnections had little effect on arrhythmia initiation, i.e., the first few rotations of a reentry generated from unidirectional conduction block.

As the reentrant arrhythmia persisted, the role of both anterograde and retrograde conduction within the HPS became important regardless of the arrhythmia initiation protocol that was used (Figure 4; Table 2). A previous study by our group showed that defibrillation success using low-energy approaches relies heavily on eliminating reentrant pathways through the HPS (Bayer et al., 2022). We also showed that rapidly pacing the His bundle helps to eliminate HPS reentrant pathways, where at specific frequencies this caused the reentrant arrhythmia to terminate (Bayer et al., 2024). Therefore, when there are more Purkinje fiber reconnections within the Purkinje fiber network, the number of possible reentrant pathways in the HPS should also increase to promote the maintenance of reentrant arrhythmias. Future work will investigate the mechanism of specific types and locations of distal Purkinje reconnections regarding these pathways in the HPN.

Further supporting the role of the Purkinje network in lethal ventricular arrhythmias, it has been shown that removing Purkinje activation sites with radiofrequency ablation is anti-arrhythmic (Coronel et al., 2021). Thus, modifying the structure of the Purkinje fiber network to remove Purkinje fiber reconnections in patients with life threatening ventricular arrhythmia may be antiarrhythmic. This could theoretically be done with gene therapy (Wang et al., 2025), ablation (Imnadze and Zerm, 2019), or pacing (Bayer et al., 2024). Based on our recent findings and this body of work on the role of the Purkinje network in ventricular arrhythmias, further imaging studies should investigate how Purkinje fiber reconnections within the Purkinje fiber network vary between patients, and if patients with more distal Purkinje fiber reconnections are more susceptible to arrhythmias.

The propensity of sustained ventricular arrhythmias in the model with the mesh HPS structure may be explained by the microstructure of the HPS. For example, there could be current source-sink mismatches during retrograde activation of the HPS when thinner Purkinje fibers merge into a single thicker Purkinje fiber. When these current source-sink mismatches become large enough, which would be expected at fast rates of activation, they could lead to unidirectional conduction block and sustained reentry if the surrounding HPS architecture and coupled myocardium provide a suitable pathway to support reentry (Ciaccio et al., 2018). Since the model with the mesh HPS structure has more interconnections between Purkinje fibers than the tree HPS structure, this may explain its higher propensity towards sustained ventricular reentrant arrhythmias. Future studies are warranted to identify the occurrence and conditions for these current source-sink mismatches to occur in the Purkinje network of the HPS, in addition to determining the specific micro-architectures in the finer branches of the HPS that are able to support sustained reentry. To validate this study, imaging data will be required to verify the existence of these micro-architectural structures.

In addition to HPS microstructure, there is evidence that spatial heterogeneity exists in the repolarization of the HPS which could impact HPS-mediated reentrant arrhythmias. In isolated Purkinje/myocardial tissue preparations from canine and human ventricles, APD prolongs from the His bundle to the distal regions of the Purkinje network, and then shortens again closer to PMJs (Myerburg et al., 1970). In optical mapping studies using *ex vivo* rabbit hearts (Logantha et al., 2021), APD is longer near the His bundle than in distal Purkinje fibers. Consequently, this spatial heterogeneity in APD could impact the initiation and/or maintenance of the reentries observed in our human ventricles model with the HPS. To address this issue, future studies are planned with our model to investigate the mechanisms of HPS-mediated reentrant arrhythmias in relation to spatial heterogeneities in the HPS from calcium handling, ion channel currents, and cellular coupling.

Clinical significance

The findings of this study may have clinical significance to noninvasive therapies for ventricular tachyarrhythmias, such as Sterotactic body radiotherapy (SBRT) (Blanck et al., 2020). When anti-arrhythmic drugs and radiofrequency ablation fail to terminate and prevent the reoccurrence of ventricular tachyarrhythmias, SBRT is an alternative for permanently removing the arrhythmic substrate. During SBRT the entire myocardium is exposed to doses of radiation in the range of 15–40 Gy, which in turn has been shown in rats to increase conduction velocity, shorten action potential duration, and increase the peak of the calcium transient in the ventricular myocardium (Mages et al., 2025). These changes are antiarrhythmic in cardiac tissue by reducing the wavelength of reentry (APD*CV). Furthermore, SBRT is non-selective and likely reduces the APD gradient across the PMJs, which our studies suggest could be antiarrhythmic. Future simulation studies will hopefully provide valuable mechanistic insight into the effectiveness of SBRT for treating lethal ventricular arrhythmias.

Limitations

Due to the computational expense of performing simulations in the human model of the ventricular conduction system, we only used a single human ventricular geometry and HPS to investigate anterograde activation, retrograde activation, and reentrant arrhythmias. To speed up simulation times and reduce computational costs, using eikonal approaches as done for solving anterograde ventricular activation maps (Gillette et al., 2021) is not practical for retrograde activation maps and reentry in the HPS. We plan to expand this study to multiple hearts, both healthy and diseased, when new approaches arise that are capable of achieving this feature. Specifically, we till target hearts with fibrosis, scars, and age/sex-related changes in cardiac electrophysiology and geometry. Secondly, we artificially introduced the arrhythmic substrate for S1S2 programmed stimulation to induce reentrant arrhythmias by decreasing G_{Ks} in the HPS. For now, we deem this acceptable since little is known regarding the structure and function of the HPS in diseased hearts. When such data becomes available in the future, this study will be expanded to include specific pathological abnormalities in the structure and electrophysiology of the HPS. We will also thoroughly perform a sensitivity analysis of our results to a wider range of GKs values than used for this study. Thirdly, we used a fixed 15 PMJs per cm^3 density in the human ventricles model. According to the study by Behradfar et al. (Behradfar et al., 2014), increasing PMJ density above this value is not expected to impact arrhythmia dynamics, but reducing it below 13 PMJs per cm^3 could. Thus, future studies are warranted to investigate the impact of lower PMJs densities in the model on the arrhythmia outcome of our study. Fourth, we only performed programmed electrical stimulation using a clinical S1S2 protocol administered to the right ventricular endocardial apex for studying retrograde activation and arrhythmogenesis. It is possible that retrograde activation and arrhythmia initiation/maintenance could be impacted by the pacing location in the ventricles. In future studies we plan to investigate how various cardiac resynchronization therapy setups impact retrograde activation patterns and arrhythmogenesis. Fifth, we assume that the HPS structure at the left and right ventricular apex is continuous with the lower portion of the septum. We also assume that only major fascicles without PMJs exist in the middle to upper sections of the right ventricular septum. This is notably different from other approaches constructing rule-based HPSs for digital twinning purposes (Gillette et al., 2021). The

impact of these differences in HPS structure on retrograde activation and arrhythmogenesis will also be explored in future studies and validated with imaging and electrophysiology data from human hearts when available. Lastly, our simulation study lacked mechano-electric and neural feedback. While it is acknowledged that both can influence activation patterns and arrhythmogenesis in the human ventricles, they were not included in our study at this time in order to keep the computational expenses and complexity of our simulations manageable. When possible and appropriate to do so, they will be included in future studies to help refine the model and provide confidence to the simulation results.

Conclusion

Retrograde activation times increased and the duration of reentrant arrhythmias shortened in the absence of distal Purkinje fiber reconnections observed in histological and imaging studies. The reconnection of distal Purkinje fibers could be an important structural HPS property to incorporate into computational heart models when investigating retrograde activation and/or reentrant arrhythmias. Modifying the structure of the Purkinje fiber network to remove Purkinje fiber reconnections in patients with life threatening ventricular arrhythmia may be antiarrhythmic.

Data availability statement

The raw data supporting the conclusions of this article will be made available by the authors, without undue reservation.

Author contributions

JB: Writing – review and editing, Writing – original draft. KG: Writing – review and editing. RC: Writing – review and editing. GP: Writing – review and editing. EV: Writing – original draft, Writing – review and editing.

Funding

The author(s) declare that financial support was received for the research and/or publication of this article. We acknowledge the support of GENCI computing resources, allocation A0080310517 utilized at the TGCC supercomputing center. This research was funded by the French National Research Agency grant ANR-10-IAHU-04 (to JB and EV) and the Austrian Science Fund grant 10.55776/ESP592 (to KG) and 10.55776/I6540 (to GP).

Conflict of interest

The authors declare that the research was conducted in the absence of any commercial or financial relationships that could be construed as a potential conflict of interest.

The author(s) declared that they were an editorial board member of Frontiers, at the time of submission. This had no impact on the peer review process and the final decision.

Generative AI statement

The author(s) declare that no Generative AI was used in the creation of this manuscript.

Publisher's note

References

Al-Nashash, H., and Lvov, B. (1997). Three-dimensional model for the simulation of the HPS electrogram. *Biomed. Mater Eng.* 7 (6), 401–410.

Álvarez-Barrientos, F., Salinas-Camus, M., Pezzuto, S., and Costabal, F. S. (2025). Probabilistic learning of the purkinje network from the electrocardiogram. *Med. Image Anal.* 101, 103460. doi:10.1016/j.media.2025.103460

Atkinson, A., Inada, S., Li, J., Tellez, J. O., Yanni, J., Sleiman, R., et al. (2011). Anatomical and molecular mapping of the left and right ventricular his-purkinje conduction networks. *J. Mol. Cell Cardiol.* 51 (5), 689–701. doi:10.1016/j.yjmcc.2011.05.020

Bayer, J. D., Lalani, G. G., Vigmond, E. J., Narayan, S. M., and Trayanova, N. A. (2016). Mechanisms linking electrical alternans and clinical ventricular arrhythmia in human heart failure. *Hear Rhythm* 13, 1922–1931. doi:10.1016/j.hrthm.2016.05.017

Bayer, J. D., Sobota, V., Moreno, A., Jaïs, P., and Vigmond, E. J. (2022). The purkinje network plays a major role in low-energy ventricular defibrillation. *Comput. Biol. Med.* 141, 105133. doi:10.1016/j.compbiomed.2021.105133

Bayer, J. D., Sobota, V., Bear, L. R., Haïssaguerre, M., and Vigmond, E. J. (2024). A his bundle pacing protocol for suppressing ventricular arrhythmia maintenance and improving defibrillation efficacy. *Comput. Methods Programs Biomed.* 253, 108239. doi:10.1016/j.cmpb.2024.108239

Behradfar, E., Nygren, A., and Vigmond, E. J. (2014). The role of purkinje-myocardial coupling during ventricular arrhythmia: a modeling study. *PLoS One* 9 (2), e88000. doi:10.1371/journal.pone.0088000

Blanck, O., Buergy, D., Vens, M., Eidinger, L., Zaman, A., Krug, D., et al. (2020). Radiosurgery for ventricular tachycardia: preclinical and clinical evidence and study design for a German multi-center multi-platform feasibility trial (RAVENTA). *Clin. Res. Cardiol.* 109 (11), 1319–1332. doi:10.1007/s00392-020-01650-9

Cha, M.-J., Seo, J.-W., Kim, H., Kim, M., Choi, J., Kang, D.-H., et al. (2020). Visualization of left ventricular purkinje fiber distribution using widefield optical coherence microscopy. *Int. J. Clin. Exp. Pathol.* 13 (12), 3013–3020.

Ciaccio, E. J., Coromilas, J., Wit, A. L., Peters, N. S., and Garan, H. (2018). Source-sink mismatch causing functional conduction block in Re-Entrant ventricular tachycardia. *Jacc Clin. Electrophysiol.* 4 (1), 1–16. doi:10.1016/j.jacep.2017.08.019

Coronel, R., Potse, M., Haïssaguerre, M., Derval, N., Rivaud, M. R., Meijborg, V. M. F., et al. (2021). Why ablation of sites with purkinje activation is antiarrhythmic: the interplay between fast activation and arrhythmogenesis. *Front. Physiol.* 12, 648396. doi:10.3389/fphys.2021.648396

Costabal, F. S., Hurtado, D. E., and Kuhl, E. (2016). Generating purkinje networks in the human heart. *J. Biomech.* 49 (12), 2455–2465. doi:10.1016/j.jbiomech.2015.12.025

De Almeida, M. C., Lopes, F., Fontes, P., Barra, F., Guimaraes, R., and Vilhena, V. (2015). Ungulates heart model: a study of the purkinje network using India ink injection, transparent specimens and computer tomography. *Anat. Sci. Int.* 90 (4), 240–250. doi:10.1007/s12565-014-0255-9

Durrer, D., van Dam, R. T., Freud, G. E., Janse, M. J., Meijler, F. L., and Arzbaecher, R. C. (1970). Total excitation of the isolated human heart. *Circulation* 41 (6), 899–912. doi:10.1161/01.cir.41.6.899

Gillette, K., Gsell, M. A. F., Bouyssier, J., Prassl, A. J., Neic, A., Vigmond, E. J., et al. (2021). Automated framework for the inclusion of a his-purkinje system in cardiac digital twins of ventricular electrophysiology. *Ann. Biomed. Eng.* 49 (12), 3143–3153. doi:10.1007/s10439-021-02825-9

Haissaguerre, M., Vigmond, E., Stuyvers, B., Hocini, M., and Bernus, O. (2016). Ventricular arrhythmias and the his–purkinje system. *Nat. Rev. Cardiol.* 13 (3), 155–166. doi:10.1038/nrcardio.2015.193

Han, C., Pogwizd, S. M., Killingsworth, C. R., and He, B. (2012). Noninvasive reconstruction of the three-dimensional ventricular activation sequence during pacing and ventricular tachycardia in the canine heart. *Am. J. Physiol. - Hear Circ. Physiol.* 302 (1), 244–252. doi:10.1152/ajpheart.00618.2011

Han, B., Trew, M. L., and Zgierski-Johnston, C. M. (2021). Cardiac conduction velocity, remodeling and arrhythmogenesis. *Cells* 10 (11), 2923. doi:10.3390/cells10112923

Ijiri, T., Ashihara, T., Yamaguchi, T., Takayama, K., Igarashi, T., Shimada, T., et al. (2008). A procedural method for modeling the purkinje fibers of the heart. *J. Physiol. Sci.* 58 (7), 481–486. doi:10.2170/physiolsci.RP003208

Imnadze, G., and Zerm, T. (2019). Prevention of ventricular fibrillation through de-networking of the purkinje system: proof-Of-concept paper on the substrate modification of the purkinje network. *PACE - Pacing Clin. Electrophysiol.* 42 (10), 1285–1290. doi:10.1111/pace.13782

Liu, B. R., and Cherry, E. M. (2015). Image-based structural modeling of the cardiac purkinje network. *Biomed. Res. Int.* 2015, 621034. doi:10.1155/2015/621034

Logantha, SJRJ, Cai, X. J., Yanni, J., Jones, C. B., Stephenson, R. S., Stuart, L., et al. (2021). Remodeling of the purkinje network in congestive heart failure in the rabbit. *Circ. Hear Fail* 14 (7), E007505. doi:10.1161/CIRCHEARTFAILURE.120.007505

Mages, C., Gampp, H., Rahm, A. K., Hackbarth, J., Pfeiffer, J., Petersenn, F., et al. (2025). Cardiac stereotactic body radiotherapy to treat malignant ventricular arrhythmias directly affects the cardiomyocyte electrophysiology. *Hear Rhythm* 22 (1), 90–99. doi:10.1016/j.hrthm.2024.06.043

Martinez, M. E., Walton, R. D., Bayer, J. D., Haïssaguerre, M., Vigmond, E. J., Hocini, M., et al. (2018). Role of the purkinje-muscle junction on the ventricular repolarization heterogeneity in the healthy and ischemic ovine ventricular myocardium. *Front. Physiol.* 9, 718. doi:10.3389/fphys.2018.00718

Moreno, A., Walton, R. D., Constantin, M., Bernus, O., Vigmond, E. J., and Bayer, J. D. (2019). Wide-area low-energy surface stimulation of large Mammalian ventricular tissue. *Sci. Rep.* 9 (1), 15863–11. doi:10.1038/s41598-019-51364-w

Moreno, A., Walton, R. D., Bernus, O., Vigmond, E. J., and Bayer, J. D. (2022). Low-energy, single-pulse surface stimulation defibrillates large Mammalian ventricles. *Hear Rhythm* 19 (2), 308–317. doi:10.1016/j.hrthm.2021.10.006

Myerburg, R. J., Stewart, J. W., and Hoffman, B. F. (1970). Electrophysiological propertiesf the canine peripheral A-V conducting system. *Circ. Res.* 26 (3), 361–378. doi:10.1161/01.res.26.3.361

Nagy, N., Szél, T., Jost, N., Tóth, A., Papp, J. G., and Varró, A. (2015). Novel experimental results in human cardiac electrophysiology: measurement of the purkinje fibre action potential from the undiseased human heart. *Can. J. Physiol. Pharmacol.* 93 (9), 803–810. doi:10.1139/cjpp-2014-0532

Okada, J. I., Washio, T., Nakagawa, M., Watanabe, M., Kadooka, Y., Kariya, T., et al. (2018). Absence of rapid propagation through the purkinje network as a potential cause of line block in the human heart with left bundle branch block. *Front. Physiol.* 9, 56. doi:10.3389/fphys.2018.00056

Ono, N., Yamaguchi, T., Ishikawa, H., Arakawa, M., Takahashi, N., Saikawa, T., et al. (2009). Morphological varieties of the purkinje fiber network in Mammalian hearts, as revealed by light and electron microscopy. *Arch. Histol. Cytol.* 72 (3), 139–149. doi:10.1679/aohc.72.139

Park, D. S., and Fishman, G. I. (2017). Development and function of the cardiac conduction system in health and disease. *J. Cardiovasc Dev. Dis.* 4 (2), 7. doi:10.3390/jcdd4020007

Peirlinck, M., Costabal, F. S., Yao, J., Guccione, J. M., Tripathy, S., Wang, Y., et al. (2021). Precision medicine in human heart modeling: perspectives, challenges, and opportunities. *Biomech. Model Mechanobiol.* 20 (3), 803–831. doi:10.1007/s10237-021-01421-z

Sedmera, D., and Gourdie, R. G. (2014). Why do we have purkinje fibers deep in our heart? *Physiol. Res.* 63, 9–18. doi:10.33549/physiolres.932686

Stephenson, R. S., Atkinson, A., Kottas, P., Perde, F., Jafarzadeh, F., Bateman, M., et al. (2017). High resolution 3-Dimensional imaging of the human cardiac conduction system from microanatomy to mathematical modeling. *Sci. Rep.* 71 (1), 7188–13. doi:10.1038/s41598-017-07694-8

Sung, R. J., Waxman, H. L., Saksena, S., and Juma, Z. (1981). Sequence of retrograde atrial activation in patients with dual atrioventricular nodal pathways. *Circulation* 64 (5), 1059–1067. doi:10.1161/01.cir.64.5.1059

Tawara, S. (1906). *Das Reizleitungenssystem des Säugetierherzens: eine anatomisch-histologische Studie über das Atrioventrikularbündel und die Purkinjeschen Fäden*. Germany: Jena, Fischer. Available online at: https://catalog.nlm.nih.gov/discovery/fulldisplay?vid=01NLM_INST:01NLM_INST&docid=alma99438083340 6676&context=L

Tusscher, K., Noble, D., Noble, P. J., and Panfilov, A. V. (2004). A model for human ventricular tissue. 286(4):1573–1589. doi:10.1152/ajpheart.00794.2003

Varshneya, M., Devenyi, R. A., and Sobie, E. A. (2018). Slow delayed rectifier current protects ventricular myocytes from arrhythmic dynamics across multiple species: a computational study. *Circ. Arrhythm. Electrophysiol.* 11 (10), e006558. doi:10.1161/CIRCEP.118.006558

Vigmond, E. J., and Clements, C. (2007). Construction of a computer model to investigate sawtooth effects in the purkinje system. *IEEE Trans. Biomed. Eng.* 54 (3), 389–399. doi:10.1109/TBME.2006.888817

Walton, R. D., Martinez, M. E., Bishop, M. J., Hocini, M., Haïssaguerre, M., Plank, G., et al. (2014). Influence of the Purkinje-muscle junction on transmural repolarization heterogeneity. *Cardiovasc Res.* 103, 629–640. doi:10.1093/cvr/cvu165

Wang, J., Verkerk, A. O., Wilders, R., Zhang, Y., Zhang, K., Prakosa, A., et al. (2025). SCN10A-short gene therapy to restore conduction and protect against malignant cardiac arrhythmias. *Eur. Heart J.* 46 (18), 1747–1762. doi:10.1093/eurheartj/ehaf053

frontiers | Frontiers in Cardiovascular Medicine

TYPE Original Research
PUBLISHED 05 September 2025
DOI 10.3389/fcvm.2025.1663243

OPEN ACCESS

EDITED BY
Edward Joseph Vigmond,
Université de Bordeaux, France

REVIEWED BY
Maria Joao Baptista,
Centro Hospitalar Universitário de São João (CHUSJ), Portugal
Alessandro Lianza,
Hospital Israelita Albert Einstein, Brazil

*CORRESPONDENCE
Tingting Yu
✉ 2536515650@qq.com

RECEIVED 10 July 2025
ACCEPTED 04 August 2025
PUBLISHED 05 September 2025

CITATION
Li H, Wei X, Zhu F, Zheng F and Yu T (2025) The λ pattern on time-RR interval scatter plot of neonatal ambulatory ECG: a marker of transient bradycardia.
Front. Cardiovasc. Med. 12:1663243.
doi: 10.3389/fcvm.2025.1663243

The λ pattern on time-RR interval scatter plot of neonatal ambulatory ECG: a marker of transient bradycardia

Hualian Li[1], Xin Wei[1], Fengna Zhu[2], Fei Zheng[1] and Tingting Yu[1]*

[1]Electrocardiogram Diagnostic Department, Hubei Maternal and Child Health Hospital, Wuhan, China, [2]Neonatology Department, Hubei Maternal and Child Health Hospital, Wuhan, China

Background: Neonatal bradycardia often triggers transient escape rhythms that challenge clinical diagnosis, with current methods lacking dynamic biomarkers for risk stratification.
Objective: To validate the λ pattern, a heart rate dynamic signature on time-RR interval scatter plot, for distinguishing escape rhythms from transient sinus bradycardia and predicting recovery timelines in neonates.
Methods: Retrospective analysis of 36 neonates (≤28 days) with 24 h electrocardiogram (ECG) monitoring. Holter data identified λ patterns (abrupt ≥20% RR prolongation and >3 s gradual recovery). Reverse-engineering ECG validated rhythm origins. Survival models assessed λ burden-prognosis correlations.
Results: 487 λ patterns (15.5 ± 3.2/neonate) were detected: 80.3% escape rhythms, 19.7% sinus bradycardia. High λ burden (≥21/24 h) predicted delayed recovery vs. low burden (≤10/24 h) [HR = 4.22 (95% CI: 1.98–9.01), $p < 0.0001$]. All cases resolved spontaneously within 6 months.
Conclusion: The λ pattern shows promise as a noninvasive biomarker for stratifying neonatal bradycardia and shows potential to guide recovery timeline prediction. Integration of this approach could optimize neonatal arrhythmia management.

KEYWORDS

AECG, bradycardia, neonate, T-RR scatter plot, escape rhythm

1 Introduction

Bradycardia represents a relatively common arrhythmia in neonates (1). Neonatal bradycardia is diagnosed when the heart rate falls below 100 beats per minute (BPM), with etiologies broadly categorized into two mechanistic pathways: (1) suppression of normal sinus node activity due to autonomic instability (non-cardiac factors), and (2) intrinsic sinus node dysfunction caused by congenital structural anomalies, reversible perinatal insults like hypoxia, severe infection or metabolic disturbances or sinoatrial conduction block (2, 3).

When bradycardia or sinus arrest occurs, the most frequent compensatory mechanism is escape rhythm (ER), a passive arrhythmia originating from the atrioventricular junction, atrium or ventricle to maintain hemodynamic stability (4). In neonates, junctional ER (JER) emerges as the predominant cardiac rhythm disturbance, typically demonstrating a characteristic rate range of 80–120 BPM. This rhythm exhibits electrocardiographic features including narrow QRS complexes (<80 ms duration) with regular RR intervals.

While JER may transiently reflect physiological sinus node immaturity, its persistence often signals underlying pathology requiring clinical vigilance (5).

Conventional 12 lead ECG, limited by brief recording periods (seconds to minutes), frequently fails to capture paroxysmal JER episodes (6). This modality cannot assess circadian rhythm variations or transient sinus node junctional pacemaker transitions. Ambulatory ECG (AECG) monitoring resolves these limitations through extended continuous recording (7, 8). Modern AECG software further enhances diagnostic precision through analytical tools including t-RR scatter plot, RR interval histograms, and heart rate variability analysis (9). The t-RR scatter plots were constructed by plotting RR intervals (the duration between consecutive heartbeats) on the vertical axis against corresponding time points on the horizontal axis, forming a sequential scatter plot representation of cardiac rhythm dynamics (10, 11). The λ pattern, a novel electrophysiological signature observed on t-RR scatter plots, reflects dynamic interactions between sinus node suppression and compensatory escape rhythms.

Our preliminary investigations revealed a distinctive λ shaped signature on t-RR scatter plots in neonates with bradycardia, reflecting dynamic interplay between suppressed sinus node activity and the emergence of dominant escape rhythms from subsidiary pacemakers. In this study, we integrated t-RR plot analysis with reverse-engineering techniques. This approach enables targeted retrieval and quantification of ECG segments that correspond to specific scatter plot regions, particularly characteristic λ patterns. Such integration facilitates rapid and accurate clinical diagnosis. We identified the *λ* pattern in bradycardic neonates, defined by abrupt heart rate reduction (manifested as RR interval prolongation) followed by gradual rhythm normalization (sinus node recovery), as a consistent electrophysiological signature across atrial ER (AER), JER, and ventricular ER (VER) subtypes. Subsequently, we conducted comprehensive analysis of clinical characteristics and prognostic outcomes, establishing predictive value guiding clinical management. By bridging transient arrhythmia phenomena with actionable clinical insights, this work transforms λ pattern analysis from an observational curiosity into an effective diagnostic-prognostic tool in neonatal cardiology.

2 Materials and methods

2.1 Population

This retrospective cohort study analyzed AECG recordings from neonates (≤28 days old) admitted to a tertiary neonatal intensive care unit (NICU) between January 2018 and December 2022. Inclusion criteria comprised: (1) ≥24 h AECG monitoring for suspected bradycardia or sinus arrest, and (2) availability of raw rhythm data for t-RR scatter plot generation. Screening identified 52 eligible neonates, with 16 excluded due to insufficient ECG data ($n = 9$) or monitoring <24 h ($n = 7$), leaving 36 for analysis. AECG recordings were initiated within 48 h of NICU admission. At the time of recording, all neonates were hemodynamically stable (defined as no requirement for vasoactive/inotropic agents). As detailed in Results 3.1, common indications included prematurity-related apnea, suspected infection, and metabolic disorders. No patients received autonomic modulators (e.g., atropine, theophylline) during monitoring. Retrospective consent was obtained via structured telephone interviews with legal guardians using IRB-approved scripts. All participants provided verbal consent documented in medical records, with written confirmation mailed.

2.2 T-RR plot and reverse-engineering

AECG recordings were obtained using Holter monitors (CT-082, Baihui Company Ltd. Hangzhou, China) and t-RR scatter plots were generated using Holter analysis software (version1.2, Baihui Company Ltd. Hangzhou, China), with each point representing an RR interval plotted against time (*x*-axis: elapsed time in hours; *y*-axis: RR interval). Baseline was defined as the mean RR interval during stable, non-bradycardic periods. The *λ* pattern was defined as a triangular cluster of points showing abrupt RR interval prolongation [≥20% above baseline (12)] indicating heart rate deceleration followed by gradual gradual RR interval shortening indicating rhythm recovery [>3 s: based on sinus node recovery time thresholds (13)]. The λ patterns were reverse-engineered to raw ECG segments through this workflow: Upon identifying λ coordinates within t-RR scatter plots using Holter analysis software, synchronized playback functionality automatically extracted corresponding ECG segments containing QRS complexes. Two board-certified electrophysiologists subsequently performed blinded, independent evaluation of these waveform segments using dual-monitor verification. Cardiac rhythm classification was ultimately determined through consensus adjudication applying established electrophysiological criteria.

2.3 Statistical analysis

Statistical analysis was performed using SPSS 26.0. Numerical data were expressed as mean ± SD, and categorical data were expressed as percentages. A *p*-value <0.05 was considered statistically significant.

3 Results

3.1 Cohort characteristic

The cohort comprised 36 neonates (male: 58.3%) with mean gestational age 35.4 ± 3.8 weeks (range: 28–41 weeks) and birth weight 2.8 ± 0.7 kg. Critical comorbidities included: Respiratory support: CPAP ($n = 11$, 30.6%), mechanical ventilation ($n = 5$, 13.9%). Metabolic disturbances: hypoglycemia ($n = 7$, 19.4%), hypocalcemia ($n = 3$, 8.3%). Hemodynamic status: 31 (86.1%)

Abbreviations
T-RR, time-RR interval; ECG, electrocardiogram; ER, escape rhythm; JER, junctional escape rhythm; AECG, ambulatory ECG; BPM, beats per minute.

were asymptomatic; 5 (13.9%) had feeding intolerance. No patients required vasoactive agents.

3.2 Rhythm characterization

The AECG showed that all infants exhibited transient bradycardia, with a mean heart rate of 123 ± 30 BPM and a nadir heart rate of 55 BPM. T-RR scatter plot analysis identified 487 λ patterns (mean 15.5 ± 3.2 per neonate). Reverse-engineering confirmed 391 λ patterns (80.3%) as ERs (predominantly junctional origin) and 96 (19.7%) as transient sinus bradycardia (Figure 1).

3.3 Clinical outcome

Among 36 neonates with confirmed bradycardia, 8 cases (22.2%) exhibited I to II degree atrioventricular block or prolongation of the QT interval (I degree: 3, II degree: 2, prolonged QT interval: 3), all resolving spontaneously within 6 months post-discharge (median recovery time 98 days). We constructed a scatter plot with λ pattern counts as the *x*-axis (using the maximum count from multiple Holter recordings when applicable) and recovery duration as the *y*-axis. The analysis revealed a significant positive correlation (Figure 2).

Following tertile-based stratification of neonates into λ-pattern burden groups [low (≤10 episodes/24 h), moderate (10–20 episodes/24 h), and high (≥21 episodes/24 h)], Kaplan–Meier analysis demonstrated a significant association between λ-pattern burden and delayed rhythm normalization (log-rank $\chi^2 = 22.39$, $p < 0.0001$). Neonates in the high-burden group (≥21 episodes/24 h) showed a 4.22-fold increased risk of delayed recovery compared to those in the low-burden group (≤10 episodes/24 h; Figure 3). Median recovery time differed substantially between groups: 62 days (IQR 45–78) in the low-burden cohort vs. 121 days (IQR 89–152) in the high-burden cohort.

4 Discussion

Neonatal bradycardia, defined as a heart rate <100 bpm, primarily stems from autonomic nervous system immaturity

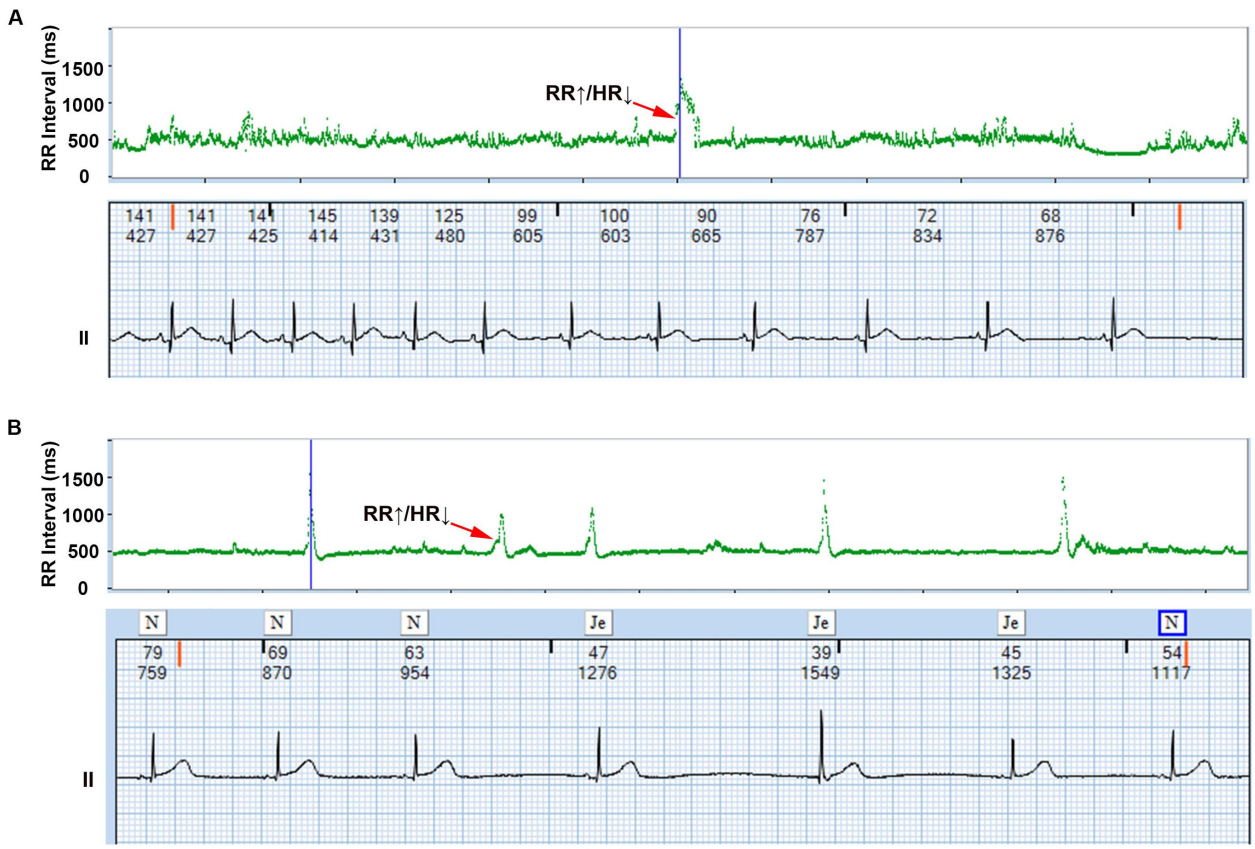

FIGURE 1
λ pattern of neonatal bradycardia. The upper section displays the λ pattern on the T-RR scatter plot, while the lower section shows the detailed electrocardiogram corresponding to the λ pattern obtained through reverse-engineering technology, and the numbers above the ECG represent the instantaneous heart rate and the RR interval, respectively. Representative examples of λ patterns from study cohort: **(A)** Transient sinus bradycardia (Patient #12); **(B)** Junctional escape rhythm (Patient #27). ↑RR interval = ↓Heart rate (Bradycardia), ↓RR interval = ↑Heart rate (Recovery).

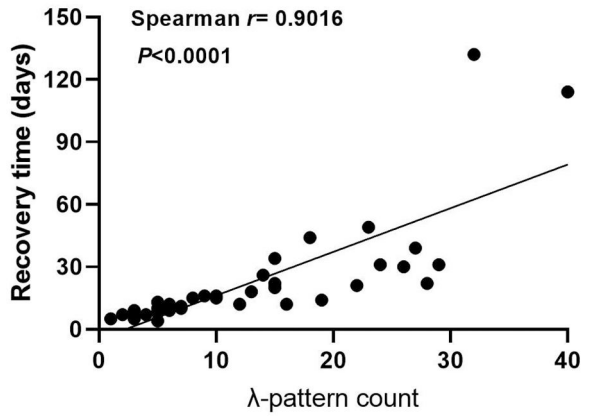

FIGURE 2
Association between λ pattern counts and rhythm normalization time. Each point represents an individual patient.

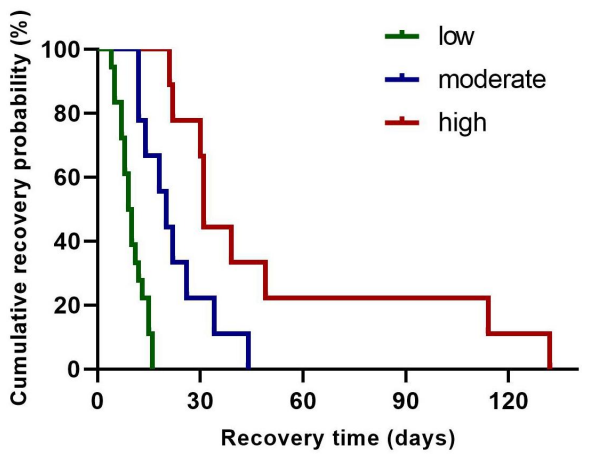

FIGURE 3
Kaplan–Meier survival analysis of rhythm normalization time across λ pattern groups. The survival curve represents the probability of patients remaining in arrhythmia over time. Groups are stratified by λ pattern: low (green line), moderate (blue line), and high (red line).

during the perinatal period (2, 14). Characterized by heightened vagal tone, this condition manifests through clinically observable triggers including apneic episodes, feeding, and defecation (15). While most instances exhibit benign self-limiting behavior, recurrent bradycardic events warrant thorough investigation for potential systemic stressors such as infection, sepsis or hypoxic-ischemic injury (5, 16). ERs act as critical physiological safeguards against severe bradyarrhythmias (17). Our study introduces λ-wave morphology, derived from T-RR scatter plot analysis, as both a diagnostic biomarker and dynamic tracker of sinus node dysfunction. This triphasic electrophysiological signature enables real-time assessment of sinus node recovery capacity.

The λ pattern demonstrates a distinctive biphasic morphology characterized by a sharp heart rate deceleration phase followed by gradual acceleration. This pattern physiologically reflects the dynamic interaction between primary and subsidiary cardiac pacemakers. Reverse ECG mapping analysis confirms that this pattern signifies either escape rhythms or transient sinus bradycardia, with the initial acceleration phase corresponding to either the emergence of ERs (atrial, junctional, or ventricular) during sinus node dysfunction or transient sinus bradycardia triggered by autonomic fluctuations. The subsequent deceleration phase marks sinus node functional recovery through overdrive suppression of ectopic foci, a process dynamically regulated by autonomic balance (18). This mechanistic framework aligns with established electrophysiological principles while introducing a novel noninvasive diagnostic parameter—the λ pattern. The integration of λ pattern kinetics with ECG reverse-mapping technology enables rapid, intuitive bradycardia identification, representing a paradigm shift in neonatal cardiac monitoring. Clinically, this advancement may improve prediction accuracy for pacemaker requirements while reducing unnecessary interventions in transient autonomic dysfunction cases.

Furthermore, our retrospective cohort analysis revealed a correlation between λ pattern burden and both arrhythmia severity ($p < 0.01$) and recovery duration ($p = 0.003$), potentially positioning it as a potential prognostic biomarker. Quantitative assessment of λ pattern dynamics may provide an innovative clinical framework for predicting recovery trajectories, bridging critical diagnostic gaps in detecting evolving conduction abnormalities, inflammatory cascades, and autonomic instability. This methodology could enhance diagnostic precision and conservative management efficacy in neonates, enabling personalized arrhythmia management strategies that optimize both therapeutic precision and healthcare resource allocation.

This retrospective observational study has several limitations. Given the moderate sample size ($n = 36$), our findings require validation in larger cohorts. While λ-pattern burden suggests prognostic utility, clinical applications should be cautious pending multicenter confirmation. The design inherently prevents establishing causal relationships between λ pattern characteristics and clinical outcomes, while the ≥24 h AECG monitoring inclusion criterion introduces selection bias by potentially excluding mild/asymptomatic cases. Single-center enrollment limits generalizability to broader populations, and methodological constraints include semi-automated λ pattern identification with inherent subjectivity, compounded by incomplete therapeutic documentation that hindered precise physiology treatment correlation. Universal standardized care in our cohort precluded assessment of λ specific therapeutic effects, and the moderate sample size requires external validation in larger cohorts. These limitations highlight the need for prospective multicenter studies employing protocolized monitoring and detailed therapeutic records to verify clinical applications.

Data availability statement

The original contributions presented in the study are included in the article/Supplementary Material, further inquiries can be directed to the corresponding author.

Ethics statement

The studies involving humans were approved by Institutional Review Board of Maternal and Child Health Hospital of Hubei Province. The studies were conducted in accordance with the local legislation and institutional requirements. Written informed consent was obtained from the participants' legal guardians/next of kin, for the publication of any potentially identifiable images or data included in this article.

Author contributions

HL: Data curation, Methodology, Investigation, Writing – review & editing, Formal analysis. XW: Writing – review & editing, Software, Investigation, Supervision. FZhu: Formal analysis, Writing – review & editing, Writing – original draft, Investigation, Validation. FZhe: Data curation, Methodology, Writing – review & editing, Writing – original draft, Visualization. TY: Investigation, Writing – review & editing, Conceptualization, Writing – original draft, Data curation.

Funding

The author(s) declare that no financial support was received for the research and/or publication of this article.

Acknowledgments

We extend our appreciation to all participating families for entrusting us with their children's care and contributing to advancements in pediatric pharmacovigilance. We thank Baihui Company Ltd. for providing technical assistance with the Holter analysis software.

Conflict of interest

The authors declare that the research was conducted in the absence of any commercial or financial relationships that could be construed as a potential conflict of interest.

Generative AI statement

The author(s) declare that no Generative AI was used in the creation of this manuscript.

Any alternative text (alt text) provided alongside figures in this article has been generated by Frontiers with the support of artificial intelligence and reasonable efforts have been made to ensure accuracy, including review by the authors wherever possible. If you identify any issues, please contact us.

Publisher's note

References

1. Drago F, Battipaglia I, Di Mambro C. Neonatal and pediatric arrhythmias: clinical and electrocardiographic aspects. *Card Electrophysiol Clin*. (2018) 10:397–412. doi: 10.1016/j.ccep.2018.02.008

2. Dorostkar PC, Arko MK, Baird TM, Rodriguez S, Martin RJ. Asystole and severe bradycardia in preterm infants. *Biol Neonate*. (2005) 88:299–305. doi: 10.1159/000087627

3. Patural H, Flori S, Pichot V, Barthelemy J-C, Roche F. Autonomic regulation and bradycardia during the neonatal period. *Arch Pediatr Organe*. (2014) 21:226–30. doi: 10.1016/j.arcped.2013.10.001

4. Hafeez Y, Grossman SA. *Junctional Rhythm*. Treasure Island, FL: StatPearls Publishing (2025). Available online at: http://www.ncbi.nlm.nih.gov/books/NBK507715/ (Accessed March 31, 2025)

5. Baruteau A-E, Perry JC, Sanatani S, Horie M, Dubin AM. Evaluation and management of bradycardia in neonates and children. *Eur J Pediatr*. (2016) 175:151–61. doi: 10.1007/s00431-015-2689-z

6. Su L, Borov S, Zrenner B. 12-lead Holter electrocardiography. Review of the literature and clinical application update. *Herzschrittmacherther Elektrophysiol*. (2013) 24:92–6. doi: 10.1007/s00399-013-0268-4

7. Kusumoto FM, Schoenfeld MH, Barrett C, Edgerton JR, Ellenbogen KA, Gold MR, et al. 2018 ACC/AHA/HRS guideline on the evaluation and management of patients with bradycardia and cardiac conduction delay: a report of the American College of Cardiology/American Heart Association task force on clinical practice guidelines and the heart rhythm society. *Circ Am Heart Assoc*. (2019) 140(8): e382–482. doi: 10.1161/CIR.0000000000000628

8. Israel CW, Tribunyan S. Holter monitoring. *Herzschrittmacherther Elektrophysiol*. (2024) 35:234–49. doi: 10.1007/s00399-024-01036-8

9. Steinberg JS, Varma N, Cygankiewicz I, Aziz P, Balsam P, Baranchuk A, et al. 2017 ISHNE-HRS expert consensus statement on ambulatory ECG and external cardiac monitoring/telemetry. *Ann Noninvasive Electrocardiol*. (2017) 22(3):e12447. doi: 10.1111/anec.12447

10. Thuraisingham RA. Preprocessing RR interval time series for heart rate variability analysis and estimates of standard deviation of RR intervals. *Comput Methods Programs Biomed*. (2006) 83:78–82. doi: 10.1016/j.cmpb.2006.05.002

11. Xiang J-T. Timed RR-interval scatter plots and reverse technology. *Curr Med Sci*. (2020) 40:1191–202. doi: 10.1007/s11596-020-2308-8

12. Fleming S, Thompson M, Stevens R, Heneghan C, Plüddemann A, Maconochie I, et al. Normal ranges of heart rate and respiratory rate in children from birth to 18 years of age: a systematic review of observational studies. *Lancet Lond Engl*. (2011) 377(9770):1011–8. doi: 10.1016/S0140-6736(10)62226-X

13. Narula OS, Samet P, Javier RP. Significance of the sinus-node recovery time. *Circulation*. (1972) 45:140–58. doi: 10.1161/01.cir.45.1.140

14. Miller MS, Shannon KM, Wetzel GT. Neonatal bradycardia. *Prog Pediatr Cardiol*. (2000) 11:19–24. doi: 10.1016/s1058-9813(00)00032-1

15. McLachlan CS, Ocsan R, Spence I, Hambly B, Matthews S, Wang L-X, et al. Increased total heart rate variability and enhanced cardiac vagal autonomic activity in healthy humans with sinus bradycardia. *Proc Bayl Univ Med Cent*. (2010) 23:368–70. doi: 10.1080/08998280.2010.11928655

16. Shah MJ, Silka MJ, Avari Silva JN, Balaji S, Beach CM, Benjamin MN, et al. 2021 PACES expert consensus statement on the indications and management of cardiovascular implantable electronic devices in pediatric patients. *Indian Pacing Electrophysiol J*. (2021) 21(6):367–93. doi: 10.1016/j.ipej.2021.07.005

17. Kleinfeld MJ, Boal BH. Junctional escape rhythm in the sick sinus syndrome. *Cardiology*. (1978) 63:193–8. doi: 10.1159/000169897

18. Jordan D. Vagal control of the heart: central serotonergic (5-HT) mechanisms. *Exp Physiol*. (2005) 90:175–81. doi: 10.1113/expphysiol.2004.029058

frontiers | Frontiers in Physiology

TYPE Original Research
PUBLISHED 08 October 2025
DOI 10.3389/fphys.2025.1644520

OPEN ACCESS

EDITED BY
Pasquale Vergara,
University of Naples Federico II, Italy

REVIEWED BY
Qiang Li,
Xiamen University, China
Jing Zheng,
Quzhou City People's Hospital, China
David Zizek,
University Medical Centre Ljubljana, Slovenia

*CORRESPONDENCE
Alphonsus Liew,
alphonsus.liew@kcl.ac.uk

RECEIVED 10 June 2025
ACCEPTED 03 September 2025
PUBLISHED 08 October 2025

CITATION
Liew A, Strocchi M, Rodero C, Gillette KK, Wijesuriya N, Howell S, de Vere F, Vigmond EJ, Plank G, Niederer S and Rinaldi CA (2025) Comparing the effects of left bundle branch pacing and leadless right ventricular pacing on intraventricular and interventricular dyssynchrony using *in silico* modelling. *Front. Physiol.* 16:1644520. doi: 10.3389/fphys.2025.1644520

Comparing the effects of left bundle branch pacing and leadless right ventricular pacing on intraventricular and interventricular dyssynchrony using *in silico* modelling

Alphonsus Liew[1,2]*, Marina Strocchi[3], Cristobal Rodero[3], Karli K. Gillette[4,5,6], Nadeev Wijesuriya[1,2], Sandra Howell[1,2], Felicity de Vere[1,2], Edward J. Vigmond[7,8], Gernot Plank[4,9], Steven Niederer[3,10] and Christopher Aldo Rinaldi[1,2]

[1]School of Biomedical Engineering and Imaging Sciences, King's College London, London, United Kingdom, [2]Department of Cardiology, Guy's and St Thomas' NHS Foundation Trust, London, United Kingdom, [3]National Heart and Lung Institute, Imperial College London, London, United Kingdom, [4]Medical University of Graz, Graz, Austria, [5]Department of Biomedical Engineering, University of Utah, Salt Lake City, UT, United States, [6]Scientific Computing and Imaging Institute, University of Utah, Salt Lake City, UT, United States, [7]University of Bordeaux,Centre National de la Recherche Scientifique, Bordeaux, France, [8]IHU Liryc, Bordeaux, France, [9]BioTechMed-Graz, Graz, Austria, [10]The Alan Turing Institute, London, United Kingdom

Introduction: Non-physiological right ventricular pacing (RVP) is currently the mainstay of treatment for patients with high-degree atrioventricular (AV) block who have preserved left ventricular ejection fraction. Newer pacing strategies, such as left bundle branch pacing (LBBP) and leadless cardiac pacemakers (LCPMs), are increasingly being adopted due to their respective advantages over RVP. However, there has been no direct comparison between LCPMs and LBBP regarding their risk of pacing-induced cardiomyopathy, which is thought to arise from interventricular and intraventricular dyssynchrony. Using *in silico* modelling, we compared the effects of LBBP and LCPMs on interventricular and intraventricular synchrony.

Methods: Using 19 four-chamber healthy heart geometries, we simulated LCPMs at the level of the right ventricular outflow tract-septum (RVOT-S), mid-septum (MS), and apical septum (AS), along with proximal left bundle pacing (PLBBP) and distal left bundle pacing (DLBBP) in 3 different settings: 1) intact left bundle branch conduction, 2) left bundle branch block (LBBB), and 3) septal scar involving the His-Purkinje system (HPS). Ventricular electrical uncoupling (VEU), absolute VEU, and left ventricular dyssynchrony index (LVDI) were measured. The shortest interval required to activate 90% of both ventricles (BIVAT-90) was also recorded.

Results: In the setting of intact left bundle branch conduction, combined LBBP configurations had significantly lower VEU (LBBP: −3.3 ± 5.1 vs. LCPM: 24.2 ± 7.6 ms, $p < 0.01$) and absolute VEU (LBBP: 5.0 ± 3.5 vs. LCPM: 24.2 ± 7.6 ms, $p < 0.01$) than combined LCPM configurations. In the presence of proximal LBBB, combined LBBP configurations also had significantly lower VEU (LBBP

−22.1 ± 0.5 vs. LCPM 25.9 ± 7.9, $p < 0.01$) and absolute VEU (LBBP 22.1 ± 0.5 vs. LCPM 25.9 ± 7.9 ms, $p < 0.01$) than combined LCPM configurations. However, there was no significant difference in absolute VEU when combined LBBP configurations was compared with RVOT-S configuration alone (LBBP 22.1 ± 0.5 vs. RVOT-S 21.7 ± 9.0 ms, $p = 0.86$). In the presence of septal scar, combined LCPM configurations had significantly lower VEU compared with combined LBBP configurations (VEU: LCPM 31.0 ± 8.4 vs. LBBP 41.7 ± 20.2 ms, respectively; $p < 0.01$). Combined LBBP configurations had significantly lower LVDI and BIVAT-90 compared with combined LCPM configurations in both the presence and absence of LBBB, but there was no significant difference between the two in the setting of a septal scar.

Conclusion: LCPM produces less interventricular dyssynchrony than LBBP in the presence of extensive septal scarring involving the HPS. In the setting of proximal LBBB, LCPM at the RVOT-S level may be non-inferior to LBBP in terms of interventricular dyssynchrony.

KEYWORDS

left bundle branch pacing, leadless right ventricular pacing, intraventricular dyssynchrony, interventricular dyssynchrony, *in silico* modelling

1 Introduction

Non-physiological right ventricular pacing (RVP) is currently the mainstay treatment for high-degree atrioventricular (AV) block. However, RVP is associated with the increased risk of pacing-induced cardiomyopathy, tricuspid regurgitation progression, and right ventricular dysfunction (Höke et al., 2014; Kanawati et al., 2021; Riesenhuber et al., 2021; Tatum et al., 2021; Chung et al., 2023; Boyle et al., 2024). In recent years, alternative forms of ventricular pacing, including left bundle branch pacing (LBBP) and leadless right ventricular pacing (LCPM), have been increasingly adopted due to their respective advantages over RVP. LBBP provides more physiological activation of the ventricles by engaging the His-Purkinje system (HPS), whereas LCPMs have been associated with significantly reduced progression of tricuspid regurgitation compared with RVP (Salaun et al., 2018; Garweg et al., 2023; El-Chami et al., 2024).

Both European and American guidelines recommend the use of cardiac resynchronisation therapy (CRT) in patients with an indication for ventricular pacing and impaired LV ejection fraction (LVEF) (Glikson et al., 2021; Chung et al., 2023). The European guidelines use a lower LVEF cut-off of <40% (Class I, Level A recommendation), whereas the American guidelines use a cut-off of <50% (2a, B-NR recommendation). However, in patients with preserved LVEF (i.e., >50%), the benefit of CRT is less clear, even in those with anticipated high ventricular pacing burden (Funck et al., 2025). LBBP prevents pacing-induced cardiomyopathy in those with preserved LVEF at baseline and preserves right ventricular function, but current available evidence points towards an increased risk of tricuspid regurgitation progression with LBBP (Chung et al., 2023; Hu et al., 2023; Li et al., 2023; Tian et al., 2023; Bednarek et al., 2024). In contrast, studies, including the 5-year Micra registry and a meta-analysis, have found that LCPM is associated with a significantly lower risk of tricuspid regurgitation (TR) progression (Salaun et al., 2018; Garweg et al., 2023; El-Chami et al., 2024; Yuyun et al., 2024). It is important to note, however, that septal positioning of LCPMs may exacerbate TR due to interaction with the tricuspid valve (Beurskens et al., 2019; Hai et al., 2021). Furthermore, LCPM eliminates the risk of pocket- and lead-related issues, including infection, lead fracture, pneumothorax, and haematoma (Salaun et al., 2018; Garweg et al., 2023). Moreover, LCPM appears to have significantly lower rates of pacing-induced cardiomyopathy when placed in a high septal position compared to RVP (0.3%–4% vs. 10%–25%, respectively). This makes LCPM an attractive alternative in patients with AV block requiring pacing and preserved LVEF. However, the comparison between LCPM and LBBP in terms of pacing-induced dyssynchrony, which may lead to pacing-induced cardiomyopathy (Tops et al., 2007; Pastore et al., 2008; Fang et al., 2016; Bansal et al., 2019), remains poorly understood.

1.1 Role and clinical relevance of *in silico* modelling

The role of *in silico* modelling has expanded rapidly over the past few decades. In silico modelling allows hypotheses to be tested noninvasively in the first instance, thereby informing and providing justification for *in vivo* studies and maximising the likelihood of detecting relevant outcomes. Patients with a pacing indication exhibit heterogeneous responses to pacing, influenced by individual and anatomical differences. In addition, septal scarring affects the feasibility and efficacy of LBBP, but the extent of septal scarring is highly variable among individuals. In silico modelling enables direct comparison of LBBP and LCPM under identical conditions, such as in the presence of extensive septal scarring and proximal LBBB, ensuring that any observed differences can be solely attributable to the pacing strategy.

In this study, we aim to compare the effects of LBBP and LCPM on interventricular and intraventricular dyssynchrony in the setting of complete AV block and preserved LVEF using *in silico* modelling.

2 Methods

2.1 *In silico* modelling

To perform our electrophysiology simulations, we used 19 publicly available four-chamber heart geometries from healthy subjects, obtained from a previous study (Rodero et al., 2021). The heart meshes were composed of linear tetrahedral elements with an average resolution of approximately 1 mm. A His-Purkinje network was added to each heart geometry based on previous studies (Gillette et al., 2021; 2022; Pathmanathan et al., 2024), as described in the Supplementary Material. The His-Purkinje network included three LV (anterior, septal, and posterior) and two RV (septal and moderator band) fascicles that were used to initiate the activation of the ventricular myocardium during sinus rhythm. Ventricular activation was computed using a reaction–Eikonal model with the Cardiac Arrhythmia Research Package (CARP) (Vigmond et al., 2002; Neic et al., 2017). The His-Purkinje network was assigned a conduction velocity (CV) of 3 m/s, while the ventricular myocardium was modelled as a transversely isotropic conduction medium, with a CV of 0.6 m/s along the fibres and 0.24 m/s in the transverse direction, in accordance with normal CV ranges measured in mammals (Draper and Mya-Tu, 1959). Proximal LBBB was simulated by cutting the connection of the left bundle to the LV His-Purkinje system along the His. In the Supplementary Material, we outline the fascicles for each of the patient-specific geometries. We also demonstrate that the sinus rhythm activation simulated by the model is physiological, aligns with the Durrer maps (Durrer et al., 1970) and that the resulting activation metrics are within the ranges reported in the literature. Finally, we demonstrate that the simulated activation during LBBB leads to prolonged activation times and delayed LV activation, in line with data from the published literature (Neic et al., 2017).

2.2 Pacing simulations

Using the *in silico* model, we simulated ventricular activation during sinus rhythm under the conditions of intranodal block with junctional escape rhythm (AV node blocked but intact His bundle), LBBP in two configurations (Figure 1B)—proximal left bundle pacing (PLBBP) and distal left bundle pacing (DLBBP)—and LCPM in three configurations (Figure 1A): at the level of the RVOT-septum (RVOT-S), mid-septum (MS), and apical septum (AS). We considered three different baseline rhythm scenarios: 1) intact left bundle branch conduction, 2) left bundle branch block (LBBB) and 3) septal scar involving the HPS. Complete AV block at the level of the AV node was simulated in all pacing settings, such that the intrinsic rhythm did not contribute to ventricular activation.

2.3 Septal scar mapping

To simulate septal scarring, we integrated a patient-specific scar and border zone geometry from a publicly available 1 mm resolution LV patient-specific mesh into our 19 heart geometries using the universal ventricular coordinates (UVCs) (Bayer et al., 2018; Mendonca Costa et al., 2019). The septal scar was mapped to the meshes in our cohort (as shown in the Supplementary Material), and the scar core was simulated as non-conducting tissue. The Purkinje fibres overlapping the scar tissue were identified and assumed to be non-conducting, under the assumption that scarred Purkinje is affected by tissue hypoxia the same way as normal myocardium (Mendonca Costa et al., 2019).

2.4 Measures of intraventricular and interventricular dyssynchrony

To assess interventricular dyssynchrony, we computed ventricular electrical uncoupling (VEU) and absolute VEU. VEU was calculated as the difference between the mean LV and RV epicardial activation times (i.e., mean LV epicardial activation time–mean RV epicardial activation time) and indicates the directionality of dyssynchrony (a positive value indicates that LV takes longer to activate than RV, and a negative value indicates that RV takes longer to activate than LV). Absolute VEU values were also defined to reflect the degree of dyssynchrony between the LV and RV, irrespective of directionality. Left ventricular dyssynchrony index (LVDI) was used to represent LV intraventricular dyssynchrony and calculated as the standard deviation of activation times within the LV. The shortest interval taken to activate 90% of both ventricles (BIVAT-90) was used to reflect biventricular activation time. When computing response to pacing, the areas around the AV valves and outflow tracts were excluded.

2.5 Statistical analysis

Means and standard deviations were used to summarise and present continuous variables. The Shapiro–Wilk test was used to test for normality of continuous data. Two-tailed Student's t-tests were used to compare two continuous variables with a normal distribution. The Wilcoxon rank–sum test was used to compare two continuous variables with a non-parametric distribution. A p-value of <0.05 was considered significant for all tests. All statistical analyses were performed using STATA 18.0 (StataCorp. 2019. *Stata Statistical Software: Release 18*. College Station, TX: StataCorp LLC).

3 Results

Measures including VEU, absolute VEU, LVDI, and BIVAT-90 of each pacing configuration in all three settings (intact left bundle conduction, LBBB, and septal scar affecting the HPS) are summarised in Table 1.

3.1 Biventricular activation times

In the presence of normal left bundle conduction, combined LBBP configurations (PLBBP and DLBBP) produced lower BIVAT-90 than combined LCPM configurations (RVOT-S, MS, and AS) (42.8 ± 3.8 vs. 71.9 ± 8.2 ms, respectively; $p < 0.01$) (Figure 2A). In the presence of LBBB, combined LBBP configurations produced higher BIVAT-90 values but remained significantly lower than

10.3389/fphys.2025.1644520

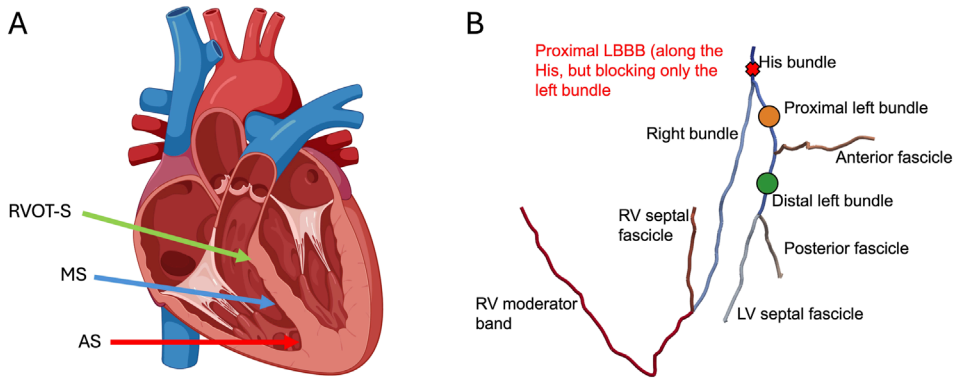

FIGURE 1
(A) Leadless cardiac pacing (LCPM) locations: right ventricular outflow tract-septum (RVOT-S) denoted by the green arrow, mid-septum (MS) denoted by the blue arrow, and apical septum (AS) denoted by the red arrow. **(B)** Simulated pacing locations of LBBP and proximal LBBB. Left bundle branch pacing was performed along the proximal left bundle (orange dot) and distal left bundle (green dot). Where present, LBBB was simulated at the level of the His, affecting only the left bundle (red cross).

TABLE 1 VEU, absolute VEU, LVDI, and BIVAT-90 values in response to each pacing configuration in three different settings (intact left bundle conduction, LBBB, and septal scar); (*) *p*-value comparing combined LBBP and combined LCPM configurations; and (**) *p*-value comparing RVOT-S vs. combined LBBP configurations.

	Baseline	PLBBP	DLBBP	RVOT-S	MS	AS	Combined LBBP	Combined LCPM	*p*-value*	*p*-value**
Intact left bundle conduction										
VEU	6.8 ± 4.6	−0.4 ± 4.5	−6.1 ± 4.1	21.7 ± 9.0	25.7 ± 7.5	25.2 ± 5.7	−3.3 ± 5.1	24.2 ± 7.6	<0.01	<0.01
Absolute VEU	6.9 ± 4.6	3.6 ± 2.5	6.3 ± 3.9	21.7 ± 9.0	25.7 ± 7.5	25.2 ± 5.7	5.0 ± 3.5	24.2 ± 7.6	<0.01	<0.01
LVDI	12.0 ± 1.6	12.0 ± 1.5	12.3 ± 1.6	22.1 ± 2.1	23.0 ± 2.9	24.1 ± 2.0	12.1 ± 1.6	23.0 ± 2.5	<0.01	<0.01
BIVAT-90	38.2 ± 4.3	40.9 ± 3.5	44.7 ± 3.0	70.1 ± 7.3	70.7 ± 9.4	74.9 ± 7.2	42.8 ± 3.8	71.9 ± 8.2	<0.01	<0.01
LBBB										
VEU	47.2 ± 5.6	−22.6 ± 3.2	−21.6 ± 3.3	21.7 ± 9.0	30.8 ± 6.0	25.2 ± 5.7	−22.1 ± 0.5	25.9 ± 7.9	<0.01	<0.01
Absolute VEU	47.2 ± 5.6	22.6 ± 3.2	21.6 ± 3.3	21.7 ± 9.0	30.8 ± 6.0	25.2 ± 5.7	22.1 ± 0.5	25.9 ± 7.9	<0.01	0.86
LVDI	24.4 ± 2.8	12.2 ± 1.6	12.4 ± 1.7	22.1 ± 0.1	23.1 ± 2.9	24.0 ± 2.0	12.3 ± 0.3	23.0 ± 0.3	<0.01	<0.01
BIVAT-90	78.9 ± 9.0	62.7 ± 5.6	62.0 ± 5.6	70.1 ± 7.3	70.7 ± 9.5	74.9 ± 7.2	62.3 ± 0.90	71.9 ± 1.1	<0.01	<0.01
Septal scar with non-conducting HPS										
VEU	44.1 ± 16.7	42.3 ± 19.5	41.0 ± 21.4	24.8 ± 9.0	35.7 ± 5.6	32.7 ± 6.4	41.7 ± 20.2	31.0 ± 8.4	<0.01	<0.01
Absolute VEU	44.1 ± 16.7	42.3 ± 19.5	41.0 ± 21.4	24.8 ± 9.0	35.7 ± 5.6	32.7 ± 6.4	41.7 ± 20.2	31.0 ± 8.4	<0.01	<0.01
LVDI	25.4 ± 6.6	25.4 ± 6.6	25.5 ± 6.5	24.5 ± 2.2	29.1 ± 2.4	27.9 ± 2.4	25.5 ± 6.5	27.2 ± 3.0	0.93	0.08
BIVAT-90	80.5 ± 22.1	80.2 ± 22.6	80.5 ± 22.2	75.7 ± 7.3	88.9 ± 7.9	87.5 ± 7.9	80.3 ± 22.1	84.0 ± 9.6	0.47	0.052

Abbreviations: LBBB, left bundle branch block; DLBBP, left bundle branch pacing at the level of left posterior fascicle; PLBBP, left bundle branch pacing at the level of the proximal left bundle; RVOT-S, right ventricular outflow tract-septal pacing; MS, mid-septal pacing; AS, apical-septal pacing; VEU, ventricular electrical uncoupling; LVDI, left ventricular dyssynchrony index; BIVAT-90, time taken to activate 90% of both ventricles.

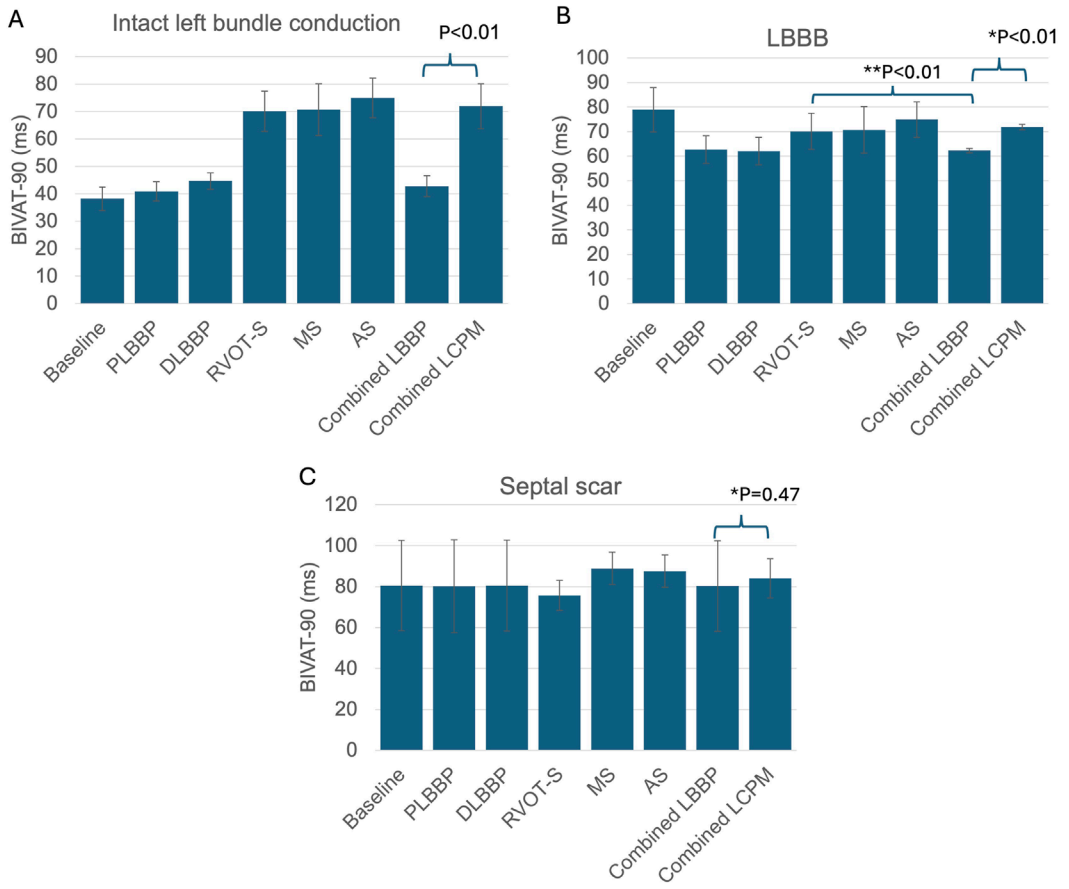

FIGURE 2
BIVAT-90 values in different settings: **(A)** intact left bundle conduction, **(B)** proximal left bundle branch block, and **(C)** septal scar affecting the HPS. (*) Comparison between combined LBBP and combined LCPM configurations; (**) comparison between RVOT-S and mean LBBP. PLBBP, proximal left bundle branch pacing; DLBBP, distal left bundle branch pacing; AS, leadless pacing at the apical septum level; MS, leadless pacing at the mid-septum level; RVOT-S, leadless pacing at the right ventricular outflow tract-septum level.

those of combined LCPM configurations (62.3 ± 0.9 vs. 71.9 ± 1.1 ms, respectively; $p < 0.01$) (Figure 2B). In the presence of a septal scar involving the HPS, there was no significant difference in BIVAT-90 between combined LBBP and combined LCPM configurations (80.3 ± 22.1 vs. 84.0 ± 9.6 ms, respectively; $p = 0.47$) (Figure 2C).

3.2 Interventricular dyssynchrony

In the presence of intact left bundle conduction, combined LBBP configurations had significantly lower VEU (−3.3 ± 5.1 vs. 24.2 ± 7.6 ms, respectively; $p < 0.01$) and absolute VEU (5.0 ± 3.5 vs. 24.2 ± 7.6 ms, respectively; $p < 0.01$) than those of combined LCPM configurations (Figure 3A). Similarly, in the presence of LBBB, combined LBBP configurations produced significantly lower absolute VEU (LBBP 22.1 ± 0.5 ms vs. LCPM 25.9 ± 7.9 ms; $p < 0.01$) than combined LCPM configurations (Figure 3B). However, when combined LBBP configurations were compared to RVOT-S alone, there was no significant difference in absolute VEU (RVOT-S 21.7 ± 9.0 vs. combined LBBP 22.1 ± 0.5 ms; $p = 0.86$). Conversely, in the setting of a non-conducting septal scar, combined LCPM configurations produced significantly lower VEU and absolute VEU than those of combined LBBP configurations (both VEU and absolute VEU: combined LCPM 31.0 ± 8.4 vs. combined LBBP 41.7 ± 20.2 ms; $p < 0.01$) (Figure 3C). Notably, in 6 of the 19 heart models, a proportion of Purkinje fibres supplied by the left anterior fascicle remained conductive as they were located beyond the area of scar tissue (Figure 4A). In these models, LBBP produced significantly lower VEU than the RVOT-S (combined LBBP 13.3 ± 4.9 vs. combined LCPM 31.0 ± 8.4 ms; $P < 0.01$). In the remaining 13 out of 19 heart models, both the anterior and posterior fascicles were within the non-conducting scar zone, with no activation of the Purkinje network (Figure 4B). This resulted in combined LCPM configurations producing less interventricular dyssynchrony than LBBP configurations (combined LCPM 31.3 ± 8.4 vs. combined LBBP 54.7 ± 5.4 ms; $p < 0.01$).

3.3 Intraventricular dyssynchrony

In the presence of intact left bundle conduction, combined LBBP configurations produced significantly lower LVDI than that of combined LCPM configurations (12.1 ± 1.6 vs. 23.0 ± 2.5 ms,

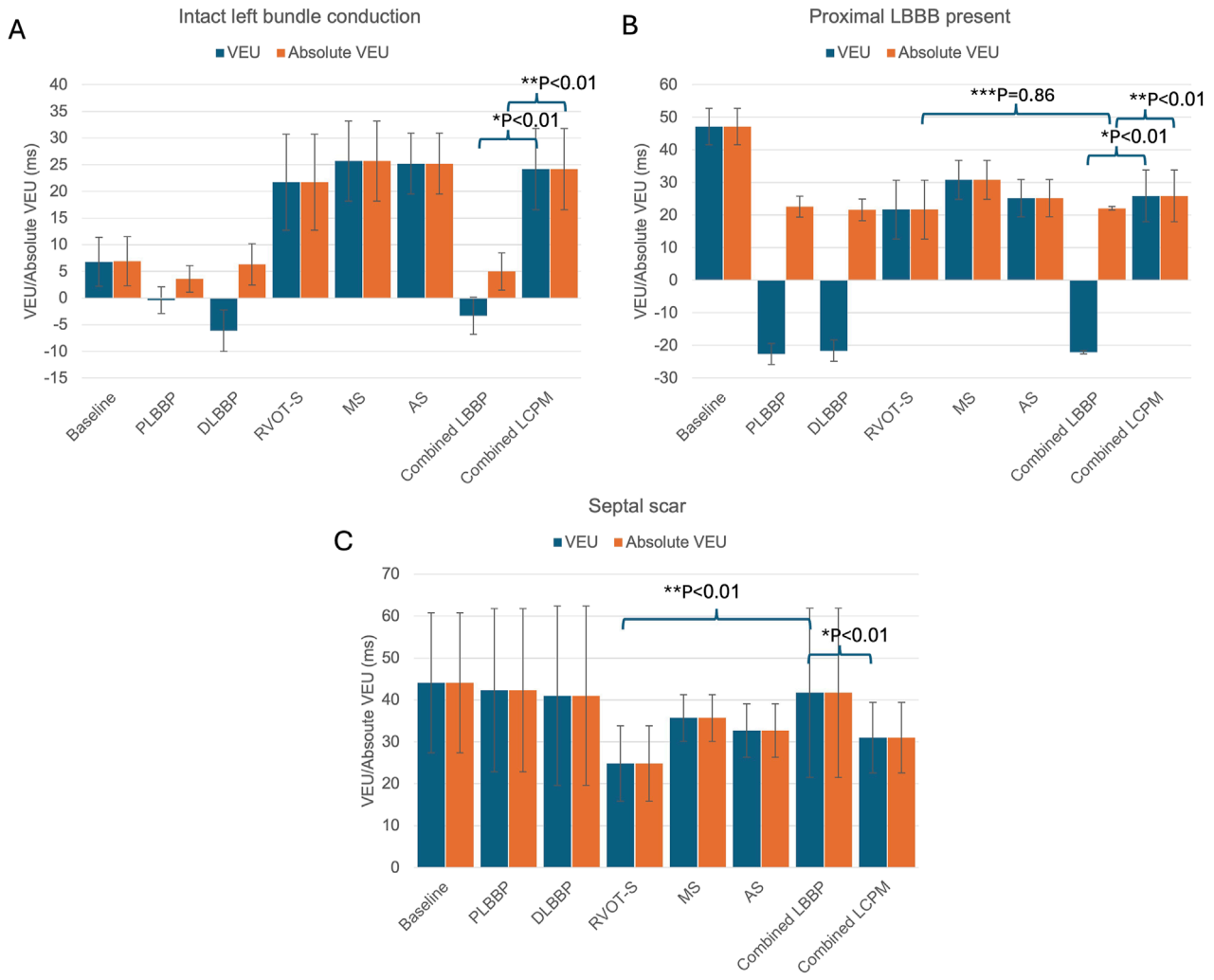

FIGURE 3
VEU values in different settings: **(A)** intact left bundle conduction, **(B)** proximal left bundle branch block, **(C)** and septal scar affecting the HPS. (*) Comparison of VEU between mean LBBP and mean LCPM, (**) comparison of absolute VEU between mean LBBP and mean LCPM, and (***) comparison of VEU between RVOT-S and mean LBBP. Blue charts denote VEU, and orange charts denote absolute VEU. PLBBP, proximal left bundle branch pacing; DLBBP, distal left bundle branch pacing; AS, leadless pacing at the apical septum level; MS, leadless pacing at the mid-septum level; RVOT-S, leadless pacing at the right ventricular outflow tract-septum level.

respectively; $p < 0.01$) (Figure 5A). Similarly, in the context of LBBB, LBBP configurations had significantly lower LVDI than LCPM configurations (12.3 ± 1.6 vs. 23.0 ± 2.5 ms, respectively; $p < 0.01$, Figure 5B). However, in the setting of a septal scar, combined LBBP configurations produced similar LVDI to combined LCPM configurations (25.5 ± 6.5 vs. 27.2 ± 3.0 ms, respectively; $p = 0.93$) (Figure 5C).

4 Discussion

4.1 Intraventricular dyssynchrony

LBBP produced improved intraventricular synchrony in the presence and absence of LBBB, but this effect on intraventricular synchrony was attenuated in the setting of a non-conducting septal scar. In the presence of a septal scar affecting the HPS, rapid conduction *via* the specialised cells of the Purkinje network is no longer feasible, resulting in slower conduction through the ventricular myocardium, which has a considerably lower inherent conduction velocity, and, consequently, markedly heterogeneous and prolonged LV activation times. This is consistent with the *in vivo* findings of Elliott et al. (2023), who reported that the presence of a septal scar is associated with an attenuation of LBBP's beneficial effects on intraventricular dyssynchrony. In contrast, the effects of LBBP were not attenuated in the presence of proximal LBBB. Because the LBBB is located more proximally relative to the site of left bundle pacing, normal rapid activation of the left ventricle distal to the block is still possible *via* the specialised cells of the left bundle branches, resulting in significantly less heterogeneity in LV activation times.

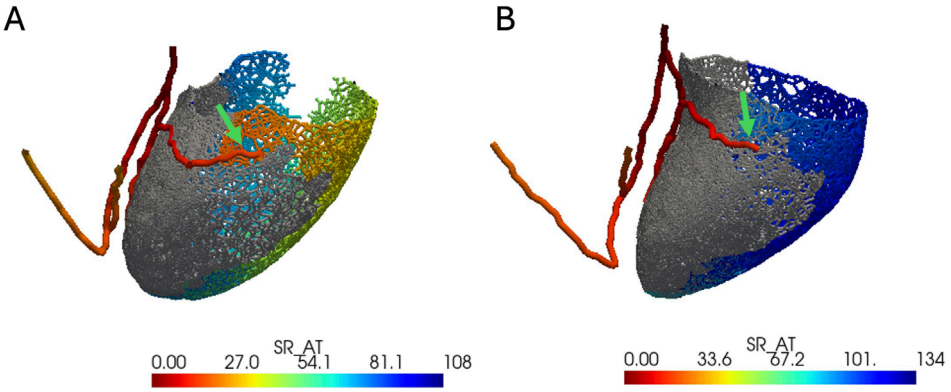

FIGURE 4
Anterior–posterior view of LV with an electrical activation map. Grey color denotes the area of a non-conducting scar. Red color denotes earliest activation, and dark blue denotes latest activation. The green arrow marks the terminal of the left anterior fascicle. **(A)** Heart model where the left anterior fascicle terminates beyond the area of the scar (where the Purkinje network is viable). **(B)** Heart model where the anterior fascicle terminates within the scar (where the Purkinje network is not viable).

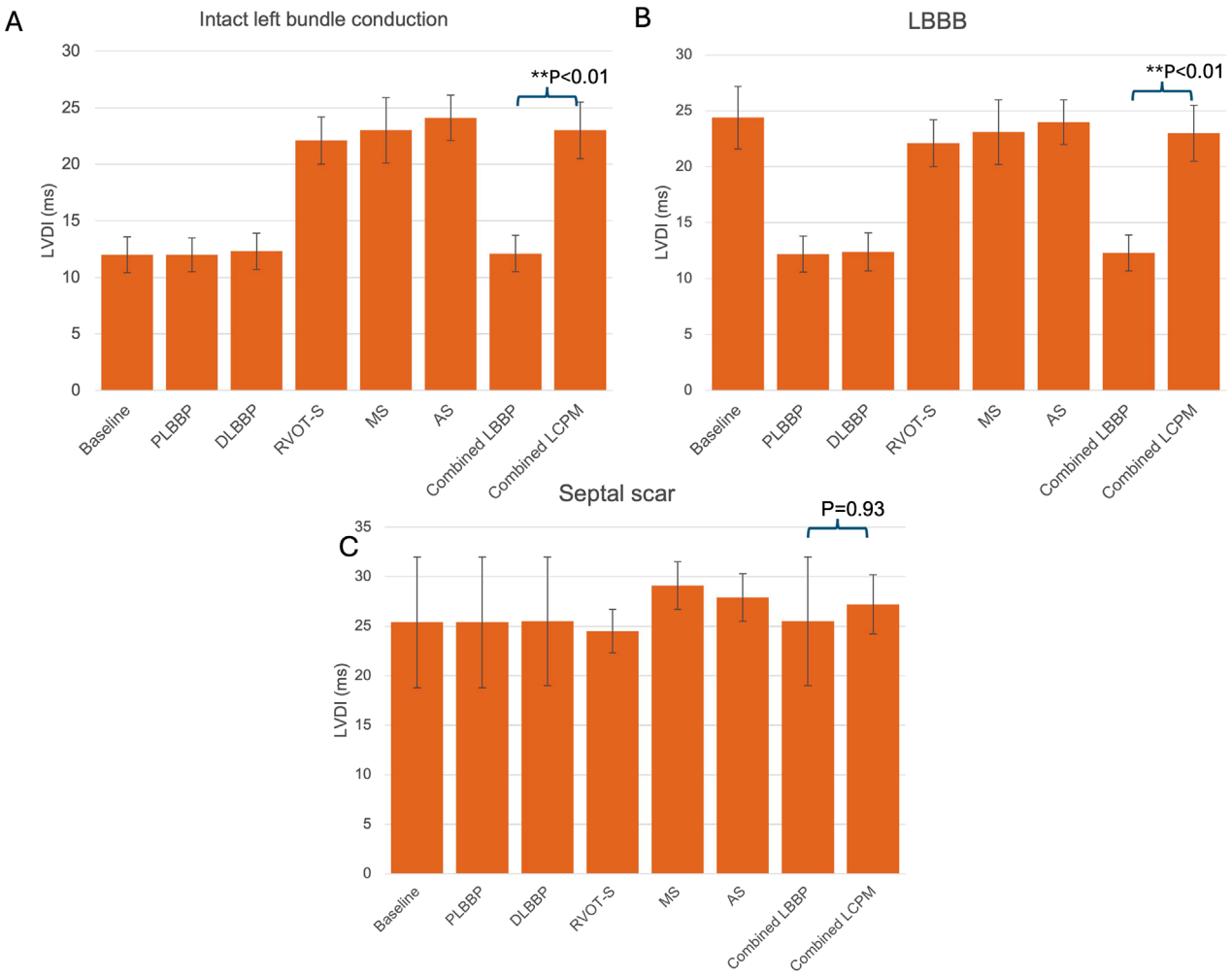

FIGURE 5
LVDI values in different settings: **(A)** intact left bundle conduction, **(B)** proximal left bundle branch block, and **(C)** septal scar involving the HPS. PLBBP, proximal left bundle branch pacing; DLBBP, distal left bundle branch pacing; AS, leadless pacing at the apical septum level; MS, leadless pacing at the mid-septum level; RVOT-S, leadless pacing at the right ventricular outflow tract-septum level.

4.2 Interventricular dyssynchrony

We computed both VEU and absolute VEU in our in silico modelling. VEU is a measure of interventricular dyssynchrony with directionality. A positive VEU indicates that the LV epicardial activation time is longer than the RV epicardial activation time, resembling LBBB, whereas a negative VEU indicates that the RV epicardial activation time is longer than the LV epicardial activation time, resembling RBBB. Absolute VEU simply reflects the degree of dyssynchrony between ventricles, without directionality.

Our *in silico* modelling demonstrated that combined LBBP configurations resulted in significantly less interventricular dyssynchrony (as reflected by VEU and absolute VEU) than combined LCPM configurations in the presence of intact left bundle branch conduction. In contrast, when proximal LBBB was present, combined LBBP configurations produced a greater amount of dyssynchrony, owing to later RV activation, than when left bundle branch conduction was intact. This prolonged RV activation is because, in the presence of proximal LBBB, activation of the right bundle *via* the left bundle is not possible during LBBP, and electrical propagation takes place *via* non-specialised cell-to-cell conduction, leading to delayed RV activation. This is reflected in the increase in the mean biventricular activation time (BIVAT-90) from 42.8 ms, in the presence of intact left bundle conduction, to 62.3 ms in the presence of proximal LBBB. Our *in silico* modelling finding replicates the *in vivo* finding of Ali et al. (2023a), who investigated the electrical response, using ECGi, of patients with LBBB to LBBP, His bundle pacing, and conventional biventricular pacing. They found that LBBP resulted in prolonged RV activation and, consequently, greater interventricular dyssynchrony than His bundle pacing, in which both the right and left bundles could be activated simultaneously. The prolonged RV activation in the presence of proximal LBBB also explains why combined LBBP configurations yielded similar absolute VEU values as LCPMs in the RVOT-S configuration–because both LBBP and RVOT-S produced a small amount of dyssynchrony but in opposite directions (VEU: combined LBBP: −22.1 ± 0.5 ms, RVOT-S: 21.7 ± 9.0 ms). This is important because, although much of the focus has been on pacing-induced left ventricular delay, pacing-induced right ventricular delay has also been linked to poor prognosis, including a higher risk of impaired haemodynamics and increased mortality (Hesse et al., 2001; Ploux et al., 2015; Sillanmäki et al., 2020). Although this issue may be mitigated with RV anodal capture, this requires significantly higher pacing output, resulting in impaired battery longevity with no significant improvement in biventricular haemodynamics (Ali et al., 2023b). In our simulations, we did not consider different types of pacing configurations (bipolar vs unipolar or RV anodal capture). Although RV anodal capture might provide better interventricular synchrony in some cases, it is not always clinically possible as it relies on direct contact of the anode electrode with the RV septum (Ali et al., 2023b). Therefore, we did not include this scenario in our study. Notwithstanding, Lu et al. (2023) found that implanting factors such as deployment of the lead tip in an oblique fashion and in the anterior-middle septum area increase the chances of successful RV anodal capture.

In the setting of a septal scar, LBBP configurations still resulted in a significant reduction in interventricular dyssynchrony in the models where the left anterior fascicle terminates beyond the area of scar tissue (6 out of 19). In the remaining 13 models where the left anterior fascicle terminated within scar tissue, the positive effect of LBBP on interventricular dyssynchrony is attenuated, and in these cases, LCPM configurations were superior in reducing interventricular dyssynchrony. This shows that the extent of a septal scar matters when implanting LBBP.

Figure 6 illustrates the activation patterns in response to different pacing configurations in one of the heart models.

4.3 Septal scar involving the HPS

In the presence of a septal scar rendering the HPS nonconductive, LBBP resulted in more interventricular dyssynchrony than LCPM (VEU 41.7 ± 20.2 vs. 31.0 ± 8.4 ms, respectively, $p < 0.01$) with the RVOT-S configuration producing the lowest VEU (24.8 ± 9.0 ms) compared to all other LBBP and LCPM configurations. This is because in the majority (13 out of 19) of our heart models, where the scar renders the Purkinje fibres of the left bundle non-conducting, the activation wavefront travels retrogradely from the pacing stimulus up the left bundle into the right bundle, with RV depolarisation first, followed by LV depolarisation *via* non-specialised myocardial conduction. In contrast, pacing at the site of the RVOT-S, away from the scar tissue, affords a degree of biventricular activation *via* non-HPS septal myocardium, leading to overall lower interventricular dyssynchrony. In real-world cases, complete interruption of the HPS is relatively uncommon, and septal scars are often heterogeneous in their transmurality and conductivity. More than one location on the septum can usually be explored to achieve left bundle branch area capture when the initial deployment fails to achieve this. The findings from 6 out of 19 of our heart models, where a portion of the Purkinje network supplied by the left anterior fascicle located just beyond the area of scar remained conducting, demonstrate that LBBP may still have a beneficial effect in the presence of a less extensive septal scar. In rare cases where extensive transmural septal scarring occurs and renders the HPS non-conducting, such as in severe cases of septal viral myocarditis, advanced infiltrative diseases such as amyloidosis and sarcoidosis, and extensive myocardial infarction caused by proximal left anterior descending artery occlusion (Imran et al., 2010; Cheng et al., 2024), our modelling suggests that LCPM may yield less interventricular dyssynchrony than LBBP.

Interestingly, Elliot et al. investigated the effects of LBBP with the use of ECG in 10 patients (five had LBBB, one had RBBB, and four had RV-paced rhythm) and found that the presence of septal scar, either midwall or subendocardial, attenuated the resynchronisation effects of LBBP on the LV (i.e., reduced intraventricular synchrony). This suggests that the resynchronisation effects of LBBP may be reduced even when the septal scar is not transmural and the conductivity of the HPS is not completely abolished. Although Elliot et al. did not compare biventricular activation times or VEU between those with and without the septal scar, our *in silico* modelling suggests that LBBP effects on interventricular synchrony are also reduced by septal scarring.

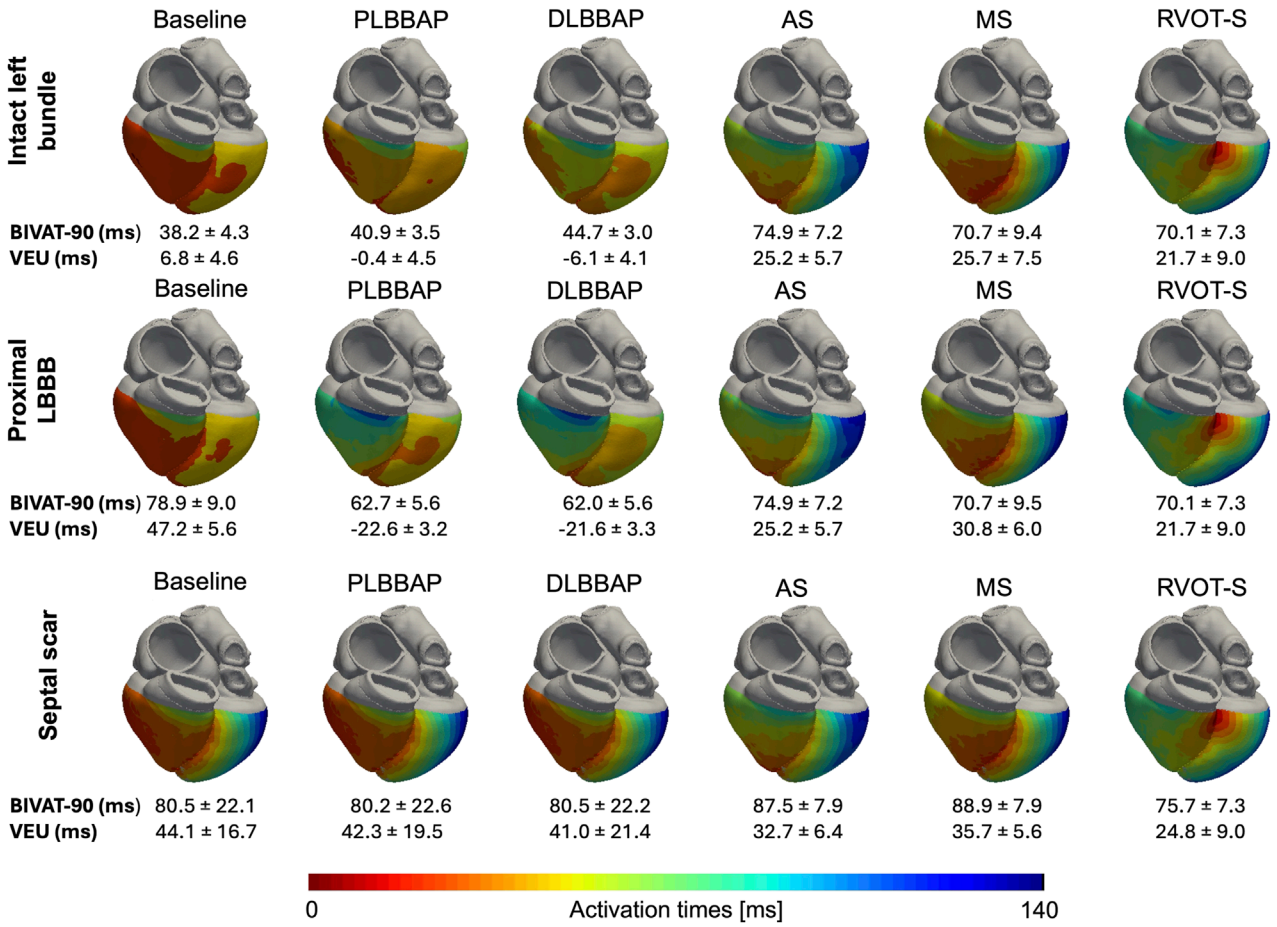

FIGURE 6
Anterior–posterior epicardial activation maps of each pacing configuration in different settings of one of the heart models. Top row: intact left bundle conduction. Middle row: presence of proximal LBBB at the level of the His bundle. RV activation is delayed during LBBP in the presence of proximal LBBB compared to that during intact left bundle conduction. Bottom row: septal scar rendering HPS non-conductive. PLBBP, LBBP at the level of proximal left bundle; DLBBP, LBBP at the distal left bundle; AS, leadless pacing at the apical septum level; MS, Leadless pacing at the mid-septum level; RVOT-S, Leadless pacing at the right ventricular outflow tract-septum level. Activation scale: the extreme left of the scale (dark red) denotes earliest activation (0 ms), and the extreme right of the scale (dark blue) denotes latest activation (140 ms). BIVAT-90 and VEU values are presented as the mean ± standard deviation.

4.4 Clinical implications

The implications of our *in silico* modelling are as follows:

1. LCPM is superior to LBBP with respect to interventricular synchrony in the presence of extensive septal scarring affecting the HPS. This finding is consistent with previous *in silico* and *in vivo* studies demonstrating an attenuation of the beneficial effects of LBBP on LV resynchronisation and positive remodelling in the presence of a septal scar (Chen et al., 2023; Elliott et al., 2023; Strocchi et al., 2023). This may make LCPM a more suitable option than LBBP in those with a ventricular pacing indication and preserved LV function, considering the absence of pocket- and lead-related complications and the increased technical complexity of LBBP implantation in the setting of septal scarring (Ponnusamy et al., 2020). Furthermore, the recent introduction of the Abbott AVEIR dual-chamber leadless pacemaker—which maintains atrioventricular (AV) synchrony—has positioned LCPM as a viable alternative for patients with persistent high-degree AV block (Knops et al., 2023). Although LCPM is associated with a lower overall risk of TR progression, studies have shown that implantation close to the tricuspid valve, such as in the high septal position, may increase the risk of TR progression (Salaun et al., 2018; Beurskens et al., 2019; Hai et al., 2021; Garweg et al., 2023; El-Chami et al., 2024; Yuyun et al., 2024). Therefore, further clarification is required through *in vivo* studies to determine whether the benefits of LCPM implantation in the RVOT-S position to minimise interventricular dyssynchrony are offset by the increased risk of TR progression.
2. There is possible equipoise between LBBP and RVOT-S in interventricular dyssynchrony in the presence of LBBB. First, LCPM at the RVOT-S position yielded similar absolute VEU values as LBBP. Second, even considering VEU (with directionality) instead of absolute VEU (without directionality), both LBBP and RVOT-S produced VEU

values of <40 ms (combined LBBP −22.1 ± 3.3 vs. RVOT-S +21.7 ± 9.0 ms), below the threshold for the widely accepted definition for interventricular mechanical delay (Cleland et al., 2005). This is a new finding and warrants further *in vivo* comparison between LBBP and LCPM, specifically in the RVOT-S configuration, in patients with LBBB.

4.5 Limitations

The heart geometries used in this study were derived from healthy subjects to closely reflect the cardiac morphology of patients with preserved LV function and high-degree AV block. Therefore, results from this study may not be translatable to patients with heart failure with reduced ejection fraction. We did not simulate RV anodal capture in our *in silico* modelling. Although this may have mitigated delayed RV activation caused by LBBP in our simulation, particularly in the context of LBBB, real-world data suggest that it is not always clinically possible, comes at a considerable cost of significantly higher pacing output, and does not improve acute haemodynamics (Ali et al., 2023b). Similarly, although the use of epicardial biventricular pacing may reduce RV activation delay by optimising LV-RV delay in the context of LBBB, the aim of our study was to compare LCPM and LBBP in those with preserved LV function and complete AV block, where the use of conventional epicardial biventricular pacing is not guideline-recommended. In our study, the location of LBBB was simulated to be within the bundle of His. Therefore, the results of this modelling may not be translatable to scenarios where the location of LBBB is different, such as distal and diffuse LBBB. Depending on the level and nature of the block (focal or diffuse), left bundle capture or retrograde RV activation *via* the right bundle may or may not be possible, affecting VEU and overall biventricular activation times. In our modelling of proximal left bundle branch block, where the level of block is at the left intra-Hisian level, the activation wavefront starts in the RV and spreads across the septum slowly. If the activation wavefront came into contact with the LV Purkinje system, it was activated, and depolarisation within the LV could take place *via* the Purkinje network. It is unclear whether such Purkinje network activation takes place within the LV, but the close correlation of our generated *in silico* measurements of total ventricular activation time (TAT) with an *in vivo* study by Ploux et al. (2015) supports the validity of our left bundle branch block simulations.

Animal studies have shown that some Purkinje cells may survive an infarct with partial to complete recovery of function (Friedman et al., 1973; Garcia-Bustos et al., 2019; Sayers et al., 2025). In our models, Purkinje fibres that overlap the scar zone were treated as non-conducting under the assumption that Purkinje fibres are affected by hypoxia the same way as normal myocardium, to illustrate the impact of the most severe cases of myocardial scarring on the Purkinje system. Our *in silico* modelling results demonstrated that interventricular dyssynchrony can be minimised when LCPM is placed in the RVOT-S position. Although the high septal placement simulated in our *in silico* modelling is feasible (Garweg et al., 2023; Shantha et al., 2023; El-Chami et al., 2024), specific target deployment of LCPM onto the septum may not always be possible, particularly in smaller hearts. Our study did not account for the mechanical effects of lead implantation, particularly its impact on tricuspid valve function. Mechanical simulations are computationally more demanding, and their application remains limited to studies involving a small number of simulations. In the future, this study could be extended to include mechanics and investigate the effects of leadless pacing on valve function. Finally, this is a computational modelling study with a small number of heart models. Although statistical significance is presented, due to the small sample size, these values should be interpreted with caution.

5 Conclusion

To date, no direct comparison between LBBP and LCPM has been performed to investigate their effects on intraventricular and interventricular dyssynchrony, which are implicated in the development of pacing-induced cardiomyopathy. Our *in silico* modelling suggests that, in the presence of an extensive septal scarring rendering the Purkinje network non-conducting, LCPM is superior to LBBP in terms of interventricular synchrony, consistent with findings from previous studies. More interestingly, in the setting of LBBB, LCPM at a high septal position may be non-inferior to LBBP in interventricular dyssynchrony. Further *in vivo* studies are required to validate these findings.

Data availability statement

The original contributions presented in the study are included in the article/Supplementary Material; further inquiries can be directed to the corresponding author.

Author contributions

AL: Investigation, Writing – review and editing, Data curation, Methodology, Conceptualization, Visualization, Writing – original draft, Project administration, Formal Analysis. MS: Data curation, Methodology, Formal analysis, Writing – review and editing. CR: Writing – review and editing, Resources. KG: Writing – review and editing. NW: Writing – review and editing. SH: Writing – review and editing. FdV: Writing – review and editing. EV: Resources, Writing – review and editing. GP: Writing – review and editing. SN: Supervision, Funding acquisition, Writing – review and editing. CR: Supervision, Writing – review and editing, Funding acquisition.

Funding

The author(s) declare that no financial support was received for the research and/or publication of this article.

Conflict of interest

The authors declare that the research was conducted in the absence of any commercial or financial relationships that could be construed as a potential conflict of interest.

The author(s) declared that they were an editorial board member of Frontiers, at the time of submission. This had no impact on the peer review process and the final decision

Generative AI statement

The author(s) declare that no Generative AI was used in the creation of this manuscript.

Any alternative text (alt text) provided alongside figures in this article has been generated by Frontiers with the support of artificial intelligence and reasonable efforts have been made to ensure accuracy, including review by the authors wherever possible. If you identify any issues, please contact us.

Publisher's note

All claims expressed in this article are solely those of the authors and do not necessarily represent those of their affiliated organizations, or those of the publisher, the editors and the reviewers. Any product that may be evaluated in this article, or claim that may be made by its manufacturer, is not guaranteed or endorsed by the publisher.

References

Ali, N., Arnold, A. D., Miyazawa, A. A., Keene, D., Chow, J.-J., Little, I., et al. (2023a). Comparison of methods for delivering cardiac resynchronization therapy: an acute electrical and haemodynamic within-patient comparison of left bundle branch area, his bundle, and biventricular pacing. *EP Eur.* 25, 1060–1067. doi:10.1093/europace/euac245

Ali, N., Saqi, K., Arnold, A. D., Miyazawa, A. A., Keene, D., Chow, J.-J., et al. (2023b). Left bundle branch pacing with and without anodal capture: impact on ventricular activation pattern and acute haemodynamics. *EP Eur.* 25, euad264. doi:10.1093/europace/euad264

Bansal, R., Parakh, N., Gupta, A., Juneja, R., Naik, N., Yadav, R., et al. (2019). Incidence and predictors of pacemaker-induced cardiomyopathy with comparison between apical and non-apical right ventricular pacing sites. *J. Interventional Cardiac Electrophysiol.* 56, 63–70. doi:10.1007/s10840-019-00602-2

Bayer, J., Prassl, A. J., Pashaei, A., Gomez, J. F., Frontera, A., Neic, A., et al. (2018). Universal ventricular coordinates: a generic framework for describing position within the heart and transferring data. *Med. Image Anal.* 45, 83–93. doi:10.1016/j.media.2018.01.005

Bednarek, A., Kiełbasa, G., Moskal, P., Ostrowska, A., Bednarski, A., Sondej, T., et al. (2024). Left bundle branch area pacing improves right ventricular function and synchrony. *Heart Rhythm.* 21, 2234–2241. doi:10.1016/j.hrthm.2024.05.019

Beurskens, N. E. G., Tjong, F. V. Y., de Bruin-Bon, R. H. A., Dasselaar, K. J., Kuijt, W. J., Wilde, A. A. M., et al. (2019). Impact of leadless pacemaker therapy on cardiac and atrioventricular valve function through 12 months of Follow-Up. *Circ. Arrhythm. Electrophysiol.* 12, e007124. doi:10.1161/CIRCEP.118.007124

Boyle, T. A., Pothineni, N. V. K., Austin, M., Shivamurthy, P., Markman, T., Guandalini, G., et al. (2024). Incidence and predictors of pacing-induced right ventricular cardiomyopathy. *Circ. Arrhythm. Electrophysiol.* 17, e013070. doi:10.1161/CIRCEP.124.013070

Chen, Z., Ma, X., Gao, Y., Wu, S., Xu, N., Chen, F., et al. (2023). Cardiac magnetic resonance–derived myocardial scar is associated with echocardiographic response and clinical prognosis of left bundle branch area pacing for cardiac resynchronization therapy. *EP Eur.* 25, euad326. doi:10.1093/europace/euad326

Cheng, R. K., Kittleson, M. M., Beavers, C. J., Birnie, D. H., Blankstein, R., Bravo, P. E., et al. (2024). Diagnosis and management of cardiac sarcoidosis: a scientific statement from the American heart association. *Circulation* 149, e1197–e1216. doi:10.1161/CIR.0000000000001240

Chung, M. K., Patton, K. K., Lau, C.-P., Dal Forno, A. R. J., Al-Khatib, S. M., Arora, V., et al. (2023). 2023 HRS/APHRS/LAHRS guideline on cardiac physiologic pacing for the avoidance and mitigation of heart failure. *Heart Rhythm.* 20, e17–e91. doi:10.1016/j.hrthm.2023.03.1538

Cleland, J. G. F., Jean-Claude, D., Erland, E., Nick, F., Daniel, G., Lukas, K., et al. (2005). The effect of cardiac resynchronization on morbidity and mortality in heart failure. *N. Engl. J. Med.* 352, 1539–1549. doi:10.1056/NEJMoa050496

Draper, M. H., and Mya-Tu, M. (1959). A comparison of the conduction velocity in cardiac tissues of various mammals. *Q. J. Exp. Physiology Cogn. Med. Sci. Transl. Integration* 44, 91–109. doi:10.1113/expphysiol.1959.sp001379

Durrer, D., Van Dam, R. T., Freud, G. E., Janse, M. J., Meijler, F. L., and Arzbaecher, R. C. (1970). Total excitation of the isolated human heart. *Circulation* 41, 899–912. doi:10.1161/01.cir.41.6.899

El-Chami, M. F., Garweg, C., Clementy, N., Al-Samadi, F., Iacopino, S., Martinez-Sande, J. L., et al. (2024). Leadless pacemakers at 5-year follow-up: the micra transcatheter pacing system post-approval registry. *Eur. Heart J.* 45, 1241–1251. doi:10.1093/eurheartj/ehae101

Elliott, M. K., Strocchi, M., Sieniewicz, B. J., Sidhu, B., Mehta, V., Wijesuriya, N., et al. (2023). Biventricular endocardial pacing and left bundle branch area pacing for cardiac resynchronization: mechanistic insights from electrocardiographic imaging, acute hemodynamic response, and magnetic resonance imaging. *Heart Rhythm.* 20, 207–216. doi:10.1016/j.hrthm.2022.10.019

Fang, F., Luo, X.-X., Zhang, Q., Azlan, H., Razali, O., Ma, Z., et al. (2016). Deterioration of left ventricular systolic function in extended pacing to avoid cardiac enlargement (PACE) trial: the predictive value of early systolic dyssynchrony. *EP Eur.* 17, ii47–ii53. doi:10.1093/europace/euv130

Friedman, P. L., Stewart, J. R., Fenoglio Jr, J. J., and Wit, A. L. (1973). Survival of subendocardial purkinje fibers after extensive myocardial infarction in dogs: *in vitro* and *in vivo* correlations. *Circ. Res.* 33, 597–611. doi:10.1161/01.res.33.5.597

Funck, R. C., Müller, H.-H., Lunati, M., De Roy, L., Klein, N., Meisel, E., et al. (2025). Biventricular vs. right ventricular pacing devices in patients anticipated to require frequent ventricular pacing (BioPace). *EP Eur.* 27, euaf029. doi:10.1093/europace/euaf029

Garcia-Bustos, V., Sebastian, R., Izquierdo, M., Rios-Navarro, C., Bodí, V., Chorro, F. J., et al. (2019). Changes in the spatial distribution of the Purkinje network after acute myocardial infarction in the pig. *PLoS One* 14, e0212096. doi:10.1371/journal.pone.0212096

Garweg, C., Duchenne, J., Vandenberk, B., Mao, Y., Ector, J., Haemers, P., et al. (2023). Evolution of ventricular and valve function in patients with right ventricular pacing – a randomized controlled trial comparing leadless and conventional pacing. *PACE - Pacing Clin. Electrophysiol.* 46, 1455–1464. doi:10.1111/pace.14870

Gillette, K., Gsell, M. A. F., Bouyssier, J., Prassl, A. J., Neic, A., Vigmond, E. J., et al. (2021). Automated framework for the inclusion of a his–Purkinje system in cardiac digital twins of ventricular electrophysiology. *Ann. Biomed. Eng.* 49, 3143–3153. doi:10.1007/s10439-021-02825-9

Gillette, K., Gsell, M. A. F., Strocchi, M., Grandits, T., Neic, A., Manninger, M., et al. (2022). A personalized real-time virtual model of whole heart electrophysiology. *Front. Physiol.* 13, 907190. doi:10.3389/fphys.2022.907190

Glikson, M., Nielsen, J. C., Kronborg, M. B., Michowitz, Y., Auricchio, A., Barbash, I. M., et al. (2021). 2021 ESC guidelines on cardiac pacing and cardiac resynchronization therapy: developed by the task force on cardiac pacing and cardiac resynchronization therapy of the European Society of Cardiology (ESC) with the special contribution of the European Heart Rhythm Association (EHRA). *Eur. Heart J.* 42, 3427–3520. doi:10.1093/eurheartj/ehab364

Hai, J. J., Mao, Y., Zhen, Z., Fang, J., Wong, C. K., Siu, C. W., et al. (2021). Close proximity of leadless pacemaker to tricuspid annulus predicts worse tricuspid regurgitation following septal implantation. *Circ. Arrhythm. Electrophysiol.* 14, E009530. doi:10.1161/CIRCEP.120.009530

Hesse, B., Diaz, L. A., Snader, C. E., Blackstone, E. H., and Lauer, M. S. (2001). Complete bundle branch block as an independent predictor of all-cause mortality: report of 7,073 patients referred for nuclear exercise testing. *Am. J. Med.* 110, 253–259. doi:10.1016/S0002-9343(00)00713-0

Höke, U., Auger, D., Thijssen, J., Wolterbeek, R., Van Der Velde, E. T., Holman, E. R., et al. (2014). Significant lead-induced tricuspid regurgitation is associated with poor prognosis at long-term follow-up. *Heart* 100, 960–968. doi:10.1136/heartjnl-2013-304673

Hu, Q., You, H., Chen, K., Dai, Y., Lu, W., Li, Y., et al. (2023). Distance between the lead-implanted site and tricuspid valve annulus in patients with left bundle branch pacing: effects on postoperative tricuspid regurgitation deterioration. *Heart Rhythm.* 20, 217–223. doi:10.1016/j.hrthm.2022.10.027

Imran, S., F, G. J., DaLi, F., A, A. P., W, M. M., D, E. W., et al. (2010). Role of cardiac magnetic resonance imaging in the detection of cardiac amyloidosis. *JACC Cardiovasc Imaging* 3, 155–164. doi:10.1016/j.jcmg.2009.09.023

Kanawati, J., Ng, A. C. C., Khan, H., Yu, C., Hyun, K., Abed, H., et al. (2021). Long-term Follow-Up of mortality and heart failure hospitalisation in patients with intracardiac device-related tricuspid regurgitation. *Heart Lung Circ.* 30, 692–697. doi:10.1016/j.hlc.2020.08.028

Knops, R. E., Reddy, V. Y., Ip, J. E., Doshi, R., Exner, D. V., Defaye, P., et al. (2023). A dual-chamber leadless pacemaker. *N. Engl. J. Med.* 388, 2360–2370. doi:10.1056/nejmoa2300080

Li, X., Fan, X., Wang, Q., Wang, Z., Zhu, H., Li, H., et al. (2023). Tricuspid regurgitation following pacemaker implantation for bradycardia: a two-year study comparing different pacing strategies. *Chin. Med. J. Engl.* 136, 2508–2510. doi:10.1097/CM9.0000000000002825

Lu, W., Lin, J., Li, Y., Hu, Q., Cheng, C., Chen, R., et al. (2023). Quantitative analysis reveals influencing factors to facilitate successful anodal-ring capture in left bundle branch pacing. *EP Eur.* 25, euad172. doi:10.1093/europace/euad172

Mendonca Costa, C., Neic, A., Kerfoot, E., Porter, B., Sieniewicz, B., Gould, J., et al. (2019). Pacing in proximity to scar during cardiac resynchronization therapy increases local dispersion of repolarization and susceptibility to ventricular arrhythmogenesis. *Heart Rhythm.* 16, 1475–1483. doi:10.1016/j.hrthm.2019.03.027

Neic, A., Campos, F. O., Prassl, A. J., Niederer, S. A., Bishop, M. J., Vigmond, E. J., et al. (2017). Efficient computation of electrograms and ECGs in human whole heart simulations using a reaction-eikonal model. *J. Comput. Phys.* 346, 191–211. doi:10.1016/j.jcp.2017.06.020

Pastore, G., Noventa, F., Piovesana, P., Cazzin, R., Aggio, S., Verlato, R., et al. (2008). Left ventricular dyssynchrony resulting from right ventricular apical pacing: relevance of baseline assessment. *Pacing Clin. Electrophysiol.* 31, 1456–1462. doi:10.1111/j.1540-8159.2008.01209.x

Pathmanathan, P., Aycock, K., Badal, A., Bighamian, R., Bodner, J., Craven, B. A., et al. (2024). Credibility assessment of *in silico* clinical trials for medical devices. *PLoS Comput. Biol.* 20, e1012289. doi:10.1371/journal.pcbi.1012289

Ploux, S., Eschalier, R., Whinnett, Z. I., Lumens, J., Derval, N., Sacher, F., et al. (2015). Electrical dyssynchrony induced by biventricular pacing: implications for patient selection and therapy improvement. *Heart Rhythm.* 12, 782–791. doi:10.1016/j.hrthm.2014.12.031

Ponnusamy, S. S., Arora, V., Namboodiri, N., Kumar, V., Kapoor, A., and Vijayaraman, P. (2020). Left bundle branch pacing: a comprehensive review. *J. Cardiovasc Electrophysiol.* 31, 2462–2473. doi:10.1111/jce.14681

Riesenhuber, M., Spannbauer, A., Gwechenberger, M., Pezawas, T., Schukro, C., Stix, G., et al. (2021). Pacemaker lead-associated tricuspid regurgitation in patients with or without pre-existing right ventricular dilatation. *Clin. Res. Cardiol.* 110, 884–894. doi:10.1007/s00392-021-01812-3

Rodero, C., Strocchi, M., Marciniak, M., Longobardi, S., Whitaker, J., O'Neill, M. D., et al. (2021). Linking statistical shape models and simulated function in the healthy adult human heart. *PLoS Comput. Biol.* 17, e1008851. doi:10.1371/journal.pcbi.1008851

Salaun, E., Tovmassian, L., Simonnet, B., Giorgi, R., Deharo, J., Koutbi-Franceschi, L., et al. (2018). Right ventricular and tricuspid valve function in patients chronically implanted with leadless pacemakers. *Europace* 20, 823–828. doi:10.1093/europace/eux101

Sayers, J. R., Martinez-Navarro, H., Sun, X., de Villiers, C., Sigal, S., Weinberger, M., et al. (2025). Cardiac conduction system regeneration prevents arrhythmias after myocardial infarction. *Nat. Cardiovasc. Res.* 4, 163–179. doi:10.1038/s44161-024-00586-x

Shantha, G., Brock, J., Singleton, M., Kozak, P., Bodziock, G., Bradford, N., et al. (2023). Anatomical location of leadless pacemaker and the risk of pacing-induced cardiomyopathy. *J. Cardiovasc Electrophysiol.* 34, 1418–1426. doi:10.1111/jce.15925

Sillanmäki, S., Aapro, S., Lipponen, J. A., Tarvainen, M. P., Laitinen, T., Hedman, M., et al. (2020). Electrical and mechanical dyssynchrony in patients with right bundle branch block. *J. Nucl. Cardiol.* 27, 621–630. doi:10.1007/s12350-018-1418-1

Strocchi, M., Gillette, K., Neic, A., Elliott, M. K., Wijesuriya, N., Mehta, V., et al. (2023). Effect of scar and his–purkinje and myocardium conduction on response to conduction system pacing. *J. Cardiovasc Electrophysiol.* 34, 984–993. doi:10.1111/jce.15847

Tatum, R., Maynes, E. J., Wood, C. T., Deb, A. K., Austin, M. A., O'Malley, T. J., et al. (2021). Tricuspid regurgitation associated with implantable electrical device insertion: a systematic review and meta-analysis. *Pacing Clin. Electrophysiol.* 44, 1297–1302. doi:10.1111/pace.14287

Tian, F., Weng, H., Liu, A., Liu, W., Zhang, B., Wang, Y., et al. (2023). Effect of left bundle branch pacing on right ventricular function: a 3-dimensional echocardiography study. *Heart Rhythm.* 21, 445–453. doi:10.1016/j.hrthm.2023.12.012

Tops, L. F., Suffoletto, M. S., Bleeker, G. B., Boersma, E., van der Wall, E. E., Gorcsan, J., et al. (2007). Speckle-tracking radial strain reveals left ventricular dyssynchrony in patients with permanent right ventricular pacing. *J. Am. Coll. Cardiol.* 50, 1180–1188. doi:10.1016/j.jacc.2007.06.011

Vigmond, E. J., Aguel, F., and Trayanova, N. A. (2002). Computational techniques for solving the bidomain equations in three dimensions. *IEEE Trans. Biomed. Eng.* 49, 1260–1269. doi:10.1109/TBME.2002.804597

Yuyun, M. F., Joseph, J., Erqou, S. A., Kinlay, S., Echouffo-Tcheugui, J. B., Peralta, A. O., et al. (2024). Evolution and prognosis of tricuspid and mitral regurgitation following cardiac implantable electronic devices: a systematic review and meta-analysis. *EP Eur.* 26, euae143. doi:10.1093/europace/euae143

frontiers | Frontiers in Pediatrics

TYPE Case Report
PUBLISHED 27 October 2025
DOI 10.3389/fped.2025.1662114

OPEN ACCESS

EDITED BY
Edward Joseph Vigmond,
Université de Bordeaux, France

REVIEWED BY
Giovanni Malanchini,
Papa Giovanni XXIII Hospital, Italy
Muhammad Mohsin,
National Institute of Cardiovascular Diseases, Pakistan

*CORRESPONDENCE
Peng Liu
✉ wanguyisu@163.com

†These authors have contributed equally to this work

RECEIVED 08 July 2025
ACCEPTED 14 October 2025
PUBLISHED 27 October 2025

CITATION
Wang F, Wu B, Huang J, Yaletai B and Liu P (2025) Case Report: Adenosine-induced atrioventricular dissociation: unmasking monomorphic tachycardia as a diagnostic challenge in a neonate.
Front. Pediatr. 13:1662114.
doi: 10.3389/fped.2025.1662114

Case Report: Adenosine-induced atrioventricular dissociation: unmasking monomorphic tachycardia as a diagnostic challenge in a neonate

Feifei Wang[1†], Bin Wu[2†], Jiaqi Huang[3†], Ba Yaletai[4] and Peng Liu[3*]

[1]Department of Electrocardiogram Laboratory, Ordos Central Hospital, Ordos School of Clinical Medicine, Inner Mongolia Medical University, Inner Mongolia, China, [2]Department of Endocrinology, Qingdao Municipal Hospital, Qingdao, China, [3]Department of Cardiology, Ordos Central Hospital, Ordos School of Clinical Medicine, Inner Mongolia Medical University, Inner Mongolia, China, [4]Department of Neonatology, Ordos Central Hospital, Ordos School of Clinical Medicine, Inner Mongolia Medical University, Inner Mongolia, China

Background: Neonatal monomorphic tachycardia poses a diagnostic challenge. This report demonstrates how adenosine-induced AV dissociation confirmed ventricular tachycardia.
Case: A 3-day-old preterm neonate (34 + 2 weeks) presented with refractory monomorphic tachycardia (217 bpm; QRS 92 ms) initially diagnosed as SVT based on 1:1 retrograde P-waves. Adenosine administration induced atrioventricular dissociation without termination—a finding inconsistent with SVT. Retrospective ECG analysis revealed prolonged QRS duration during tachycardia (92 ms vs. 60 ms post-cardioversion) and delta wave-like slurring, confirming VT diagnosis. Synchronized cardioversion (0.5 J/kg) restored sinus rhythm, followed by metoprolol prophylaxis.
Conclusion: This case highlights that monomorphic tachycardia in neonates may represent VT. Adenosine's role in inducing AV dissociation is pivotal for diagnosis, and low-energy cardioversion with β-blocker maintenance offers an effective rescue strategy. Clinicians must reassess ECG features dynamically to avoid misclassification.

KEYWORDS

monomorphic, tachycardia, neonate, electrocardiography, adenosine

Introduction

Neonatal arrhythmias, though relatively uncommon with an estimated incidence of 1% in general populations and up to 5% in neonatal intensive care units (NICUs), represent critical clinical challenges due to their potential for hemodynamic compromise and long-term sequelae (1). While most cases are transient and benign, non-benign arrhythmias such as supraventricular tachycardia (SVT) or ventricular tachycardia (VT) require urgent intervention to prevent cardiac failure or sudden death (2). This case report describes a 3-day-old preterm neonate with life-threatening relatively narrow QRS complex tachycardia tachycardia unresponsive to adenosine, successfully managed with electrical cardioversion and sustained by metoprolol.

Case presentation

A male neonate was electively delivered via lower segment cesarean section at 34 + 2 weeks gestation to a 30-year-old primigravida with an unremarkable antenatal history. Serial fetal surveillance ultrasonography demonstrated normal anatomical development, complemented by negative maternal TORCH serological profiling. The procedure was performed under spinal anesthesia for persistent breech presentation, achieving Apgar scores of 9 and 10 at 1 and 5 min respectively. Neonatal biometric parameters included a birth weight of 2,180 g (30th percentile for gestational age).

At 30 min postnatally, the infant developed acute respiratory decompensation manifesting as tachypnea (40 breaths/min), intercostal and subxiphoid retractions, with concurrent cyanosis. Radiographic evaluation identified decreased permeability of both lungs on chest x-ray. Echocardiographic evaluation confirmed transitional circulation patterns (patent foramen ovale with left-to-right shunting, patent ductus arteriosus) without structural anomalies. Laboratory analysis demonstrated marked elevation of cardiac biomarkers: White blood cell (WBC) 6.99×10^9/L, Hemoglobin (HGB) 178 g/L. High-sensitivity troponin T (hs-TnT) 0.0605 μg/L (reference <0.014 μg/L) and NT-proBNP 3,596 pg/mL (reference <125 pg/mL). Hepatic derangement was evidenced by alanine aminotransferase (ALT) 15 U/L (13–35) and aspartate aminotransferase (AST) 37 U/L (7–40). Electrolyte profiling showed venous potassium 4.37 mmol/L (3.5–5.3) and magnesium 0.86 mmol/L (0.75–1.02), excluding significant ionic disturbances. Pulse oximetry demonstrated profound desaturation (SpO_2 84% in room air), prompting immediate escalation to non-invasive positive pressure ventilation (NIPPV mode: FiO_2 30%, PIP 16 cmH_2O, Ti 0.35 s, RR 40 breaths/min). This intervention achieved partial oxygenation improvement (SpO_2 93%, pH 7.48, pO_2 82 mmHg, pCO_2 24 mmHg, Base Excess −5.6 mmol/L, and Lactate 2.2 mmol/L), while telemetry detected sustained wide-complex tachycardia (ventricular rate 217 bpm; QRS 92 ms) with a delta wave-like slurring at its onset and 1:1 conduction retrograde P-wave morphology, consistent with paroxysmal supraventricular tachycardia (Figure 1). Blood pressure (BP) was 68/35 mmHg. Intravenous adenosine administration (0.1 mg/kg) can reduce the heart rate to 175 beats per minute and show the phenomenon of atrioventricular dissociation and fusion beats with qrs-wave morphology unchanged (Figure 2). Ultimately, we diagnosed this tachycardia as ventricular tachycardia. Electrical cardioversion (0.5 J/kg) subsequently achieved successful sinus rhythm restoration (Figure 3) and BP was 70/34 mmHg. The infant's acute respiratory decompensation and profound desaturation were initially attributed to respiratory distress syndrome; however, their temporal coincidence with the onset of sustained tachycardia and the marked, immediate clinical improvement post-cardioversion strongly implicated the arrhythmia-induced hemodynamic compromise as the primary etiology. Initiation of metoprolol tartrate (0.1 mg/kg q12h)

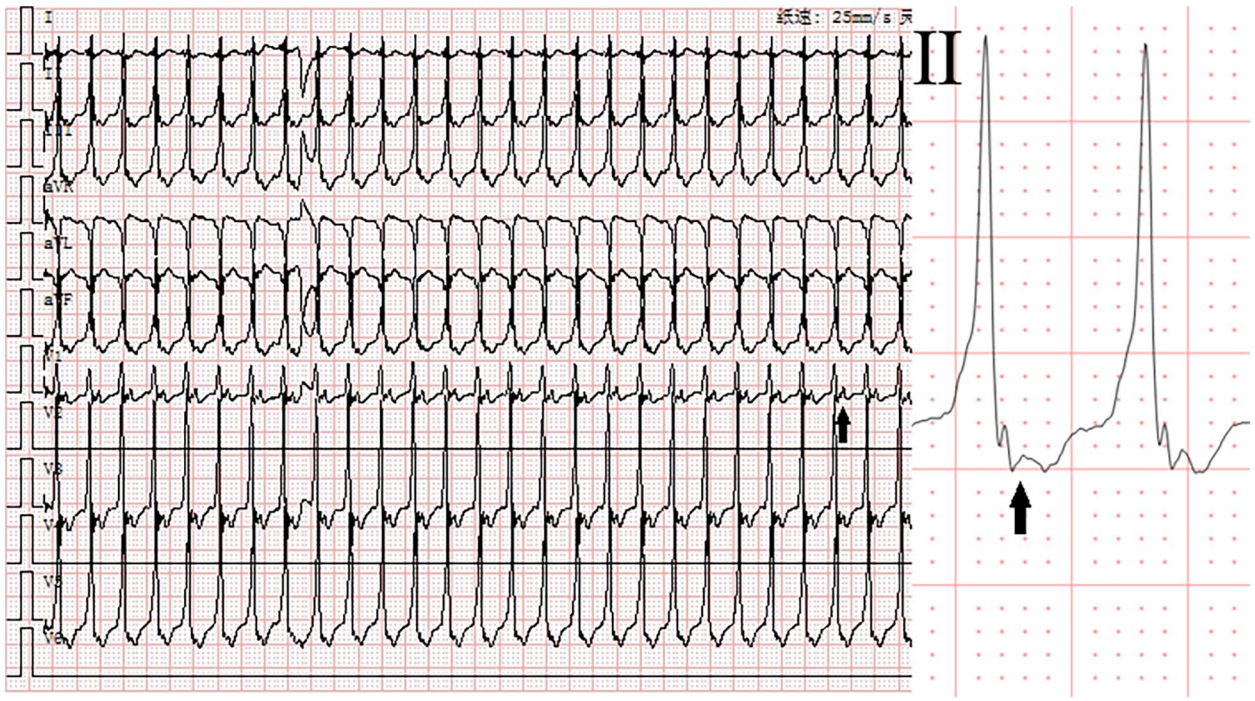

FIGURE 1
Electrocardiogram before adenosine. Monomorphic tachycardia (heart rate: 217 beats per minute, QRS duration: 92 ms) with retrograde P-wave (1:1). Solid arrows indicate P-waves.

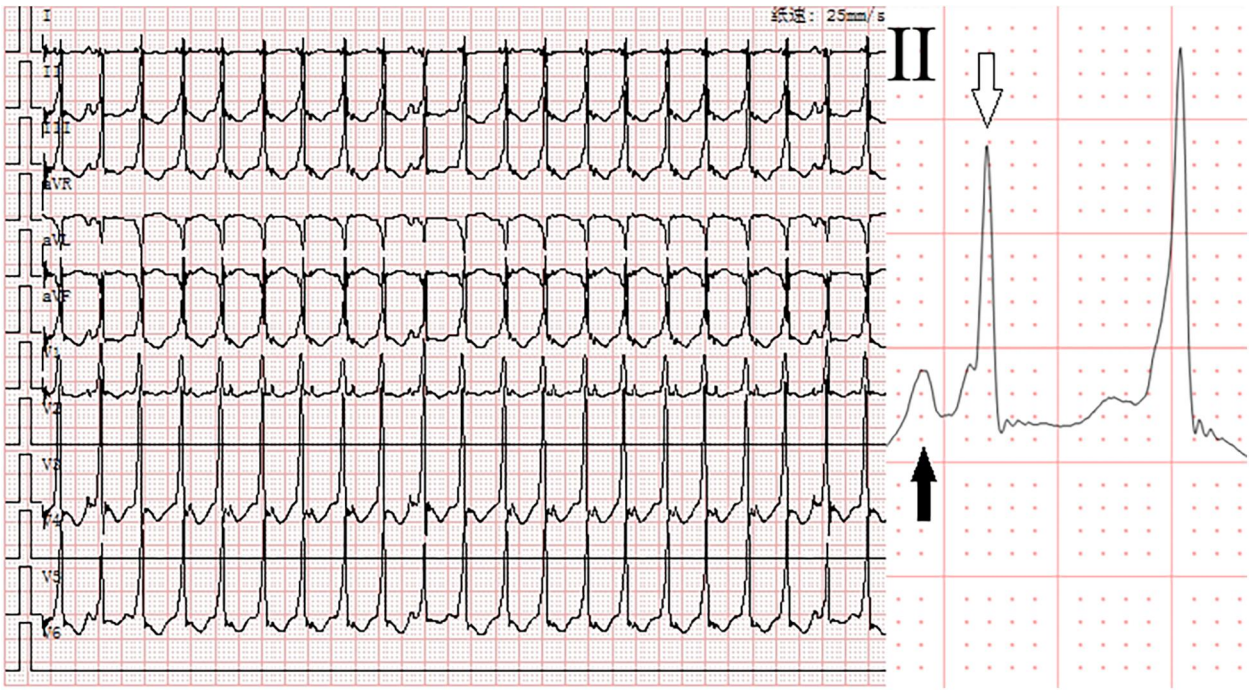

FIGURE 2
Electrocardiogram after adenosine. Monomorphic complex tachycardia (heart rate: 175 beats per minute, QRS duration: 92 ms) with atrioventricular dissociation and fusion beats. Solid arrows indicate P-waves, and hollow arrows indicate fusion beats.

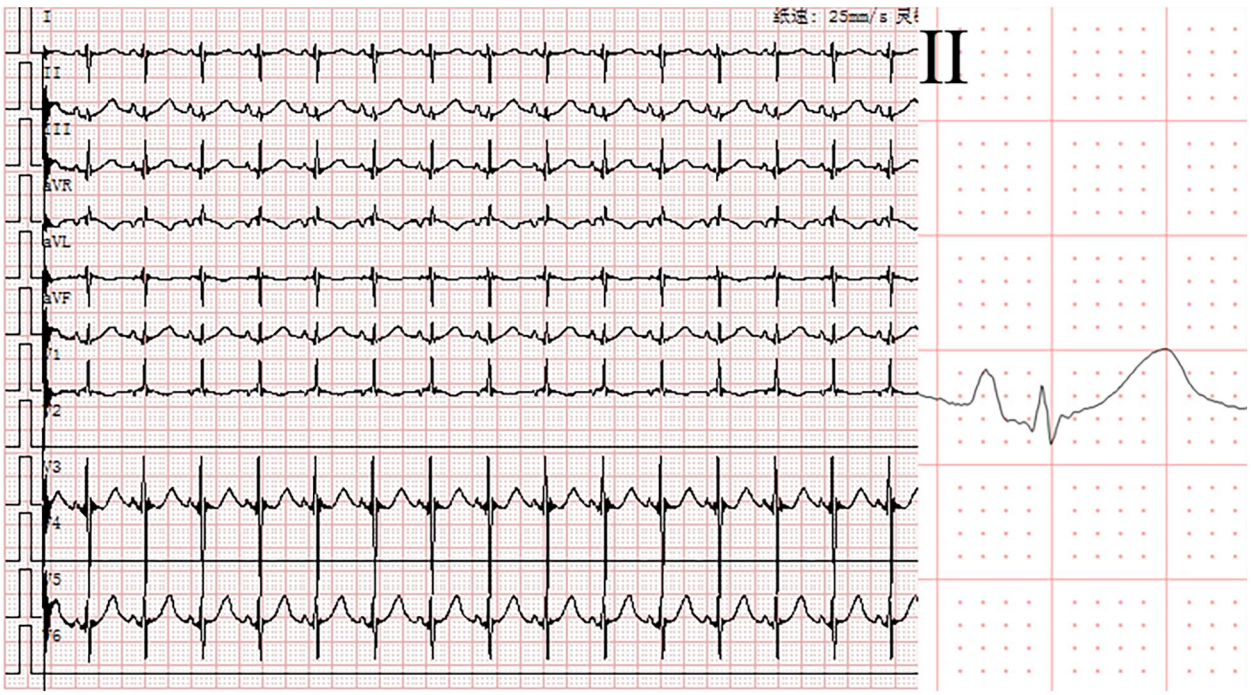

FIGURE 3
Electrocardiogram after electrical cardioversion. Sinus rhythm (heart rate: 123 beats per minute, QRS duration: 60 ms).

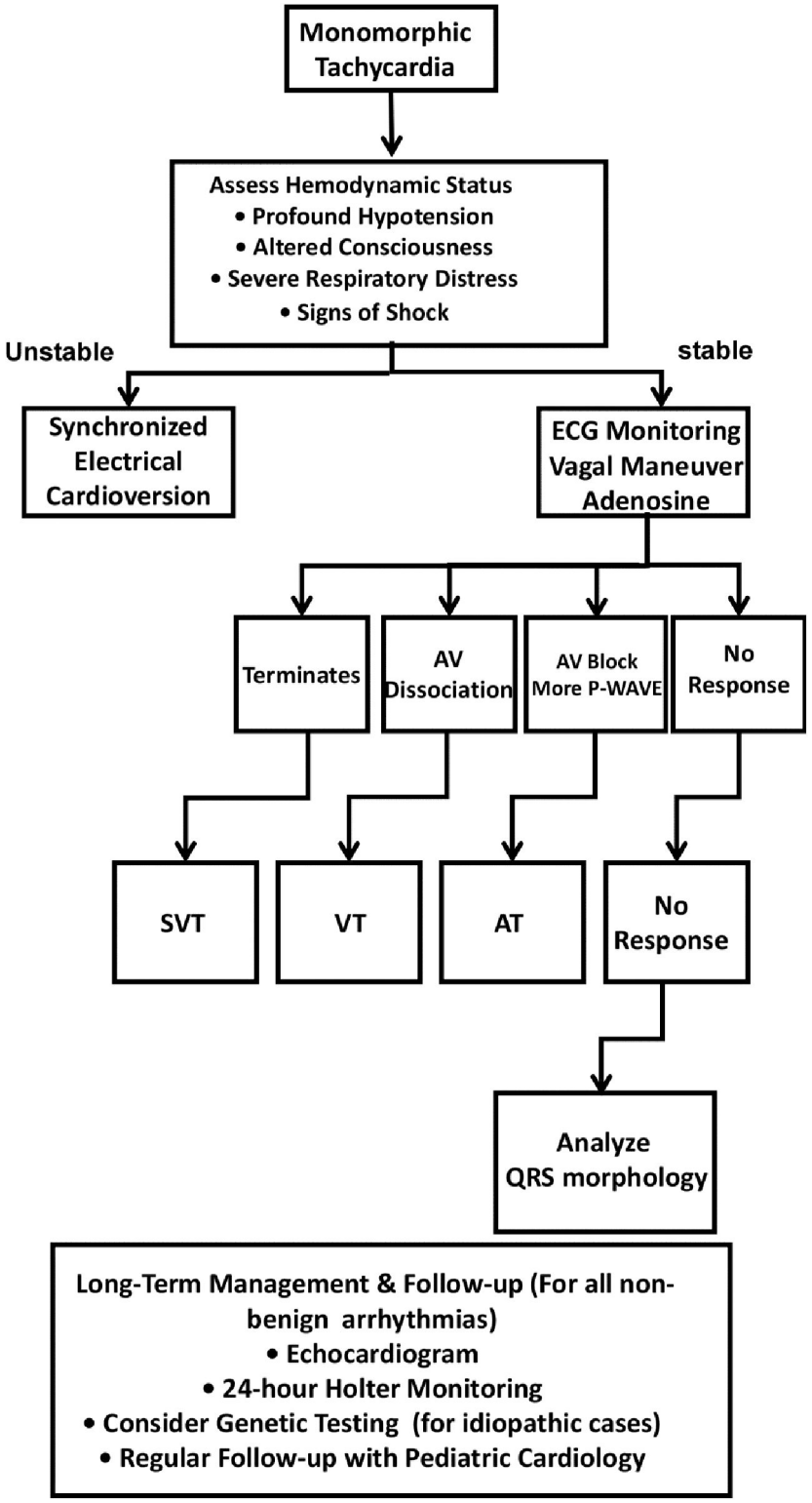

FIGURE 4
Proposed diagnostic algorithm for monomorphic tachycardia in neonates and infants. SVT, Supraventricular Tachycardia; VT, Ventricular Tachycardia; AT, Atrial Tachycardia.

maintained arrhythmia-free status throughout 48 h monitoring and the patient maintained clinical stability with preserved cardiac function at 8-week reassessment.

Discussion

Neonatal arrhythmias, particularly in preterm infants with structurally normal hearts, often pose diagnostic challenges (3). The neonate presented with refractory relatively narrow QRS complex tachycardia. Initially, the tachycardia was presumed to be supraventricular in origin based on the relatively narrow QRS duration (92 ms) and 1:1 retrograde P-wave morphology, prompting adenosine administration for attempted termination. Although adenosine failed to terminate the tachycardia, it played a crucial role in clarifying the diagnosis by inducing atrioventricular dissociation—a phenomenon inconsistent with SVT. Ultimately, the arrhythmia was successfully terminated via synchronized cardioversion. Additionally, retrospective comparison of the ECGs before and after cardioversion revealed two key features supporting ventricular tachycardia: (1) prolonged QRS complex duration during tachycardia (92 ms vs. 60 ms in sinus rhythm), and (2) delta wave-like slurring at the QRS onset. This diagnostic evolution underscores the importance of dynamic ECG reassessment and targeted therapeutic interventions in neonatal arrhythmia management.

The absence of structural heart defects or familial arrhythmia history in this case underscores the multifactorial nature of neonatal tachycardia (2). While congenital heart disease and electrolyte imbalances are common triggers, this neonate exhibited unremarkable echocardiographic and metabolic profiles. Elevated cardiac biomarkers (hs-TnT and NT-proBNP) further reflect myocardial strain, a phenomenon documented in arrhythmia-associated injury. We focus on supraventricular tachycardia (SVT) with aberrant conduction vs. ventricular tachycardia (VT). In this context, the administration of adenosine was instrumental. The induction of atrioventricular dissociation and fusion complex without termination of the tachycardia provided incontrovertible evidence for a diagnosis of VT, thereby excluding SVT with aberrancy as the underlying mechanism.

We wish to underscore that the administration of adenosine (or the use of vagal maneuvers) during continuous 12-lead ECG monitoring is a critical diagnostic step in the evaluation of every monomorphic, relatively narrow-complex tachycardia. This approach is essential not only for potential termination of SVT but, as demonstrated in this case, for its ability to induce atrioventricular dissociation—a pathognomonic sign of VT. Furthermore, a meticulous analysis of QRS morphology, including the presence of slurring or patterns suggestive of underlying cardiomyopathy, should be routinely performed alongside response to adenosine. Based on the diagnostic challenge encountered in this case, we propose a systematic diagnostic algorithm for clinicians facing regular tachycardia in neonates (Figure 4).

Electrical cardioversion—a strategy supported by recent guidelines for hemodynamically unstable arrhythmias. The successful restoration of sinus rhythm at 0.5 J/kg aligns with recommended energy doses (5–15 J), minimizing myocardial injury risk. Post-conversion metoprolol maintenance prevented recurrence. In this case, a comprehensive echocardiogram ruled out structural anomalies such as cardiac tumors or cardiomyopathy. In the context of idiopathic VT with a structurally normal heart, as was present here, empirical beta-blocker therapy is a standard and often effective prophylactic strategy to suppress adrenergically-mediated triggers. The patient's sustained positive response to metoprolol supports this approach, though long-term follow-up and consideration of advanced genetic testing remain important.

The patient's sustained stability at 8 weeks supports the efficacy of combined electrical and pharmacological intervention. However, neonatal arrhythmias even when transient may signal latent conduction abnormalities, warranting extended follow-up. Studies indicate that 13.4%–25% of neonates with SVT/VT exhibit recurrence within the first year, often associated with accessory pathways or channelopathies (4, 5). Genetic testing was not performed here but should be considered in idiopathic cases to exclude inherited arrhythmogenic disorders.

Conclusion

This case report underscores that life-threatening neonatal arrhythmias, including monomorphic tachycardias, may manifest in the absence of structural cardiac anomalies or familial predispositions, thereby presenting formidable diagnostic and therapeutic challenges. The diagnostic intricacy is accentuated by the pivotal role of pharmacologic agents that induce atrioventricular block, which can facilitate the differentiation of the underlying arrhythmogenic mechanisms. Expedient intervention, encompassing synchronized cardioversion when indicated, in conjunction with β-blocker prophylaxis, constitutes a salutary and efficacious management paradigm, particularly in preterm neonates undergoing transitional circulatory adaptations.

Data availability statement

The original contributions presented in the study are included in the article/Supplementary Material, further inquiries can be directed to the corresponding author.

Ethics statement

The studies involving humans were approved by Ethics Committee of Ordos Central Hospital. The studies were conducted in accordance with the local legislation and institutional requirements. Written informed consent for participation was not required from the participants or the participants' legal guardians/next of kin in accordance with the national legislation and institutional requirements. Written informed consent was obtained from the individual(s), and

minor(s)' legal guardian/next of kin, for the publication of any potentially identifiable images or data included in this article.

Author contributions

FW: Data curation, Writing – review & editing. BW: Writing – review & editing. JH: Writing – review & editing. BY: Writing – review & editing. PL: Data curation, Resources, Writing – original draft, Writing – review & editing.

Funding

The author(s) declare that no financial support was received for the research and/or publication of this article.

Conflict of interest

The authors declare that the research was conducted in the absence of any commercial or financial relationships that could be construed as a potential conflict of interest.

Generative AI statement

The author(s) declare that Generative AI was used in the creation of this manuscript. AI-assisted language optimization was applied under author supervision. Final content responsibility remains with authors.

Any alternative text (alt text) provided alongside figures in this article has been generated by Frontiers with the support of artificial intelligence and reasonable efforts have been made to ensure accuracy, including review by the authors wherever possible. If you identify any issues, please contact us.

Publisher's note

References

1. Ban J-E. Neonatal arrhythmias: diagnosis, treatment, and clinical outcome. *Korean J Pediatr*. (2017) 60:344–52. doi: 10.3345/kjp.2017.60.11.344

2. Jaeggi E, Öhman A. Fetal and neonatal arrhythmias. *Clin Perinatol*. (2016) 43:99–112. doi: 10.1016/j.clp.2015.11.007

3. Ciriello GD, Sorice D, Orlando A, Papaccioli G, Colonna D, Correra A, et al. Antiarrhythmic therapy for narrow QRS supraventricular tachyarrhythmias in newborns and infants in the first year of life: potent tools to be handled with care. *Indian Pacing Electrophysiol J*. (2024) 24:271–81. doi: 10.1016/j.ipej.2024.07.005

4. Chiu S-N, Wu W-L, Lu C-W, Tseng W-C, Wu K-L, Wang J-K, et al. Primary ventricular tachycardia in paediatric population in a tertiary centre. *Arch Dis Child*. (2017) 102:1137–42. doi: 10.1136/archdischild-2016-312418

5. Wei N, Lamba A, Franciosi S, Law IH, Ochoa LA, Johnsrude CL, et al. Medical management of infants with supraventricular tachycardia: results from a registry and review of the literature. *CJC Pediatr Congenital Heart Dis*. (2022) 1:11–22. doi: 10.1016/j.cjcpc.2021.09.001

frontiers | Frontiers in Physiology

TYPE Mini Review
PUBLISHED 30 October 2025
DOI 10.3389/fphys.2025.1676701

OPEN ACCESS

EDITED BY
Federico Landra,
University of Siena, Italy

REVIEWED BY
Hussam Ali,
MultiMedica Holding SpA (IRCCS), Italy

*CORRESPONDENCE
Bruno D. Stuyvers,
stuyvers@mun.ca

RECEIVED 30 July 2025
ACCEPTED 15 October 2025
PUBLISHED 30 October 2025

CITATION
Stuyvers BD (2025) Calcium arrhythmogenicity of Purkinje fibers: importance of the animal model.
Front. Physiol. 16:1676701.
doi: 10.3389/fphys.2025.1676701

Calcium arrhythmogenicity of Purkinje fibers: importance of the animal model

Bruno D. Stuyvers*

Faculty of Medicine–Division of Biomedical Sciences–Memorial University of Newfoundland, St. John's, NL, Canada

Ventricular tachycardias (VTs) and fibrillations (VFs) are frequent complications of ischemic myocardial infarction (MI). Because their initiation mechanism remains unknown, these arrhythmias are virtually unpredictable and often degenerate into cardiac arrest and syncope without immediate medical assistance. Electrical mapping and ablation techniques have located the origin of ischemic arrhythmias in the terminal arborizations of the cardiac conduction system, the Purkinje fibers. A classical model of MI in the dog has demonstrated that abnormal calcium (Ca^{2+}) cycling in the Purkinje cells (Pcells) is the source of non-driven depolarizations (DADs) in the conduction tissue and is likely to create the pro-arrhythmic conditions of human ischemic heart. A better understanding of Ca^{2+} abnormalities in Pcells post infarction is an evident prerequisite for elucidating the mechanism of ischemic arrhythmias. Nevertheless, a unique Ca^{2+} handling system was discovered in Pcells, exhibiting fundamental differences compared with the well-known model of Excitation-Contraction coupling of ventricular cardiomyocytes. This cellular specificity of Purkinje fibers was observed in large mammalian species but not in murine hearts, where Purkinje cells are comparable to ventricular myocytes and designed to respond to 400–600 stimulations/min. The present report reviews the mechanism of Ca^{2+} arrhythmogenicity in Pcells of large mammalian hearts and documents the need for animal models that simulate the size and function of human hearts to study ischemic arrhythmias.

KEYWORDS

calcium, arrhythmia, vt, VF, Purkinje fiber, Purkinje cell, myocardial ischemia, myocardial infarction

Introduction

Sudden cardiac death (SCD) accounts for 15%–20% of the mortality in adults worldwide. This dramatic issue is most frequently associated with ischemic heart disease (or coronary artery disease) and is caused by life-threatening ventricular tachycardia (VTs) and fibrillation (VFs). These tachyarrhythmias commonly arise in the setting of myocardial ischemia secondary to a coronary occlusion, particularly in the early stage of the myocardial infarction (MI) (Haissaguerre et al., 2016). The pathophysiology of those arrhythmias involves a complex interplay between ischemia-induced changes in ion channel function, cellular metabolism, and structural remodelling in the ventricular

myocardium (Ter Keurs and Boyden, 2007). However, the Purkinje fibers have been increasingly recognized as key contributors to the specific arrhythmogenesis post-MI (Haissaguerre et al., 2016; Nogami, 2011; Benali et al., 2024). There is a consensual agreement that this arrhythmic risk originates from intracellular calcium dysregulation in Purkinje cells (Ter Keurs and Boyden, 2007). Intracellular Ca^{2+} concentration oscillations in these cells generate non-driven (non-sinusal) electric impulses in the fibers, which trigger focal ectopic activity and reentry mechanisms in the myocardium. Understanding these Ca^{2+} abnormalities in Purkinje cells is the key to identifying and treating a fundamental cause of SCD post myocardial infarction. As with most human diseases, animal models are indispensable for investigating the underlying mechanisms of arrhythmia. Nevertheless, many questions regarding the physiology of Purkinje fibers still make it difficult to choose a suitable model. Even though our understanding of Purkinje cells is incomplete, it already indicates that the classical model of cardiac "excitation-contraction" coupling (Bers, 2002) does not apply to those cells. In addition, numerous observations have demonstrated that Purkinje cells exhibit structural differences that result in their Ca^{2+} handling varying across species. Considering the consensual implication of Ca^{2+} in the triggered arrhythmias of ischemic heart (see (Ter Keurs and Boyden, 2007) for review), the choice of animal models is crucial for investigating the origins of ischemic arrhythmias post infarction in human patients. This brief review summarizes our current knowledge of Purkinje cells and highlights some key elements in selecting the most suitable animal model for the pathophysiology of human Purkinje fibers.

Structural and electrophysiological characteristics of Purkinje cells

The Purkinje fibers

As initially described by Sunao Tawara (Akiyama, 2010), the Purkinje fibers (Figure 1A) form the terminal arborizations of the conduction system, branching in every region of the ventricles as prolongations of the His-Purkinje bundles. They are responsible for transmitting the nodal impulses to the working cardiomyocytes and coordinating the contraction of the ventricular chambers during the heartbeat. The Purkinje tissue is present in the ventricles as free-running strands in the subendocardial region and transmural fibers in the endocardium (Pauziene et al., 2017; Boyden et al., 1989). To date, no evidence has been found to support fundamental differences between the two types of fibers. However, the ratio of free strands to transmural varies among species. This ratio determines the accessibility of these fibers in animal models, such as the rat, which has a high density of intramural fibers, or the dog, which has a high density of free strands in the subendocardial region. The fibers are connected to the myocardium by transitional cells (Martinez-Palomo et al., 1970). Although very little is known about transitional cells, a possible role in the regulation of the conduction at the Purkinje-myocardium interface has been proposed, and some studies have implicated these cells as potential sources of arrhythmogenicity (Blackwell et al., 2022; Behradfar et al., 2014).

The cardiac Purkinje cells: structure and morphology

Purkinje cells and ventricular cardiomyocytes share the same rod shape and sarcomeric striation due to an organized myofibrillar system (Figure 1A). Although their density and arrangement in Purkinje cells vary among species (see Table 1), the myofibrils give both cell types a similar macroscopic appearance. This explains why the Purkinje cells are still referred to as "Purkinje myocytes" and have been considered a model for cardiac cell physiology in many past studies. In both cell types, the sarcomeres shorten when the surrounding Ca^{2+} concentration rises, but with apparently slower kinetics in Purkinje cells, suggesting differences in the protein composition of the sarcomeres. The reasons Purkinje cells encompass a functional contractile machinery remains unclear. It could be to coordinate the position of the Purkinje and myocardial fibers during the contraction.

As shown in Table 1, the morphology of Purkinje cells varies among mammalian species, but the major differences are observed between small and large hearts, likely due to distinct electrophysiological constraints (see Table 2).

The cardiac Purkinje cells: electrophysiology

The impulse velocity in the fibers varies with the heart size, likely related to the propagation distance, ranging from 1–2 m/s in small rodents to more than 4 m/s in larger animals (see Table 2), i. e., approximately tenfold larger compared to myocardium (0.3–0.4 m/s) (Durrer et al., 1970). The low resistance of Purkinje fibers (compared to myocardium) facilitates the rapid conduction of nodal impulses across the ventricle. Gap junctions in the intercalated disks participate in this low resistance. Electric and Ca^{2+} signals propagate cell-to-cell in the Purkinje fiber through the gap junctions, which, like those in ventricular myocytes, contain channels composed of connexins 40 (Cx40) and 43 (Cx43) (Table 1). The conductance of the Cx40 channel is twice as high as that of the Cx43 channel, and Cx40 is three times more concentrated in Purkinje cells compared to ventricular cells (Sivagangabalan et al., 2014; Kanter et al., 1993). This predominance of C x 40 is likely to facilitate the rapid intercellular current flow and contribute to the high conduction velocity in the Purkinje fibers. Connexin 45 forms low-conductance gap junction channels and is also expressed in the Purkinje cells, possibly modulating the conduction in the fibers (Dun and Boyden, 2008).

At the cellular level, presumably still related to the conduction function of Purkinje tissue, there are significant differences in the electrophysiology of Purkinje cells compared to ventricular myocytes, as thoroughly reviewed in (Dun and Boyden, 2008; Boyden et al., 2010). In brief, the Purkinje cells have a longer action potential with a prominent phase 1 of repolarization, longer APD50 and APD90, a more negative plateau, and larger AP amplitude than ventricular cells (Dun and Boyden, 2008). Although two levels of resting membrane potential (RMP) have been reported in Purkinje fibers (Gadsby and Cranefield, 1977), it is widely recognized that, under normal physiological conditions, the RP (~-80 mV) is comparable to that of ventricular myocytes

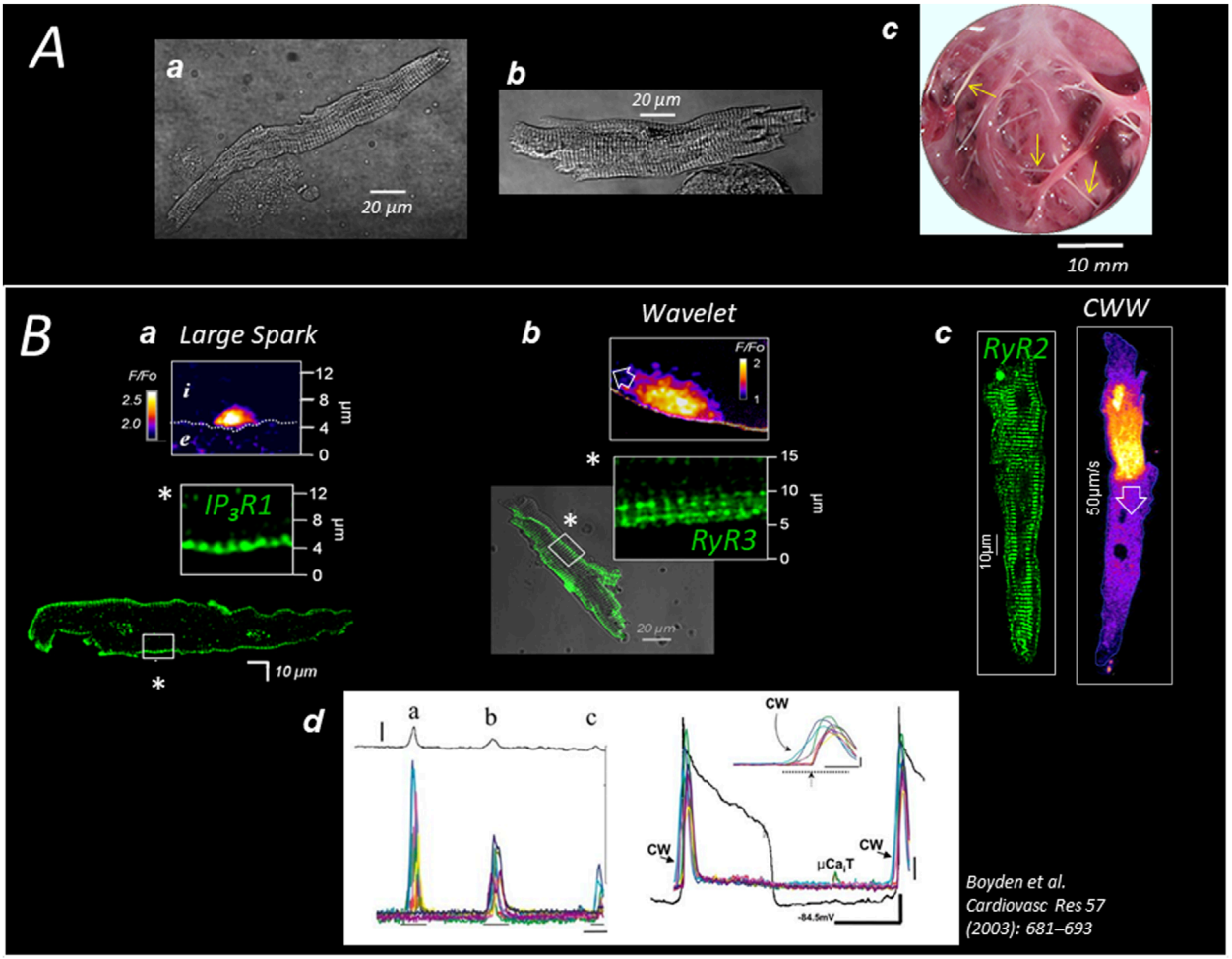

FIGURE 1
Specific Ca^{2+} handling of cardiac Purkinje cells in large mammalian species **(A)** Pig (a) and human (b) Purkinje cells are enzymatically dispersed from sub-endocardial (free-running) Purkinje strands (c; see arrows in pig heart). **(B)** The expression of 3 different channels (here in dog heart) delimits three concentric regions of SR-Ca^{2+} release; the first region (a) extends 2–3 µm under the sarcolemma (SL) and expresses the Inositol Phosphate Receptor *IP3R1* which generates large Ca^{2+} sparks; the second layer (b) extends 5–10 µm under the SL and expresses the (non-cardiac) ryanodine receptor *RyR3;* the RyR3 region produces small waves (Wavelets) which propagate on short distances exclusively at the cell periphery and are of the same amplitude than sparks; the third layer (c) fills most of the cell core, expressing the typical cardiac ryanodine receptor *RyR2* which produces large cell-wide waves (CWWs); CWWs (d) induce membrane depolarizations (DADs) proportional to the density and amplitude of the waves present in the cell or in the cell aggregate (left panel) and, occasionally, can trigger a full action potential (right panel).

(Boyden et al., 2010). However, a slow diastolic depolarization due to the presence of I_F current can arise in Purkinje fibers in the absence of overdrive suppression by the sinus rhythm (Dun and Boyden, 2008). Although the regular activity of Purkinje fibers in the heart is triggered, the presence of I_F current attributes the Purkinje tissue with a natural tendency towards automaticity, ranging from 20 to 40 beats per minute in large mammalian species, including humans (Vassalle, 1977).

Ca^{2+} handling and Ca^{2+} mobilization of Purkinje cells

The primary function of Purkinje cells is to generate an AP in response to evoked depolarization from adjacent cells in the fiber. The membrane depolarization and formation of action potential in Purkinje cells involve voltage-gated channels, with specific isoform profiles explicitly expressed in those cells as listed in (Dun and Boyden, 2008). Nearly as a side effect of the electrical transmission function of Purkinje cells, the depolarization is accompanied by an influx of Ca^{2+} in the cytosol due to the activation of two voltage gated Ca^{2+} channels: the L-type Ca^{2+} channel (LTCC) with the two isoforms Cav1.2 and Cav1.3, and the T-type Ca^{2+} channel (TTCC) with the three isoforms Cav3.1, Cav3.2, and Cav3.3 (Dun and Boyden, 2008; Rosati et al., 2007). Unlike ventricular myocytes, a large representation of T-type Ca^{2+} current (ICaT) compared to L-type Ca^{2+} current (ICaL) has been reported in Purkinje fibers (Tseng and Boyden, 1989). ICa,T activates at more hyperpolarizing potentials than the high-voltage ICa,L, which is predominant in cardiomyocytes. Strongly expressed in nodal cells and Purkinje cells, a role in pacemaker activity has been attributed to ICa,T (Mangoni and Nargeot, 2008). These Ca^{2+} currents trigger

TABLE 1 This table summarizes the comparative morphology and ultrastructure of cardiac Purkinje cells across several mammalian species.

Species	Cell morphology and size (Comparison vs. human)	Intercalated disks (IDs) and connexins (Cx)	Ultrastructure	References
Mouse	Small, cylindrical; length <80 µm; diameter 10 µm; (smaller than human)	Simple (staircase) IDs with few gap junctions; mainly Cx40, minimal Cx43, rare Cx45	Few myofibrils, Abundant SR (junctional); Normal T-tubules (vs. ventricular myocytes)	Ono et al. (2009), Miquerol et al. (2010)
Rat	Cylindrical, short bundles; length <120 µm, diameter <10 µm; (smaller than human)	Short (staircase) IDs with moderate gap junctions; mainly Cx40, low Cx43, rare Cx45	Few myofibrils; Abundant SR (junctional) Normal T-tubules (vs. ventricular myocytes)	Ono et al. (2009), Matsushita et al. (1999), Di Maio et al. (2007)
Rabbit	Cylindrical, elongated; Length 120 Diameter ~20 µm (smaller than human)	disks distinct (limited data) Cx40 present, Cx43 minimal	Moderate, Peripheral myofibrils Well-developed SR (junctional); Limited to abundant T-tubules	Sommer and Johnson (1968), Cordeiro et al. (2001)
Cat	Cylindrical, branched, elongated; Length ~120 µm Diameter ~15 µm (slightly shorter and thinner than human)	disks distinct (limited data) Cx40 high (likely), Cx43 moderate	Moderate, peripheral myofibrils Well-developed SR (junctional and corbular); Limited to abundant T-tubules	Sommer and Johnson (1968)
Dog	Cylindrical or fusiform; length 120–180 µm, diameter 20–40 µm; (slightly shorter and thinner than human)	Large, complex (finger-like) IDs; abundant Cx40, moderate Cx43, minor Cx45	Abundant, peripheral myofibrils; Developed SR (junctional and corbular) T-tubules parse/discontinuous	Boyden et al. (1989), Sommer and Johnson (1968), Kanter et al. (1993)
Sheep	Cylindrical or Oval; length 150–220 µm, diameter 20–30 µm; (similar diameter but shorter than human)	Well-developed (finger-like) IDs; abundant Cx40, moderate Cx43, minor Cx45	Peripheral, abundant myofibrils Developed SR (junctional and corbular) T-tubules sparse	Mobley and Page (1972), Oliphant and Loewen (1976)
Pig	Cylindrical or Oval; length 150–200 µm, diameter 25–35 µm; (slightly shorter and thinner than human)	Complex (finger-like) IDs; abundant Cx40, moderate Cx43, minor Cx45	Peripheral, abundant myofibrils; Developed SR (junctional and corbular) T-tubules sparse	Garcia-Bustos et al. (2017), Daniels et al. (2017), Stankovičová et al. (2003)
Cow	Polygonal; length 180–250 µm, diameter 25–40 µm; (similar diameter but longer than human)	Numerous IDs; abundant Cx40, moderate Cx43, minor Cx45	Sparse myofibrils; Developed SR (corbular) T-tubules sparse	Ono et al. (2009), Forsgren and Thornell (1981)
Human	Cylindrical/fusiform; length 120–200 µm, diameter 30–50 µm	Well-developed (finger-like) IDs; abundant Cx40, moderate Cx43, minor Cx45	Peripheral abundant myofibrils; Developed SR (junctional and corbular) T-tubules sparse/discontinuous	Sommer and Johnson (1968), Anderson et al. (2013)

further Ca^{2+} release from the intracellular Ca^{2+} compartment, the sarcoplasmic reticulum (SR), in a process called "Ca^{2+} induced Ca^{2+} Release" (CICR) (Fabiato, 1983). In ventricular cardiomyocytes, the SR is arranged around the myofibrils. Tubular invaginations of the sarcolemma, called transverse tubules (T tubules), extend deep in the cell at the level of every Z-disc in the myofibrils. In this region, referred to as the "dyadic cleft", the T-tubules are close to the terminal cisternae of the SR (junctional SR) so that L-type Ca^{2+} channels in the membrane of the tubules face clusters of Ca^{2+} channels, RyR2, in the SR membrane. This arrangement is ubiquitously distributed in cardiomyocytes and is crucial for the uniform CICR and synchronous contraction of those cells. Ca^{2+} is released from the junctional SR in the dyadic cleft, but it can also occur outside, from isolated extremities of the SR called corbular SR (Franzini-Armstrong et al., 1999).

In large mammalian species, such as dogs, sheep, pigs, and humans (see Table 1), Purkinje cells are devoid of organized transverse tubular system (Sommer and Johnson, 1968; Cordeiro et al., 2001; Daniels et al., 2017; Sommer and Johnson, 1970) and exhibit an internal structure comparable to that of atrial myocytes (Bootman et al., 2011; Mackenzie et al., 2004). In this condition, the intracellular Ca^{2+} mobilization in Purkinje cells primarily relies on the release of Ca^{2+} by the corbular SR in the core and, to a lesser extent, by the junctional SR under the membrane

TABLE 2 Comparative Electrophysiology of Cardiac Purkinje Cells Across Mammals.

Species	RMP (mV)	AP amp (mV)	dV/dt_max (V/s)	APD50/APD90 (ms)	CV (m/s)	Automaticity	Major ionic currents	Refs
Mouse	≈ −70 to −80	Large AP amplitude (~80–100)	Higher than ventricular myocytes	APD longer than ventricular myocytes	0.5–2	Spontaneous pacemaker activity observed in some isolated PCells	INa density larger than VMs; ICa,L and ICa,T present; Ito reduced; IK1 similar to VMs	Vaidyanathan et al. (2013)
Rabbit	≈ −75 to −85 (Purkinje strands)	~80–110	~150–300 higher than ventricular myocytes	APD90 often ~200–400 ms at 1 Hz in tissue studies	~1–2.5 multi- cellular prep	Uncommon *in situ*; more frequent in isolated cells	INa robust; ICaL present; Ito and Ikr present; contributions from ICaT variable	Cordeiro et al. (1998)
Dog	≈ −80 to −90 isolated canine Purkinje fibers	~90–110	~150–300 High upstroke velocities	APD90 200–400 ms at 1 Hz (long plateau)	0.8–2.5	Can show automaticity in isolated preparations; implication in arrhythmias	Prominent INa; ICaL present; lower Ito	Dun and Boyden (2008), Saitoh et al. (1989), Reder et al. (1981)
Sheep	~ −80 to −90	AP amplitude large; exact values vary	high dV/dt and long APDs; no precise numeric values	APD90 often long (hundreds of ms)	1.5–3	Spontaneous activity occasionally observed	Major currents: INa, ICaL prominent; lower Ito vs. myocardium	Verkerk et al. (1999)
Pig	≈ −80 to −90	AP amplitude large (~90–110 mV)	dV/dt_max high; numerical values vary with prep	APD50/APD90 long (hundreds of ms) in pig PF preparations at 1 Hz	~1.5–3	Automaticity less common *in situ*; isolated cells may show pacemaker activity	Prominent INa, ICaL; Ito lower; connexin Cx40 expression strong	Garcia-Bustos et al. (2017), Gettes and Surawicz (1968), Dosdall et al. (2007)
Human	≈ −80 to −90 (varies with disease and sample)	~80–110	>100	long APDs; APD90 ~100	~1–2.5	can show automaticity in isolated prep and are implicated in clinical arrhythmias	INa prominent; ICaL present; human PF vs. VM large differences	Dangman et al. (1982), Ideker et al. (2009)

Parameters: RMP, resting membrane potential; AP amp, action potential amplitude; dV/dt_max, maximum upstroke velocity; APD50/APD90, action potential duration at 50%/90% repolarization; CV, conduction velocity; Refs, References.

10.3389/fphys.2025.1676701

(Ter Keurs and Boyden, 2007). Upon electric stimulation, Ca^{2+} enters the cell mostly across the peripheral membrane through the voltage-gated inward Ca^{2+} currents. The absence of T tubules in the core predicts that, in Purkinje cells, the influence of Na-Ca exchange (NCX) is limited to a restricted space under the sarcolemma, known as the "SubSL" compartment (Stuyvers et al., 2005), and Ca^{2+} in the center is modulated by diffusion and SR Ca^{2+} transport systems.

In large mammalian species, the absence of T tubules reduces the total membrane surface area of the cell, which likely also contributes to the low total membrane resistance and rapid conduction of Purkinje fibers. The functional consequence of this structural particularity in Purkinje cells is a non-uniform and slower intracellular Ca^{2+} mobilization compared to that of ventricular cardiomyocytes (Boyden et al., 2003). A biphasic Ca^{2+} response to electrical stimulation was reported in Purkinje cells, based on the aequorin signal, by Wier 45 years ago (Gil and Hess, 1984). Consistently, using more recent Ca^{2+} probes and advanced Ca^{2+} imaging techniques, we found that stimulation induces a first release of Ca^{2+} under the sarcolemma, probably from junctional SR in the SubSL, followed by the progression of a front of elevated Ca^{2+} toward the cell center (Haq et al., 2013); see Figure 2. Sarcomere shortening is observed at the end of the progression, when the cytosol is fully loaded with Ca^{2+}. A specific model of Ca^{2+} mobilization demonstrated that this "centripetal" propagation results from a combination of Ca^{2+} diffusion and consecutive Ca^{2+} release (by CICR) from concentric layers of the SR (Dun and Boyden, 2008; Boyden et al., 2010); Figure 2B. Presumably supporting this centripetal Ca^{2+} mobilization and, more generally, possibly compensating for the absence of T tubules, Purkinje cells were shown to express in canine heart three types of SR-Ca^{2+} channels (Daniels et al., 2017; Stuyvers et al., 2005) (Figures 1B, 2A): IP_3R1 under the sarcolemma, RyR3 deeper but still in the peripheral region of the SR, and the "cardiac" RyR2 in the central SR. The distinct localization of these channels defines three specific regions of SR-Ca^{2+} release (Stuyvers et al., 2005). So far, we have observed the same arrangement of channels and the same centripetal Ca^{2+} mobilization in dog, sheep, pig, and human Purkinje cells.

In summary, as shown in Figure 2D, the electric stimulation of Purkinje cells mediates a typical centripetal Ca^{2+} mobilization, which is produced by the consecutive activation of IP3R1-, RyR3-, and RyR2-Ca^{2+} release regions. A computational model of this mechanism has been proposed in (Haq et al., 2013).

Like RyR2 in the ventricular myocytes, the three SR-Ca^{2+} release channels of the Purkinje cell spontaneously generate stochastic spark- and wave-like events (Stuyvers et al., 2005), as illustrated in Figure 1B. Because of different biophysical properties, the three channels open at distinct Ca^{2+} concentrations and with different kinetics, creating three regions of specific spontaneous Ca^{2+} events (Figure 1B); (Stuyvers et al., 2005; Daniels et al., 2017): large asymmetrical Ca^{2+} sparks under the sarcolemma, small Ca^{2+} waves ("wavelets") that propagate over short distances in the peripheral RyR3-region, and large Ca^{2+} waves ("Cell-Wide-Waves" or "CWWs") spanning the entire width of the cell and travelling in the cell and cell-to-cell in the longitudinal direction of the fibers. The CWWs are of sufficient magnitude to depolarize the membrane through NCX activation and are the Ca^{2+} events underlying the DADs in Purkinje cells (Boyden et al., 2000); see Panel B in Figure 1. Wavelets are thought to be the triggering events (by CICR) of the CWWs in the cell periphery (Stuyvers et al., 2005). Regular Ca^{2+} sparks were observed in the three regions of Ca^{2+} release (Stuyvers et al., 2005; Hirose et al., 2006).

Ca^{2+} arrhythmogenicity of Purkinje fibers post infarction

Delayed afterdepolarization (DAD) is the electrical event that initiates triggered arrhythmias in the Purkinje fibers. DADs are observed in all cardiac cells and are caused by spontaneous rises in cytoplasmic Ca^{2+} concentration (Figure 1B), commonly resulting from SR Ca^{2+} release (Hirose et al., 2006), and, occasionally in cardiomyocytes, by sudden Ca^{2+} demobilization from the myofibrillar troponin C (Ter Keurs et al., 2006). The increase of cytosolic Ca^{2+} activates NCX, generating a forward mode I_{NCX} current, as well as other Ca^{2+}–sensitive currents, such as chloride currents and non-selective cationic currents (Ter Keurs and Boyden, 2007). The resulting ionic imbalance depolarizes the membrane, generating a DAD. Technically, the amplitude of the DAD depends on the size of the resting K^+ conductance, mainly determined by the inward-rectifier K^+-current I_{K1}, relative to I_{NCX} amplitude (Landstrom et al., 2017). A spontaneous AP can arise when the DAD amplitude reaches the threshold of the inward I_{Na} current (Figure 1B). The spontaneous APs in Purkinje fibers activate the surrounding myocardium, producing a premature ventricular beat/contraction (PVB/PVC), the first marker of a more severe tachycardic occurrence (Reder et al., 1981; Dosdall et al., 2007). The frequency and amplitude of DADs and PVBs determine the onset of the tachyarrhythmia in the ventricle.

Therefore, Ca^{2+} is the principal player in the generation of DADs, and the abnormal spontaneous Ca^{2+} activity in the Purkinje cells is widely recognized as a cause of tachyarrhythmias in the ischemic heart (Haissaguerre et al., 2016).

Although the fundamental alteration that leads to the "electrogenic" Ca^{2+} release in Purkinje cells remains unknown, several hypotheses can be discussed from our current understanding of Purkinje cells. First, inspired by the alteration of the RyR2 reported in inherited tachycardic diseases, such as CPVT (Priori and Chen, 2011; Herron et al., 2010; Kang et al., 2010), aberrant SR-Ca^{2+} release has been proposed to explain the arrhythmogenicity of Purkinje cells post-infarction (Hirose et al., 2006; Hirose et al., 2008). Similarly, an upregulation of SR-Ca^{2+} release by the reticular protein CASQ2 (Chen et al., 2013) or a reduction of its Ca^{2+} buffering capacity due, e.g., to an alteration similar to the mutation discussed in (Faggioni and Knollmann, 2012; Galimberti and Knollmann, 2011), could increase the Ca^{2+} liberation by the SR. Alternatively, a potentiation of SR-Ca^{2+} uptake would be expected to accelerate the transfer of Ca^{2+} from Ca^{2+} pumps to the Ca^{2+} release channels, possibly causing the abnormal increase in SR-Ca^{2+} release in Purkinje cells.

Beyond the alteration underlying the pro-arrhythmic augmentation of spontaneous Ca^{2+} release, another striking question is how ischemia in the ventricular myocardium induces the Ca^{2+} arrhythmogenicity in the Purkinje fibers.

It is well known that Ca^{2+} overload arises in cells directly exposed to ischemia, mainly due to the depletion of cellular energy and depression of ATP-dependent Ca^{2+} extrusion from the

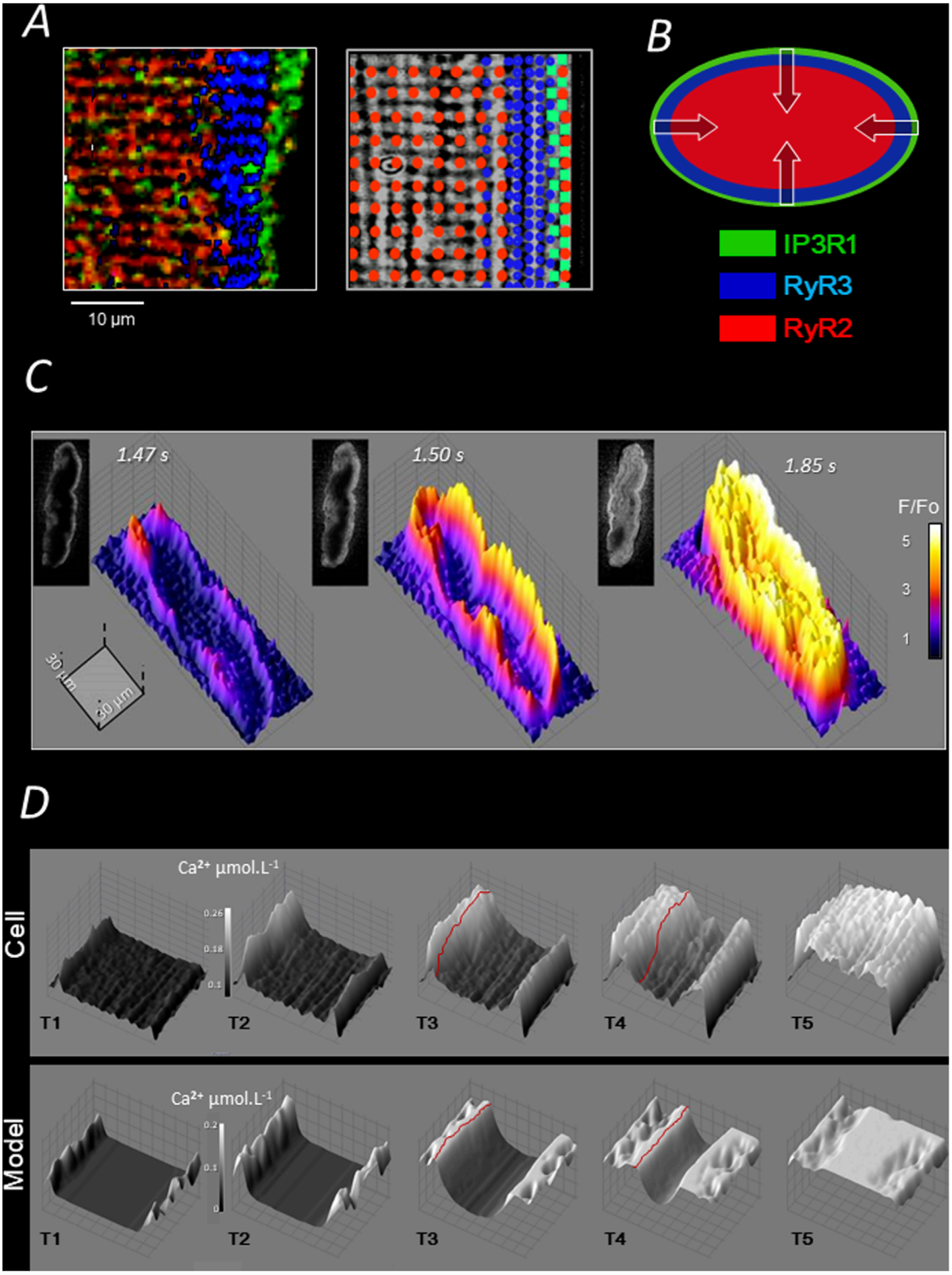

FIGURE 2
Ca^{2+} handling and electrically evoked Ca^{2+} mobilization of pig Purkinje cells. **(A)** Each of the three channel regions described in Figure 1B is stained with a specific antibody in the left panel (color legend is represented in B); the three regions partially overlap over a few micrometers; as shown in the right panel, the intermediate expression of RyR3 overlaps with both RyR2 and IP3R regions and some RyR2 are expressed in the IP3R region (Stuyvers et al., 2005); **(B)** the layered arrangement of SR Ca^{2+} channels shown in A allows for centripetal "layer-to-layer" activation by CICR and Ca^{2+} diffusion (Daniels et al., 2017). **(C)** 2D and 3D illustrations of three representative sequences of the (AP-mediated) centripetal Ca^{2+} propagation in pig Purkinje cells (see text). **(D)** Computational modelling of the centripetal propagation of Ca2+ in pig Purkinje cells; red lines underline the Ca^{2+} front moving toward the cell centre by CICR and diffusion (Haq et al., 2013).

cytosol. In addition to loading the SR with Ca^{2+} and increasing the spontaneous SR-Ca^{2+} release ("SR Ca^{2+} leak"), the excess of Ca^{2+} in the cell triggers multiple reactions involved in apoptosis, hibernation, and cell death (Webster, 2012; Lüss et al., 1998). This is the case in ventricular myocytes of the infarction area. However, the early evidence of increased spontaneous Ca^{2+} activity in Purkinje cells after MI has been found in free-running Purkinje fibers spanning the subendocardial region. Except at the Purkinje-myocardium interface, these fibers are anatomically independent of the ventricular myocardium and are frequently connected to the endocardium outside the ischemic area. In this situation, it is logical to anticipate that these free-running strands primarily rely on O_2 and nutrients from the surrounding blood flow in the chamber (Janse and Wit, 1989) and are not directly exposed to the ischemic conditions affecting the myocardium. Interestingly, this may suggest a potential release of bioactive (paracrine) agents by the ischemic myocardial cells and "remote" impact on the intracellular Ca^{2+} handling of subendocardial Purkinje strands.

Purkinje fibers are involved in many different types of cardiac arrhythmias, with a majority related to myocardial ischemia and infarction, as reviewed in (Nogami et al., 2023). The mechanisms of these arrhythmias evolve with the different stages of the MI, but the exact time course of Purkinje-mediated arrhythmicity from the onset of an acute ischemic attack to the healed MI and scar formation is not clearly established in human patients. In the dog model of coronary ligation, the Purkinje arrhythmogenicity has been reported under the form of Purkinje-mediated triggers of VTs and VFs after reperfusion during the acute phase 1b (~30 min) (Xing and Martins, 2001; Arnar and Martins, 2002). After the scar formation, in the long-term chronic phase 3 (weeks, months) post MI, Purkinje fibers surviving in the healed MI area, remain excitable but more prone to Ca^{2+}-mediated DADs. The Purkinje focal activity could occasionally trigger monomorphic VTs or participate in reentrant circuits in a minority of patients (less than 5%) (Bogun et al., 2006). Ablation of these foci usually abolishes those late and often recurrent arrhythmias (Charton et al., 2023). Nevertheless, animal models have shown that Ca^{2+}-mediated arrhythmogenicity is a specific feature of Purkinje fibers located in the border zone of the infarct and arises during the subacute phase 2 (within 48–72 h) while the infarct is still evolving (Haissaguerre et al., 2016). Despite the known large prevalence of VTs and VFs, likely due to abnormal Ca^{2+} handling-induced DADs in Purkinje cells, and the high risk of sudden cardiac death during this phase (Frampton et al., 2023), no precise quantification of phase 2 arrhythmic incidence has been reported in humans (Sattler et al., 2019).

Importance of animal models for the study of Ca^{2+} arrhythmogenicity

Animal models are indispensable for providing not only mechanistic insight into the Ca^{2+} arrhythmogenicity of Purkinje fibers in humans but also assisting the development of targeted antiarrhythmic therapies. Pursuing these goals requires high-resolution tools and invasive techniques that further justify the use of animal models of the human heart.

Nevertheless, the differences identified so far between Purkinje cells and ventricular myocytes have been observed in the hearts of large mammalian species. In small rodents, Purkinje cells are comparable to ventricular myocytes as both cell types contain the same arrangement of myofibrils, abundant transverse tubules, and well-developed sarcoplasmic reticulum (Di Maio et al., 2007). Interestingly, the presence of T tubules in mouse and rat Purkinje cells suggests that Ca^{2+} handling and Ca^{2+} mobilization in small rodents do not show the specific characteristics found in cells of large animals, potentially including humans. Supposing that these differences of Purkinje fibers compared to myocardium found in large-sized hearts are to facilitate the conduction, their absence in mice and rats is not surprising, since the impulse propagation distance is shorter and, therefore, the need for low-resistance fibers is less than in larger hearts.

To date, experimental and clinical data support the conclusion that the post-MI risk of ventricular fibrillation and cardiac arrest in humans is linked to a deficient component of Ca^{2+} handling in Purkinje cells (Haissaguerre et al., 2016). Models addressing this deficiency must consider the interspecies differences, specifically the discrepancy in Ca^{2+} handling systems and Ca^{2+} mobilization between small and large animals. For instance, the hypothesis of aberrant SR Ca^{2+} release as the source of arrhythmogenicity may ultimately apply to mouse or rat models in which Purkinje cells are likely to express only one SR Ca^{2+} channel (RyR2). The same hypothesis is less likely in large animal species. Increased SR-Ca^{2+} release has been evidenced 48 h after coronary ligation in canine Purkinje cells, in the three regions expressing distinct channels (Hirose et al., 2006). The simultaneous alteration of the three channels in distinct subcellular regions within 2 days is improbable. As another example, the IP_3R1 channel has been recently implicated in the arrhythmogenesis of the human heart (Sun et al., 2025). However, confirmation of this implication has been achieved by inducing IP3R1 expression in a mouse model of Purkinje cells, which are expected to express a radically different Ca^{2+} handling system compared to that predicted in human Purkinje cells, where IP3R1 is likely to play a role in the centripetal Ca^{2+} mobilization.

Our current knowledge of Purkinje cells in large animal species strongly suggests that the subcellular foundations of Ca^{2+} arrhythmogenicity differ between mouse and human Purkinje cells. Considering the arguments supporting abnormal Ca^{2+} handling as a probable source of Purkinje pro-arrhythmicity in ischemic human hearts, only cell models with a Ca^{2+} management system consistent with that of common large mammalian species will be suitable for identifying the molecular origins of triggered arrhythmias in humans.

In addition, the anatomy of the Purkinje tissue influences the cardiac conduction (Vigmond and Stuyvers, 2016) and also displays notable differences among animals. For example, horses have more abundant and thicker Purkinje fibers compared to dogs. Like human and rabbit Purkinje fibers, most dog Purkinje fibers extend in the subendocardial region as free strands with many subendocardial connections with the myocardium. On the contrary, most pig Purkinje fibers are transmural and connect with the myocardium throughout the ventricular wall (Gómez-Torres et al., 2021; Šolc, 2007; Lelovas et al., 2014). Overall, the pig heart is currently recognized as one of the most effectiv

translational models for cardiovascular diseases (Mackenzie et al., 2004; Stuyvers et al., 2005), while the dog heart is widely used in cardiac electrophysiology (Willis and Oliveira, 2018). Nevertheless, the Purkinje cells of both species appear to exhibit the same features currently predicted in human cells. This aspect may also be considered when selecting translational models for ischemic arrhythmias.

Finally, while murine models are well adapted to study a specific protein expression the distinctive features of the heart, including the Purkinje system, in the small animals should be considered in the mechanistic studies of Purkinje-induced Ca^{2+} arrhythmia in humans.

Conclusion

Purkinje fibers, once considered passive conductors, are now clinically recognized as active arrhythmogenic agents in the ischemic and infarcted heart. Animal models strongly suggest that the unique Ca^{2+} handling of Purkinje cells is involved in the spontaneous depolarizations that initiate lethal ventricular tachyarrhythmias upon ischemic myocardial infarction. The discovery of specific features in the Ca^{2+} handling of Purkinje cells is relatively recent. Numerous questions remain concerning the evoked and spontaneous activation of these cells in the current translational animal models, and the applicability of many findings to humans, although highly probable, has not yet been formally established. However, the level of our knowledge is sufficient to indicate that the choice of animal models for human ischemic arrhythmias must integrate the unique features recently discovered in the Purkinje cells of large mammalian species.

Intracellular Ca^{2+} manipulations have already been considered for treating the ischemic arrhythmic risk (Ter Keurs and Boyden, 2007; Boyden and Ter Keurs, 2005). Still, the lethal arrhythmias will remain unpredictable as long as the exact origin of Ca^{2+} dysfunctions in Purkinje fibers of ischemic heart is not clarified.

Author contributions

BS: Writing – original draft, Writing – review and editing.

Funding

The author(s) declare that no financial support was received for the research and/or publication of this article.

Conflict of interest

The author declares that the research was conducted in the absence of any commercial or financial relationships that could be construed as a potential conflict of interest.

Generative AI statement

The author(s) declare that no Generative AI was used in the creation of this manuscript.

Any alternative text (alt text) provided alongside figures in this article has been generated by Frontiers with the support of artificial intelligence and reasonable efforts have been made to ensure accuracy, including review by the authors wherever possible. If you identify any issues, please contact us.

Publisher's note

References

Akiyama, T. (2010). Sunao tawara: discoverer of the atrioventricular conduction system of the heart. *Cardiol. J.* 17, 428–434.

Anderson, R. H., Boyett, M. R., Dobrzynski, H., and Moorman, A. F. M. (2013). The anatomy of the conduction system: implications for the clinical cardiologist. *J. Cardiovasc Transl. Res.* 6, 187–196. doi:10.1007/s12265-012-9433-0

Arnar, D. O., and Martins, J. B. (2002). Purkinje involvement in arrhythmias after coronary artery reperfusion. *Am. J. Physiol. Hear Circ. Physiol.* 282, 1189–1196. doi:10.1152/ajpheart.00227.2001

Behradfar, E., Nygren, A., and Vigmond, E. J. (2014). The role of purkinje-myocardial coupling during ventricular arrhythmia: a modeling study. *PLoS One* 9, e88000. doi:10.1371/journal.pone.0088000

Benali, K., Vigmond, E. J., and Haissaguerre, M. (2024). Identifying Purkinje involvement in ventricular fibrillation substrate. *JACC Clin. Electrophysiol.* 10, 1791–1793. doi:10.1016/j.jacep.2024.05.036

Bers, D. M. (2002). Cardiac excitation-contraction coupling. *Nature* 415, 198–205. doi:10.1038/415198a

Blackwell, D. J., Faggioni, M., Wleklinski, M. J., Gomez-Hurtado, N., Venkataraman, R., Gibbs, C. E., et al. (2022). The Purkinje-myocardial junction is the anatomic origin of ventricular arrhythmia in CPVT. *JCI Insight* 7, e151893. doi:10.1172/jci.insight.151893

Bogun, F., Good, E., Reich, S., Elmouchi, D., Igic, P., Tschopp, D., et al. (2006). Role of Purkinje fibers in post-infarction ventricular tachycardia. *J. Am. Coll. Cardiol.* 48, 2500–2507. doi:10.1016/j.jacc.2006.07.062

Bootman, M. D., Smyrnias, I., Thul, R., Coombes, S., and Roderick, H. L. (2011). Atrial cardiomyocyte calcium signalling. *Biochim. Biophys. Acta. Mol. Cell Res.* 1813, 922–934. doi:10.1016/j.bbamcr.2011.01.030

Boyden, P. A., and Ter Keurs, H. (2005). Would modulation of intracellular Ca2+ be antiarrhythmic? *Pharmacol. Ther.* 108, 149–179. doi:10.1016/j.pharmthera.2005.03.011

Boyden, P. A., Albala, A., and Dresdner, K. P. (1989). Electrophysiology and ultrastructure of canine subendocardial Purkinje cells isolated from control and 24-hour infarcted hearts. *Circ. Res.* 65, 955–970. doi:10.1161/01.RES.65.4.955

Boyden, P. A., Pu, J., Pinto, J., and Ter Keurs, HEDJ (2000). Ca2+ transients and Ca2+ waves in purkinje cells: role in action potential initiation. *Circ. Res.* 86, 448–455. doi:10.1161/01.RES.86.4.448

Boyden, P. A., Barbhaiya, C., Lee, T., and Ter Keurs, HEDJ (2003). Nonuniform Ca 2+ transients in arrhythmogenic Purkinje cells that survive in the infarcted canine heart. *Cardiovasc Res.* 57, 681–693. doi:10.1016/s0008-6363(02)00725-3

Boyden, P. A., Hirose, M., and Dun, W. (2010). Cardiac Purkinje cells. *Hear Rhythm* 7, 127–135. doi:10.1016/j.hrthm.2009.09.017

Charton, J., Tixier, R., Sacher, F., Hocini, M., Haissaguerre, M., and Duchateau, J. (2023). Stepwise ablation strategy for post–myocardial infarction ventricular fibrillation: from arrhythmia suppression to ablation. *Hear Case Rep.* 9, 133–137. doi:10.1016/j.hrcr.2022.10.021

Chen, H., Valle, G., Furlan, S., Nani, A., Gyorke, S., Fill, M., et al. (2013). Mechanism of calsequestrin regulation of single cardiac ryanodine receptor in normal and pathological conditions. *J. Gen. Physiol.* 142, 127–136. doi:10.1085/jgp.201311022

Cordeiro, J. M., Spitzer, K. W., and Giles, W. R. (1998). Repolarizing K+ currents in rabbit heart Purkinje cells. *J. Physiol.* 508, 811–823. doi:10.1111/j.1469-7793.1998.811bp.x

Cordeiro, J. M., Spitzer, K. W., Giles, W. R., Ershler, P. E., Cannell, M. B., and Bridge, J. H. B. (2001). Location of the initiation site of calcium transients and sparks in rabbit heart Purkinje cells. *J. Physiol.* 531, 301–314. doi:10.1111/j.1469-7793.2001.0301i.x

Dangman, K. H., Danilo, P., Hordof, A. J., Mary-Rabine, L., Reder, R. F., and Rosen, M. R. (1982). Electrophysiologic characteristics of human ventricular and Purkinje fibers. *Circulation* 65, 362–368. doi:10.1161/01.cir.65.2.362

Daniels, R. E., Haq, K. T., Miller, L. S., Chia, E. W., Miura, M., Sorrentino, V., et al. (2017). Cardiac expression of ryanodine receptor subtype 3; a strategic component in the intracellular Ca2 + release system of Purkinje fibers in large mammalian heart. *J. Mol. Cell Cardiol.* 104, 31–42. doi:10.1016/j.yjmcc.2017.01.011

Di Maio, A., Ter, K. H. E., and Franzini-Armstrong, C. (2007). T-tubule profiles in Purkinje fibres of mammalian myocardium. *J. Muscle Res. Cell Motil.* 28, 115–121. doi:10.1007/s10974-007-9109-6

Dosdall, D. J., Cheng, K.-A., Huang, J., Allison, J. S., Allred, J. D., Smith, W. M., et al. (2007). Transmural and endocardial Purkinje activation in pigs before local myocardial activation after defibrillation shocks. *Hear Rhythm* 4, 758–765. doi:10.1016/j.hrthm.2007.02.017

Dun, W., and Boyden, P. A. (2008). The Purkinje cell; 2008 style. *J. Mol. Cell Cardiol.* 45, 617–624. doi:10.1016/j.yjmcc.2008.08.001

Durrer, D., van Dam, R. T., Freud, G. E., Janse, M. J., Meijler, F. L., and Arzbaecher, R. C. (1970). Total excitation of the isolated human heart. *Circulation* 41, 899–912. doi:10.1161/01.CIR.41.6.899

Fabiato, A. (1983). Calcium-induced release of calcium from the cardiac sarcoplasmic reticulum. *Am. J. Physiol. Cell Physiol.* 245, C1–C14. doi:10.1152/ajpcell.1983.245.1.C1

Faggioni, M., and Knollmann, B. C. (2012). Calsequestrin 2 and arrhythmias. *Am. J. Physiol. Hear Circ. Physiol.* 302, 1250–1260. doi:10.1152/ajpheart.00779.2011

Forsgren, S., and Thornell, L.-E. (1981). The development of Purkinje fibres and ordinary myocytes in the bovine fetal heart. An ultrastructural study. *Anat. Embryol.* 162, 127–136. doi:10.1007/BF00306485

Frampton, J., Ortengren, A. R., and Zeitler, E. P. (2023). Arrhythmias after acute myocardial infarction. *Yale J. Biol. Med.* 96, 83–94. doi:10.59249/LSWK8578

Franzini-Armstrong, C., Protasi, F., and Ramesh, V. (1999). Shape, size, and distribution of Ca2+ release units and couplons in skeletal and cardiac muscles. *Biophys. J.* 77, 1528–1539. doi:10.1016/S0006-3495(99)77000-1

Gadsby, D. C., and Cranefield, P. F. (1977). Two levels of resting potential in cardiac purkinje fibers. *J. Gen. Physiol.* 70, 725–746. doi:10.1085/jgp.70.6.725

Galimberti, E. S., and Knollmann, B. C. (2011). Efficacy and potency of class I antiarrhythmic drugs for suppression of Ca 2+ waves in permeabilized myocytes lacking calsequestrin. *J. Mol. Cell Cardiol.* 51, 760–768. doi:10.1016/j.yjmcc.2011.07.002

Garcia-Bustos, V., Sebastian, R., Izquierdo, M., Molina, P., Chorro, F. J., and Ruiz-Sauri, A. (2017). A quantitative structural and morphometric analysis of the Purkinje network and the Purkinje–myocardial junctions in pig hearts. *J. Anat.* 230, 664–678. doi:10.1111/joa.12594

Gettes, L., and Surawicz, B. (1968). Effects of low and high concentrations of potassium on the simultaneously recorded Purkinje and ventricular action potentials of the perfused pig moderator band. *Circ. Res.* 23, 717–729. doi:10.1161/01.res.23.6.717

Gil, W. W., and Hess, P. (1984). Excitation-contraction coupling in cardiac purkinje fibers: effects of cardiotonic steroids on the intracellular [Ca2+] transient, membrane potential, and contraction. *J. Gen. Physiol.* 83, 395–415. doi:10.1085/jgp.83.3.395

Gómez-Torres, F. A., Estupiñán, H. Y., and Ruíz-Saurí, A. (2021). Morphometric analysis of cardiac conduction fibers in horses and dogs, a comparative histological and immunohistochemical study with findings in human hearts. *Res. Vet. Sci.* 135, 200–216. doi:10.1016/j.rvsc.2021.02.013

Haissaguerre, M., Vigmond, E., Stuyvers, B., Hocini, M., and Bernus, O. (2016). Ventricular arrhythmias and the his-Purkinje system. *Nat. Rev. Cardiol.* 13, 155–166. doi:10.1038/nrcardio.2015.193

Haq, K. T., Daniels, R. E., Miller, L. S., Miura, M., ter Keurs, HEDJ, Bungay, S. D., et al. (2013). Evoked centripetal Ca2+ mobilization in cardiac Purkinje cells: insight from a model of three Ca2+ release regions. *J. Physiol.* 591, 4301–4319. doi:10.1113/jphysiol.2013.253583

Herron, T. J., Milstein, M. L., Anumonwo, J., Priori, S. G., and Jalife, J. (2010). Purkinje cell calcium dysregulation is the cellular mechanism that underlies catecholaminergic polymorphic ventricular tachycardia. *Hear Rhythm* 7, 1122–1128. doi:10.1016/j.hrthm.2010.06.010

Hirose, M., Stuyvers, B. D., Dun, W., Ter Keurs, H. E., and Boyden, P. A. (2006). Increased spontaneous Ca2+ release in arrhythmogenic Purkinje cells from infarcted canine heart is due to a lowered threshold of Ca2+ release channels. *Circulation* 114, 9–10.

Hirose, M., Stuyvers, B., Dun, W., ter Keurs, HEDJ, and Boyden, P. A. P. (2008). Function of Ca2+ release channels in Purkinje cells that survive in the infarcted canine heart: a mechanism for triggered Purkinje ectopy. *Circ. Arrhythm. Electrophysiol.* 1, 387–395. doi:10.1161/CIRCEP.107.758110

Ideker, R. E., Kong, W., and Pogwizd, S. (2009). Purkinje fibers and arrhythmias. *Pacing Clin. Electrophysiol.* 32, 283–285. doi:10.1111/j.1540-8159.2008.02232.x

Janse, M. J., and Wit, A. L. (1989). Electrophysiological mechanisms of ventricular arrhythmias resulting from myocardial ischemia and infarction. *Physiol. Rev.* 69, 1049–1169. doi:10.1152/physrev.1989.69.4.1049

Kang, G., Giovannone, S. F., Liu, N., Liu, F. Y., Zhang, J., Priori, S. G., et al. (2010). Purkinje cells from RyR2 mutant mice are highly arrhythmogenic but responsive to targeted therapy. *Circ. Res.* 107, 512–519. doi:10.1161/CIRCRESAHA.110.221481

Kanter, H. L., Laing, J. G., Beau, S. L., Beyer, E. C., and Saffitz, J. E. (1993). Distinct patterns of connexin expression in canine Purkinje fibers and ventricular muscle. *Circ. Res.* 72, 1124–1131. doi:10.1161/01.res.72.5.1124

Landstrom, A. P., Dobrev, D., and Wehrens, X. H. T. (2017). Calcium signaling and cardiac arrhythmias. *Circ. Res.* 120, 1969–1993. doi:10.1161/CIRCRESAHA.117.310083

Lelovas, P. P., Kostomitsopoulos, N. G., and Xanthos, T. T. (2014). A comparative anatomic and physiologic overview of the porcine heart. *J. Am. Assoc. Lab. Anim. Sci.* 53, 432–438.

Lüss, H., Boknıék, P., Heusch, G., Müller, F. U., Neumann, J., Schmitz, W., et al. (1998). Expression of calcium regulatory proteins in short-term hibernation and stunning in the *in situ* porcine heart1. *Cardiovasc Res.* 37, 606–617. doi:10.1016/S0008-6363(97)00238-1

Mackenzie, L., Roderick, H. L., Berridge, M. J., Conway, S. J., and Bootman, M. D. (2004). The spatial pattern of atrial cardiomyocyte calcium signalling modulates contraction. *J. Cell Sci.* 117, 6327–6337. doi:10.1242/jcs.01559

Mangoni, M. E., and Nargeot, J. (2008). Genesis and regulation of the heart automaticity. *Physiol. Rev.* 88, 919–982. doi:10.1152/physrev.00018.2007

Martinez-Palomo, A., Alanis, J., and Benitez, D. (1970). Transitional cardiac cells of the conductive system of the dog heart: distinguishing morphological and electrophysiological features. *J. Cell Biol.* 47, 1–17. doi:10.1083/jcb.47.1.1

Matsushita, T., Oyamada, M., Fujimoto, K., Yasuda, Y., Masuda, S., Wada, Y., et al. (1999). Remodeling of cell-cell and cell-extracellular matrix interactions at the border zone of rat myocardial infarcts. *Circ. Res.* 85, 1046–1055. doi:10.1161/01.RES.85.11.1046

Miquerol, L., Moreno-Rascon, N., Beyer, S., Dupays, L., Meilhac, S. M., Buckingham, M. E., et al. (2010). Biphasic development of the mammalian ventricular conduction system. *Circ. Res.* 107, 153–161. doi:10.1161/CIRCRESAHA.110.218156

Mobley, B. A., and Page, E. (1972). The surface area of sheep cardiac Purkinje fibres. *J. Physiol.* 220, 547–563. doi:10.1113/jphysiol.1972.sp009722

Nogami, A. (2011). Purkinje-related arrhythmias. *J. Arrhythmia* 27, 6–27. doi:10.1016/s1880-4276(11)80004-9

Nogami, A., Komatsu, Y., Talib, A. K., Phanthawimol, W., Naeemah, Q. J., Haruna, T., et al. (2023). Purkinje-related ventricular tachycardia and ventricular fibrillation: solved and unsolved questions. *JACC Clin. Electrophysiol.* 9, 2172–2196. doi:10.1016/j.jacep.2023.05.040

Oliphant, L., and Loewen, R. (1976). Filament systems in Purkinje cells of the sheep heart: possible alterations of myofibrillogenesis. *J. Mol. Cell Cardiol.* 8, 76AD.

Ono, N., Yamaguchi, T., Ishikawa, H., Arakawa, M., Saikawa, T., Shimada, T., et al. (2009). Morphological varieties of the Purkinje fiber network in mammalian hearts, as revealed by light and electron microscopy. *Arch. Histol. Cytol.* 72, 139–149. doi:10.1679/aohc.72.139

Pauziene, N., Rysevaite-Kyguoliene, K., Alaburda, P., Pauza, A. G., Skukauskaite, M., Masaityte, A., et al. (2017). Neuroanatomy of the pig Cardiac ventricles. A stereomicroscopic, confocal and electron microscope study. *Anat. Rec.* 300, 1756–1780. doi:10.1002/ar.23619

Priori, S. G., and Chen, S. R. W. (2011). Inherited dysfunction of sarcoplasmic reticulum Ca2+ handling and arrhythmogenesis. *Circ. Res.* 108, 871–883. doi:10.1161/CIRCRESAHA.110.226845

Reder, R. F., Miura, D. S., Danilo, P., and Rosen, M. R. (1981). The electrophysiological properties of normal neonatal and adult canine cardiac Purkinje fibers. *Circ. Res.* 48, 658–668. doi:10.1161/01.res.48.5.658

Rosati, B., Dun, W., Hirose, M., Boyden, P. A., and McKinnon, D. (2007). Molecular basis of the T- and L-type Ca2+ currents in canine Purkinje fibres. *J. Physiol.* 579, 465–471. doi:10.1113/jphysiol.2006.127480

Saitoh, H., Bailey, J. C., and Surawicz, B. (1989). Action potential duration alternans in dog Purkinje and ventricular muscle fibers. Further evidence in support of two different mechanisms. *Circulation* 80, 1421–1431. doi:10.1161/01.cir.80.5.1421

Sattler, S. M., Skibsbye, L., Linz, D., Lubberding, A. F., Tfelt-Hansen, J., and Jespersen, T. (2019). Ventricular arrhythmias in first acute myocardial infarction: epidemiology,

mechanisms, and interventions in large animal models. *Front. Cardiovasc Med.* 6, 158. doi:10.3389/fcvm.2019.00158

Sivagangabalan, G., Nazzari, H., Bignolais, O., Maguy, A., Naud, P., Farid, T., et al. (2014). Regional ion channel gene expression heterogeneity and ventricular fibrillation dynamics in human hearts. *PLoS One* 9, e82179. doi:10.1371/journal.pone.0082179

Šolc, D. (2007). The heart and heart conducting system in the kingdom of animals: a comparative approach to its evolution. *Exp. Clin. Cardiol.* 12, 113–118.

Sommer, J. R., and Johnson, E. A. (1968). Cardiac muscle. A comparative study of Purkinje fibers and ventricular fibers. *J. Cell Biol.* 36, 497–526. doi:10.1083/jcb.36.3.497

Sommer, J. R., and Johnson, E. A. (1970). Comparative ultrastructure of cardiac cell membrane specializations. A review. *Am. J. Cardiol.* 25, 184–194. doi:10.1016/0002-9149(70)90578-3

Stankovičová, T., Bito, V., Heinzel, F., Mubagwa, K., and Sipido, K. R. (2003). Isolation and morphology of single Purkinje cells from the porcine heart. *Gen. Physiol. Biophys.* 22, 329–340.

Stuyvers, B. D., Dun, W., Matkovich, S., Sorrentino, V., Boyden, P. A., and Ter Keurs, HEDJ (2005). Ca2+ sparks and waves in canine Purkinje cells: a triple layered system of Ca2+ activation. *Circ. Res.* 97, 35–43. doi:10.1161/01.res.0000173375.26489.fe

Sun, B., Ni, M., Li, Y., Song, Z., Wang, H., Zhu, H. L., et al. (2025). Inositol 1,4,5-Trisphosphate receptor 1 gain-of-function increases the risk for cardiac arrhythmias in mice and humans. *Circulation* 151, 847–862. doi:10.1161/CIRCULATIONAHA.124.070563

Ter Keurs, HEDJ, and Boyden, P. A. (2007). Calcium and arrhythmogenesis. *Physiol. Rev.* 87, 457–506. doi:10.1152/physrev.00011.2006

Ter Keurs, HEDJ, Wakayama, Y., Miura, M., Shinozaki, T., Stuyvers, B. D., Boyden, P. A., et al. (2006). Arrhythmogenic Ca^{2+} release from cardiac myofilaments. *Prog. Biophys. Mol. Biol.* 90, 151–171. doi:10.1016/j.pbiomolbio.2005.07.002

Tseng, G. N., and Boyden, P. A. (1989). Multiple types of Ca2+ currents in single canine Purkinje cells. *Circ. Res.* 65, 1735–1750. doi:10.1161/01.RES.65.6.1735

Vaidyanathan, R., O'Connell, R. P., Deo, M., Milstein, M. L., Furspan, P., Herron, T. J., et al. (2013). The ionic bases of the action potential in isolated mouse cardiac Purkinje cell. *Hear Rhythm* 10, 80–87. doi:10.1016/j.hrthm.2012.10.002

Vassalle, M. (1977). The relationship among cardiac pacemakers. Overdrive suppression. *Circ. Res.* 41, 269–277. doi:10.1161/01.RES.41.3.269

Verkerk, A. O., Veldkamp, M. W., Abbate, F., Antoons, G., Bouman, L. N., Ravesloot, J. H., et al. (1999). Two types of action potential configuration in single cardiac Purkinje cells of sheep. *Am. J. Physiol. Hear Circ. Physiol.* 277, H1299–H1310. doi:10.1152/ajpheart.1999.277.4.h1299

Vigmond, E. J., and Stuyvers, B. D. (2016). Modeling our understanding of the his-Purkinje system. *Prog. Biophys. Mol. Biol.* 120, 179–188. doi:10.1016/j.pbiomolbio.2015.12.013

Webster, K. A. (2012). Mitochondrial membrane permeabilization and cell death during myocardial infarction: roles of calcium and reactive oxygen species. *Future Cardiol.* 8, 863–884. doi:10.2217/fca.12.58

Willis, R., and Oliveira, P. (2018). *Guide to canine and feline electrocardiography*. Hoboken, New Jersey: Wiley.

Xing, D., and Martins, J. B. (2001). Myocardial ischemia-reperfusion damage impacts occurrence of ventricular fibrillation in dogs. *Am. J. Physiol. Heart Circ. Physiol.* 280, H684–H692. doi:10.1152/ajpheart.2001.280.2.H684

Frontiers in Physiology

Understanding how an organism's components work together to maintain a healthy state

The second most-cited physiology journal, promoting a multidisciplinary approach to the physiology of living systems - from the subcellular and molecular domains to the intact organism and its interaction with the environment.

Discover the latest Research Topics

See more →

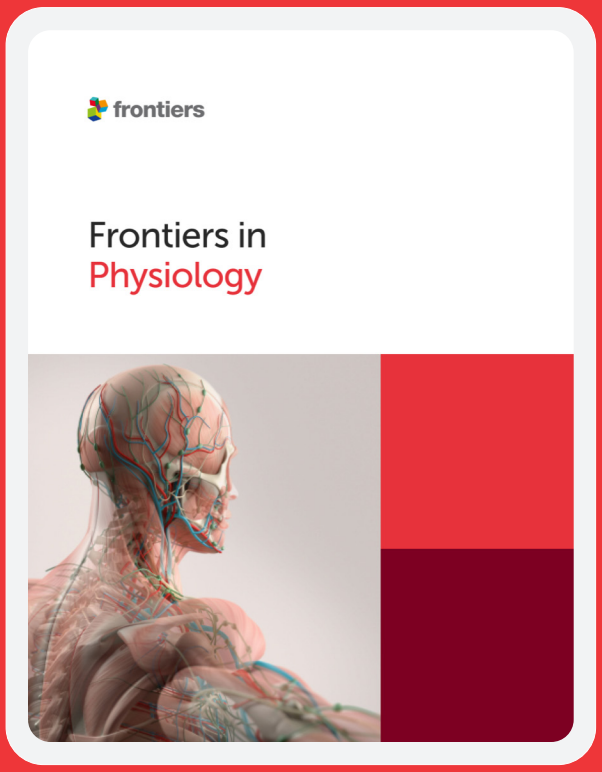

Frontiers

Avenue du Tribunal-Fédéral 34
1005 Lausanne, Switzerland
frontiersin.org

Contact us

+41 (0)21 510 17 00
frontiersin.org/about/contact